De l'astrophysique des amas de galaxies à la physique des microcalorimètres en rayons X : performances scientifiques et calibration du X-ray integral field unit de la mission Athena

Edoardo Cucchetti

THÈSE

En vue de l'obtention du

DOCTORAT DE L'UNIVERSITÉ DE TOULOUSE

Délivré par : *l'Université Toulouse 3 Paul Sabatier (UT3 Paul Sabatier)*

Présentée et soutenue le *01/10/2019* **par :**

Edoardo CUCCHETTI

De l'astrophysique des amas de galaxies à la physique des microcalorimètres en rayons X : performances scientifiques et calibration du X-ray Integral Field Unit de la mission *Athena*

JURY

Sophie HENROT-VERSILLE	Directeur de Recherche	Présidente du jury
Jelle KAASTRA	Professeur des Universités	Rapporteur
Alessandro MONFARDINI	Directeur de Recherche	Rapporteur
Doreen WERNICKE	Ingénieure	Examinateur
François PAJOT	Directeur de Recherche	Directeur de thèse
Etienne POINTECOUTEAU	Directeur de Recherche	Directeur de thèse

---

École doctorale et spécialité :
SDU2E : Astrophysique, Sciences de l'Espace, Planétologie
Unité de Recherche :
Institut de Recherche en Astrophysique et Planétologie (UMR 5277)
Directeur(s) de Thèse :
François PAJOT et *Etienne POINTECOUTEAU*
Rapporteurs :
Jelle KAASTRA et *Alessandro MONFARDINI*

A tutti coloro che mi sono accanto,
per il vostro sostegno e i vostri incoraggiamenti.

A tutti coloro che non ci sono più,
il vostro ricordo è sempre presente.

A tutti,
per avermi sopportato
e per dover continuare a farlo.

Abstract

Future breakthroughs in X-ray astronomy require a new generation of X-ray instruments, capable of observing the sky with high spectral and spatial resolutions combined. This need drives the development of the X-ray Integral Field Unit (X-IFU) onboard the future European X-ray observatory *Athena*, scheduled for a launch in 2031.

The complexity of the X-IFU and of its readout chain calls for a close monitoring of its instrumental effects. This can be investigated using dedicated end-to-end simulators, which reproduce an X-ray observation, from the emission of X-rays by an astrophysical source to their detection. In the first part of this thesis, I use this approach to quantify the impact of crosstalk between pixels, to derive the requirement on the reproducibility of the instrumental background, and to estimate the line sensitivity of the instrument. I demonstrate that the X-IFU will be capable of observing bright extended sources with a required high-resolution throughput above 80%. I also show that an accurate knowledge of the spectral lines (their energy and their profile), as well as of the non-X-ray background level (to better than 2%) are needed to minimise systematic errors in the observation.

Analysis of the instrumental effects need to be coupled with feasibility studies of the core science objectives of the X-IFU to verify the potential of the instrument. This is valid in particular for extended sources, which will use this integral field unit at its full capabilities. In the second part of this work, I investigate the ability of the X-IFU to characterise the properties of the intra-cluster medium and its turbulent motions. To guarantee a representative result, both toy models and hydrodynamical simulations of clusters are used as inputs of end-to-end simulations. My results underline the strengths of the X-IFU, which will provide an accurate view of the physics and the chemical enrichment of clusters, even at high redshift ($z \sim 2$) with typical 100 ks exposure. I also put forward an analytical way to estimate the systematic errors on line diagnostics in turbulence-related studies, which will be of particular interest to optimise future observations.

To fulfil its science objectives, the X-IFU will require a careful calibration. The third part of this thesis presents studies on this topic related to the energy scale, the instrumental background, or the quantum efficiency. I demonstrate that new methods of gain drift correction and background monitoring are required to meet the expected requirements. These results provide constraints on the design of the instrument (e.g., modulated X-ray sources, correction strategies) and can be used to plan ground or in-flight calibration activities. Calibration studies will also be performed experimentally, notably using the test bench developed and characterised at IRAP during my thesis.

Key words: Calibration – Clusters of galaxies – Cryogenic detection – End-to-end simulations – Feasibility studies – Instrumental performance – X-ray astronomy – X-IFU

Résumé

Des découvertes inédites dans le domaine de l'astronomie en rayons X nécessitent une nouvelle génération d'instruments, pouvant observer le ciel en combinant des hautes résolutions spatiales et spectrales. Ce besoin constitue le fondement du X-ray Integral Field Unit (X-IFU) de la mission *Athena* de l'ESA, dont le lancement est prévu en 2031.

La complexité de la chaîne de détection du X-IFU nécessite un suivi de ses perturbations instrumentales. Des simulations bout-à-bout, reproduisant les observations en rayons X de l'émission des photons d'une source représentative à leur détection, sont un outil de choix pour ces études. Dans la première partie de cette thèse, j'utilise ces simulateurs pour quantifier l'effet de la diaphonie entre les pixels, pour dériver une spécification sur la connaissance du bruit de fond instrumental, ou encore pour estimer la sensibilité spectrale de l'instrument. Mes résultats confirment que le X-IFU atteindra ses exigences en taux de comptage pour des sources étendues brillantes. Ils démontrent aussi qu'une bonne connaissance des raies spectrales, ainsi que du niveau bruit de fond instrumental (à mieux que 2%) est indispensable pour éviter des erreurs systématiques dans le traitement des données.

L'analyse des performances doit cependant être couplée à des études de faisabilité des objectifs scientifiques du X-IFU. Cela concerne particulièrement les observations de sources étendues, qui feront appel à tout le potentiel de l'instrument. La deuxième partie de ce travail analyse les capacités du X-IFU à caractériser les propriétés physiques et chimiques du milieu intra-amas, ainsi que sa turbulence. Pour obtenir des simulations représentatives, des modèles ou d'autres simulations numériques sont utilisés comme point de départ de ces études. Mes résultats montrent la puissance du X-IFU à mesurer les propriétés des amas de galaxies, même à haut redshift ($z \sim 2$) et sur des temps d'exposition de 100 ks. Je présente également une nouvelle façon d'aborder les biais sur les diagnostics spectraux. Elle permettra d'optimiser les observations de la turbulence dans les amas.

Enfin, pour remplir ses objectifs scientifiques, le X-IFU nécessitera une calibration très précise. La troisième partie de cette thèse aborde différents points de la calibration du X-IFU, notamment la connaissance de son échelle de gain, de son efficacité quantique et de son bruit de fond instrumental. Je démontre que de nouvelles méthodes de correction de gain et de surveillance du niveau de bruit de fond instrumental sont nécessaires pour vérifier les spécifications attendues. Ces résultats permettent d'optimiser l'architecture de l'instrument (par ex., sources modulées de rayons X, stratégies de corrections) et de mieux préparer ses phases de calibration au sol et en vol. Les études de calibration se feront aussi et surtout par des essais en conditions représentatives, comme dans le banc cryogénique développé et caractérisé à l'IRAP au cours de ma thèse.

Mots clés : Amas de galaxies – Astronomie rayons X – Calibration – Détection cryogénique – Études de faisabilité – Performances instrumentales – Simulations end-to-end – X-IFU

Contents

Acknowledgements

Here we are, the end of three years of hard work, of excitement and of adventures. To be honest, I never thought my thesis would turn out as it did. It was a wonderful (and overall fun) experience, and I learnt more than I could ever imagine on science, on soft skills and on myself. This would not have been possible without all the people I met over these last years. You are all thanked. These acknowledgements will be multi-lingual, as a proper polyglot it is my duty to thank people in their corresponding language. Hopefully I did not forget anyone, if I did, you are thanked nonetheless. Please take into account this is not an easy exercise (and please do complain, at least it gives us an excuse to chat !)

First and foremost, I would like to thank Prof. Dr. Jelle Kaastra and Dr. Alessandro Monfardini for reviewing this manuscript with a keen eye, as well as for their implication over the course of the defence. My gratitude also extends to all the other members of my jury (present or not), Dr. Sophie Hernot-Versillé, Prof. Peter Von Ballmoos, Ms. Doreen Wernicke and Prof. Dr. Joern Wilms.

Mes remerciements s'étendent ensuite à toute l'équipe de l'IRAP travaillant sur le X-IFU. Tout d'abord je voudrais remercier Didier Barret, qui a su me faire confiance depuis mon stage et sans qui je ne serais pas là aujourd'hui. Merci également à mes maîtres de thèse, Etienne Pointecouteau et François Pajot, pour votre soutien et votre aide au cours de ma thèse, pour ces discussions interminables sur les fits de 1000 spectres avec Etienne (sic), ou encore pour les diverses conversations à rallonge sur la calibration dans ton bureau François (dérangeant d'abord Gabriele, puis Morgane !). Les tigres ne seraient pas au complet sans remercier Laurent Ravera (avec mes questions pointues, ou pédantes, au choix, et mes envies de courir), Nicolas Clerc (pour des après-midis à faire des calculs de turbulence à n'en plus finir), Gabriele Betancourt-Martinez (qui m'a « suivi » du Goddard à l'IRAP), Mégane Hébert (et nos allers-retours sur le film X-IFU) et Natalie Webb (de prof du master à amie). Merci aussi à toute l'équipe du banc de test lors de nos travaux – Gilles, Michel, Bernard, Baptiste, Sophie – et les divers stagiaires sans qui les manips et simus n'auraient pas beaucoup avancé lors de ma rédaction (Annaelle, Thomas, Raphaël, Simon, James, Mehdy, Mélina). Au bout de trois ans, je me sens véritablement intégré dans cette équipe. Ce sera difficile de vous quitter. J'étends les remerciements à ceux avec qui j'ai travaillé, que ce soit sur X-IFU ou pas. Merci donc à Ludovik, Eric, David, Odile,

Christophe, Antoine, Maëva, Pierre, Olivier, Peter, Geneviève, Pierre-Yves, Pierrick, Yann, Michael et Martin.

C'est ensuite autour de toute l'équipe du CNES X-IFU que j'ai pu côtoyer au cours de réunions de travail, réunions projet, conférences et autres évenéments. Une mention très particulière à Philippe Peille (Ppeille !), ô grand prédécesseur de thèse, sans qui mon travail aurait été bien plus difficile. Ce fut un honneur de débugger tes codes de simulations d'amas ! Merci de ton aide, de ta disponibilité pendant des appels téléphoniques à en plus en finir (je connais ton numéro maintenant !) et de ton soutien au cours de la thèse (plus les petites questions innocentes du style « et au fait ... »). Merci enfin à Thien pour ta confiance en moi, et pour m'avoir aidé à réaliser un rêve, intégrer le CNES à partir d'octobre 2019 (je passe « de l'autre côté de la clôture », comme dirait Didier).

I would like to thank also the team at NASA Goddard Space Flight Center for their help during my thesis, and for welcoming me during my internship. Thanks to Antoine, Caroline, Kazu, Nick, Joe, Richard, Scott, Simon, Sophie (among us too), Steve, and Wonsik. Most of all, I would like to thank Megan Eckart (back in California now) for what you have done during these three years. Working alongside you at GSFC, then during my thesis was very rewarding. Vielen dank auch an der Gruppe im Bamberg : Christian, Joern, Max, Thomas. Arbeiten zusammen war prima, und ich verbracht ein wunderschönes hackathon Woche in Bamberg. Grazie anche a tutti gli italiani con cui ho lavorato in questi ultimi anni, Simone, Claudio, Luigi, Silvano, Fabio, Veronica, Elena, Mauro, Massimo (entrambi !), Stefano (entrambi !) e Luca (è sempre un piacere chiederti un milioncino di tabelle di yields !). Finally, thanks to all those within or outside the consortium with whom I had the chance to interact (in particular François Mernier, Samantha Stevers, and Roland den Hartog).

Viennent maintenant les remerciements plus personnels, à ceux et celles qui ont rendu la thèse plus que trois ans de travail (ou pas !) dans le bureau J014bis. En premier, et je ne peux m'en passer, je voudrais remercier mon Tusken préféré, un homme hors pair par sa (non) présence mentale et/ou physique, j'ai nommé mon co-bureau Paul ! Et n'oublions pas l'équipe du J014 (mon secretariat), celle historique avec Thomas (si si la famille) et la nouvelle avec Mathias et Abraham. Un souvenir pour tous les stagiaires ou doctorants qui ont subi Paul et moi, i.e. Cyril (pupuuuce !), Virginie (Vivi !), Tiziana (« l'autre » disait Paul), Annaelle (« la stagiaire » disait Paul) et enfin Sophie (qui a piqué la place de Paul) et Mélina (qui n'a jamais connu Paul). Mes plus grands remerciements vont à l'équipe des « Bras Cassés », à Didi, Jeff, Louise, Mathilde (ou Matchilde ?) et Pauline. Des recontres superbes et des beaux moments (à l'interieur d'une salle d'escape game, autour d'un apéro, à regarder la télévision (Deniiiiiiiis) ou simplement au quotidien). Merci aussi aux 3D et nos playlists. Merci à Jeff et Babak, compagnons d'escapades à deux roues, en plaine ou dans les cols (facile le col de Menté non Babak ?). Merci enfin à l'équipe du tarot, là aussi celle historique (Annick et ses plis au féminin, David, WRapin et ses randoms valets, Ppeille, Turpin, Fitous', Armelle) et la récente (Didi, Louise, Jeff, Florian, Anthony, Babak, Gaylor, Michmich, Benjamin, Etienne). Merci aux coureurs du marathon, Didier, Laurent et Nicolas, nous avons fait un score digne d'un coureur éthiopien (unijambiste), mais on essaie toujours de s'améliorer ! Le défi est lancé dans le consortium !

Comme ils méritent un paragraphe à part, merci aussi à toute l'équipe d'UniverSCiel pour ces trois ans de péripéties ! Tout d'abord merci aux bureaux respectifs (v1 : Marina,

Jason, Gab, Ppeille – v2 : Didi, Jeff, Ines, Marina, Ppeille – v3 : Sacha, Mika, Babak, Simon, Didi), et tous ceux de l'association : Annick, Niprut, Ppeille, Gab, Jason, Willou (et ses géo-caches), Marina (ou Marinez, ou Rhinez, ou nez), Didi, Jeff, Louise, Mika, Babak, Ines, Amaury (Momo !), Pierre-Marie (<3), Bernard, Sacha(tte), Hadrien, Simon, Anne (ou Neuha, ou ma bonne Anne), Lucile (Lulu, Juju powa, dont l'histoire retiendra qu'elle m'a porté et traîné lors d'un trail), Gabi, David, Claire, Clara, Lucie, Heussaff (il est pas aux toilettes d'ailleurs ?), Margaux, Daniel, Anthony, Nicolas, Sébastien et Chafik. Merci aux élèves de l'IME de Plaisance, à ceux de l'ITEP de Cugnaux et à leurs encadrants. Dédicace aux équipes ballon, à Jipeyyy Mirouze, à la Dacia Logan de l'IRAP (100k !), à Christian et Jean-Claude et tous les radioamateurs du Gers, à l'équipe de Planète Sciences et du F@briquet (Michel et Philippe en particulier), à ceux de Tenum, ainsi qu'à M. Gros (de Gourdon), M. Henault et Mme Louvrier (de Maillergues) : désolé d'avoir fait atterrir des nacelles chez vous, dans le futur, on retentra un étang, comme en 2017.

Merci à tous mes amis de Polytechnique et d'avant qui ont cru en moi (et y croient encore !). Merci à Jeff (aloa houlala), Tîbo et Frobs (félicatations !), Rémi et Albert (best couple ever), Maxime (pour ses tisanes et son hard rock), Louise, Nathan, Tallec, Momo, Raphaël, Tavant et Marmuse. Je tiens à remercier particulièrement Frédéric, aussi appelé Freddick la marmule, ou Freddie la marmelade, pour nos deux ans de vie commune au 54 Rue du Printemps à faire de la mixologie et des rave parties. Tu restera le meilleur des colocs ! Une pensée pour Paul (ou π-Well) pour être une ami hors pair depuis le jour où tu as décidé de te mettre dans mon groupe de colle parce que mon nom sonnait bien ! Tu es le meilleur.

Per finire, vorrei ringraziare i miei genitori, per avermi sempre incoraggiato durante questi tre anni, e mia sorella, Margot, che mi ripeteva di fare una tesi. Ho cercato di non ascoltarla, ma come al solito, non ci sono riuscito. Grazie anche a tutta la mia famiglia, che vedo poco ma che mi è sempre vicina, che siano gli zii, i cugini o i nonni.

Enfin, je remercie ma championne de classe intergalactique, ma meilleure amie et compagne d'aventure, Pauline. J'ai beaucoup bougé depuis qu'on se connaît, mais ma vie n'a vraiment changé que deux fois, quand je t'ai connue et quand tu es venue vivre à Toulouse. Merci pour tout, ce que tu me donnes au quotidien est difficilement repayable, mais je sais te corrompre à coup de bons repas. Tu as été plus qu'un soutien, merci.

Avant-propos

L'Univers tel que nous le voyons aujourd'hui est structuré en une « toile cosmique », composée de larges espaces vides et de filaments de matière. Cette matière progresse le long des filaments, attirée par les surdensités locales générées lors des fluctuations quantiques qui ont eu lieu aux premiers instants de l'Univers. Au croisement de ces filaments, la matière accumulée se découple de l'expansion cosmique pour former des halos de matière massifs, liés par la gravitation. Celle-ci a donné naissance, au cours du temps, aux groupes et amas de galaxies que nous observons aujourd'hui. Ces derniers sont essentiellement composés de matière noire, et seulement $\sim 10\%$ de leur masse totale (entre 10^{13} et $10^{15}\,M_\odot$) est due aux baryons. Parmi cette fraction plus de 85% est sous forme de gaz chaud, composant le milieu intra-amas, tandis que le reste est contenu dans les galaxies de l'amas. Le milieu intra-amas est chauffé par son effondrement gravitationnel à des températures de $10^{7-8}\,\mathrm{K}$ (i.e. 1 à 10 keV), créant ainsi un plasma ionisé optiquement mince, qui se refroidit par émission Bremsstrahlung observable dans les rayons X. Cette émission permet d'étudier le milieu intra-amas de l'Univers local jusqu'à un redshift élevé ($z \sim 2$).

Les amas grandissent par accrétion de matière (matière noire, gaz chaud, galaxies) depuis les filaments auxquels ils sont connectés. Bien que les parties centrales de ces objets soient considérées comme virialisées, cela n'est pas le cas de leurs périphéries, où des chocs d'accrétion, des mouvements grande échelle de gaz induits lors de la formation du halo, ou encore la dissipation d'énergie par le biais de la turbulence perturbent l'équilibre hydrostatique. L'observation du milieu intra-amas, en particulier en périphérie de ces structures, permet donc de mieux comprendre la formation des halos. Cette accrétion et les phénomènes de fusion successifs dans l'histoire du halo ont également modifié l'entropie et les propriétés thermodynamiques au centre des amas. L'étude des profils de température et d'entropie du gaz sont donc des indicateurs de l'évolution de ces objets. La masse des amas est aussi un paramètre important pour la cosmologie, puisque la distribution en masse et en redshift des halos dépend de la densité de matière dans l'Univers et de sa géométrie.

En plus de la gravité, l'équilibre de l'amas est régi par des phénomènes complexes. Le trou noir supermassif au cœur de ces objets en est un exemple. Ce dernier régule la chute du gaz vers le centre de l'amas par de puissants jets. La turbulence du milieu intra-amas induite par le trou noir ou par l'accrétion à grande échelle, ainsi que la dissipation

de l'énergie cinétique due à la viscosité du gaz sont d'autres hypothèses pour expliquer l'équilibre de ces structures. Ces mécanismes sont critiques pour comprendre les amas, car ils relient des échelles allant du kiloparsec au mégaparsec, influençant donc leur évolution. Les éléments atomiques produits au cours de la vie des étoiles sont, au cours du temps, transportés jusque dans le milieu intra-amas par les jets du trou noir central, des vents galactiques, des fusions de galaxies ou par la pression ambiante du milieu intra-amas. Piégés dans ce gaz, ils deviennent des fossiles de l'évolution chimique de l'amas. L'observation de ce contenu métallique grâce à la spectroscopie en rayons X permet ainsi de donner des informations sur l'enrichissement de ces objets (et donc de l'Univers) au cours du temps.

L'astronomie en rayons X permet d'obtenir des informations sur les grandes structures. De nombreuses autres sources et phénomènes énergétiques peuvent également être étudiés via leurs émissions en rayons X. C'est le cas des sursauts Gamma, de la dynamique des trous noirs, de la composition interne d'objets compacts tels que les étoiles à neutrons, ou même des événements observés sur les planètes de notre Système Solaire. L'astronomie en rayons X s'intéresse ainsi à des problématiques de l'Univers chaud et énergétique. Elle cherche notamment à répondre aux deux questions fondamentales suivantes : *« Comment les trous noirs évoluent-ils et comment façonnent-ils l'Univers ?»* et *« Comment la matière ordinaire s'assemble dans les grandes structures que nous voyons aujourd'hui ? »*. La génération actuelle d'observatoires en rayons X, tels *XMM-Newton* et *Chandra*, ainsi que des missions récentes (par ex., *Suzaku*, *Hitomi*) ont obtenu des résultats impressionnants. En revanche, ils ne permettent pas de donner une réponse définitive aux deux questionnements précédents, en raison de leur surface efficace limitée et de leur manque (sauf pour *Hitomi*) de spectroscopie haute résolution résolue spatialement. Pour apporter de nouvelles réponses et pallier le manque de ces capacités, l'Agence Spatiale Européenne a sélectionné, en 2014, l'observatoire en rayons X *Athena* en tant que deuxième mission « Large » du programme scientifique *Cosmic Vision*. Ce dernier est prévu pour un lancement en 2031.

Des deux instruments de cette mission, le X-ray Integral Field Unit (X-IFU) représente un défi de taille pour toute la communauté scientifique. Avec sa matrice de 3168 pixels composée de microcalorimètres supraconducteurs « transition-edge sensor » opérés à une température proche du zéro absolu (90 mK), le X-IFU observera la bande d'énergie de 0.2 à 12 keV avec une résolution spectrale de 2.5 eV jusqu'à 7 keV inclus, ainsi qu'une résolution angulaire de $5''$ sur un champ de vue hexagonal de $5'$ en diamètre équivalent. Les photons X sont arrêtés par les absorbeurs de ces pixels, produisant de la chaleur. Celle-ci sera mesurée comme un changement de résistance, et lue sous polarisation AC grâce à un multiplexage fréquentiel, des étages d'amplification et des boucles de rétroaction actives pour linéariser la chaîne de détection. Pour remplir sa mission, le X-IFU requiert une extrême précision de mesure (stabilité thermique, opérations à températures supraconductrices avec un très faible niveau de bruit, sensibilité des capteurs, lecture rapide à grande dynamique), et manipule des technologies critiques du spatial (convertisseurs numériques/analogiques bas bruit, magnétomètres supraconducteurs SQUIDs, supraconducteurs opérés dans leur transition). Le développement de cet instrument est porté par une collaboration internationale de 13 pays, impliquant plus de 300 ingénieurs et scientifiques à travers le monde.

Le X-IFU est actuellement dans sa phase d'étude de faisabilité et de consolidation. Son développement technologique est motivé par un besoin accru en résolution spectrale. Pour obtenir une configuration optimale qui maximise les résultats scientifiques en vol, une vue

complète du système est nécessaire. Cependant, comme pour de nombreux instruments en développement, le matériel de vol n'est pas encore disponible. Des simulations numériques sont donc indispensables pour comprendre les performances de l'instrument et pour vérifier la cohérence de ses objectifs scientifiques. Des simulateurs « end-to-end » (bout-à-bout) de la chaîne de détection du X-IFU ont ainsi été développés pour ces études (`xifupipeline` et `XIFUSIM`). Ils font encore aujourd'hui l'objet d'améliorations afin de refléter le plus fidèlement possible le futur comportement de l'instrument. L'utilisation de ces simulateurs est nécessaire pour analyser les effets fins de l'environnement sur la performance instrumentale, tels que la diaphonie entre les pixels ou le bruit de fond instrumental, et pour étudier la faisabilité des objectifs scientifiques de la mission. Ils fournissent aussi une manière de tester les outils courants de traitement de données de la communauté. A ce sujet, la mission *Hitomi* a mis en lumière de profondes lacunes dans notre connaissance de la physique atomique et dans la modélisation de raies spectrales. La calibration et les tests au sol du X-IFU seront donc des étapes cruciales de la mission. Au cours de ma thèse, je me suis intéressé à trois problématiques relatives au développement du X-IFU :

- Quels sont les effets des perturbations sur les performances de l'instrument en vol et comment pouvons-nous les quantifier au travers de simulations numériques ?
- Quelles sont les performances scientifiques du X-IFU et comment pouvons-nous les vérifier avant le lancement ?
- Comment calibrer les grandeurs physiques nécessaires à la compréhension des données de vol de l'instrument et comment compenser d'éventuelles erreurs systématiques induites par des incertitudes de calibration ?

Ce manuscrit est la synthèse de mes contributions aux trois questions ci-dessus. En premier lieu, je présente dans le Chapitre 1 une vision générale de l'astronomie en rayons X, afin d'introduire la thématique de l'Univers chaud et énergétique. Je détaille notamment la formation et l'évolution des amas de galaxies, qui ont été un point majeur de mes travaux de thèse. Ce chapitre constitue également un résumé de résultats récents et de questions ouvertes à ce jour dans le domaine de l'astronomie en rayons X. Il démontre ainsi l'importance des nouveaux observatoires spatiaux tels *Athena*. Le Chapitre 2 est dédié à la description du satellite *Athena* et à la configuration de vol du X-IFU, telle que prévue lors de la rédaction de ce manuscrit. L'ensemble de la chaîne instrumentale y est présenté. Le Chapitre 3 met en avant le besoin de simulations numériques pour étudier les performances de l'instrument. En particulier, j'y décris les simulateurs end-to-end de l'instrument, ainsi que les divers modules ajoutés au cours de ma thèse. Des applications de ces simulations à la diaphonie et au bruit de fond instrumental y sont discutées. Les simulations des effets instrumentaux sont importantes, mais se doivent d'être couplées à des études de faisabilité des objectifs scientifiques du X-IFU, afin de mieux en comprendre ses capacités. Cela est d'autant plus critique pour des sources étendues, comme les amas de galaxies, qui profiteront du potentiel de ce spectromètre à intégrale de champ. Ce point est abordé au Chapitre 4 via des simulations end-to-end d'amas de galaxies. Plus particulièrement, j'y analyse les capacités du X-IFU à étudier les grandeurs physiques du milieu intra-amas, son enrichissement chimique et ses mouvements turbulents. La calibration de l'instrument est analysée au Chapitre 5. Ce chapitre regroupe des études réalisées au sein de l'équipe de calibration du X-IFU visant à caractériser des quantités comme l'échelle de gain, l'efficacité

quantique ou encore le bruit de fond instrumental. Pour terminer, je résume au Chapitre 6 les propriétés du banc cryogénique développé à l'IRAP ainsi que les premiers résultats obtenus lors de sa caractérisation. Ce dernier servira à vérifier les spécifications relatives à la calibration et testera la chaîne de lecture numérique de l'instrument.

Foreword

The Universe as we see it today is structured in a cosmic web, composed of large voids and filaments. Matter flows along these filaments and is attracted by the local overdensities, remainders of the quantum fluctuations that occurred in the primordial Universe. At the connection between filaments, the accumulated matter decouples from the cosmic expansion and creates massive halos bound by gravitation. The matter accreted within these halos evolved over time to form the groups and clusters of galaxies we observe today. Clusters are mainly composed of dark matter. Only $\sim 10\%$ of their total mass (between 10^{13} and $10^{15}\,M_{\odot}$) is due to baryons. Among this fraction, $\sim 85\%$ is made of hot gas, composing the intra-cluster medium (ICM), while the rest remains locked within galaxies. The ICM is heated by its gravitational infall in the halo potential well to temperatures of $10^{7-8}\,\mathrm{K}$ (i.e. 1 to 10 keV), creating a fully ionised optically-thin plasma which cools through a Bremsstrahlung radiation observable in the X-rays. This emission allows the study of the ICM from the local Universe up to high redshifts ($z \sim 2$).

Clusters grow through constant accretion of matter (dark matter, clumps of gas, galaxies) from the filaments of the cosmic web to which they connect. Although the central parts of these objects can be considered virialised, this is not the case of their outskirts, where accretion shocks, large-scale movements of gas induced by the halo formation, and dissipation of energy through turbulent eddies break the local equilibrium. Measurements of the gas motions and its turbulence, in particular in the outskirts, is a probe of the cluster assembly. This continuous accretion and the successive merger events of the halo have also modified the entropy and other thermodynamical properties of the gas. Temperature and entropy profiles can therefore provide insight on the evolution of these objects. Clusters masses are key to cosmology as well, as the distribution of halos in mass and in redshift is sensitive to the density of matter and the geometry of the Universe.

Aside from gravitation, the global equilibrium of clusters is governed by complex physical processes. The supermassive black hole (SMBH) within the innermost galaxy plays for instance a major role, as it regulates the gas cooling towards the centre of the cluster through powerful jets and outflows. Turbulence induced by the SMBH and by large-scale motions, and the subsequent dissipation of kinetic energy through small-scale viscosity are also candidates to explain deviations from a purely hydrostatic equilibrium. These

mechanisms are critical to understand, as they bridge scales from the kiloparsec to the megaparsec thus influencing the evolution of these structures. The elements produced by stars are, over time, circulated into the ICM through SMBH outflows, galactic winds, galaxy-galaxy mergers, and ram-stripping pressure by the surrounding ICM. Unaltered and trapped in this hot gas, they became a fossil record of its chemical enrichment. The observation of the ICM atomic content using X-ray spectroscopy thus gives a view of the metal production of these objects (and at the scale of the Universe) across cosmic time.

X-ray astronomy is a powerful tool to derive the properties of large-scale structures. Number of other sources and energetic phenomena can be traced through their X-ray emission, such as the evolution of compact objects, the origins of Gamma-ray bursts, the interiors of neutron stars, or even extreme events occurring within our Solar System. The study of these objects gives information on the hot and energetic Universe, and can bring answers to two larger fundamental questions: *"How do black holes grow and shape the Universe?"* and *"How does ordinary matter assemble into the large-scale structures we observe today?"*. The current generation of active X-ray observatories, including *Chandra*, *XMM-Newton*, as well as other recent missions (e.g. *Suzaku*, *Hitomi*), have obtained outstanding results. However, in most cases, they are no longer sufficient to provide definitive answers on these questions and their declinations, due to their limited effective area and (except for *Hitomi*) their lack of spatially resolved high-resolution spectroscopy. To answer these interrogations and provide these much-needed capabilities, the European Space Agency has selected in 2014 the X-ray observatory *Athena* as its second "Large" mission of the *Cosmic Vision* program. This observatory is scheduled for launch in 2031.

Of the two instruments on board *Athena*, the X-ray Integral Field Unit (X-IFU) represents a challenging and ambitious milestone for the scientific community. With its array of 3168 superconducting transition-edge sensors micro-calorimeter pixels operated at near absolute zero temperatures (90 mK), the X-IFU will provide high-resolution spectroscopy over the 0.2 – 12 keV energy bandpass, with a spectral resolution of 2.5 eV out to 7 keV, and an angular resolution of $5''$ over a hexagonal field-of-view of $5'$ in equivalent diameter. X-rays photons will be stopped by the pixel absorbers, producing heat. This increase in temperature will result in a change of the pixel resistance, read out under AC bias using frequency multiplexing schemes, active amplification at all thermal stages and active feedback loops to linearise the electronics. To fulfil its mission, the X-IFU requires remarkable accuracy in its measurements (thermal stability, extreme low-noise operations at superconducting temperatures, high sensitivities, fast readout with high dynamic ranges) and handles some of the most critical technologies for space applications (high-quality digital-to-analogue converters, superconducting quantum-interference devices, bi-layers of superconductors). The development of the X-IFU is a joint venture between 13 countries, involving more than 300 scientists and engineers across the world.

The X-IFU is undergoing its feasibility and consolidation phases. Its design is driven by the need for an unprecedented spectral resolution. To ensure an optimal configuration and maximise the scientific returns, a view of the integrated capabilities of the system is required. However, as any preliminary instrument, hardware material is not always available at this stage. Numerical simulations are imperative to verify the performances and the coherence of the science objectives laid out for the X-IFU. For these investigations, dedicated end-to-end simulators (`xifupipeline` and `XIFUSIM`) were developed, and are to

this day continuously improved to reflect, as accurately as possible, the behaviour of the instrument. Their use is essential to understand the finest effects on the performance, such as crosstalk between pixels or background, and to assess the feasibility of the X-IFU science objectives. They can also be an interesting way to test our current post-processing tools. In this regard, as highlighted by the recent mission *Hitomi*, the advent of high-resolution spectroscopy demonstrated that our fundamental understanding of X-ray atomic lines and their modelling needs to be improved. The calibration and ground testing of the X-IFU will thus be crucial for the final success of the mission. My thesis took a specific interest into different questions related to the X-IFU development:

- What are the effects of perturbations on the in-flight performances of the instrument, and how can they be quantified using numerical simulations?
- What are the actual scientific performances of the X-IFU and how can we assess the feasibility of the main science cases of the instrument?
- How can we calibrate the physical quantities needed to understand in-flight data of the X-IFU and what are the systematic errors caused by calibration uncertainties?

This manuscript summarises my contributions to the three previous questions. In Chapter 1, I present an overview of X-ray astronomy, and introduce the general context of the hot and energetic Universe. I notably explain the formation and evolution of clusters of galaxy, which were a major topic in my studies. This chapter also provides a summary of recent results and some of the current open questions in X-ray astronomy. It demonstrates the importance of a new generation of X-ray observatories like *Athena*. Chapter 2 is dedicated to the description of the *Athena* satellite and the X-IFU baseline configuration, and details the entire instrumental chain. Chapter 3 puts forward the need for numerical simulations in the investigation of the performance of the instrument. In particular, the instrument-specific simulators are presented, as well as additional models included over the course of my thesis. Several applications on crosstalk studies, background or line sensitivity are discussed. Simulations of instrumental effects are important, but must be coupled with feasibility studies of the main science objective to assess the capabilities of the X-IFU. This is particularly important for the observation of extended sources, which will benefit of the full potential of this integral field unit. Chapter 4 focuses on this specific point, by presenting end-to-end simulations of complex astrophysical sources such as clusters of galaxies. More specifically, I study the ability of the instrument to analyse the intra-cluster medium physical properties, its chemical enrichment across time and its turbulent motions. The calibration of the instrument is discussed in Chapter 5, which describes several studies I conducted as member of the X-IFU calibration team to characterise the energy scale, the quantum efficiency or the background of the instrument. Finally, I outline in Chapter 6 the cryogenic experiment developed at IRAP and its first characterisation results. This bench will be used to test calibration requirements and the digital readout electronics in the years to come.

CHAPTER 1

An introduction to X-ray astronomy

1.1 Observing the X-ray sky

The first evidences of X-ray radiation were reported throughout the 18$^{\text{th}}$ and 19$^{\text{th}}$ century during investigations on high-voltage experiments. The first confirmed detection shortly followed, in 1895, with measurements performed by Röntgen[1] on electrical discharge tubes. A classical nomenclature of X-rays covers the electromagnetic spectrum from ~ 0.025 to 10 nm in wavelength (i.e. energies from 100 eV to $\sim$ 50 keV) between the ultra-violet radiation and the Gamma radiation. X-rays are often divided into two categories: 'soft' X-rays whenever their energy is lower than $\sim 5/10$ keV, or "hard" X-rays otherwise.

1.1.1 How are X-rays observed?

X-rays are rarely met in everyday life, except for medical or scientific use. Most of the 'natural' X-ray radiation seen on Earth is related to the radioactive decay of unstable isotopes. However, due to scattering or photoelectric absorption in the dense Earth's atmosphere, X-rays seldom propagate above a few cm or m in air (Henke et al., 1993). All X-ray astrophysical sources thus appear invisible to a terrestrial observer (see Figure 1.1),

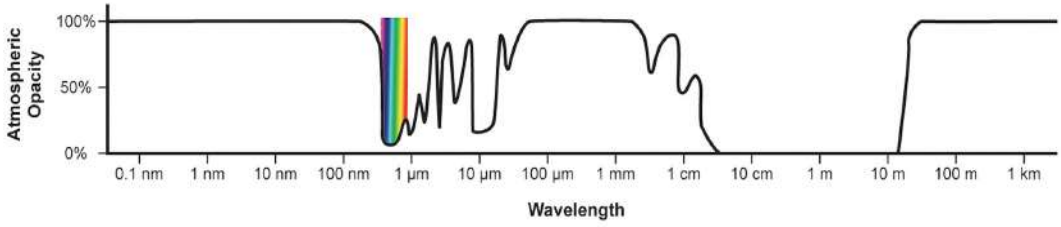

Figure 1.1: Opacity of the atmosphere to the electromagnetic spectrum (shown in terms of wavelength). Visible light is shown (in colours).

[1] Number of languages still define X-rays as "Röntgen radiation".

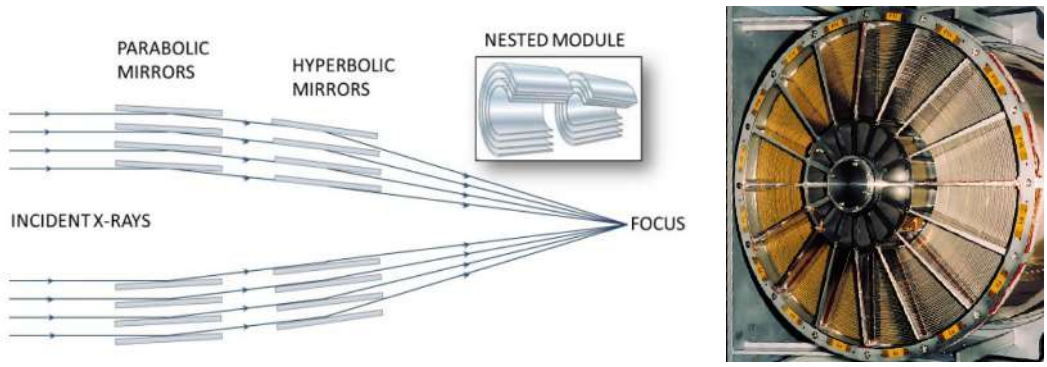

Figure 1.2: (*Left*) Schematic of a Wolter type I telescope (reproduced from Gaskin et al. 2015, Figure 4). (*Right*) *XMM-Newton* Wolter telescope before assembly (Credits: ESA).

and require near-space (e.g. balloons or rockets) or satellite missions to be observed.

X-ray observations of the sky use space-based telescopes, which take advantage of the reflection of X-rays when observed under grazing incidences. Most of the current and foreseen missions use this technique to create so-called 'Wolter'-type telescopes (Figure 1.2) and focus X-ray photons onto a detector plane. Design and efficiency of X-ray detectors has evolved throughout the years (scintillators, proportional counters...). The current generation of space-based soft X-ray detectors is mainly divided into two categories: charged-coupled devices (CCD) detectors, and diffraction gratings.

CCD detectors

Many X-ray instruments are based on CCD detectors. This is notably the case of the advanced CCD imaging spectrometer (ACIS, Garmire et al. 2003) on the *Chandra* space telescope (Weisskopf et al., 2000, 2002), the European photon imaging cameras (EPIC *pn* and MOS, Strüder et al. 2001; Turner et al. 2001) onboard *XMM-Newton* (Jansen et al., 2001), the X-ray imaging spectrometer (XIS, Koyama et al. 2007) on *Suzaku* (Mitsuda et al., 2007), and more recently of the soft x-ray imager (SXI, Tanaka et al. 2018) on the mission *Hitomi* (Takahashi et al., 2018). The main detection principle of these instruments is based on pair-hole recombination in semi-conductors. When an X-ray is absorbed by a CCD, it will generate charges in the detector, which will be read out as a current. The corresponding intensity provides an estimate of the energy of the incident photon.

CCDs are widely used due to their large operational experience in science (e.g. optics, photography), which also enables to readout large matrices of pixels with little complexity. Coupled with a high angular resolution telescope (such as *Chandra*'s $0.5''$ on-axis angular resolution), CCDs provide exquisite images of the X-ray sky (see Fabian et al., 2006; Markevitch & Vikhlinin, 2007). Their intrinsic spectral resolution is however limited to $\sim 100\,\mathrm{eV}$ over the soft X-ray band due to intrinsic semi-conductor properties (Fano noise).

Diffraction gratings

Diffraction gratings are also widely used in X-ray observatories, such as the reflection grating spectrometer (RGS, den Herder et al. 2001) on board *XMM-Newton*, or the high-

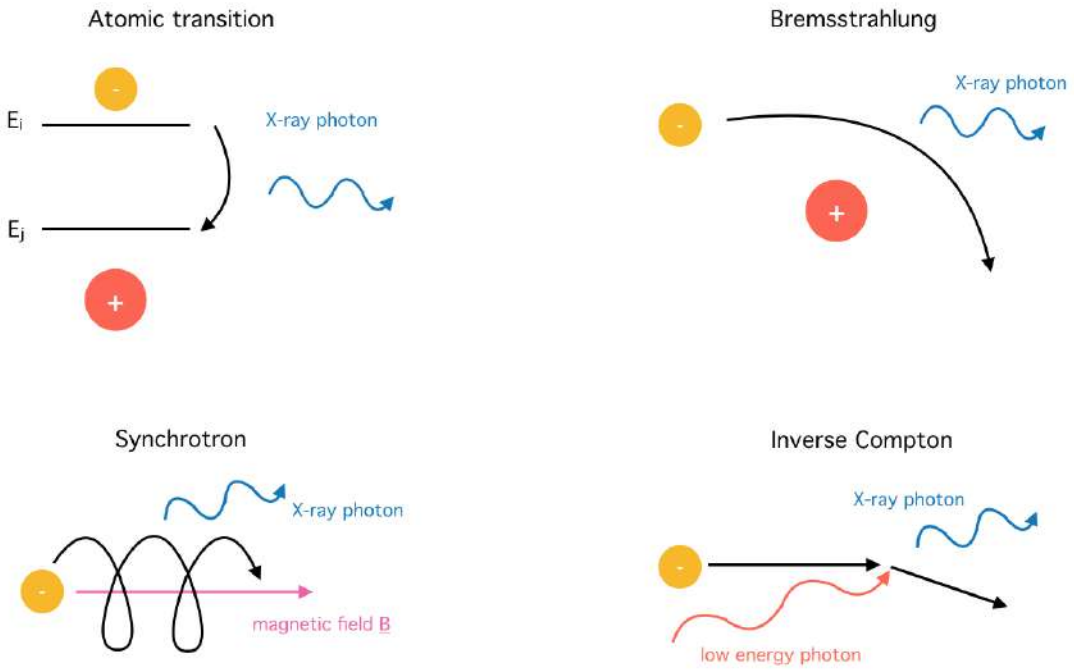

Figure 1.3: Schematic view of the main astrophysical processes producing X-ray emission.

energy transmission grating (HETG, Canizares et al. 2005) on *Chandra*. Diffraction allows the separation of an incoming photon flux according to its wavelength, thus providing high-resolution spectra. However, most of these instruments use the overall incoming flux, at the expense of any spatial resolution. Due to the low mirror effective area at high energies and to dispersion, the use of X-ray gratings is often limited to soft X-ray bands ($\leq 2\,\mathrm{keV}$).

1.1.2 How are astrophysical X-rays created?

The origin of astrophysical X-ray photons can be traced, in general, to four distinct physical mechanisms. Each occurs in certain conditions, and therefore provides a view of the properties of the overall region in which it was created (Figure 1.3).

Atomic transitions of electrons

The most common production mechanism of X-ray photons is related to atomic transitions of electrons within atoms or ions, which create emission or absorption lines. Due to Heisenberg uncertainty principle, electrons populating a level of energy E are never exactly at that given energy level, but verify $\Delta E \Delta t \geq \hbar$. Consequently, each level has a finite lifetime t and electrons may transit between levels by emitting or absorbing a photon.

When solving the equation related to the oscillation of an electron in the potential well of the nucleus (Demtröder, 2003), the probability distribution function $\mathcal{P}$ of the photon emitted/absorbed by an electron transiting between two levels $i \leftrightarrow j$ follows a Lorentzian

distribution. If we note E_0 the energy of this transition (centroid):

$$\mathcal{P}(E, E_0) = \frac{1}{\pi\gamma} \frac{\gamma^2}{(E - E_0)^2 + \gamma^2} \tag{1.1}$$

where γ is the so-called damping factor, related to the lifetime of the transition $i \leftrightarrow j$. Natural atomic lines therefore possess an intrinsic broadening related to quantum physics. Given the distances between L and K shell levels ($\lesssim 1\,\text{nm}$), the associated wavelengths of the transitions photons fall in the X-ray regime. Emission or absorption in the X-rays generally occurs in high-temperature plasma, or via radioactive decays.

Braking radiation or Bremsstrahlung

A second source of X-ray emission is the Bremsstrahlung 'braking' radiation (free-free emission), related to the movement of particles in an electric field created by nearby charged particles. The interaction will cause an acceleration, thus forcing a photon emission. The larger the mass difference between the particles, the more effective the process. Given the mass difference between electrons ($m_e = 9.109 \times 10^{-31}\,\text{kg}$) and protons ($m_p = 1.673 \times 10^{-27}\,\text{kg}$) this effect is often related to electrons of charge $-e$ passing near a heavy ion nucleus of charge Ze, where Z is the number of protons in the nucleus. Assuming electrons follow a Maxwell-Boltzmann distribution of temperature T_e and density n_e in a collisionless plasma, the corresponding emissivity ϵ related to Bremsstrahlung can be expressed as (see Rybicki & Lightman, 1979, for a full development):

$$\epsilon(E) \propto T_e^{-\frac{1}{2}} Z^2 n_e^2 e^{-\frac{E}{k_B T}} \tag{1.2}$$

where k_B is the Boltzmann constant. Bremsstrahlung in the X-rays needs high-temperature plasma (of the order of 10^7-$10^8\,\text{K}$) to become a dominant mechanism.

Synchrotron radiation

Synchrotron radiation is similar to Bremsstrahlung, but is related to the movement of charged particles in a macroscopic electromagnetic field (i.e. does not involve a companion particle). When a particle enters an area of strong field perpendicular to its velocity, the radial acceleration of the particle causes a photon emission. To create a photon in the X-rays, this mechanism requires either strong fields or high velocities particles.

Compton and inverse Compton scattering

The last main production mechanism encountered in X-ray astronomy is related to Compton scattering. When a photon enters a dense medium, it can be scattered by other charged particles, causing a loss in energy of the photon and an increase of the particle energy by recoil. In general, direct X-ray Compton scattering is rare, as it reduces the energy of the incident photon below the X-ray level except for very strong incident Gamma-ray radiation. The inverse Compton mechanism however, can generate X-rays when high-energy electrons interact with low-energy photons to increase their energy.

1.1.3 Reminders of spectroscopy

In addition to imaging, which provides an idea of the integrated flux of the observed source, the study of X-ray physical mechanisms also requires the use of spectroscopy. As in any other wavelength, measurements of the spectral properties of photons are a tracer of the physical properties of environment in which they were emitted (Figure 1.4).

Line intensity

The line intensity is measured by evaluating the peak height of the line with respect to the continuum emission. It can also be estimated by integrating the line flux, $\mathcal{F}_\ell$, above the continuum flux, $\mathcal{F}_c$, and deduce the equivalent width of the line, EW:

$$EW = \int \frac{\mathcal{F}_\ell - \mathcal{F}_c}{\mathcal{F}_c} dE \tag{1.3}$$

This value is related to the number of photons emitted/absorbed in a given transition, hence to the density of a specific ion in the plasma. The relative strength of the lines also gives an indication of the chemical composition of the plasma. Accurate measurements of the line intensity require a good signal-to-noise (S/N) ratio of the spectral lines with respect to the continuum and to the noise level, as well as high spectral resolutions.

Line shift

Each atomic transition is defined by a specific energy level. The measurement of the line centroid is therefore a way to investigate which ions are present in the plasma. However, several physical processes can alter the line centroid, notably Doppler effect (either cosmological, thermal or related to the motion of the particles). Measurements of line shifts provide an idea of the intrinsic motion of the various populations of ions in the plasma. Instrumentally, the line shift is related to the energy scale accuracy, which provides the conversion between the detector units and the photon energies. The more accurate the energy scale, the lower the uncertainties on the velocity associated to the line shift.

Line broadening and shape

The line broadening is generally computed by measuring the line width, or more commonly its full width at half maximum (FWHM). This broadening is due to multiple factors. The most fundamental is the intrinsic Lorentzian width of the line distribution $\mathcal{P}$. Small motions of the particles along the line-of-sight, related either to thermal Doppler effect or turbulent motions in the plasma, will also result – due to projection effects – into an additional Gaussian broadening, which will be convolved with the intrinsic atomic profile. Finer physical effects (e.g. charge exchange or resonant scattering, Hitomi Collaboration 2018d) may equally modify the overall width of the line.

Instrumental effects also participate to line broadening. In any detector, a monochromatic line will be broadened due to, e.g, detector physics or readout effects. This feature is described, as a function of energy, by the line spread function (LSF), often modelled by a Gaussian core and non-Gaussian wings. The energy resolution of the instrument,

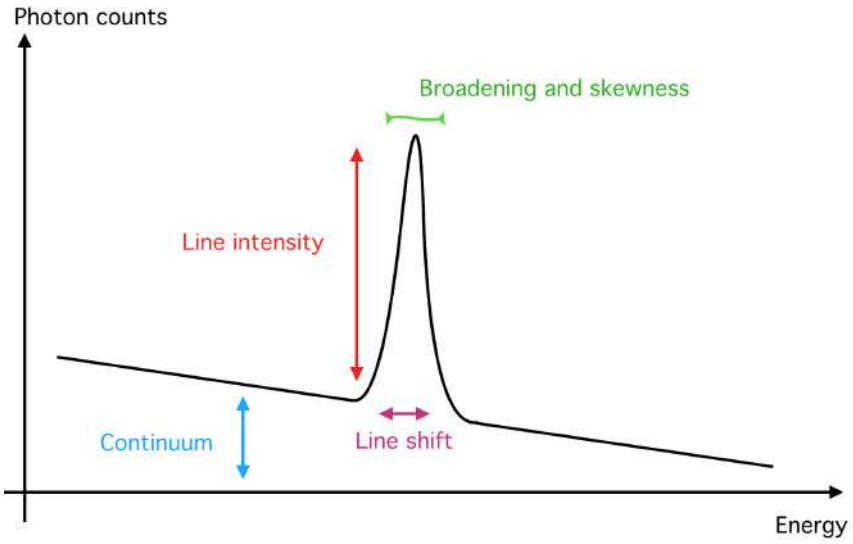

Figure 1.4: Schematic view of the main quantities measurable on a spectrum.

$\Delta E(E)$, is the FWHM of the LSF. The performances of a spectrometer are expressed by the resolving power (i.e. capability to observe narrow lines), $R = {}^{E}/_{\Delta E}$. For X-ray CCD detectors $R \sim 10 - 50$ while for X-ray grating spectrometers $R \geq 1000$. By contrast, ground-based optical spectrometers and integral field units, such as the multi-unit spectroscopic explorer (MUSE, Bacon et al. 2010) routinely reach $R \geq 3000$. The knowledge of the energy resolution is crucial to disentangle between instrumental and physical effects.

The total broadening of a line results in a convolution of all these effects to create Voigt profiles. Depending on the velocity structure, the line can also be deformed and depart from a symmetric Voigt profile. Provided an accurate knowledge of the energy resolution and the atomic physics, the line broadening can deliver information on the thermal and dynamic structure of the emitting plasma. Measurements of the skewness of the line can instead be a diagnostic of the physics of the plasma along the line-of-sight.

Continuum measurements

Continuum measurements are the least complex to perform, as they do not require high spectroscopic accuracies in terms of energy scale or energy resolution. Depending on the shape of the continuum (e.g. power law), it is possible to determine the emission mechanism of the observed region (Bremsstrahlung, synchrotron, Compton scattering) and thus infer some of its physical properties (temperature, magnetic field, average metallic content).

1.1.4 X-ray astronomy

The first steps of X-ray astronomy date to the early detections of extra-galactic X-ray astrophysical sources in the 1960s with rocket- and balloon-borne experiments equipped with scintillators (Giacconi et al., 1962). These experiments were shortly followed by the very first X-ray satellites, such as *UHURU*, *Ariel V* or *Einstein*. Full sky surveys

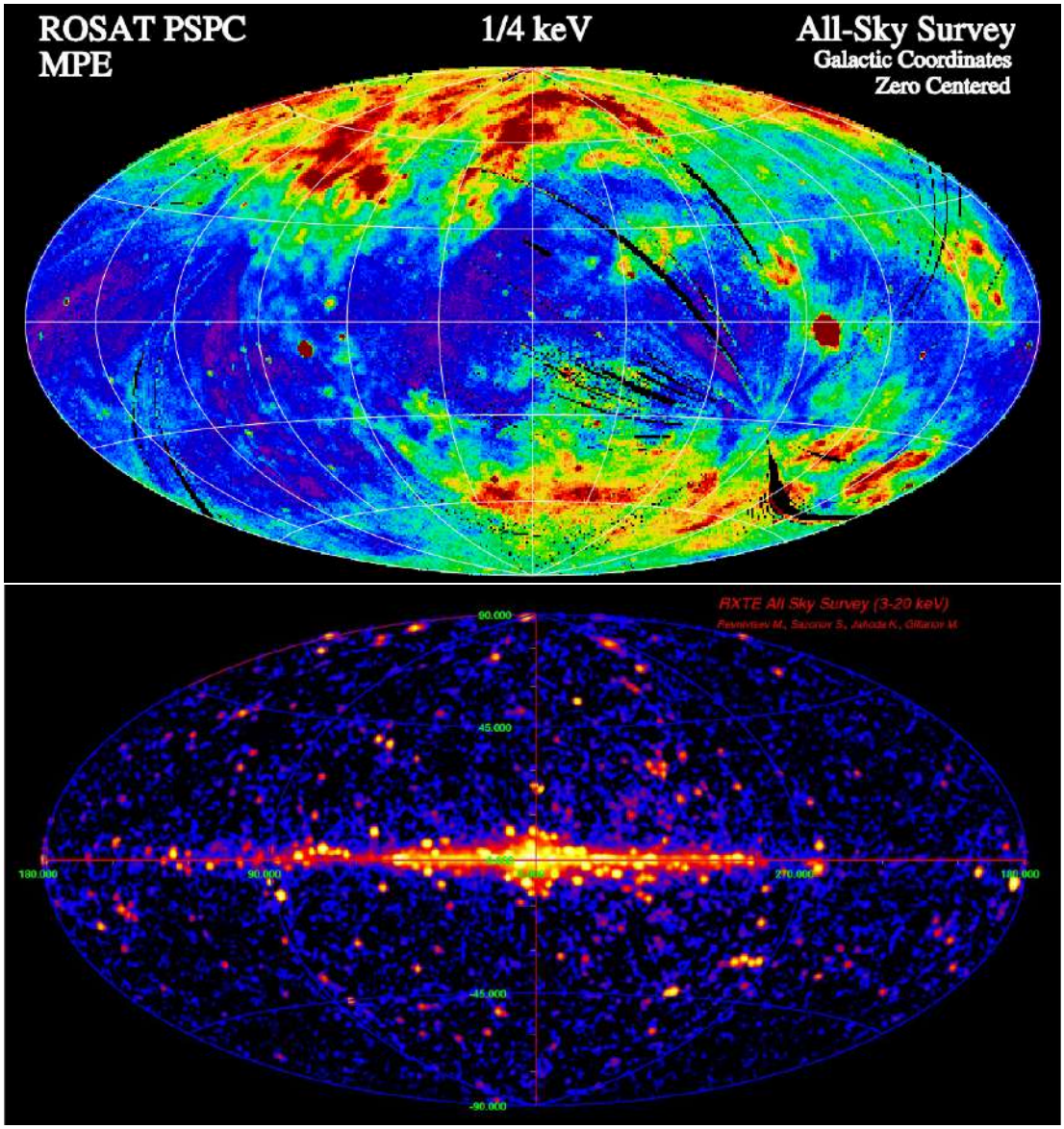

Figure 1.5: (*Top*) Sky survey in the 0.25 – 2 keV energy band performed using *ROSAT* (Snowden et al., 1995). (*Bottom*) Sky survey in the 3 – 20 keV energy band performed using *RXTE* (Revnivtsev et al., 2004; Sazonov & Revnivtsev, 2004).

were performed later, in the 1990s, by the *ROSAT* (Pfeffermann et al., 1987) and *RXTE* missions (Jahoda et al., 1996), and remain up to today one of the few all-sky pictures in X-ray astronomy (see Figure 1.5), awaiting for the eROSITA instrument onboard the spectrum Roentgen-Gamma (*SRG*) mission, launched in 2019 (Merloni et al., 2012).

Most X-ray sources have photon fluxes well approximated by a Poisson regime of a few hundreds of counts per second (cps) on each detector (at the most) on board current observatories. Such count rates facilitate simultaneous measurements of timing, spatial and

spectral information of the observed sources in non-dispersive ways. In this regard, detector technologies have substantially improved over the last fifty years to achieve unprecedented accuracies in both imaging and spectroscopy. X-ray observations have since allowed the identification of the main X-ray production mechanisms and the main X-ray sources of our Universe, opening many new questions. These investigations have become over the years a multi-wavelength field, and more recently even a multi-messenger field with the detection of the gravitational wave events, such as *GW150914* (Abbott et al., 2016a,b). X-rays are intrinsically associated with high-energy phenomena and represent one of the few messengers available to probe the hot and energetic phenomena across cosmic time.

From the very first detections of compact objects such as pulsars (first X-ray detection by Fritz et al. 1969), and first hints of black hole (BH) detection in the central parts of galaxy clusters (Salpeter, 1964), we are now able to observe with great detail the spectral, spatial and time dynamics of pulsars such as the Crab nebula (Kirsch et al., 2005), but also to observe thousands of distant supermassive black holes (SMBHs) candidates located at the center of other galaxies. These observations provide a pristine laboratory to test current theories in particle physics (Özel & Freire, 2016), cosmology (Planck Collaboration et al., 2016) or even general relativity (Weinberg et al., 2013).

The correlation of diffuse X-ray emission with extended objects improved our understanding of the formation and development of large-scale structures such as groups and clusters of galaxies (Sarazin, 1988). Regular observations of X-ray counterparts of Gamma-ray bursts (GRBs) also provided hints of hitherto undetected baryons in the warm hot intergalactic medium (WHIM, e.g. Nicastro et al. 2018). Finally, improvements of galactic observations allowed the observation of supernovæ remnants (SNR), e.g. E0102 (Plucinsky et al., 2008), or Tycho (Warren et al., 2005), or even provided new understanding in the dynamics of giant planets within our own Solar System (Bhardwaj et al., 2007).

1.2 The formation of large structures

1.2.1 A brief history of the Universe

Within the standard model, the observable Universe as we know it has originated from a singularity, the so-called 'Big Bang' (Figure 1.6). The early instants of our Universe are however poorly known, and are hardly accessible using conventional astrophysical observations. After the initial singularity, it is likely that the Universe sustained, in its primordial times, a rapid exponential expansion phase (i.e. a phase of inflation, Planck Collaboration et al. 2016). This expansion then gradually decreased, creating a cooling phase from which the first leptons, then the first baryons, appeared as combinations of quarks became possible. Most of the light elements (e.g. H, He, Li) were also formed as a result of this first primordial nucleosynthesis (see Cyburt et al., 2016, for a review).

A second major milestone of this evolution occurred when the primordial plasma reached temperatures and densities that allowed for proton/electron recombination. From that moment, the Universe became transparent to electromagnetic waves. The fossil record of this era constitutes the cosmic microwave background (CMB), predicted by Gamow (1953) and discovered serendipitously in 1965 by Penzias & Wilson (1965). The CMB provides a glimpse of the Universe $\sim 400\,000$ years after the Big Bang. Due to the expansion,

the radiation emitted at high temperatures at the dawn of the Universe is now seen as a nearly perfect isotropic micro-wave black-body emission of temperature 2.73 K.

Although isotropic, the primordial quantum fluctuations of the singularity were echoed as ripples in the initial matter density distribution throughout the inflation phase, which were first highlighted by the anisotropies in the CMB observed by the *COBE* mission (Mather et al., 1990; Smoot et al., 1992). These fluctuations evolved by gravitational infall to create the first dark matter (DM) halos (see Bernardeau, 2013, for an analytical review on the evolution of the primordial anisotropies in mass distribution) and massive clouds of baryonic matter, which evolved by spherical collapse to create the first population of stars (see Wise, 2012, for a review on early 'Population III' stars). These in turn gathered to create the first galaxies and, more recently ($z \sim 2$, i.e. 10.4 Gyr ago), clusters of galaxies (see Silk & Mamon, 2012, for a review on the early galaxies).

Recent observations, pioneered by Edwin Hubble (Hubble, 1929), showed that the expansion of the Universe remains ongoing, with a rate $H_0 = 67.3$ km/s/Mpc, as shown by the *Planck* mission (Planck Collaboration et al., 2016). The study of the CMB coupled with general relativity also provided renewed understanding in the field of cosmology. It showed for instance that the Universe is consistent with cold dark matter (CDM) Universe with a cosmological constant (Λ-CDM model, Blumenthal et al. 1984), composed of 31.4% of matter (including baryons and dark matter), $\Omega_m = 0.316$, and of 68.4% of dark energy, $\Omega_\Lambda = 0.684$ (Planck Collaboration et al., 2018), whose nature remains unknown. This composition is yet to be explained by modern astrophysics.

1.2.2 Clusters of galaxies

Discovery of clusters and of the intra-cluster medium

The discovery of large-scale structures dates to early observations of nebulæ in the sky. It's only a century ago however, in the early 1920s, that the understanding of these objects evolved, showing that some of them were in fact composed of many galaxies, similar to our own, clustered in small volumes (Hubble, 1925). Since then, clusters of galaxies have become a target of interest for astronomers. Surprisingly, the first measurements of radial

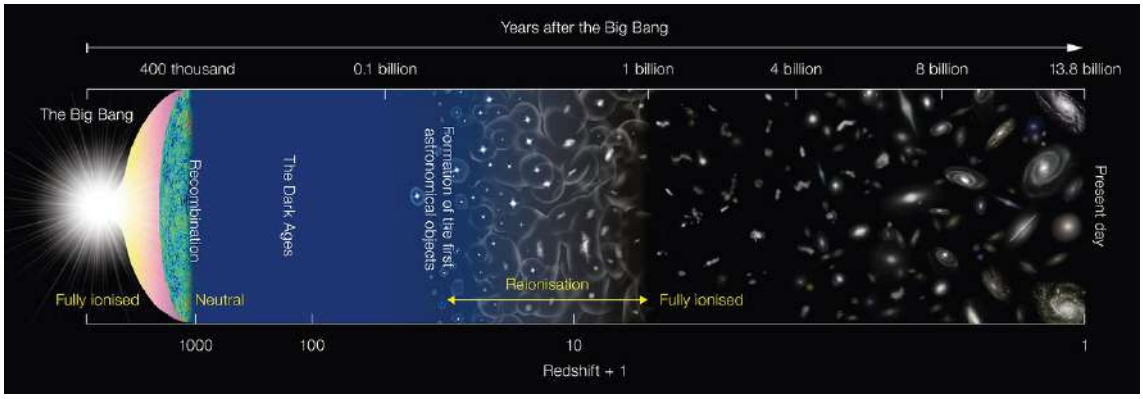

Figure 1.6: Schematic history of the Universe as a function of time. (Credits: ESO)

velocities of galaxies within clusters resulted into a dynamical mass (derived from the rotation curve of the galaxies) inconsistent with the cumulative mass of individual galaxies (Smith, 1936; Zwicky, 1937). To explain this discrepancy, Zwicky postulated the existence of a 'dark matter' component, subject only to gravitation, filling the potential well of these structures (see Bertone & Hooper, 2018, for a review). A few years later, a similar result was found measuring rotation curves of stars within the Andromeda galaxy (Rubin & Ford, 1970), suggesting the presence of DM even at galactic scales. Modern measurements now comfort the idea that galaxy clusters are closely connected to the presence of DM halos, in which they form by infall of matter onto the DM gravitational potential.

Historically, the total mass of the galaxies was also inconsistent with the estimated baryonic mass of the cluster. This difference was explained in the 1970s, by the pioneering work of Cavaliere, Gursky and Tucker (Cavaliere et al., 1971), who demonstrated the existence of a diffuse X-ray emission related to the hot gas filling the intergalactic medium (IGM) between the galaxies within the cluster. The matter in the intra-cluster medium (ICM) and in individual galaxies is now in agreement with the expected baryonic content of clusters (Pratt et al., 2009). The ICM also provides a window of observations of the structures using X-rays, out to unprecedented redshift values (i.e. to the early days of the clusters at $z \geq 1$, Rosati et al. 2002). Furthermore, as clusters are the largest known structures bound by gravitation, they represent excellent cosmological probes to test our understanding of the Universe (Planck Collaboration et al., 2018).

Formation and properties of galaxy clusters and their outskirts

As all other structures in the Universe, the formation of galaxy clusters is linked to the early anisotropies in the mass distribution following the primordial expansion of the Universe. The formation scenario involves self-similar collapse of these initial perturbations to create denser regions (Press & Schechter, 1974), which led to a hierarchical growth of structures out to modern groups and clusters of galaxies within DM halos (see Allen et al., 2011; Kravtsov & Borgani, 2012; Planelles et al., 2015, for recent reviews).

Clusters of galaxies typically contain $\geq 10^2$ galaxies within a region of a few Mpc of diameter. Their baryonic mass, trapped into DM gravitational potential wells (White et al., 1993), corresponds to $\sim 10\%$ of the total estimated mass of the cluster, ranging between 10^{13} to $10^{15} M_{\odot}$. Among this baryonic fraction, 85% is related to the hot gas in the ICM, and the rest to galaxies and stars (Sarazin, 1988). The ICM reaches temperatures around $10^7 - 10^8$ K, and emits in the X-rays, making it an excellent probe to measure the dynamics of the hot gas, to investigate the underlying DM potential of these structures or to understand the geometry and matter content of the Universe (Figure 1.7).

Due to the extension of such structures beyond their inner regions (following the DM halo in which they form), an exact definition of the volume occupied by the cluster is difficult to estimate. Strictly speaking, the spatial scale of the cluster is characterised by the radius of the external accretion shock, $R_{\rm shock}$, due to the infall of low density gas onto the cluster gravitational potential. In practice, the generic definition of the volume, often used in the literature, encloses the *virialised* region of the cluster at its redshift, i.e. where the virial condition relating the kinetic energy of the cluster, E_c, and its potential energy, E_p, is satisfied ($2E_p + E_c = 0$). Using the spherical models of collapse of nonlinear

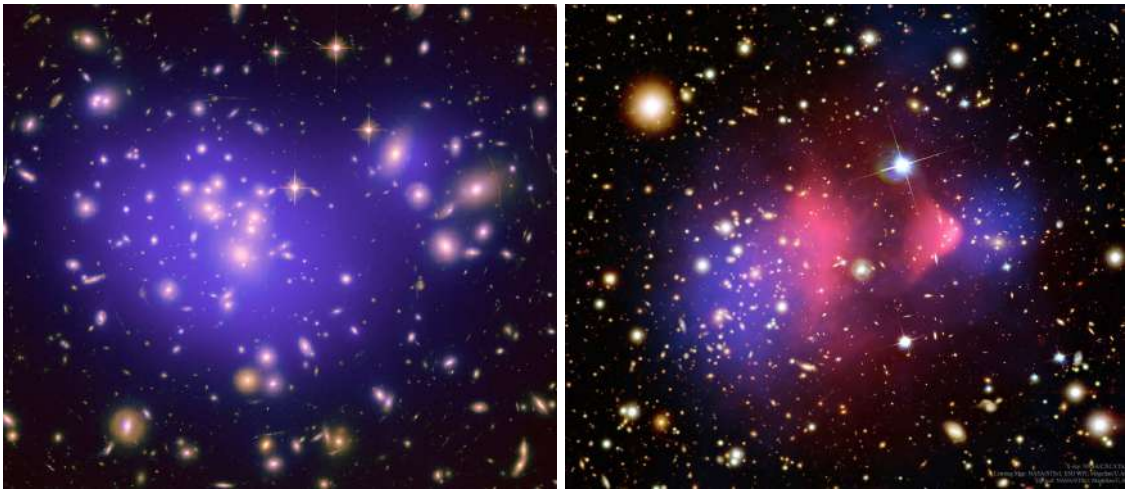

Figure 1.7: (*Left*) Composite X-ray and optical image of the Abell 1689 galaxy cluster, located at $z = 0.18$. The optical image was obtained using the *Hubble Space Telescope* and is superimposed with the emission of the ICM (purple) observed with *Chandra*. Credits: X-rays: NASA/CXC/MIT/E – Optical: NASA/STScI. (*Right*) Similar observation for the 1E 0657-558 'Bullet cluster'. Optical image is superimposed with X-rays (in red/purple). Credits: X-ray: Markevitch & Vikhlinin (2007) – Optical: Clowe et al. (2006)

perturbations in the primordial matter distribution, the virialised region can be expressed alternatively, in terms of the virial density contrast, δ, with respect to the critical density of the Universe, ρ_c, at the cluster redshift z by

$$\rho_{\rm vir}(z) = \delta_{\rm vir}(z)\rho_c(z) \tag{1.4}$$

where $\rho_c(z) = 3H(z)^2/8\pi G$ and $H(z)$ the value of the Hubble constant at the considered redshift. In the case of a Λ-CDM model, the virial density contrast is ~ 101 for $z = 0$ (Bryan & Norman, 1998). This provides directly the virial radius by:

$$R_{\rm vir} = \left(\frac{3M_{\rm vir}}{4\pi\rho_{\rm vir}}\right)^{\frac{1}{3}} \tag{1.5}$$

if the virial mass of the cluster, $M_{\rm vir}$, is known. The physics of the ICM near and beyond $R_{\rm vir}$ are poorly known, and do not satisfy locally the virial criterion due to complex 3D shock and accretion schemes. In general, R_{200} (radius encompassing a density contrast of $200 \times \rho_c$) is used by the community to approximate $R_{\rm vir}$. This value results from historical computations of nonlinear perturbations in an Einstein-de Sitter Universe with $\Omega_m = 1$, which provide $\delta_{\rm vir} = 18\pi^2 \sim 178$ at $z = 0$ (Bryan & Norman, 1998), rounded to 200 for simplicity. In practice, current X-ray observatories such as *Chandra* or *XMM-Newton*, provide reliable density and temperature measurements only out to $\sim R_{500}$ (radius encompassing a density contrast of $500 \times \rho_c$). This radius has thereby become common to describe the inner virialised parts of the clusters and the average physical quantities within (e.g. T_{500} for the average temperature within R_{500}). Regions outside R_{500} and

out to $R_{\rm shock}$ (several times $R_{\rm vir}$) are considered the outskirts of the cluster, and are of particular interest to understand the formation and growth of clusters (see Reiprich et al., 2013; Walker et al., 2019, for reviews).

The estimation of the total virial mass of these objects is important to determine these radii and for precision cosmology (Planck Collaboration et al., 2016). Different techniques can be used to estimate it (Ettori et al., 2013a; Pratt et al., 2019). A common approach assumes the hydrostatic equilibrium of the ICM, and uses temperature, density and pressure values derived from X-ray or SZ (Sunayev Zel'dovich effect, Sunyaev & Zeldovich 1972) measurements to compute the mass. Additional estimates can be inferred using the velocity of the galaxies within the cluster (Biviano et al., 2006), or through gravitational lensing (Hoekstra et al., 2013). An accurate measurement of the mass remains nonetheless challenging, as tensions were highlighted between the different observational data (notably between hydrostatic and gravitational mass measurements, see Pratt et al. 2019 for a recent review), suggesting a 10/20% deviation from hydrostatic equilibrium, in particular in the outskirts. Numerical and semi-numerical estimations of the mass using the halo mass function (Press & Schechter, 1974) were also developed in parallel (see notably the first results by Navarro et al., 1997) and remain current practice up to this day. However, results obtained numerically show additional discrepancies with observations, and notably highlighted potential systematic errors in several observational mass estimators (Rasia et al., 2006, 2013). More accurate measurements are therefore required, especially in the outskirts of these structures where hydrostatic equilibrium (Nagai et al., 2007), equipartition and ionisation equilibrium may break (Wong et al., 2011).

The current generation of X-ray instrument has certainly provided crucial information on the ICM within R_{500}, notably temperature and entropy profiles (Vikhlinin et al., 2006; Leccardi & Molendi, 2008b), while *Suzaku* pushed this limit out to R_{200} on few study cases (Hoshino et al., 2010; Simionescu et al., 2011). This remains however a fraction of the total volume of a cluster. Observations of the outskirts are limited by the low effective area of the X-ray telescopes and the low emission of these regions (background-dominated sources). The advent of large-scale numerical simulations in the beginning of this century provided a new window to investigate cluster properties. Simulations such as Millenium (Springel, 2005), Illustris (Genel et al., 2014; Vogelsberger et al., 2014), or Eagle (Schaye et al., 2015) provide a comprehensive view of the early days of the Universe and assert the hierarchical formation of structures (Figure 1.8). The comparison of these models with observations (Leccardi & Molendi, 2008a; Biffi et al., 2017, 2018b) is used to understand the fundamental physics and cosmology involved in the formation of clusters of galaxies. They also provide a good way to test non-gravitational physics (e.g. reheating of galaxies, role of the central object of the cluster, mergers) or to estimate biases in our current estimators of physical quantities (e.g. Mazzotta et al., 2004; Rasia et al., 2008).

1.2.3 Thermodynamic and dynamic properties

Surface brightness profiles

The first spatial observations of the ICM brought countless information on the physics and the dynamics of clusters (Cavaliere et al., 1971). The understanding of these processes is closely related to the shape of their emission profile (and their surface brightness). The

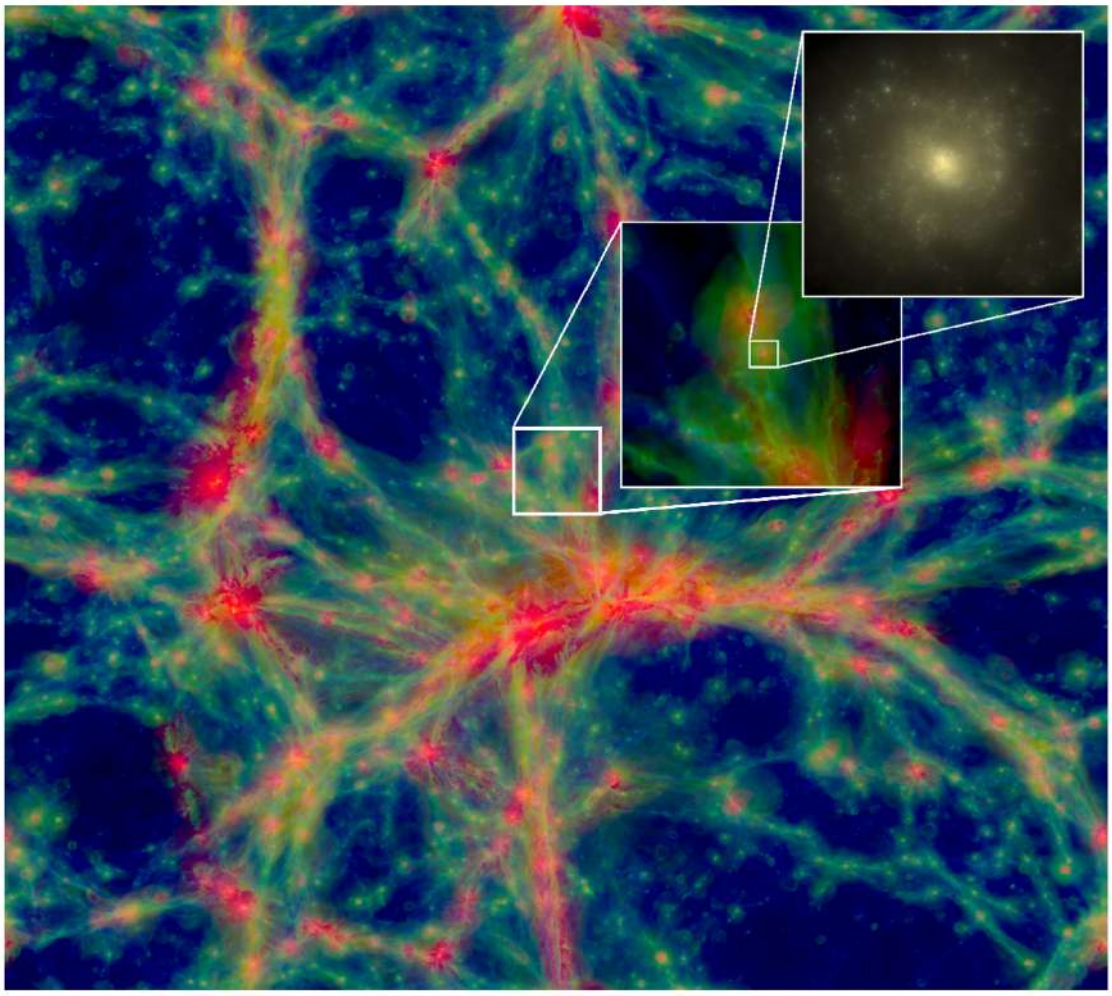

Figure 1.8: Reproduced from Schaye et al. (2015), Figure 1. Example of a $100 \times 100 \times 200$ comoving Mpc slice through the Ref-L100N1504 simulation within Eagle for z=0. The intensity shows the temperature T of the gas (green $T \leq 10^{4.5}\,\mathrm{K}$, blue $10^{4.5}\,\mathrm{K} \leq T \leq 10^{5.5}\,\mathrm{K}$ and red $10^{5.5}\,\mathrm{K} \leq T$). The sub-panels show a zoom into a filament of 10 comoving Mpc and one of the galaxies of the filament, of $3 \times 10^{10} M_{\odot}$ respectively.

early work conducted by Cavaliere & Fusco-Femiano (1976) illustrated, using a simple approach that assumes hydrostatic equilibrium and an isothermal model of the cluster, that the surface brightness could be approximated by a self-similar analytical expression. Under this assumption, the equilibrium is reduced to

$$\frac{n_{\mathrm{gas}}(r)}{n_{\mathrm{gas}}(0)} = \left(\frac{\rho_{\mathrm{gas}}(r)}{\rho_{\mathrm{gas}}(0)}\right)^{\beta} \tag{1.6}$$

where β is an adiabatic coefficient of the gas and $n_{\mathrm{gas}}(r)$ the radial density of the plasma. The breakthrough with experimental observations came when the mass distribution of the gas was approximated by a radial power law (Cavaliere & Fusco-Femiano 1978, using the

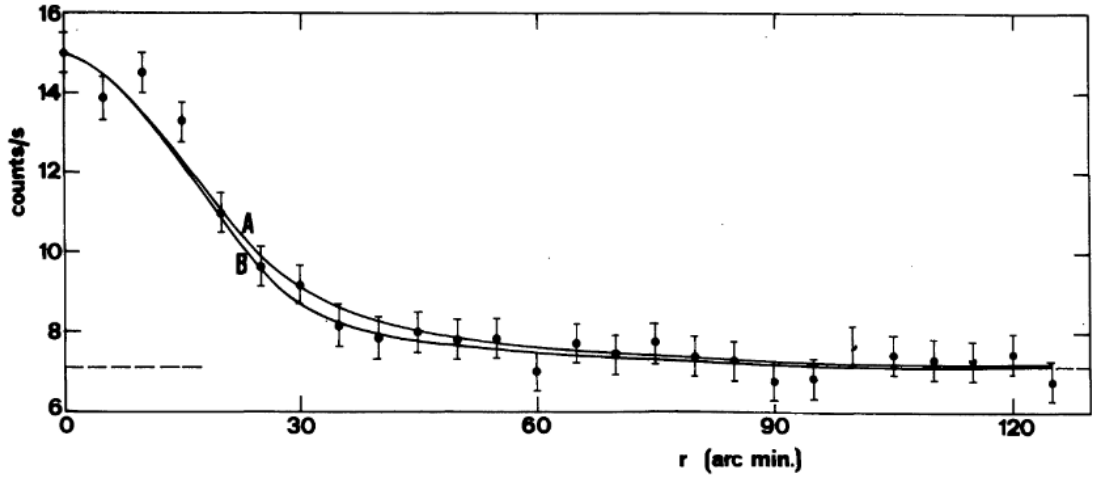

Figure 1.9: Reproduced from Cavaliere & Fusco-Femiano (1978), Figure 5. Historical first use of the β model on the surface brightness profile data of the Coma cluster reported in Lea et al. (1973). Two model (A and B) using different β values and core radii are shown.

assumptions by King 1966), creating the famous β-model approximation, still widely used to describe – at first order – the emission of relaxed clusters (Figure 1.9) with $\beta \sim 2/3$.

$$\frac{n_{\rm gas}(r)}{n_{\rm gas}(0)} = \left(1 + \left(\frac{r}{r_c}\right)^2\right)^{-\frac{3\beta}{2}} \tag{1.7}$$

In the model r_c is defined as the 'core' radius of the cluster. Typical values of $n_{\rm gas}(0)$ range between 10^{-2} and $10^{-3}\,{\rm cm}^{-3}$, while typical core radii span between ~ 100 and $500\,{\rm kpc}$.

Thermodynamic properties

Despite the good agreement of β-models to describe the central emission of the cluster, this approach fails to describe the emission at larger radii (overestimating the emission) and implies an infinite mass when integrated over r. Further, the ICM is far from isothermal as measured within R_{500} by both *Chandra* (Vikhlinin et al., 2006) and *XMM-Newton* (Churazov et al. 2003; Leccardi & Molendi 2008b). As shown in Figure 1.10, the temperature profile of the clusters decreases as expected from gravitational heating beyond $0.3\,R_{500}$. However, the behaviour of the core temperature varies, exhibiting two populations of clusters: cool-core clusters (CC) on the one hand with temperature profiles peaking around $0.1\,R_{500}$ and dropping towards the center, and non-cool-core clusters (NCC) with flatter temperature distributions (Molendi & Pizzolato, 2001). If we note S the pseudo-entropy of the cluster defined by $S = Tn^{-2/3}$ (see Voit et al. 2005 for the definition, and Rossetti & Molendi 2010 for a relation to the real deprojected entropy of the structure and its comparison), the ratio, σ_S, of the pseudo entropy in the inner parts of the cluster (typically within $0.3\,R_{500}$) and its outer part can be used to divide clusters into these two categories

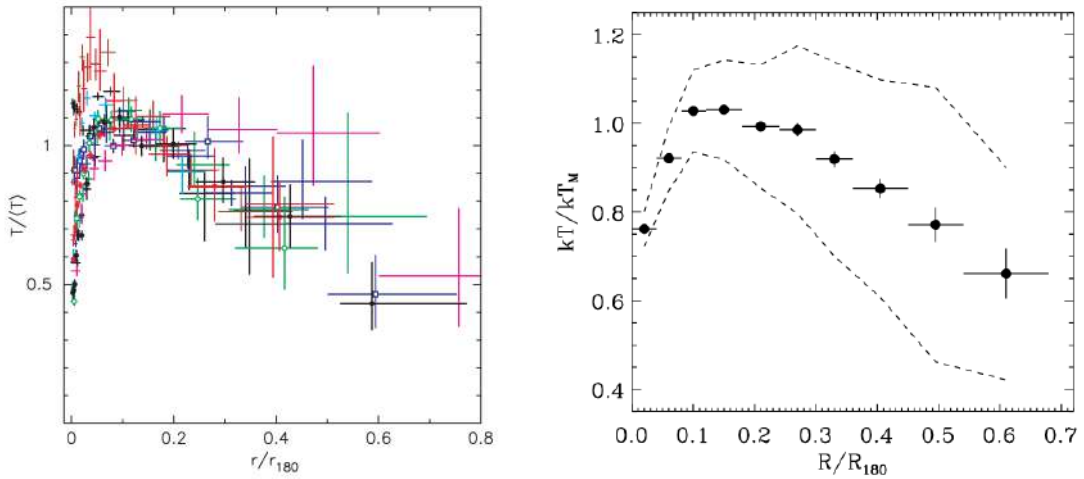

Figure 1.10: (*Left*) Reproduced from Vikhlinin et al. (2006), Figure 18, right panel. Normalised temperature profile for a sample of clusters observed with *Chandra* as a function of the normalised radius r/R_{180}. (*Right*) Reproduced from Leccardi & Molendi (2008b), Figure 6. Normalised average temperature profile for a sample of clusters observed with *XMM-Newton*. The dotted lines indicate the total scatter of the sample.

(Leccardi et al., 2010). The interesting feature of the pseudo-entropy is the little number of measurements required to compute it, and thus to classify a given cluster.

This thermodynamic behaviour is in fact related to the dynamical state of the halo, and the history of its accretions. In the case of a slow accretion of matter with no major merger event, low-entropy metal-rich gas gathers at the center of the cluster, thereby lowering the overall profile. On the contrary merging events stir the ICM, increasing the overall entropy within central regions (Leccardi et al., 2010). More recently, numerical simulations demonstrated that this classification is not fixed, and that CC and NCC clusters may evolve in either way over the course of their lifetime depending on the physics of merger events and the state of the central galaxy (Rasia et al., 2015). The pseudo-entropy therefore holds the fossil record of the dynamical history of the halo. Future measurements of entropy profiles across time are key to determine a clear scenario for this distinction.

Dynamics of the intra-cluster medium

The ICM is densest near the central potential well of the cluster. Given the time scales of the radiative cooling ($\leq 10^9$ yr), which are systematically higher than the free-fall time of the gas, cooling flows should form and accrete matter towards the central regions to withstand the weight of the outer gas (Fabian, 1994). This increase in density should replenish the central galaxies and ignite star formation. Although observed in numerical simulations with only radiative cooling or in a few observational cases (O'Dea et al., 2008; McDonald et al., 2012), this effect has not been confirmed by observations (Peterson et al., 2003). The infall must therefore be compensated by other heating mechanisms. Observations of the central regions of clusters revealed the presence within the brightest cluster galaxy (BCG)

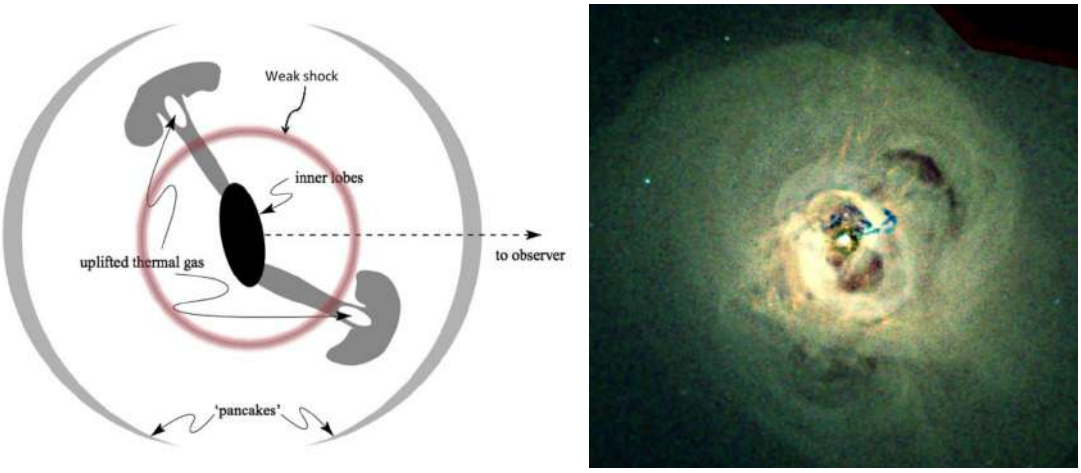

Figure 1.11: (*Left*) Reproduced from Bykov et al. (2015), Figure 4. AGN/ICM interplay near the center of the cluster. The matter infalling onto the AGN creates jets (visible by radio lobes), which in turn create shocks and bubbles. (*Right*): Example on the observation of the Perseus cluster by the *Chandra* telescope (Fabian et al., 2006)

of an active galactic nucleus (AGN), hosting a SMBH. It is now well established that this compact object plays a major role in the thermodynamic regulation of the gas, through a mechanism called 'AGN feedback' (see Bykov et al., 2015, for a review).

AGN feedback can be divided into two types, depending on the state of the central SMBH (Fabian, 2012). In several cases (the 'radiative' mode), a strong accretion mode increases the AGN luminosity to the Eddington limit, and creates powerful radiative winds capable of driving away the accreted matter (Silk & Rees, 1998). These outflows ($10^2 - 10^3 M_\odot$/yr) sweep the gas within the central galaxy over short time scales ($\sim 10^6$ years) thereby quenching star formation in the BCG (Sturm et al., 2011). This mechanism is mainly observed in high-redshift proto-clusters ($2 \leq z \leq 5$), indicating an early active stage of the SMBH (Ueda et al., 2003; Hasinger et al., 2005).

When moving to lower redshift clusters (from $z \sim 1$ to local), the radiative effect of the AGN becomes weaker, and the feedback becomes driven by kinematics instead. Whenever a large quantity of gas infalls towards the central object, accretion onto the SMBH increases, occasionally driving powerful jets or outflows from the SMBH (Gaspari et al., 2011). These mechanisms remove matter from the central object, slowing its growth and stopping the infall of the surrounding gas. This accretion can either be 'hot' (Churazov et al., 2002; Böhringer et al., 2002), i.e. related to a continuous accretion onto the SMBH (higher infall rates lead to higher accretion rates which balance the infall), or 'cold', i.e. a continuous weak accretion of gas clumps (Gaspari et al., 2012). Jets emitted by the AGN create 'cavities' around them (Fabian et al., 2006), which eventually evolve into subsonic hot bubbles that buoyantly rise within the ICM, regulating the overall gas temperature distribution (Figure 1.11 – *Left*). Such cavities are for instance well visible in the observation of the Perseus cluster (Figure 1.11 – *Right*). Part of the energy of the infall is also dissipated through acoustic waves (Fabian et al., 2005).

The rise of these bubbles, the activity of the central object, and cluster accretion

through gravitational infall of matter near the filaments connected to the DM halos stir the ICM at every spatial scale (Gaspari et al., 2018). Similarly, the accretion of matter (DM or baryons) through mergers of sub-clumps of gas creates additional shocks and instabilities (see notably Vazza et al., 2009, for numerical results). The turbulent motions created by these events transport, through a vortex cascade, the energy injected at large spatial scales (e.g. hundreds of kpc for accretion near $R_{\rm shock}$ and mergers) down to a few kpc, where it dissipates through eddies and small-scale viscosity. This mechanism releases heat to the surrounding gas (Zhuravleva et al., 2014), counteracting the cooling flows in the cluster core and regulating the ICM thermalisation. Turbulence is a likely candidate to explain deviations from hydrostatic equilibrium in the gas, and acts as an additional support in the global cluster equilibrium (Simionescu et al., 2019b).

Mapping the turbulent motions of a cluster through the broadening or the skewness of X-ray emission lines is challenging, as it requires spatially resolved high-resolution spectroscopy, unavailable on current X-ray instruments. Recent results thus take advantage of other quantities. For instance, measurements of bulk-motion velocities near shock fronts provide information on large-scale turbulent motions of the ICM (Markevitch & Vikhlinin, 2007). Similarly, the statistics of surface brightness and temperature fluctuations in the outer parts of clusters (Churazov et al., 2003, 2012; Gaspari & Churazov, 2013) correlate with the power spectrum of the turbulent velocity (Zhuravleva et al., 2015), providing insight on the turbulent cascade. On smaller scales on the other hand, results related to the AGN-driven motions are mainly derived from simulations (Gaspari et al., 2014), in a tentative to improve our understanding of the gas dynamics near the central objects. A new glimpse of the ICM turbulence was provided by the ground-breaking observation of the Perseus cluster by the soft X-ray spectrometer (SXS, Tsujimoto et al., 2018) onboard *Hitomi*, which measured a 'quiescent' turbulence velocity $\sim 200\,\mathrm{km/s}$ near the center of the cluster (Hitomi Collaboration, 2016, 2018a). Further investigations however require the use of new instruments coupling spatial and spectral capabilities.

For certain clusters, more radical events, such as mergers at the cluster level (e.g. the 'Bullet cluster', Figure 1.7 – *Right*) can also occur, creating other large-scale dynamics such as sloshing (Blanton et al., 2011; ZuHone et al., 2013) in the DM potential, which are worth investigating to understand the growth of these structures under extreme conditions.

1.2.4 A metal-rich intra-cluster medium?

Shortly after the discovery of the ICM, the first spectral observation of the hot gas within the Perseus cluster with the *Ariel V* mission (Stark et al., 1976) revealed an iron-rich hot plasma (Mitchell et al. 1976, Figure 1.12 – *Left*). Since these early observations, the metal content of the ICM has been explored by almost every X-ray mission (Zhuravleva et al. 2013, Figure 1.12 – *Right*) to understand its composition and spatial distribution.

The refinements in spatial and spectral resolution in modern spectrometers deeply changed our understanding of the ICM and its formation (de Plaa et al., 2007; Werner et al., 2007; de Plaa, 2013; Molendi et al., 2016). Trapped within the ICM where they remain unaltered, heavy elements are accumulated in the hot gas filling the massive DM halos throughout the cluster history. They therefore represent a fossil record of the cluster chemical evolution (see Werner et al., 2008, for a review).

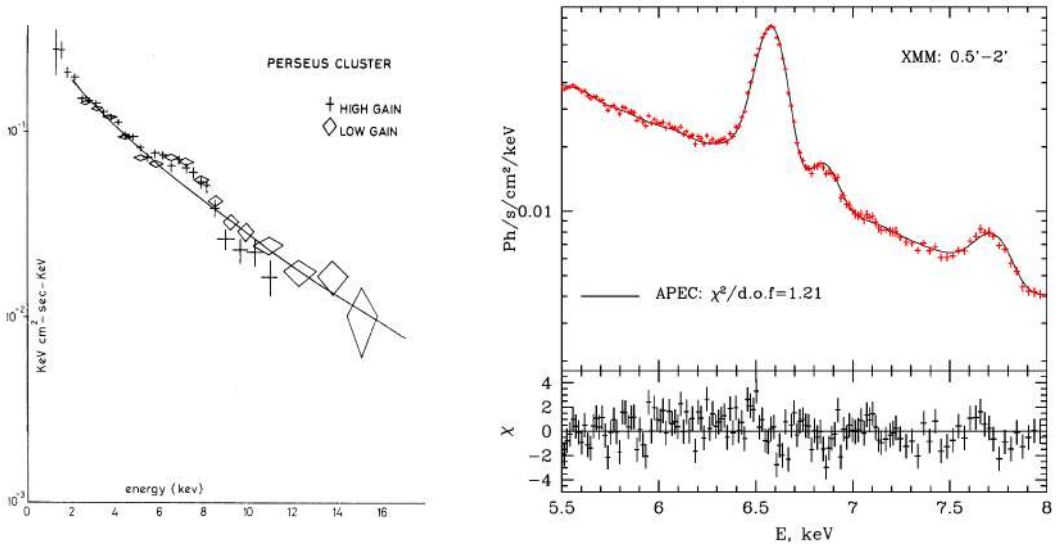

Figure 1.12: (*Left*) Reproduced from Mitchell et al. (1976), Figure 1. Historical first detection of the iron K_α doublet at $\sim 6.4\,\mathrm{keV}$ with *Ariel V*. (*Right*) Reproduced from Zhuravleva et al. (2013), Figure 2, left panel. Observation of the Perseus cluster, zoomed around the iron K_α doublet, showing the same spectrum as the left panel with EPIC-MOS on *XMM-Newton*, fitted using an `APEC` plasma model (Smith et al., 2001).

1.3 Stellar nucleosynthesis and metal enrichment

1.3.1 The role of stars in metal formation

Most of the light elements of the Universe were formed during the primordial nucleosynthesis which followed the Big Bang (Section 1.2.1). The formation of heavier elements implies necessarily the presence of nuclear fusion. Although believed to have occurred during the early days of the Universe even for heavy elements (Gamow, 1946; Alpher et al., 1948), this theory was rapidly modified due to the insufficient energy (and density) of the Universe after recombination. Long suspected, the role of stellar physics in the production of metals was first demonstrated in the 1950s with measurements of short-lived unstable isotopes in stars (Merrill, 1956), and then confirmed in the formulation of the modern theory of stellar nucleosynthesis (Burbidge et al., 1957; Cameron, 1957). These fundamental studies demonstrated that almost all elements above lithium (and therefore all composite molecules, rocks, and even planets that ensue) were one day formed by stars.

Early stars were very different from what we now observe in the Universe. The collapse of the first DM mini-halos in the young Universe is thought to be responsible for the creation of the massive early population III stars, which exclusively burned hydrogen to fuel the fusion reaction in their core. Current observations and numerical simulations indicate that these massive stars laid out the seeds for the stars and galaxies (Bromm & Yoshida, 2011) as we know them. Recent stars (populations I and II) form within nebulæ of hot gas. Whenever a local overdensity increases above the Jeans' mass (Jeans, 1902), the molecular cloud collapses onto itself. The collapse continues until atomic fusion starts, thus

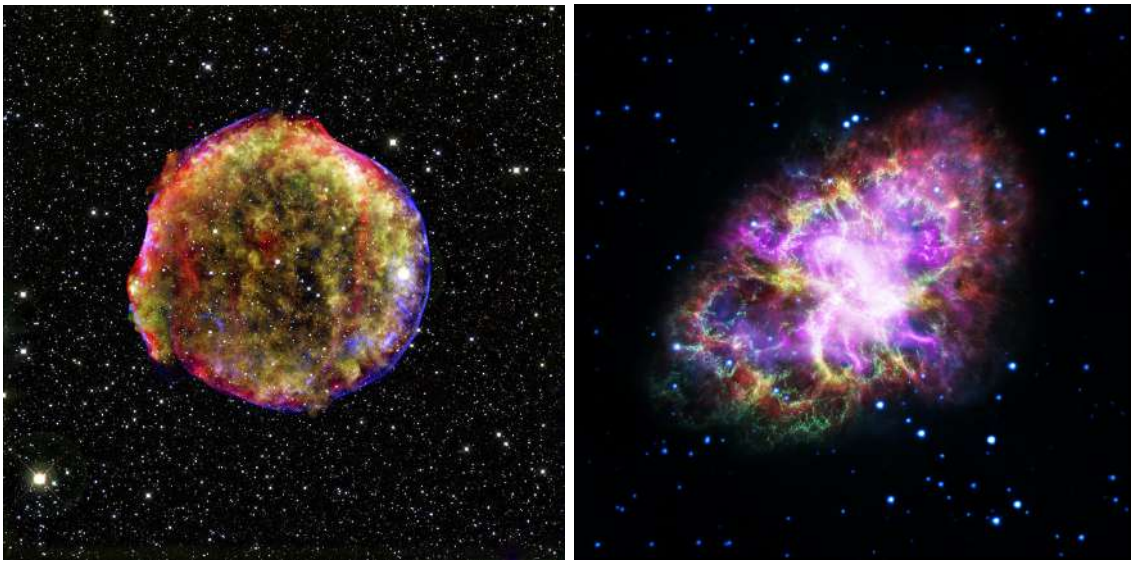

Figure 1.13: (*Left)* X-ray and infra-red image of Tycho's SN_{Ia}. The X-ray image was obtained using the *Chandra* telescope, whereas the infra-red image was taken with *Spitzer* (Credits: X-ray: NASA/CXC/SAO; Infra-red: NASA/JPL-Caltech; Optical; Krause et al. 2008). (*Right*): Composite image of the crab nebula created after SN_{cc} using the entire electromagnetic spectrum. The remaining NS is visible in the centre. (Credits: NASA, ESA, NRAO/AUI/NSF and G. Dubner, University of Buenos Aires).

regulating the infall through radiative pressure support. Proto-stars are born and continue to evolve burning their atomic fuel following a well defined cycle determined (amongst others) by their initial mass (see Nomoto et al., 2013, for a review). The formation of heavy elements (above C) out to iron is mainly related to three phenomena:

- Type Ia supernovæ (SN_{Ia})
- Core-collapse supernovæ (SN_{cc})
- Powerful winds in asymptotic giant branch (AGB) stars

Type Ia supernovæ

Low mass-stars ($\lesssim 8M_{\odot}$) evolve by burning the hydrogen in their core. When hydrogen depletion occurs, the star undergoes a subsequent contraction (thus reheating) which starts the helium fusion within its core, causing a larger expansion of its radiative envelope (red giant phase). These stars will move on to burn helium, carbon and oxygen until depleted. However, due to the low overall mass of the star, the self-regulation of the star (contraction/expansion) is not sufficient to heat the core of the star above the temperature needed to start the next fusion reaction. Gravitational collapse therefore continues until the electron degeneracy pressure is able to support the new object, a white dwarf (WD).

Newly-formed WDs remain stable as long as their mass remains below the Chandrasekhar mass, $M_c \sim 1.4\,M_{\odot}$ (Chandrasekhar, 1931). Due to mass accretion, this limit may however be crossed, igniting fusion reactions. Since the electron degeneracy pressure

is independent of temperature, WDs are unable to regulate this additional power, causing uncontrolled chained nuclear reactions, which rapidly propagate throughout the WD causing its complete thermonuclear explosion (Hillebrandt et al., 2013). These energetic SN_{Ia} phenomena consume the overall WD to synthesise elements from Ne to Fe or Ni (Figure 1.13 – *Left*). Lighter elements only remain in low proportions, as they were used as fuel to create heavier ones. The use of WDs and SN_{Ia} in astrophysics is multiple, as they for instance represent standard candles (Riess et al., 2004) or are used to determine cosmological parameters (Wright & Li, 2018). Their understanding is nonetheless limited as we known very little of their evolution, or even of their end-of-life.

All WDs are born with a mass below M_c and two models currently coexist to explain SN_{Ia} (Maoz et al., 2014). The first, 'single degenerate', model (Whelan & Iben, 1973) foresees binary systems in which the WD feeds over a companion star through the Roche lobe until M_c is reached. On the contrary, the 'double degenerate' model assumes a WD-WD binary system (Webbink, 1984), which leads over time to a WD-WD merger and an associated SN_{Ia}. Even after M_c is reached, the actual mechanism of the SN_{Ia} explosion is still debated, notably if either a deflagration or detonation occurs (Iwamoto et al., 1999).

Though explanations argue in favour of either mechanisms, the lack of a clear scenario has consequences on the enrichment associated to SN_{Ia}. Depending on the mechanism, the predicted metal formation yields have very different shapes (Figure 1.14). Although requiring more time to occur with respect to their SN_{cc} counterparts (see below), current results tend to give similar values of the enrichment to either mechanism (Nomoto et al., 2013; Seitenzahl et al., 2013). Partial answers to the enrichment processes have already been given by studying the chemical composition of the ICM (de Plaa et al., 2007; Mernier et al., 2016b), but new observations are required to disentangle these processes.

Core-collapse supernovæ

For more massive stars (typically $\gtrsim 8M_\odot$), the end-of-life differs from that of low-mass stars and WDs do not appear. Instead, heavier elements continue to fuel the stars up to iron. When Fe is reached (stable to fusion), the star loses radiative pressure support and collapses under the effect of gravity. Electron degeneracy is insufficient to stop the infall, and the star collapses either into a neutron star (NS, supported by the neutron degeneracy pressure), or becomes a BH (Figure 1.13 – *Right*) depending on the progenitor's mass. In both cases, the outer shell of the progenitor will fall onto the compact object and create a large reverse shock-wave, called SN_{cc} (the gas 'bounces' off the compact object), which causes a complete nuclear fusion of the outer layers. Because these layers are mainly composed of light elements, this mechanism is responsible for the formation of most of low-mass elements such as O, Si, or Ne. Heavier elements are also synthesised throughout the process, but at lower rates than in SN_{Ia}.

SN_{cc} mechanisms are rather well understood, but metal formation from these stars depends on many factors, among which the mass of the progenitor and its initial metallicity, Z_{init} (Figure 1.14). To understand the overall enrichment caused by SN_{cc}, the yields for single stars must be integrated over the entire population of massive stars, which involves knowing their mass distribution, generally expressed by the initial mass function (IMF - Salpeter 1955), their metallicity, and their life-time function (Padovani & Matteucci, 1993).

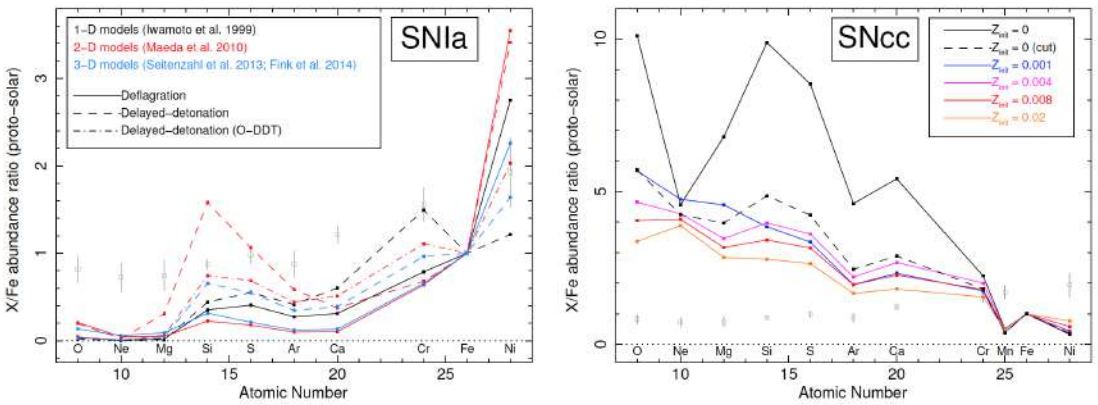

Figure 1.14: Reproduced from Mernier et al. (2016b), Figure 2. Predicted abundance ratio from various SN_{Ia} (*Left*) and SN_{cc} (*Right*). The ICM average abundance ratio derived from the CHEERS sample is also overplotted (de Plaa et al., 2017). See Mernier et al. (2016b) and references therein for details on the models (see also Appendix G.

Asymptotic giant branch stars

Lower elements such as C, N and O can also be produced by AGB stars. When low- to medium-mass stars enter their giant branch phase, these stars reach large radii. The outer shells, composed of the lightest elements, are subject to strong radiative winds. Under these conditions, part of the shell 'evaporates' in the surrounding interstellar medium (ISM), releasing low-mass metals in the process (Iben & Renzini, 1983; Karakas, 2010). Much like SN_{cc}, the overall production yield of AGB stars must be integrated using the IMF, the initial metallicity and the life-time function of the stars.

Z>26 elements

Heavy elements are rare, even at the scale of the Universe. Their formation is related to neutron-capture (Burbidge et al., 1957). Part is produced during SN_{cc}, via 'rapid' neutron-capture (r-process), though it was recently confirmed with multi-messenger astronomy that the bulk of this formation occurs in extreme NS-NS mergers, such as the *GW170817* gravitational wave detection (Abbott et al., 2018). The second part of these elements is formed in high-metallicity stars during AGB phases, by the 'slow' neutron-capture process (s-process), which creates heavy elements over long time scales.

1.3.2 Metal enrichment of the Universe

Metal circulation within clusters and abundance profiles

Across cosmic time, the previous enrichment mechanisms have filled the ISM with metals. Due to the dynamics of the galaxies and of the hot gas within the cluster, part of this metallic content is transferred over into the ICM (see Schindler & Diaferio, 2008, for a review). Two major mechanisms are identified to account for these effects: ram pressure stripping of the galactic gas by the ambient pressure of the ICM (Gunn & Gott, 1972),

or galactic winds and outflows produced by SN_e events or the bulge of the galaxy (De Young, 1978). The former is believed to be dominant towards the central parts of the cluster, where the ICM pressure is highest, while the latter should occur preferentially in the outskirts. Other mechanisms such as galaxy-galaxy mergers or AGN-related outflows can also explain this circulation into the ICM. The dynamics of the ICM finally spread the metal content throughout the entire volume of the cluster (see Section 1.2.3) .

Since clusters of galaxies act as 'closed' structures, the metals produced at stellar level and later found unaltered within the ICM are related to the integrated efficiency of SN_e or AGB mechanisms. The metallic content of the ICM thus represents an efficient way to investigate the chemical enrichment of these structures across cosmic time. Observational constraints on the metal distribution are derived using radial abundance profiles of the main ICM elements (O, Si and Fe), which show comparable behaviours (Figure 1.15 – *Left*) over a large sample of objects (de Plaa et al., 2007; Leccardi & Molendi, 2008a; Werner et al., 2013; Mernier et al., 2016a). These profiles also correlate well with temperature: NCC clusters exhibit flatter radial distributions with respect to CC near the core (De Grandi & Molendi, 2001; de Grandi & Molendi, 2009). In both cases, the abundance profile of Fe peaks near the centre (with abundances $\sim Z_\odot$) before decreasing in the outskirts, where it reaches a plateau around $0.2/0.3\,Z_\odot$ (Mernier et al. 2017; Urban et al. 2017, with solar metallicities as per Lodders et al. 2009). With higher-resolution instruments, the profiles of less abundant metals such as O, Si, Ca or Ni were also traced, showing similar distributions in nearby clusters (Mernier et al., 2017; Simionescu et al., 2017, 2019a).

Though one part of the metal escapes to the ICM, the other remains locked within galaxies. Approximately half of the overall metals is released in the ICM (Loewenstein, 2013; Renzini & Andreon, 2014). However, this fraction seems to be variable depending on the mass of the cluster or the ejection mechanism (Kirkpatrick et al., 2011), raising the question of the representativeness of the ICM metal content with respect to its overall formation history. Answers to this question require an intricate knowledge of stellar physics and stellar evolution. As shown by Iwamoto et al. (1999), the metal production model itself and its time scale have an influence on the metal propagation, with SN_{Ia} products being more likely to be released in the ICM (at later times) than SN_{cc} or AGB metals. These observations trigger in fact two larger questions regarding the metal enrichment of galaxy clusters: how and when were these metals produced? The analysis of the ICM metallic content is an exceptional window for this investigation.

How were metals formed? Testing supernovæ models

Despite improvements in the understanding of metal formation mechanisms, their interplay remains to be clarified, as it involves different physical processes and time scales. The direct use of SN_e remnants (SNR) to improve this knowledge is however complicated since

(a) supernovæ are rare events in our galaxy ($\sim$ 1 or 2 supernovæ per century per galaxy),
(b) the direct observation and analysis of SNRs is in practice difficult, due to the intrinsic motions of SNRs (high-speed winds $\geq 1000\,\mathrm{km/s}$) and the complexity to extract accurate information on abundances.

The properties of the ICM chemical content and its metal accumulation over time therefore make it an excellent target for this exercise. A way to test these models is to examine the

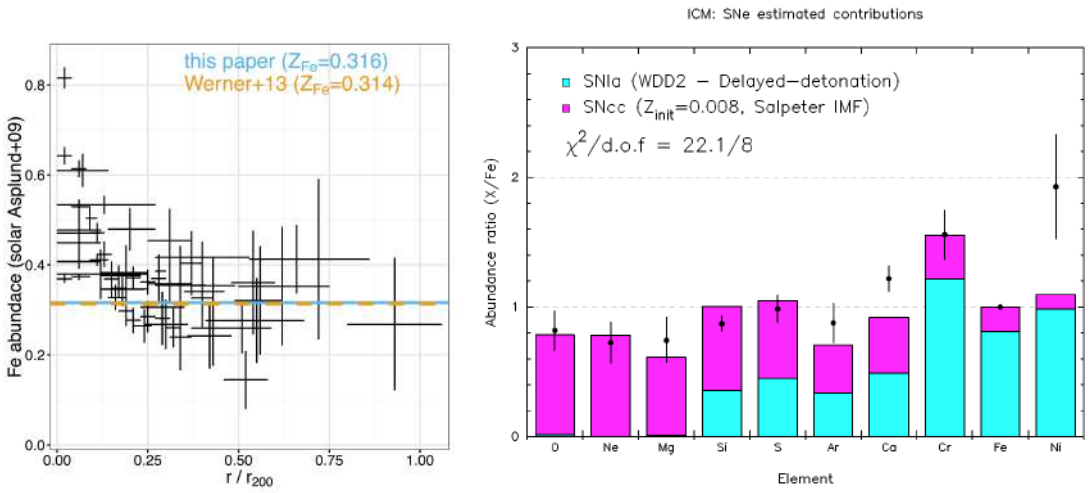

Figure 1.15: (*Left*) Reproduced from Urban et al. (2017), Figure 1. Iron abundance measured in a set of cluster relative to the solar abundance (as per Asplund et al., 2009) measured out to R_{200} using *Suzaku*. The average result in the outskirts from Werner et al. (2013) is also shown. (*Right*) Reproduced from Mernier et al. (2016b), Figure 3. Example of supernovæ models test using the CHEERS catalogue (de Plaa et al., 2017). The corresponding contributions of SN_{Ia} and SN_{cc} are given in blue and magenta respectively. See Mernier et al. (2016b) and references therein for details on the models.

abundance ratios of the metals (Mernier et al. 2016a, see Figure 1.15 – *Right*), as they are well constrained by specific physical process (e.g. the Ni/Fe ratio is almost exclusively dependent on the SN_{Ia} model). Starting from the early works of Mushotzky & Loewenstein (1997), more recent discoveries were made by pushing the current observatories to their limit (de Grandi & Molendi, 2009; Mernier et al., 2016b, 2017).

The comparison of the various models demonstrated for instance that all mechanisms coexist (notably both SN_{Ia} scenarios), with AGB stars being the less efficient enrichment overall, and SN_{Ia} and SN_{cc} being responsible for the formation of high- and low-mass elements respectively (SN_{cc} models being slightly dominant, as they involve lower time scales). These breakthroughs remain however unable to give meaningful constraints on either the IMF of stars, or the predominant mechanism for SN_{Ia}. As demonstrated by the early results of the mission *Hitomi* (Hitomi Collaboration, 2016, 2017), more accurate measurements, notably of rarer elements such as Ne, Mn or Cr, are key to understand supernovæ events (Simionescu et al., 2019a)

When were metals formed? The hints of an early enrichment

The metal production and circulation within clusters is a tracer for the overall evolution of the metal content of the Universe. All the productions mechanisms possess different time scales, suggesting that observations of clusters at different times (i.e. redshift) should yield different abundance ratios (see Mernier et al., 2018, for a review). Traces of large amounts of metals within galaxies are found up to the early epoch of the Universe, out to

$z \leq 5$ (McQuinn, 2016). It seems plausible that most of the metal production dates to the stelliferous epoch of the Universe, between $z \sim 2$ to 5, before the peak of cluster formation. Indications of an early enrichment are supported by observational evidences of the metal profiles near the outskirts of clusters, where metallicity profiles seem to reach a constant value of a few tenths of $Z_{\odot}$, regardless of the chemical species (Werner et al., 2013; Ettori et al., 2015; Ezer et al., 2017; Mantz et al., 2017). This result is consistent with the current numerical simulations (see Biffi et al., 2018a, for a review), and suggests that a large part of the metallic content was already in place before clusters formed.

Observational evidences also suggest a second, delayed enrichment within the cluster core (De Grandi et al., 2004). Due to infall of gas on the BCG, the central galaxies were replenished at more recent times, reigniting stellar activity. It is thus likely that SN_{Ia} production rates have increased at recent times, thus creating a more pronounced central peak of heavy elements (in particular Fe) compared to simple infall models.

Unfortunately, these results cannot give a definitive answer, as the observations of clusters beyond the local Universe ($z \geq 0.5$) and far in the outskirts are limited by the low effective area of the current X-ray telescopes (i.e. observation time), and by the X-ray background. Even in the local Universe, a clear understanding remains to be found.

1.4 The energetic phenomena of the Universe

1.4.1 X-ray as messengers of the energetic Universe

Beyond the observation of large structures such as groups and clusters of galaxies, the X-ray emission of the sky is also a tracer of some of the energetic phenomena of the Universe.

X-ray counterparts of Gamma-ray bursts

Starting from the early detections of GRBs (Klebesadel et al., 1973), the understanding of these powerful events has gradually evolved to distinguish two types of GRBs. Long duration GRBs ($\sim$ 70% of events) are now related to rapidly rotating low-metallicity massive stars undergoing a supernova-like collapse event (MacFadyen & Woosley, 1999). Short GRBs are instead linked to mergers of compact binary systems (e.g. NS-NS or NS-BH, Verbunt 1993). Though unsupported by direct observations at first, this latter scenario has now been verified by the birth of multi-messenger astronomy (Abbott et al., 2016a, 2017, 2018). Overall, the study of GRBs in the X-rays is not straightforward. In general, observatories look at the X-ray counterpart[2] of GRBs in emission or in absorption:

(a) **In absorption,** the observation of local bright GRBs (along with local AGNs) is a promising option to investigate the hidden WHIM (Nicastro et al., 2013), which is weakly-interacting with any other electromagnetic part of the spectrum except for X-rays and Gamma-rays. The WHIM is a likely candidate to explain the undetected baryonic mass of the local Universe. Observational hints of its detection were found with current instruments (Nicastro et al., 2018), but the S/N ratio of these measurements remains insufficient to provide a definitive answer on this question.

(b) **In emission,** the study of GRBs is equally a probe for the WHIM for local events ($z \leq 0.1$). Most of emission studies are however focused on high-redshift ($z > 5$)

[2]Not only can GRBs be redshifted into the X-band, but the GRB spectrum itself changes with time and eventually emits (weaker) counterparts in all wavelengths.

GRBs. Since high-redshift GRB progenitors lie in star-formation regions, the spectra of these events provide insight on the early population III stars and the formation of heavy elements (Thielemann et al., 2017). Finally, like SN_{Ia}, GRBs can also be used as probes to test the cosmology (Demianski et al., 2017a,b).

The unexpected and variable trait of GRBs makes them difficult to observe, and are reserved to dedicated agile observatories (e.g. *SWIFT*, Barthelmy et al. 2005, or the upcoming mission *SVOM*, Wei et al. 2016), or to targets of opportunity (ToOs) for X-ray observations. The birth of multi-messenger astronomy opens a new way to study short GRBs, as detection can now be followed first via gravitational waves (which arrive first), before using the full extent of the electromagnetic spectrum (Nakar et al., 2018).

Jets and ultra-fast outflows

Regardless of the type regulation mechanism (radiative or kinetic, Fabian 2012), the role of AGNs in the overall ICM regulation and galaxy evolution is well asserted. The physics of the AGNs and the nature of the regulating mechanisms, however, are yet to be understood. In active radiative AGNs, the SMBH is accreting matter close to its Eddington limit, which creates powerful radiation pressure on the surrounding matter (Silk & Rees, 1998). Though by far more powerful than other types of mechanism, its effect is spatially-limited, as the AGN surroundings rapidly become transparent to radiation outside the bulge of the galaxy. This spatial correlation could explain the observational agreement between the BH mass and the radial velocity distribution of the galactic bulge (Gültekin et al., 2009).

Larger regulations on a cluster scale need to be mechanically driven. More than 50% of the observed clusters reveal cavities and bubbles in the X-rays (Morganti, 2017), correlated with powerful radio jets emitted by the AGN. Further, the measurements of the ionised gas (iron) in the vicinity of these jets performed by *XMM-Newton* and *Chandra* showed significantly blue-shifted iron lines (Pounds et al., 2003; Reeves et al., 2003), compatible with outflow velocities up $\sim 0.1 - 0.3\,c$. The power involved in these ultra-fast outflows (UFOs, Tombesi et al. 2010) shows that jets and outflows are likely to be the main driver of AGN feedback at the cluster scale (McNamara & Nulsen, 2007, 2012).

The mechanisms of these jets and outflows remains debated, as different theories related to the overall accretion geometry of the SMBH (Abramowicz & Fragile, 2013) seem to explain their formation (see King & Pounds, 2015, for a review). The origin of the Fe emission near the AGN was itself disputed, on whether it rather originated from the accretion disk of the SMBH or the surrounding ISM. Recently, the step forward in spectral resolution brought by *Hitomi* (Hitomi Collaboration, 2018c) suggested that the emission is concentrated in a toroidal region rotating nearby the AGN system. Similar conclusions were also found by combining numerical and observational works (Gaspari et al., 2018). Future observations with improved spatial and spectral resolution will be key to understand the physics of these powerful phenomena and their interplay with their surroundings.

1.4.2 Understanding the evolution of compact objects

The direct observation of compact objects is challenging due to their weak intrinsic emission. In some cases however, their orbit remains locked into a binary system with a com-

panion star. The subsequent accretion of matter from the companion onto the compact object creates jets and spurs of energy in the X-rays (Galloway et al., 2008), making X-ray binaries (XRBs) a tool of choice to test the physics of extreme environments.

In the case of NS XRBs, the observation of the regularity, the frequency, and the luminosity of the accretion-driven jets provides a direct insight on the physics of the NS, specifically its equation of state (Lattimer, 2012). These observations can also be used to test general relativity in strong fields (Psaltis, 2008), or to understand the interplay of NSs with their surroundings (e.g. accretion, magnetic fields, Miller & Miller 2015). New steps forward require however improved energy and timing resolutions of these observations.

Similarly, the observation of BH environments using BH XRBs, or the direct observation of AGNs in BCGs, brought insight in the evolution of these structures. An important parameter to determine is the BH spin, related to the formation of the compact object (Berti & Volonteri, 2008) but also to its accretion (Miller et al., 2013). Measurements of broadened blue-shifted iron lines and their X-ray continuum due to a reflected component of the BH hard X-ray emission on the accretion disk (George & Fabian, 1991; Miller, 2007) are key to constrain the growth of BH, and to improve our understanding of the disk dynamics near the event horizon (for a review, see Miller & Miller, 2015). These mechanisms remain to be investigated by future observatories.

1.5 Present limits and future challenges in X-ray astronomy

1.5.1 Open questions in X-ray astronomy

Since the first generation of X-ray observatories, each new mission brought its share of breakthroughs and raised new, fundamental, questions for astronomers. I remind here several of the open questions derived from the previous introduction.

Large-scale structures and the hot Universe

Despite a general understanding of how large structures form, a clear scenario of the birth and evolution of massive halos (groups or clusters of galaxies) remains to be laid out. Similarly the question of the chemical enrichment is still open. Some of the main questions on the topic are:

- How do clusters form and evolve? (Section 1.2.2)
- How does AGN feedback interplays with the surrounding ICM? (Section 1.2.3)
- What is the role of early stars in the chemical enrichment of the Universe? (Section 1.3.1)
- When and how was the ICM enriched? (Section 1.3.2)

Energetic Universe

X-ray allowed an unprecedented understanding of compact objects and of some of the most extreme phenomena in our Universe. Several questions remain however unanswered:

- What are GRBs and can they be used to detect the WHIM or the formation of the first heavy elements? (Section 1.4.1)

- How are BH structured and what is the interplay with their surroundings (accretion, corona)? (Section 1.4.1, 1.4.2)
- What is the origin of ultra-relativistic jets and emissions from BH? (Section 1.4.1)
- What are NSs made of? (Section 1.4.2)

Though the hot and energetic Universe questions represent the bulk of modern X-ray astronomy, many other open questions are also present for numerous other scientific objectives, notably related to observational science (e.g. X-ray emission in the Solar System, detection of exoplanets using X-rays).

1.5.2 The need for a new-generation X-ray observatory

Limitations of current observatories

With two decades of operations, both *Chandra* and *XMM-Newton* have without a doubt helped in our general understanding of these questions. But even such long-lived and well-performing missions have their limitations. Both possess CCD detectors with excellent spatial capabilities, or gratings with excellent spectral resolution. The lack of these simultaneous capabilities however, prevents spatially resolved observations of fine spectral features. This currently halts key studies, such as the analysis of abundance ratios to determine the enrichment of the ICM, detailed measurements of line shifts to determine BH spins or AGN feedback power, or even measurements of line broadening to study the turbulent cascade of the ICM.

The effective area of both telescopes also hinders the exploration of the distant Universe, as prohibitive exposure times and a nearly-perfect knowledge of the background components are required. This is worsened on *Chandra* by contamination effects on the mirrors, which over time degraded the low-energy effective area of the telescope. Despite these limitations, *Chandra* and *XMM-Newton* have redefined the core questions of X-ray astronomy, pushing forward the knowledge in every subject. Open questions shall now be addressed by future observatories.

Towards a new generation of X-ray instruments

The next generation of X-ray observatories must provide a quantum leap in our knowledge of the X-ray sky. To do so, two main characteristics are needed.

Large effective area – To investigate the Universe at high redshift, the future X-ray observatories need to improve their effective area over the entire X-ray bandpass to increase signal-to-noise ratios of the lines and reduce uncertainties related to observational background (either instrumental or astrophysical). This is particularly needed at low energies, where most of the redshifted faint lines will lie (typically $\leq 2\,\mathrm{keV}$). Current developments in mirror design (particularly using silicon wafers, Bavdaz et al. 2013; Zhang et al. 2018), provide light-weight, reliable optical system to improve the overall angular resolution and effective area of the mirrors.

Spatially resolved spectroscopy – The overall picture provided by CCDs and gratings is no longer sufficient to tackle the modern challenges of X-ray astronomy. The need

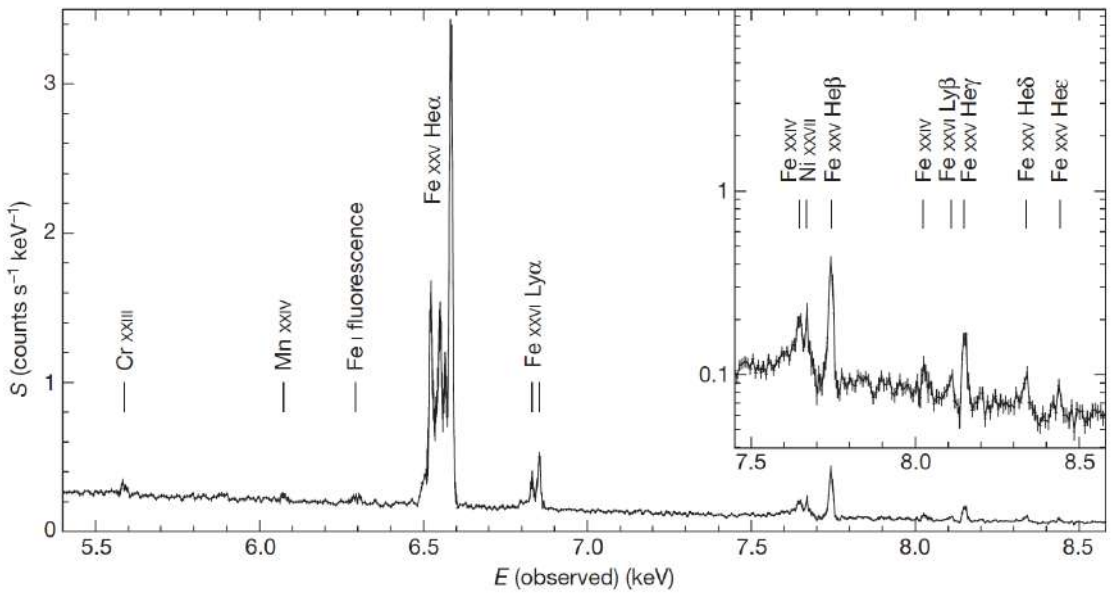

Figure 1.16: Reproduced from Hitomi Collaboration (2016), Figure 1. Full array spectrum of the Perseus cluster core seen by the SXS onboard *Hitomi*. This spectrum can be compared to the equivalent ones Figure 1.12

.

for spatially resolved X-ray spectroscopy requires a new generation of detectors. A breakthrough solution is the use of micro-calorimeter arrays (Moseley et al., 1984), which provide exquisite spectral resolution (≤ 10 eV over the soft X-ray bandpass) while maintaining the ability to spatially map photons in the count rate regime of typical astrophysical sources ($\lesssim 5$ cps/pix), provided a good angular resolution of the mirrors.

The recent mission *Hitomi* and specifically the SXS instrument are an example of the future of X-ray astronomy. Unfortunately, due to an unexpectedly short mission lifetime, the SXS only provided a glimpse of what the future of X-ray astronomy will be (Figure 1.16). This is no surprise then, that all future observatories – *XRISM* in 2021 (Tashiro et al., 2018), *Athena* in 2031 (Nandra et al., 2013) or *Lynx* in 2035 (Gaskin et al., 2018) – plan similar micro-calorimeter instruments on board.

CHAPTER 2

The *Athena* mission and the X-ray Integral Field Unit

2.1 The Advanced Telescope for High-Energy Astrophysics

2.1.1 The *Athena* mission

The fundamental open questions in X-ray astrophysics and their interplay with physics in general dictate the need to design and operate a new generation of X-ray observatories. Regrouped under the 'Hot and Energetic Universe' science theme, these questions were deemed a scientific priority by the European Space Agency (ESA), and were selected in 2013 to be at the core of an upcoming European mission. To address this theme specifically, ESA has selected in 2014 the advanced telescope for high-energy astrophysics (*Athena*) as its second 'Large' class mission (1.05 G€ of budget) of its *Cosmic Vision* program (Nandra et al., 2014). *Athena* is scheduled for a launch in 2031 on an Ariane 6 rocket and will operate in an orbit around the second Lagrange point (L2) of the Earth-Sun system. This choice ensures a constant sky coverage, a good downlink visibility with ground stations, and a stable thermal environment for the mission. The satellite will be composed of a Wolter-I type mirror of 1.4 m^2, with a focal length of 12 m (Figure 2.1). It will carry on its detector plane (spacecraft instrument module, or SIM) two instruments, the wide field imager (WFI, Meidinger et al. 2017) and the X-ray integral field unit (X-IFU, Barret et al. 2016, 2018b). The total expected mass of the satellite will be of 7.3 t, for a total power consumption above 3 kW. *Athena* is currently finishing its feasibility study phase (phase A), and will enter its definition phase (phase B) at the end of 2019, planning for a formal adoption by ESA in 2021.

Athena and its two instruments will investigate the 'Hot and energetic Universe' topic with unprecedented capabilities (see Nandra et al., 2013, and the following *Athena* white papers). On the one hand, *Athena* will address key questions of the hot Universe such as the formation and evolution of clusters and groups (Pointecouteau et al., 2013), the mechanisms of their enrichment (Ettori et al., 2013b), the dynamics of AGN feedback (Croston et al., 2013), or the detection of the missing baryons in the WHIM (Kaastra

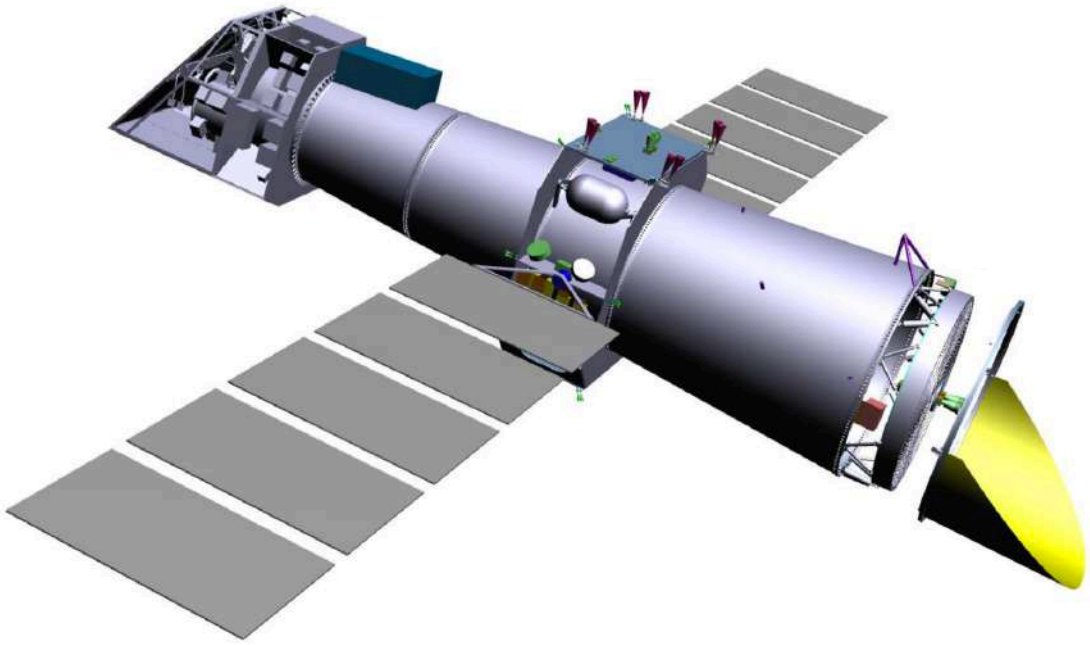

Figure 2.1: Current computer-aided design (CAD) of the *Athena* telescope. The mirror is shown on the right-hand part, while the SIM is visible on the left-hand part of the design

et al., 2013) On the other, it will tackle crucial questions related to the energetic Universe such as the formation or the dynamics of the early BHs (Aird et al., 2013; Georgakakis et al., 2013) or the astrophysics of the compact object (Cappi et al., 2013) and their accretion (Dovciak et al., 2013).

Athena was also designed to provide clues to other branches of X-ray astrophysics, such as the formation and evolution of stars (Decourchelle et al., 2013; Motch et al., 2013; Sciortino et al., 2013), the detection of exoplanets, or the exploration of the Solar System (Branduardi-Raymont et al., 2013). The agility of the satellite was considered in its design. With the ability to rapidly point targets, *Athena* will be capable of observing the transient sky (Jonker et al., 2013), and notably GRBs, supernovæ or other ToOs.

2.1.2 The *Athena* mirror assembly

To provide a quantum leap in sensitivity with respect to its predecessors, the optics of the *Athena* mirror were designed to maximise the overall effective area available over the soft X-ray bandpass, from 0.2 keV to 15 keV (see Figure 2.2 – *Left*). The current mirror design plans for an aperture of ~ 3 m in diameter, resulting in an unprecedented effective area of 1.4 m^2 at 1 keV, and 0.24 m^2 at 6 keV near the iron K_α line features. This represents a slight decrease with respect to the original proposed mirror configuration (which foresaw a 2 m^2 effective area at 1 keV, Willingale et al. 2013), but does not change the transformational capabilities of the mission and its instruments.[3] As shown in Figure 2.2 (*Right*), this represents a significant step forward with respect to its predecessors, but also to previous

[3] Which in most cases can be recovered by a slightly higher exposure time.

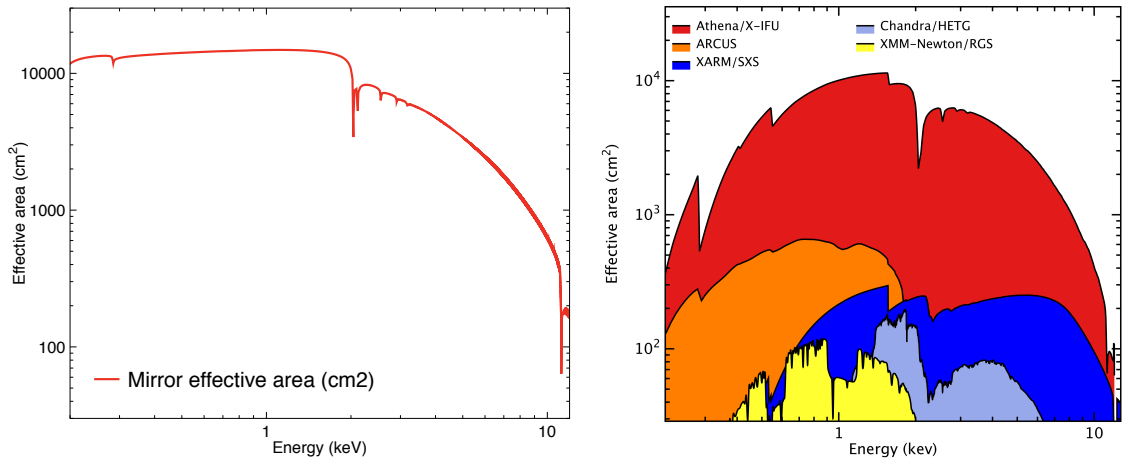

Figure 2.2: (*Left*) Effective area (cm^2) over the 0.2 – 12 keV bandpass of the *Athena* mirror. (*Right*) Total effective area of the *Athena* X-IFU instrument (cm^2) accounting for instrumental transmission over the bandpass and comparison with previous or planned high-resolution X-ray instruments (courtesy D. Barret).

or planned missions such as *Hitomi* or *XRISM*.

The mirror in itself is a Wolter-type mirror composed of a double reflection stage (paraboloidal and hyperboloidal mirrors), which will focus X-rays at grazing incidence onto the detector plane. Each mirror will be composed of silicon pore optics (SPO) mirror modules (MMs, Figure 2.3). The current design of the *Athena* mirror is composed of 678 MMs, each made of more than 100 mirror plates (for a total of $\sim$ 100 000 mirror plates, Collon et al. 2018). These plates are cut off mono-crystal wafers of silicon. Each is bent with a slightly different curvature radius (both ortho-radially and azimuthally) to maximise the overall transmission of the mirror. Inner modules (will low grazing angles) will for instance mainly focus higher energy photons, while outer rows should essentially focus lower energy photons (Figure 2.3). The silicon of each of these plates will further be coated to improve the overall X-ray reflection efficiency. Current solutions include either iridium on boron carbide (Ir/B_4C) or iridium on silicon carbide (Ir/SiC).

The expected point spread function (PSF) of the telescope should be Gaussian, with an on-axis angular resolution of 5″ half-energy width (HEW), and very shallow degradations out to 7″ at 20′ from the centre. Current experiments demonstrate much better angular resolution for a single mirror plate (around 2″, Bavdaz et al. 2013), though stacking and thermal stresses degrade the overall accuracy of the integrated mirror. Latest MMs show typically 5″ on-axis and 10″ at 20′, and major efforts are put into reducing these figures (Bavdaz et al., 2018). The vignetting effect of the telescope (related to the off-axis attenuation of the mirror effective area) is also expected to be low, with negligible effects ($\leq 4\%$) for the X-IFU field-of-view (FoV) of 5′ in equivalent diameter, and limited effects ($\leq 10\%$) for the WFI FoV ($40' \times 40'$).

Interestingly, the overall structure will be mounted on a mirror assembly module (MAM) hexapod, which will enable astronomers to switch between instruments, thus avoiding having separate mirrors and increasing the overall effective area of each instrument.[4]

[4]Preventing, however, simultaneous observations with both instruments.

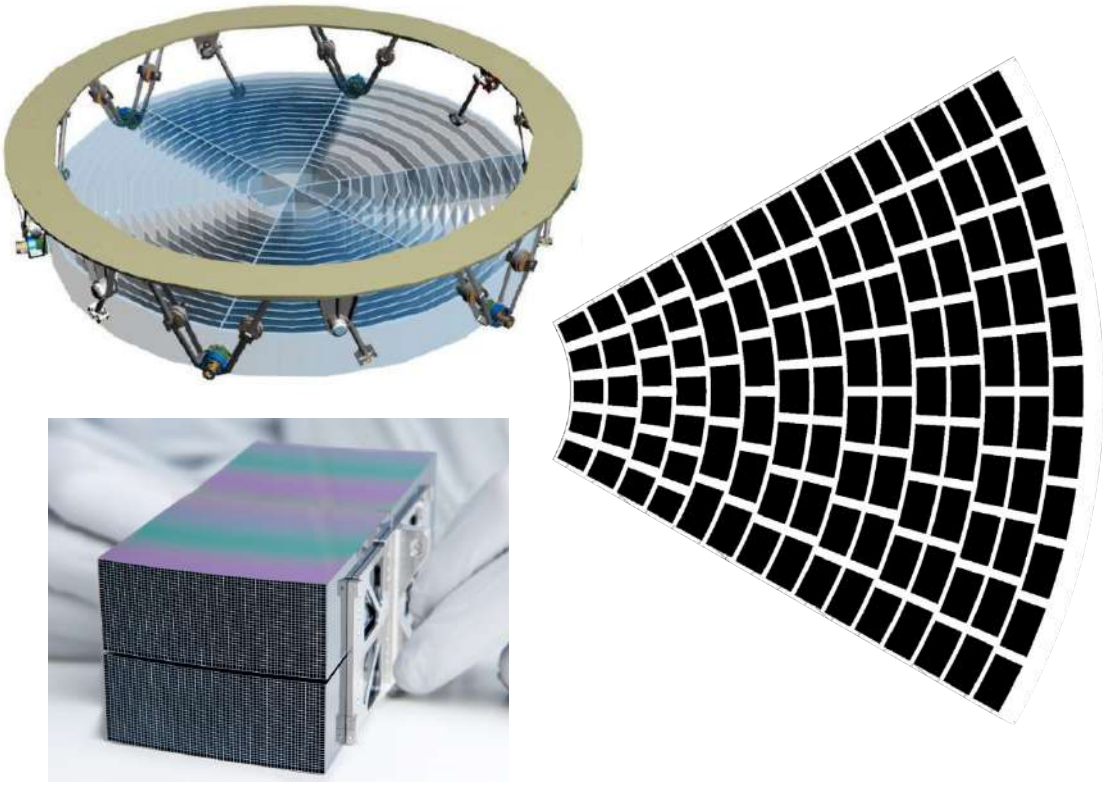

Figure 2.3: (*Top Left*) Mirror design of the *Athena* telescope mounted on the MAM (Credits: M. Bavdaz, Cosine). (*Bottom left*) Example of one SPO MM made composed of two stacks (Credits: ESA). (*Right*) Reproduced from Oosterbroeck (2018), Figure 4. Example of a mirror 'petal', showing the different MM sizes and shapes.

The movement capabilities of the MAM will also be used for in-flight tuning of the focal plane or to purposely defocus the incoming beam (Figure 2.3) to improve for instanec the overall count rate capabilities of the instrument (see Chapter 3) at the expense of spatial resolution. This defocussing capability will be specifically interesting in the observation of bright point-like sources. An additional soft proton diverter composed of a powerful magnet is also planned on the satellite structure (see Figure 2.1) to deviate energetic protons coming from the solar wind and focused by the mirror, thus substantially alleviating the charged particle background on the detectors (Fioretti et al., 2018; Lotti et al., 2018b).

2.2 The Wide Field Imager

2.2.1 Instrumental design and detection principle

The *Athena* WFI is designed to provide high-quality imaging of the X-ray sky and excellent count rate performances. Its technology is driven by the strong heritage of previous pro-

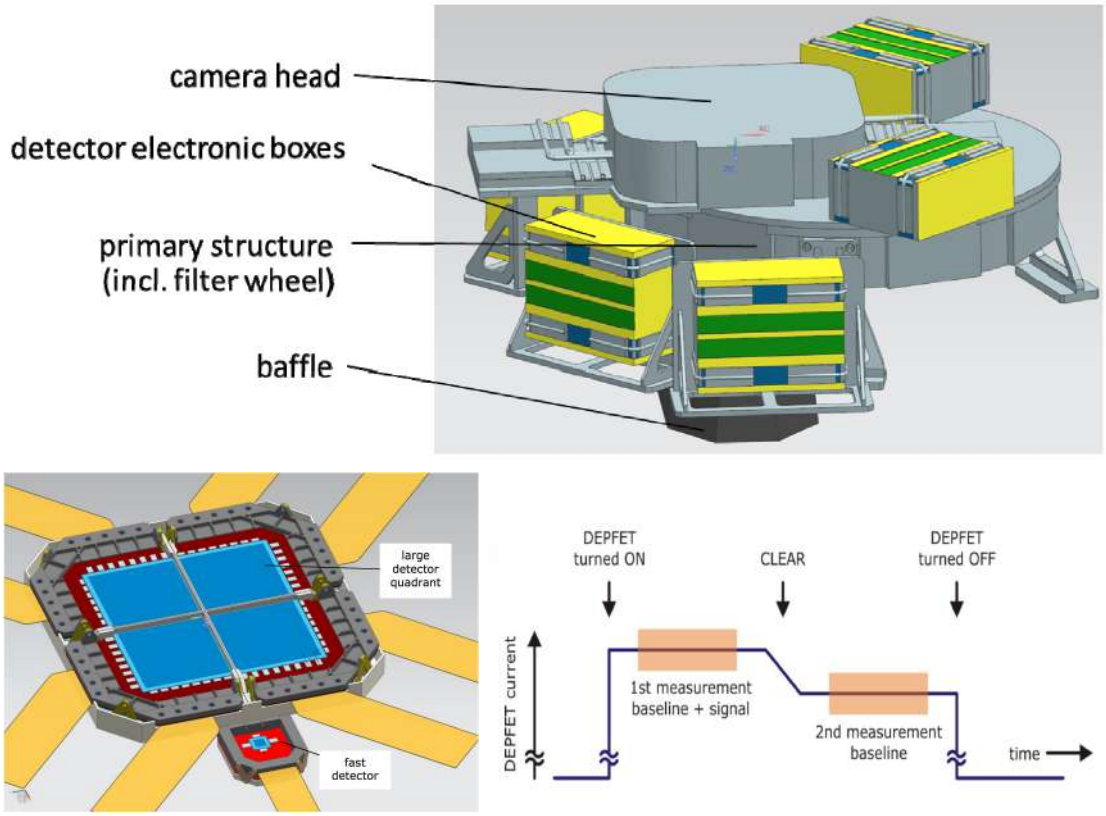

Figure 2.4: (*Top*) Reproduced from Meidinger et al. (2017), Figure 1. Current configuration of the WFI. (*Bottom left*) Reproduced from Meidinger et al. (2015a), Figure 3. Focal plane detector of the WFI with the 2x2 quadrant detector and the fast chip within the instrument camera head. (*Bottom right*) Reproduced from Meidinger et al. (2015b), Figure 5. Signal evaluation scheme for an APS.

posed missions such as the international X-ray observatory (IXO, Stefanescu et al. 2010), or the EPIC-PN instrument on *XMM-Newton* (Strüder et al., 2001). To take advantage of the *Athena* mirror effective area, the WFI will possess a large FoV of $40' \times 40'$, composed of 2×2 quadrants, each comprising 512×512 square active pixel sensors (APSs) with a timing resolution of 5 ms. Each pixel will be 130 µm of side (Figure 2.4 – *Bottom left*), thus representing $2.27''$ on the sky to ensure an oversampling of the PSF. Additionally, the WFI will carry a small FoV 'fast chip' of 64×64 pixels with a timing resolution of 80 µs to improve the throughput in the observation of point-like bright sources (up to a few times the Crab flux[5] and $\geq 90\%$ of throughput at 1 Crab with $\leq 1\%$ of pile-up).

The detectors are based on depleted p-channel field-effect transistors (DEPFETs), which are composed of a p-channel metal-oxide semiconductor field-effect transistor (MOSFET) integrated into a 450 µm-thick fully depleted silicon bulk (Meidinger et al., 2017; Treberspurg et al., 2018a). Much like typical transistors, the addition of a deep-n region in the pixels creates the 'gate' of the pixel, which can then be controlled and drained by tuning the voltage on its inputs. Whenever X-ray photons hit the semiconductor mate-

[5]The Crab flux is defined by a flux of 2.4×10^{11} W/m^2 over 2 – 10 keV.

rial, they generate electron-hole pairs proportional to the deposited energy and change the conductivity of the pixel, creating a current proportional to the input energy. This current becomes independent of other transistor currents (as the conduction tunnel forms in the MOSFET) and can only be cleared by applying sufficient voltage on the gate pin. Thus, each pixel only needs to be turned on during readout and remains off the rest of the time. The integrated charge received by a pixel during its 'on' time can be estimated by measuring the current before and after the charge is removed (Figure 2.4 – *Bottom right*).

The readout scheme is performed by ASICs (application specific integrated circuits), which control the duty cycle of the pixel (Herrmann et al., 2018). To avoid large peak power consumptions, detectors are not read individually but in rows instead. Two dedicated readout modes are considered for the large chip (Behrens et al., 2018). A normal mode ('full frame') which reads each quadrant sequentially with a ≤ 5 ms timing resolution, or a targeted mode ('window'), which can limit the readout to specific parts of the chip, thus increasing the timing resolution by an order of magnitude. Through this technology, the overall detector chip will perform powerful imaging in the 0.2 – 15 keV energy band, with an intrinsic energy resolution of 80 eV at 1 keV and 170 eV near 7 keV (thus approaching the Fano noise limit of these detectors, Treberspurg et al. 2018b).

The power consumption generated by the full frame mode requires a very challenging thermal design of the detectors, which will be passively cooled through heat-pipes to ensure a high-stability operation at 193K ($\pm$10 K). The front-end electronics are then decoupled from the main sensor chip and are operated around 280 K (Fürmetz et al., 2016).

2.2.2 Steps forward with the WFI

With its large FoV and the excellent *Athena* mirror angular resolution, the WFI will provide a significant step forward in X-ray imaging and survey with respect to previous similar instruments. This, along with its count rate capabilities, will make the WFI an excellent probe to observe the distant Universe and very bright objects. A few of the major WFI science objectives are reminded in Rau et al. (2016), I summarize here in a nutshell the main focuses of this instrument.

Previously hindered by the low effective areas of X-ray telescopes, the large collective area of the *Athena* mirror coupled to the WFI will be able to probe distant Universe ($z \geq 6$) and find the early seeds of SMBHs, to study their evolution, but also to investigate the early population III stars (Volonteri, 2012). This will provide interesting evidence of the first AGN and clues on the formation mechanisms of early massive BH. The timing capabilities of the instrument will also provide accurate measurements of BH spins or accretion physics in bright binary systems through the observation of blue-shifted lines. An improvement of at least an order of magnitude in accuracy is expected with respect to *XMM-Newton* in the bright sources capability, likewise in timing with respect to *eROSITA* (50 ms, against the 5 ms expected for the WFI, Meidinger et al. 2017). Finally, the large FoV and low particle background (5×10^{-3} cts/s/keV/cm^2 over the detector bandpass, von Kienlin et al. 2018) will also bring a step forward in the observations of local galaxy clusters or early groups, by measuring with sufficient accuracy temperature and entropy profiles out to the virial radius (Pratt et al., 2010; Eckert et al., 2013), quantities that are routinely measured only out to R_{500} by *Chandra* and *XMM-Newton*.

2.3 The X-ray Integral Field Unit

2.3.1 Instrument motivation and design

The X-IFU is the second instrument on board *Athena* (Barret et al., 2016, 2018b) and will be a ground-breaking tool for X-ray astronomy. The main concept of the X-IFU is inspired by the previous designs of the X-ray micro-calorimeter spectrometer (XMS) on IXO, and on early stages of the past *Athena* L1 mission (Barcons et al., 2011). It will fly an array of 3168 transition edge sensors (TESs) micro-calorimeters for a total 5′ FoV of equivalent diameter. Each pixel will correspond to a $4.6'' \times 4.6''$ apparent size on the sky, thus providing a limited oversampling of the PSF and a good spatial resolution. The revolutionary trait of the instrument is its unprecedented spectroscopic capabilities in the soft X-ray band between 0.2 and 12 keV, with a spectral resolution of 2.5 eV (FWHM) at 7 keV ($R = 2800$), and an even better spectral resolution expected at 1 keV for each pixel. The main other performance requirements are gathered in Table 2.1.

The design of the X-IFU is driven by the need of X-ray spatially resolved high-resolution spectroscopy. Due to the complexity of the instrument (see block diagram in Figure 2.5), the X-IFU is carried by a multinational cooperation between 13 countries (Belgium, Czech Republic, Finland, France, Germany, Ireland, Italy, Japan, Netherlands, Poland, Spain, Switzerland, United States), each responsible of one (or more) subsystem(s). The assembly, the design and the project management is entrusted to the Centre National d'Études Spatiales (CNES, France), while the scientific performance of the instrument will be ensured throughout the development by the principal investigator (PI) from the Institut de Recherche en Astrophysique et Planétologie (IRAP, France). The challenge raised by the X-IFU is not only related to the sensitivity and operation of TES detectors, but also to their readout, which requires a stable, reliable cryogenic system (see also Appendix A).

Parameter	Requirement
Field-of-view	5′ equivalent diameter
Energy bandpass	0.2 – 12 keV
Quantum efficiency	$\geq$ 67% at 1 keV $\geq$ 72% at 7 keV
Energy resolution	$\leq$ 2.5 eV up to 7 keV $\leq$ 5 eV at 10 keV
Energy scale knowledge	$\leq$ 0.4 eV over 0.2 – 7 keV
Count rate capability	(point source) 0.25 mCrab with 80% throughput (extended source) 726 cts/s/cm^2 with 80% throughput (defocused point-source) 1 Crab with 50% throughput and 10 eV resolution (5 – 8 keV), 35 mm defocusing
Timing resolution	10 µs (relative) 5 µs (absolute)
Non-X-ray Background	$\leq 5 \times 10^{-3}$ cts/s/keV/cm^2 $\geq$ 80% of the time, on 2 – 10 keV

Table 2.1: The X-IFU main performance requirements

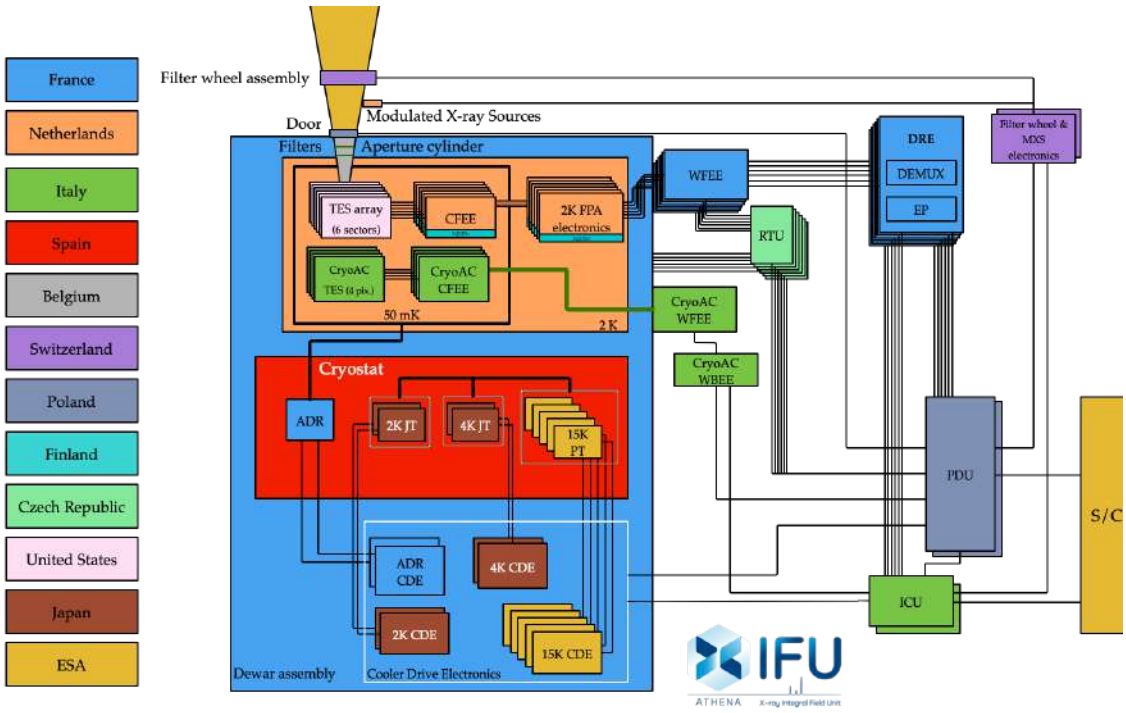

Figure 2.5: The X-IFU functional block diagram. The various subsystems are highlighted, along with the corresponding contribution of the international partners.

2.3.2 TES micro-calorimeter detection principle

Detection principle

The idea of micro-calorimeter-based instruments for X-ray detection is not recent (Moseley et al., 1984; McCammon et al., 1984; Wollman et al., 1997). Their detection principle is similar to that of a calorimeter. Each detector can be decomposed in three parts (Figure 2.6 – *Top*):

- An X-ray-thick absorber, which is hit by the incident X-ray radiation and thermalizes the incoming X-ray photon to create heat.
- A sensitive thermometer, which measures the thermal energy generated by the absorbed photon.
- A heat sink towards a thermostat (thermal bath), which evacuates the heat and sets the pixel equilibrium for future measurements.

In principle, such devices can be used to measure individual photons through their heat deposition, as long as the photon rates are low, and the heat sinking fast. This makes them particularly suited to X-ray astronomy given the overall low count rates of astrophysical sources. The efficiency of a micro-calorimeter is linked to the performance of its absorber, and its sensitivity to the quality of the thermometer (Irwin & Hilton, 2005).

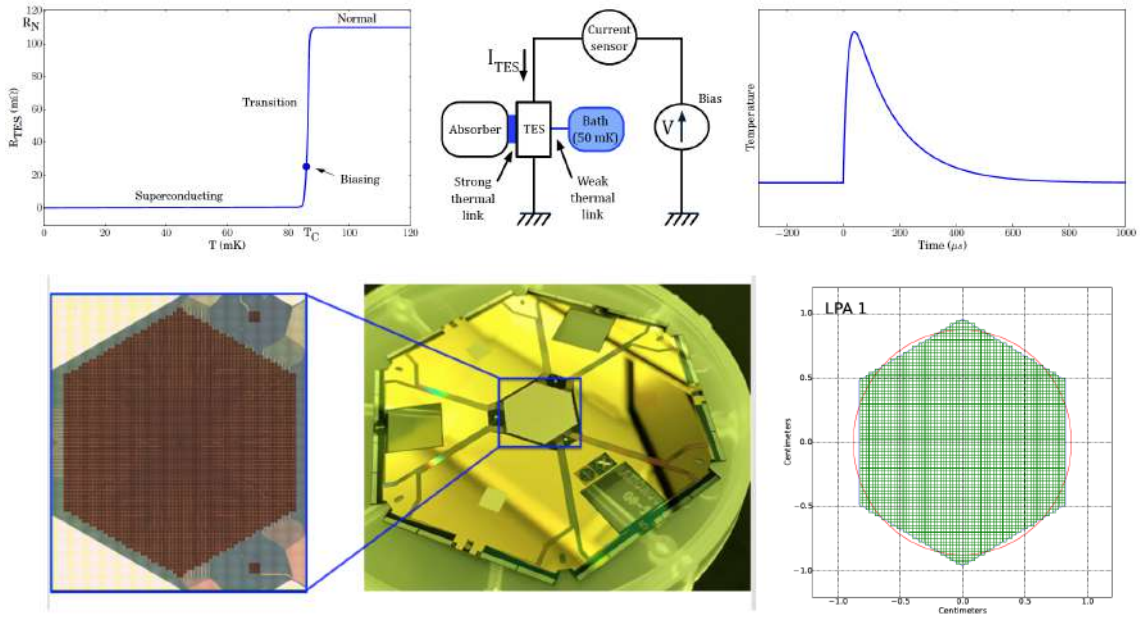

Figure 2.6: (*Top*) Reproduced from (Ravera et al., 2014a), Figure 2. Illustration of the TES detection principle. The plot on the left shows the superconducting transition of the TES, the central part the main electro-thermal circuit and the right plot the characteristic pulse associated to a photon detection. (*Bottom left*) Example of a TES array developed at GSFC (courtesy GSFC). (*Bottom right*) Example of a hexagonal detector plane considered for the X-IFU (courtesy S. Smith).

The current design of the X-IFU detector array foresees a hexagonal array of 3168 square micro-calorimeter TESs with a pitch of 275 µm. Their absorbers will be composed of a bi-layer of bismuth (4.2 µm) and gold (1.7 µm), which provide a good stopping power (Bi) and low heat capacity of the pixel (Au, Smith et al. 2016). The thermometer will be made of superconducting Mo/Au bi-layer TES detectors, operated in their superconducting transition at $\sim$ 90 mK and deposited over a silicon nitride layer. Each TES will be connected to its absorber by dot-stems, and connected through a weak thermal link (high thermal conductivity G) to a thermal bath at $T_{\rm bath} = 55$ mK. The advantage of TESs is to use the superconducting transition to increase the sensitivity and the dynamic range of the detection. As shown in Figure 2.6 (*Top*), by biasing through a fixed voltage, $V_{\rm bias}$, the TES in its transition, any absorbed photon will create large excursions in the intrinsic resistance which can be detected as a decrease in current.[6] In the case of the X-IFU, an AC voltage bias of the pixels is considered. The thermal bath will remove the excess heat, decreasing the current and returning the pixel to electro-thermal equilibrium. Each photon is seen as a current pulse, which can be measured by a current sensor.

The efficiency of TES detectors depends on the linearity and shape of their transition, in particular for AC-biased pixels (Akamatsu et al., 2016; Sakai et al., 2018). It is therefore essential to create uniform detectors with known superconducting critical temperatures, T_c, and with linear transitions. The former helps to bias the pixel with good accuracy and

[6] In other words, if $V = RI$, at constant V, if R increases, I decreases.

increase the dynamic range, the latter ensures that amplitude of the TES excursion on the transition remains in a linear range. If a large amount of heat is deposited, the TES may switch entirely to its normal state, causing saturation in the energy detection.

Unlike other detectors, TESs have the capability of providing excellent spectral resolution coupled with counting capabilities, making them an ideal solution for integral field units (IFUs) instruments (Irwin et al., 1996). Though requiring a cryogenic operation, the use of low temperatures also reduces numerous noise contributions visible at higher temperatures, and ensures a large dynamic range of the detectors throughout the bandpass. At launch, the X-IFU will be the first space-borne TES-based X-ray instrument.

2.3.3 Readout principle

The impact of a photon onto a detector creates a current pulse (a few µA). This current needs to be amplified and carried to the onboard electronics with minimal losses and minimal noise, and this for each of the 3168 TESs. The schematic diagram of the full readout chain is given Appendix B. I provide here a short explanation of its operation.

Pixel bias and frequency domain multiplexing

The TESs will be AC-voltage-biased in their transition to increase their sensitivity (Irwin & Hilton, 2005). The simplest solution to do so is to use dedicated voltage sources for each pixel. Yet, this is not possible without immense integration complexities and strong thermal loads at the 50/100 mK cryogenic level. Multiplexing strategies are therefore planned to reduce power consumption, heat loads and the total mass of the system. Three techniques are commonly used for readout (Irwin, 2009): frequency domain multiplexing (FDM), time domain multiplexing (TDM) and code domain multiplexing (CDM). For the X-IFU, the FDM represents the baseline for the readout (den Hartog et al., 2014; Akamatsu et al., 2018), with TDM as back-up (see Appendix F for more information on TDM).

For FDM (see Figure 2.7), each pixel i is associated with a specific carrier frequency f_i. The frequency comb of the pixels is created using a digital generator (e.g. a direct digital synthesizer, or DDS) with a considered frequency spacing (e.g. 100 kHz) over the 1 to 5 MHz frequency band (van der Kuur et al., 2016), and converted into an analogue signal using a digital-to-analogue converter (DAC, Ravera et al., 2014b). At pixel level, a dedicated high-Q LC bandpass filter of frequency f_i (Bruijn et al., 2018) is associated to each TES to filter, in the AC-voltage comb, the carrier whose current is used for a single-pixel amplitude modulation. Interestingly, in FDM, the amplitude of each carrier can be adapted to optimise the bias point of each pixel. Likewise, in case of imperfections in the LC filters, the frequency grid can be slightly adapted to match the bandpass frequency more accurately (van der Kuur et al., 2018). To avoid ground and electric coupling, to match the TES impedance with the readout circuit and for fabrication purposes of the LC filters inductances, each TES is decoupled from the bias circuit by a transformer, with a given transformer turns ratio (TTR) equal for each pixel.

A single, summed, signal is output from the electrical line. Since a single readout chain for ≥ 3000 pixels would be extremely complex to demodulate (due to e.g. aliasing, imperfections in the resonances, etc...), two solutions are currently considered:

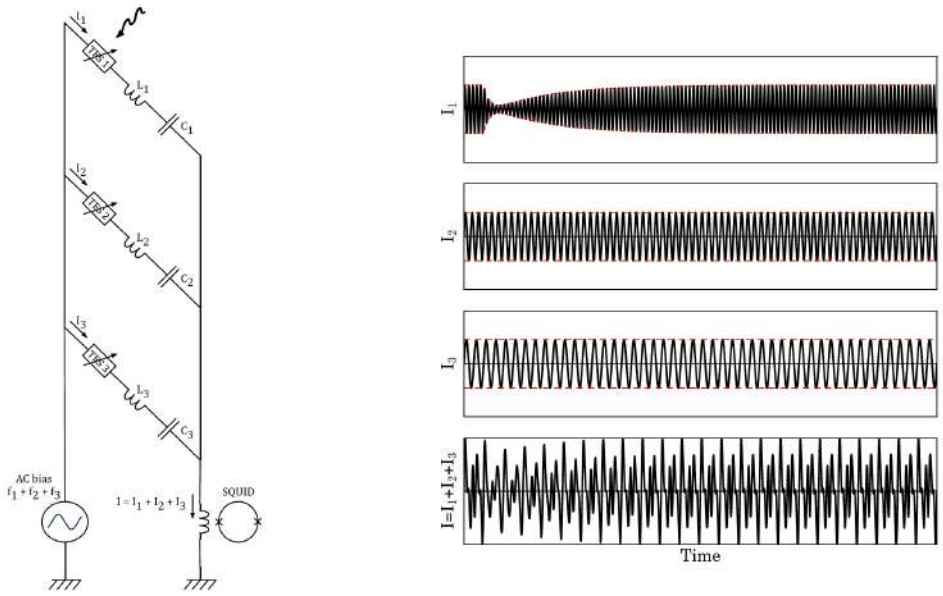

Figure 2.7: Reproduced from (Ravera et al., 2014a), Figure 4. FDM readout principle of a single channel with 3 TES detectors. Each detector is biased with a given carrier of frequency f_i. Here, a photon is visible on the amplitude modulation of the first pixels. The signals are then summed and sent to the SQUIDs for amplification.

- 96 identical readout channels of $N_{\mathrm{MUX}} = 34$ pixels (33 TESs + 1 resistive pixel).
- A reduced number of channels (e.g. 80), with a higher multiplexing factor (e.g. $N_{\mathrm{MUX}} = 48$, i.e. 40 TESs + 1 resistive pixel).

Currently, the first solution is retained as baseline, as it presents stronger engineering margins and provides a lower energy resolution degradation per pixel. An additional resistive pixel per channel is foreseen to monitor readout chain drifts. By demultiplexing the signal from each channel at warmer stages, individual pixel currents can be recovered.

Readout chain

Since signal currents are of the order of a few µA, the output measurement of the readout chain at warm temperature would be completely dominated by the thermal Johnson noise of the circuit. Multiple amplification stages are therefore required in the readout.

Front-end SQUID and amplifier SQUID – To increase S/N ratio, an amplification of the signal is planned at the focal plane level (i.e. where temperatures and noises are lowest). This amplification relies on superconducting quantum interference devices (SQUIDs, Jaklevic et al. 1964), which are very sensitive magnetometers based on a superconducting loop containing two Josephson junctions (Figure 2.8 – *Top left*). When the junctions are submitted to a magnetic field (e.g. near an inductance with the current from a channel), it will generate a current to compensate the magnetic field, as per Lenz's law. Since these devices work at superconducting temperatures, the corresponding magnetic flux enclosed

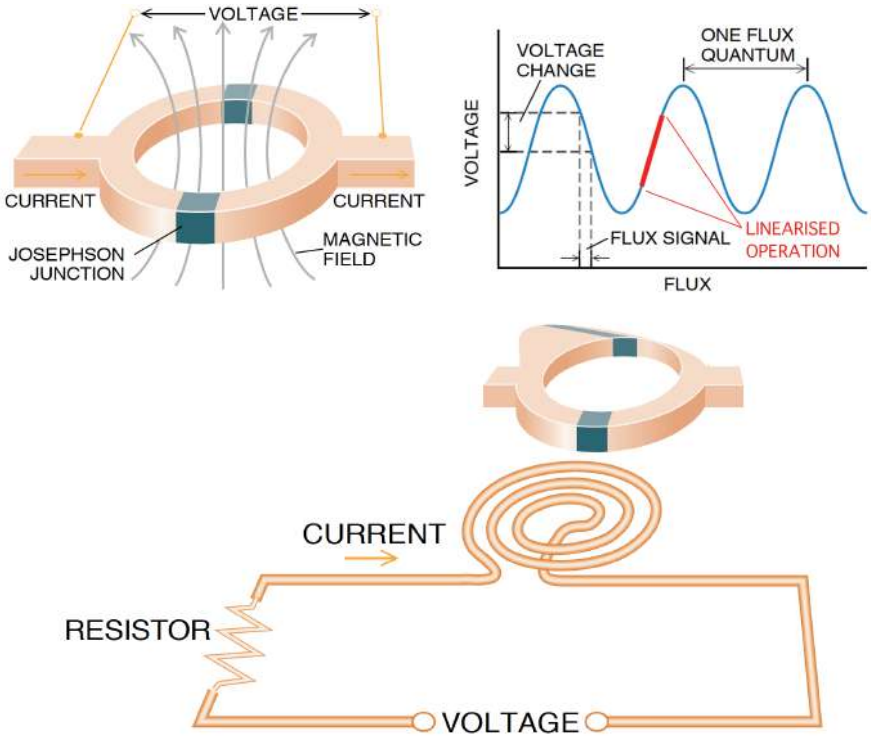

Figure 2.8: Adapted from Clarke (1994), Figures 4a, 4b, 6. (*Top left*) Schematic view of a SQUID. (*Top right*) Typical V/Φ diagram of the SQUID, the linearised operation of a given TES around the bias point is shown in red. (*Bottom*) Generic application of the SQUID in a resistive circuit (the X-IFU readout chain) to measure the TES current.

by the loop must be an integer multiple of $\Phi_0 = h/2e$ (Deaver & Fairbank, 1961). Whenever the applied flux is above $0.5\,\Phi_0$, the SQUID will compensate by generating additional current. This makes these devices highly non-linear, with sinusoidal-like V/Φ responses (Figure 2.8 – *Top right*), whose shape may be distorted by thermal noise (Enpuku effect, Enpuku et al. 1993). By biasing the SQUID in one of its sinusoidal transitions, the signal can be amplified with very low noise levels (Figure 2.8 – *Bottom*).

The cold amplification of the signal occurs in two stages. First, a front-end (FE) amplifier SQUID placed near the detectors at the 55 mK stage will amplify the signal and provide the summing of all the currents in a readout channel. A second stage of SQUIDs (amplifier SQUIDs) is placed at slightly higher temperature (2 K), where more power can be dissipated, allowing a higher amplification gain of the signal. The overall operation of the SQUIDs is controlled using the warm front-end electronic cards (WFEE).

Low noise amplifier and warm front-end electronics – Once the signal has been amplified at cold stages, a subsequent amplification occurs at warm temperature (~ 300 K) through a low noise amplifier (LNA), which boosts the signal to current values which can be read by the demultiplexer (Prêle et al., 2016). The amplification, as well as the SQUID biasing in their transition and the use of corresponding electronic buffers are part of the

WFEE cards (Chen et al., 2018).

Baseband feedback: linearising the SQUID response – The cold stage amplification relies on the SQUID V/Φ transition. As long as the excursion around the operating point is small, operations are close to linear. However, as the FE SQUID carries the sum of the signals in a channel, a significant part of its dynamic range is needed, causing non-linearities when the measured flux is above $\sim 0.12\,\Phi_0$. Hence, the system needs to be actively linearised to avoid degradations in the signal (notably in energy resolution).

This operation is done using a baseband feedback technique (BBFB, den Hartog et al., 2009, 2012), shown in Figure 2.9. BBFB compensates the measured flux of the FE SQUID, Φ_{FE}, by subtracting a nearly-equal baseline feedback flux, Φ_{FB}. This forces the SQUID, and consequently the full readout chain, into a small signal regime in which the response is linear (Figure 2.8 – *Top right*). The feedback signal for each channel is computed from the measured TES signal at time t. After demodulation, the signal is remodulated accounting for a phase-shift by a time τ (to account for the readout time delay between the direct line and the feedback line, and demultiplexing/multiplexing operations), converted into a flux, and finally subtracted from Φ_{FE} using an additional feedback coil on the FE SQUID. This technique remains stable as long as the gain-bandwidth product is sufficient, even for long line propagation delays ($\sim$ µs) or high operating frequencies (up to 5 MHz).

BBFB is a digital operation, controlled by the digital readout electronics (DRE – Figure 2.10). The process is integrated in the firmware and applied simultaneously to each pixel. The BBFB is designed to linearise SQUIDs up to a total instantaneous flux equivalent to an energy of 24 keV per channel (Peille et al., 2019). Higher fluxes lead to an 'unlock' (switching to another part of the V/Φ response) which can only be recovered after a time $t_{\rm lock}$ (10 ms is the current worst-case estimate), causing dead time in the observation.

Demodulation of the signal – Once the signal is amplified, it is demodulated to return the signal of individual pixels. This operation is also performed by the DRE, through its DEMUX card, which relies on field-programmable gate arrays (FPGAs). The data

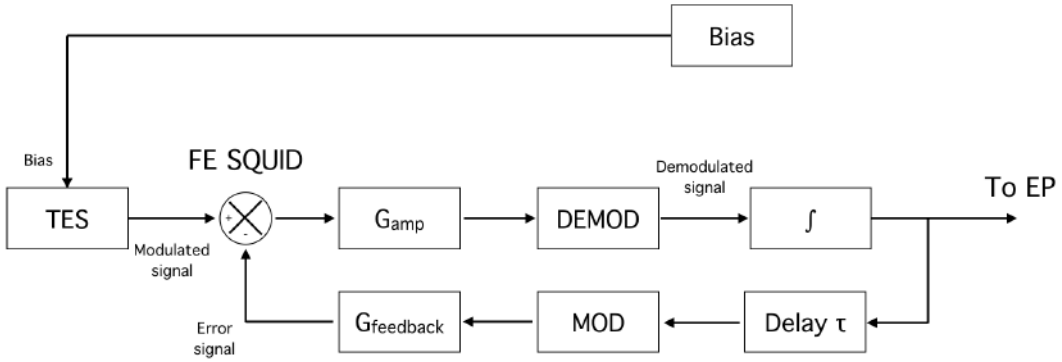

Figure 2.9: Block scheme of the BBFB operation. The subtraction of the feedback signal occurs at the FE SQUID level, through an additional feedback coil.

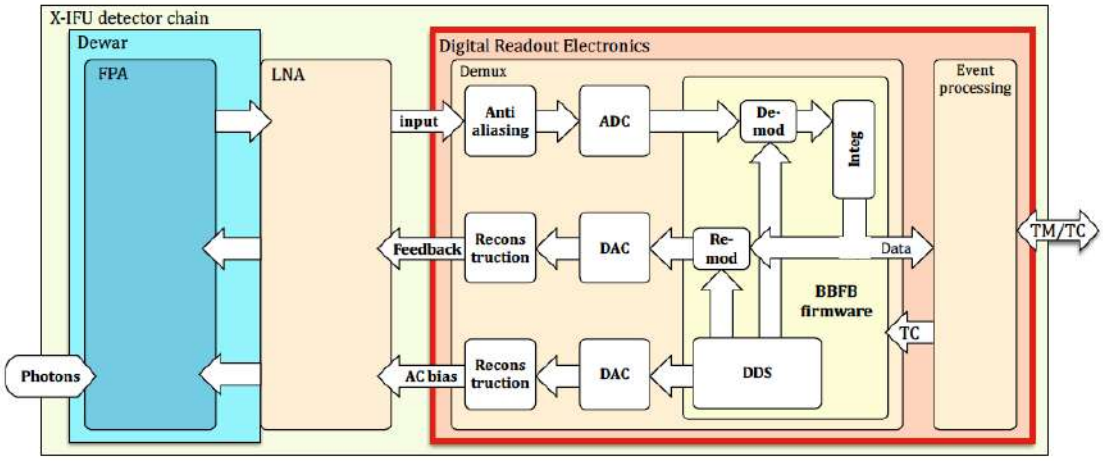

Figure 2.10: Block diagram of the DRE electronic boards. Each of the DRE tasks (bias, BBFB, demodulation and event processing) is identified (courtesy L. Ravera).

is first converted into digital units by an analogue-to-digital converter (ADC). Then, the firmware uses the same DDS technique used for AC-biasing to I/Q demodulate the input data and remove the signal from neighbouring pixels. The output provides the amplitude modulation of each carrier (i.e. the scientific signal of each pixel), which is sent to the event processor (EP). A copy of this digital output is remodulated accounting for a time-shift due to the various DRE operations to create the feedback signal (see above).

Although the largest part of the DEMUX is digital, it is the analogue part which is most critical, notably on the return line for the BBFB. To ensure a rapid and accurate response of the system, two high-quality DACs are needed to follow the pixel dynamic range in the return line and ensure a 2.5 eV energy resolution. Currently, no space-proven DAC offers the required levels of performance, setting a stringent challenge over the entire readout chain development (Ravera et al., 2018).

Event processor and pulse processing

Once the individual pixel signal has been recovered, it is processed by the DRE EP. Given the sampling frequency of the pixel (156.250 kHz) and the number of pixels, a single second would generate ~ 1 Gb of raw data. For the long observation times planned for the X-IFU ($\geq$ 50 ks), the amount of raw data to downlink would be astronomical. Since the core of the information is the time and energy of the events, and the equilibrium current of the pixel at that moment (i.e. the baseline, or Ba), the EP processes the data streams to extract these quantities only, thus substantially reducing the memory pressure on the satellite internal storage and on telemetry (TM). A possibility to retain the entire pulse streams is also investigated (for calibration purposes) in a dedicated EP mode.

The first stage of the data processing is the triggering. The data streams are convolved with a high-derivative kernel function to enhance any shape contrast (rise fronts of the pulses, Cobo et al. 2018). If a detection occurs, the pulse processing starts. This step aims

to provide a time and an energy for each incident event.

Timing – The time stamp of a photon is determined by the rise of the pulse. Through triggering, the first samples in which the signal derivative is positive (compatibly with a pulse) provide an estimate of the time with an uncertainty of one or two samples, where $t_{\mathrm{sample}} = 6.4\,\mu\mathrm{s}$. However, uncertainties in the time stamp can cause degradations of the energy resolution (Cobo et al., 2018). Mitigations are therefore required to determine with accuracy best estimate of the pulse rise within a sample itself.

Pulse processing – The amplitude of a pulse, called the pulse height (or PHA), is used as a proxy for its energy. In many TES applications, the energy of the pulse is derived through optimal filtering (Szymkowiak et al., 1993). This technique was introduced by Moseley et al. (1988) as a particular case of the Wiener filter, and approximates the pulse shape $d(t)$ by a constant multiplication of a universal pulse shape $s(t)$, such that $d(t) = \mathrm{PHA} \times s(t) + \mathrm{Ba}$. The PHA for a given pulse is then obtained by solving the following minimisation problem (in Fourier space) after baseline subtraction:

$$\mathrm{min}_{\mathrm{PHA}} \sum_{f=0}^{\infty} \frac{(\hat{d}(f) - \mathrm{PHA} \times \hat{s}(f))^2}{\hat{n}(f)^2} \tag{2.1}$$

where $\hat{n}$ is the noise spectrum of the pixel. The minimisation yields as analytical solution

$$\mathrm{PHA} = \sum_{f=0}^{\infty} \frac{\hat{d}(f)\hat{s}^*(f)}{\hat{n}(f)^2} \times \left(\sum_{f=0}^{\infty} \frac{|\hat{s}(f)|^2}{\hat{n}(f)^2} \right)^{-1} \tag{2.2}$$

with $\hat{s}^*$ the Hermitian of $\hat{s}$, which can be transposed in time space by

$$\mathrm{PHA} = \frac{1}{K} \sum_{t} d(t)h(t) \tag{2.3}$$

By definition, $h(t)$ is the inverse Fourier transform of $\frac{\hat{s}^*(f)}{\hat{n}(f)^2}$ and $K = \sum_{f=0}^{\infty} \frac{|\hat{s}(f)|^2}{\hat{n}(f)^2}$. The pulse template $s(t)$ and its noise are generally measured on the ground, during dedicated exposures at a given energy (typically 6 keV) then used for all other energies. Once the PHA is computed (in detector units), it can be transformed into the real photon energy by using the so-called energy scale function, which is calibrated on the ground using fiducial lines, and constantly monitored in flight (see Chapter 5). For each pulses, only the value of the PHA is downlinked, reducing the memory usage on board. This technique is currently planned for the X-IFU, although other more complex methods are under consideration (Bandler et al., 2006; de Vries et al., 2016; Peille et al., 2016).

Energy resolution degradation – For the optimal filtering technique, the full amplitude of the Fourier spectrum or a long time period should be used in the minimisation problem. However, TESs are often subject to strong pink noise ($1/f$). To avoid significant degradations, the first frequency bin is thus discarded in the optimal filtering computation. This

corresponds to using a finite record length of the pulse, $t_{\rm rec}$, which causes the following degradation in the overall energy resolution (Doriese et al., 2009):

$$\Delta E(t_{\rm rec}) = \frac{\lim_{t_{\rm rec}\to\infty}(\Delta E)}{\sqrt{1-\frac{1}{2t_{\rm rec}f_{\rm eff}}}} \tag{2.4}$$

where $f_{\rm eff}$ is the pixel effective roll-off frequency defined as

$$f_{\rm eff} = \frac{\int_{f=0}^{\infty}{\rm SNRD}(f)^2 df}{\lim_{f\to 0}({\rm SNRD}(f))} \tag{2.5}$$

where SNRD is the signal-to-noise ratio density in the Fourier space. Currently a record-length of 8192 processor samples (~ 52.4 ms) is considered for high-resolution events, which provides a resolution degradation below 1% for the considered TESs.

Pile-up, secondary pulses and grading – Each pulse indicates one photon, thus providing both spectral and spatial information on the source. However, this capability comes at a price when high count rate sources are observed. If photons are detected during a time interval lower than the typical record-length of a pulse, superposition occurs. If this superposition occurs in an adjacent time sample (i.e. almost simultaneous detection of two photons), we talk of 'pile-up' effect, whereas if the time interval is larger (i.e. after tens or hundreds of time samples), the new impact will be called a 'secondary'.

Pile-up will influence the energy measurements, and may provide very different values through optimal filtering. Likewise, the presence of a secondary will not allow the pulse processing to explore the full duration $t_{\rm rec}$ planned for the pulse. Intrinsically, this will cause energy resolution degradations both for the preceding and the secondary pulse. To account for such features, pulses will be graded using the EP depending on the time separation between two rise fronts of the pulses (Peille et al., 2018a), similarly to the strategy implemented on SXS (Seta et al., 2012). The corresponding grade of the event (among a finite number of grades) will be post-processed using a dedicated optimal filtering template and associated with an estimated spectral resolution (see also Chapter 3).

2.3.4 Cryogenic anti-coincidence detector

TESs detectors are based on calorimetric detection. This means that any deposition of energy, even unrelated to the photons from the observed source (e.g. cosmic rays, infra-red radiation), once converted into heat may cause pulses and noise. These events with no link with the source under study are defined as the background.

In the case of the L2 orbit planned for *Athena*, the electromagnetic environment is populated by high-energy particles coming from the solar plasma, and by galactic cosmic rays (GCRs, typically high-energy protons), created in energetic astrophysical phenomena (Lotti et al., 2017). L2 orbits offer a high thermal and particle stability, but does not offer the same protection against cosmic rays as a low Earth orbit (LEO), due to the absence of Earth's magnetic field (L2 is in the wake of the magneto-tail, in the magneto-sheath). Despite the presence of the magnetic diverter on the telescope, which deflects most of the focused charged particles away from the focal plane, isotropically-distributed high-energy

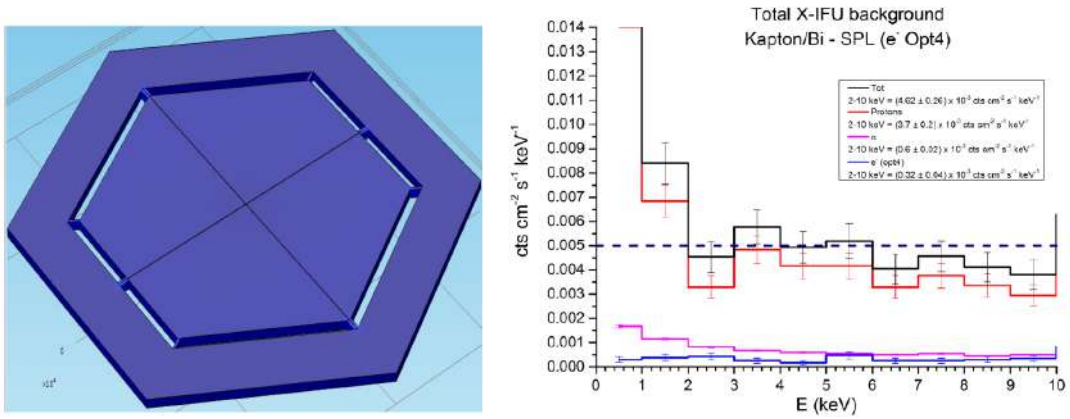

Figure 2.11: (*Left*) CAD design of the CryoAC detector. (*Right*) Reproduced from (Lotti et al., 2018a), Figure 3. Simulated residual NXB over the energy band for the different particle types (protons, α particles and electrons) after CryoAC exclusion, assuming a Bi-Kapton shield layer.

GCRs cross the spacecraft and reach the instrument. These GCRs then interact with the instrument by direct deposition of heat on the absorbers, or by generating showers of secondary particles, which can deposit energies equivalent to X-ray photons in the absorbers and thus be detected by the TESs. This background contribution is the unfocussed instrumental background, or non-X-ray background (NXB). Without correction, these particles would degrade the science information, especially for faint sources in a high-energy bandpass. To reach the requirement of 5×10^{-3} cts/s/keV/cm^2 (80% of the observing time, over 2 – 10 keV), a cryogenic anti-coincidence (CryoAC) detector (Figure 2.11) will be placed ≤ 1 mm below the instrument focal plane (Macculi et al., 2016; D'Andrea et al., 2018).

The CryoAC will be composed of a large (4.6 cm^2) 500 µm-thick four-quadrant silicon absorber deposited above ≥ 1000 iridium/gold TESs. It is designed to detect particles with energies from 20 keV up to ~ 800 keV, without saturation. These TESs are designed to have sharp athermal pulses, to improve the timing accuracy of the detection (expected ≤ 10 µs). By comparing simultaneous counts on the TES and CryoAC detector, or patterns on the detector (related to secondary showers), the level of background can be actively reduced (at the price of dead time). Coupled with a passive shielding reduction using high-Z material (Bi-Kapton shield), current simulations with the baseline design foresee a level of NXB below $\sim 4.6 \times 10^{-3}$ cts/s/keV/cm^2 throughout the mission (Lotti et al., 2018a). Much like the main array, the CryoAC will be piloted by dedicated electronic boxes.

2.3.5 Cryogenic chain and dewar structure

The cryogenic chain of the X-IFU

The X-IFU detectors need to be operated in their superconducting transition (~ 90 mK), with a stable 55 mK thermal bath with sufficient cooling power to dissipate the heat created by the incoming photons and by the entire cold front-end electronics (CFEE, Charles et al.,

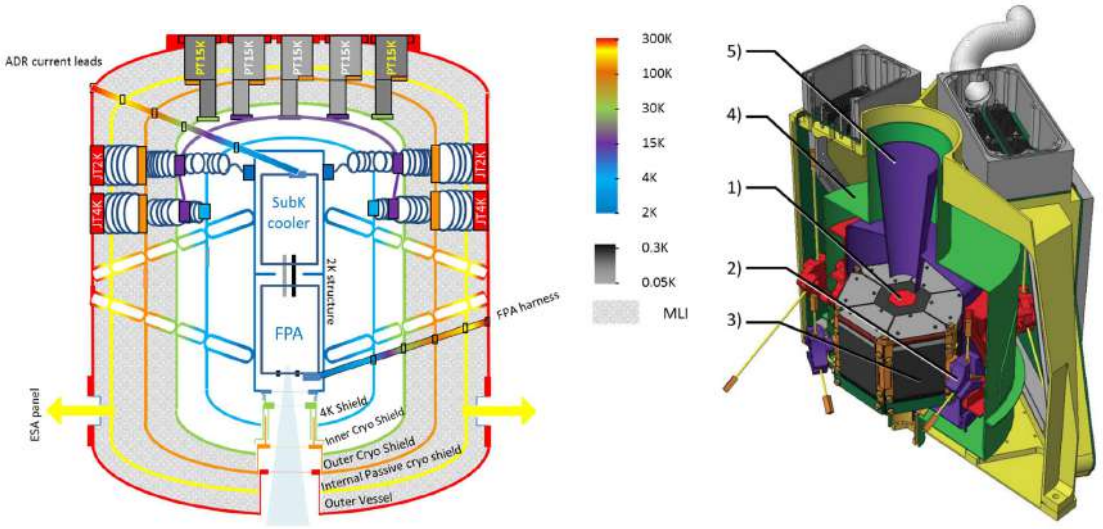

Figure 2.12: (*Left*) Schematics of the X-IFU cryogenic chain. (Credits: J. André, A. Pradines, CNES). (*Right*) CAD of the FPA. The numbers indicate respectively 1) the TES array 2) one of the six kevlar suspensions 3) the readout assembly with the LC filters and FE SQUID chip 4) the µ-metal shield and 5) the Nb shield (courtesy: SRON).

2016). Such low temperatures will be achieved using a complex cryogenic system, (Barret et al., 2018b; Pajot et al., 2018) shown in Figure 2.12 (*Left*).

Starting from the operating temperature of the outer vessel (OV) around $\sim 300\,\mathrm{K}$, the X-IFU detectors will be surrounded by a closed cryostat made of six different temperature shields. The first layer of thermalisation is obtained by an inner passive cryogenic shield (IPCS) at 200 K, which will be passively cooled through radiators placed on the SIM. This stage will reduce the heat load on the inner layers. Beyond the IPCS, a first active cooling stage composed of three pulse tube (PT) coolers will achieve a temperature of $\sim 100\,\mathrm{K}$ on the outer cryogenic shield (OCS), which acts as pre-cooling stage for the Joule-Thomson (JT) coolers. The second head of the PT coolers will be used to lower the temperature down to 15 K on the inner cryogenic shield (ICS) to create a hot interface for both the 4 K and 2 K JT coolers. The latter will be used to provide enough cooling power to reduce thermal noise on the CFEE stages and allow the final cool-down. The sub-Kelvin cooling is ensured by a hybrid adiabatic demagnetisation refrigerator (ADR), which will lower the temperature down to 55 mK onto the detectors. To increase the lifetime and the reliability of the instrument, the entire design of the cryogenic chain is based on dry coolers. All of them are fully redundant (5 PT15K, 2 JT4K and 2 JT2K) except for the last stage sub-Kelvin cooler, which is not composed of any movable part.

The hybrid sub-Kelvin cooler will be composed a ^{3}He sorption cooler coupled to an ADR salt pill to create two cold interfaces at 300 mK and 55 mK, with a cooling power of 11.3 mW and 832 nW respectively. Once the ADR salt pill is in thermal equilibrium with the 300 mK stage, a strong magnetic field ($\sim 6\,\mathrm{T}$), produced by a superconducting coil is applied to the paramagnetic salt to align its dipoles. This operation is called the recharge

(or recycling) of the salt pill and reduces the overall entropy of the salt pill system, which remains at 300 mK but whose order is increased microscopically. After recycling, the salt pill is isolated from the higher-temperature stage (e.g. by opening a heat switch) and the magnetic field is slowly reduced. To maintain the constant low entropy level, heat is absorbed by the salt pills thus creating cooling power. This process can be maintained until the magnetic field reaches 0 T, and can be repeated after a recycling phase of both the sorption cooler and the ADR. Currently, the X-IFU is planned to have 32 hours of available cooling power at 55 mK, for a recycle time of ~ 8 hours (duty cycle of 80%). The cryogenic chain of the X-IFU is a critical part of its design. It is still undergoing further optimisations to reduce its mass and power consumption, and to increase its reliability.

The focal plane array

Since TESs are extremely sensitive to their environment, a special confinement unit, the focal plane assembly (FPA, Jackson et al. 2018), will be used to shield the detectors in the cold stages (2K and below). The role of the FPA is threefold:

- Ensure the thermal stability required for the operation of the TES and CryoAC array.
- Isolation from micro-vibration of the higher-temperature coolers.
- Insulation from the magnetic field.

To do so, the FPA will encapsulate the detector assembly, providing it with the proper thermal connection to the ADR and feedthroughs from the cold electronics. Mechanical isolation is ensured by six kevlar suspensions to the 2K stage, while the magnetic insulation will be performed in two steps (Figure 2.12 – *Right*): the external and ADR magnetic fields are rejected by a *Cryoperm* shield stage (magnetic rejection coefficient ~ 100), the remaining field is rejected by a superconducting Nb shield through Meissner effect (magnetic rejection coefficient ≥ 5000).

The aperture cylinder and the optical blocking filters

To enable the observation of photons through the dewar, each cryogenic shield has an interface with the outer parts of the instrument through the aperture cylinder (Barret et al., 2016, 2018b). This conic-shaped interface closes the thermal shields and carries five optical blocking filters composed of 2×15 nm of aluminium, covering 45 nm of polyimide (Barbera et al., 2018a). Each of these filters shields the detectors against outside infra-red thermal radiation and near UV/visible photons from astrophysical sources, which could cause photon shot noise and thermal fluctuations. They also provide an isolation of the dewar from the radio frequencies of the telemetry antennæ.

To protect these structures, the dewar will be under vacuum on the ground and at launch. To withstand the vibration levels imposed by the vacuum enclosure at launch, the first four filters are deposited onto a 130 µm thick silver- (300K) or gold-plated (100K, 30K, 2K) stainless steel solid honeycomb mesh (Barbera et al., 2018b). The last thermal filter (55 mK stage) is deposited onto a 60 µm thick niobium mesh. Finally, to avoid contamination due to out-gassing both on the ground and in-flight, a dedicated heating system will ensure that the filters will be systematically at higher temperatures than their surrounding dewar shield, thus avoiding molecular condensation (Barbera et al., 2018a).

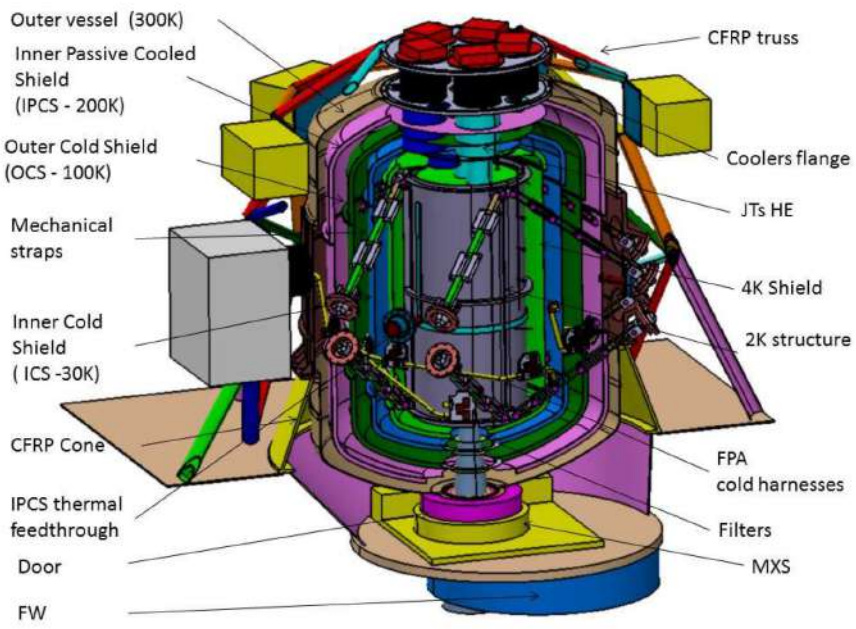

Figure 2.13: The X-IFU instrument design mounted on the SIM (courtesy: I. Maussang, A. Pradines, CNES).

Door, filter wheel and calibration sources

Door – The vacuum-tight interface generated on the ground for launch will be guaranteed by a dewar door. This door is planned to open at the end of the commissioning phase in orbit, but shall remained closed on the ground for contamination reasons. To enable photon detection while closed, the door will possess multiple Be windows. For ground calibration, a specific vacuum-tight feedthrough is planned to shine the detector array with calibration sources. This interface will however be permanently sealed before launch.

Filter wheel – A filter wheel (FW) will also be included in the instrument, between the incoming photon beam and the dewar door (see Bozzo et al., 2016, for an early design). The current design of the FW plans 6 different positions, each corresponding to a specific observation mode. One of the positions corresponds, e.g. to a thick Be filter, useful to attenuate low-energy photons in the observations of bright-point like sources. Similarly, another position will place radioactive calibration source (e.g. ^{55}Fe) above the detector for energy scale or energy resolution monitoring.

Calibration sources – To ensure a continuous high-accuracy monitoring of the energy scale, four modulated X-ray sources (MXSs) will be mounted within the conic interface. These sources will emit powerful photon flashes at fiducial X-ray energies (see Chapter 5), and will be similar to the ones flown on the *Hitomi* SXS (de Vries et al., 2010; Tsujimoto et al., 2018). Two types of sources are planned, either emitting high-energy K_α lines (e.g. Cr, Cu) or low-energy K_α lines (e.g. Al, Mg, Si).

Instrument control

The X-IFU will be driven by an instrument control unit (ICU), which will be the interface between the instrument and the spacecraft. On the one hand, the ICU will send the commands received from the ground through the satellite to the various subsystems in each operation phase (e.g. observation, recycling). On the other hand, it will transmit the telemetry packets built with the subsystems data to the ground through the satellite. The power supply needed for the instrument will be delivered by the *Athena* satellite to a power distribution unit (PDU). In turn, the PDU will dispatch the current to the various subsystems, which will be controlled by remote terminal units (RTUs).

Phase A design

Accounting for the previous considerations the overall design of the instrument at the end of phase A is given in Figure 2.13. The dewar will be mounted on the SIM through a dedicated carbon-fibre reinforced polymer (CFRP) conic interface, which will surround the lower parts of the structure (door, sources, FW). To avoid large thermal and mechanical constraints on the OV, the electronic boxes are mounted onto a truss structure. Thermal conductive links between the dewar and radiators on the *Athena* satellite (on the SIM) will allow the passive cooling of the IPCS, while mechanical straps will provide micro-vibration isolation of the different cold stages.

CHAPTER 3

Performance and sensitivity studies of the X-IFU

The challenging science objectives of the X-IFU require that the level of performances reminded in Table 2.1 are met in flight. Careful analysis is therefore required to derive, from the scientific need(s), the corresponding performance requirements on the subsystems and verify their coherence. A way to do so is to perform hands-on measurements on prototypes or models. For instruments such as the X-IFU, the operational complexity and the cost to implement such prototypes impedes a formal experimental test of all the performances (see Chapter 6). Detailed numerical simulations of the instrumental behaviour can be performed instead at this stage of the project. The X-IFU end-to-end (E2E) simulator `xifupipeline` and the X-IFU detection chain simulator `XIFUSIM` were developed for this purpose by the Erlangen Centre for Astroparticle Physics (ECAP), CNES, the Istituto de Fisica de Cantabria (IFCA) and IRAP. In this chapter, I start by introducing these tools and remind the major improvements included during my thesis. I then present several core performance and sensitivity studies performed through numerical simulations. Aside from the X-IFU specific tools, the generic X-ray spectral fitting package (XSPEC, Arnaud 1996), available through the NASA HEASARC platform,[7] was also used. This chapter recalls some of the results presented in Cucchetti et al. (2018d); Peille et al. (2018b, 2019).

3.1 End-to-end simulations using SIXTE

The E2E simulator SIXTE[8] (Wilms et al., 2014, Dauser et al., 2019, sub.) is the official simulation tool chosen for the *Athena* mission (both for the WFI and the X-IFU) to perform synthetic X-ray observations. It relies on a long experience in E2E simulations, started on the previous generation of X-ray observatories (e.g. *XMM-Newton*) to understand some of the fine physical effects observed in-flight, and pursued for future missions such as *SRG*/eRosita or *Athena* (Schmid, 2012). SIXTE is based on a Monte Carlo simulation approach. It is designed to randomly sample photons emitted from a simulated astrophysical source and follow them towards their final detection in the instrument, while including multiple geometrical and/or instrumental effects. The typical architecture of

[7] https://heasarc.gsfc.nasa.gov/xanadu/xspec/

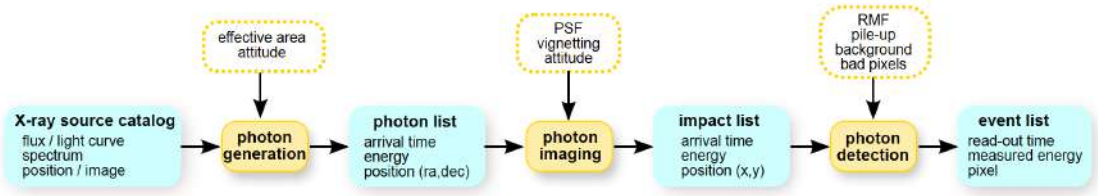

Figure 3.1: Reproduced from Wilms et al. (2014), Figure 1. Steps of a SIXTE E2E simulation. Starting from an input astrophysical source, the simulator generates a photon list, which is imaged accounting for the telescope geometry to create an impact list. Finally, the impact list is post-processed depending on the instrument to obtain an event list.

an E2E simulation of an X-ray observation can be decomposed in three main steps, each taking an input file and returning a specific output (Figure 3.1) :

- The generation of X-ray photons from a source file to create a photon list.
- The imaging of these photons through the optics to create an impact list.
- The processing of the impacts by the detectors to create an event list.

The first two phases of the simulation are similar, regardless of the considered instrument. Equivalent routines can thus be used, increasing the modularity of the code. The final processing step is however instrument-dependent, and can vary depending on the complexity of the considered readout scheme.

3.1.1 Photon generation using SIMPUT files

The first step of an E2E simulation is to recreate realistic emission spectra and images of astrophysical sources. For SIXTE, simulation input (SIMPUT) files (Schmid et al., 2013) are used as a starting point of the photon generation. These files are instrument-independent and have a very modular structure (Figure 3.2), which makes them used in other X-ray astronomy simulators beside SIXTE (e.g. SIMX, Smith 2013).

SIMPUT files are based on a `FITS` format (Wells et al., 1981). These files can be seen as catalogues of individual sources of the sky. Both extended or point-like sources can be included in a single SIMPUT. Each of the sources (a row in the file) is given an identification (`SRC_ID`, `SRC_NAME`) and is characterised by its core parameters: its position on the sky (right ascension and declination), its flux over a given energy band and its spectrum. The latter can either be included directly in the SIMPUT, or point to a separate `FITS` file if the same spectrum is used by multiple sources. Interestingly, SIMPUT files can also include real X-ray images as inputs to scale the fluxes of the sources over the field-of-view. Likewise, light curves or power spectrum dependencies can be used for timing studies of variable objects. This architecture improves the flexibility of the code, and ensures that the minimal quantity of data is saved into the files. Finally, SIMPUT files also guarantee a simple interface with common spectral codes such as XSPEC (Arnaud, 1996), the interactive spectral interpretation system (ISIS, Houck & Denicola 2000) or SPEX (Kaastra et al., 1996), as they can be created starting from the basic `.xcm` text files of the models. More information is available in the SIMPUT manual.[9]

[8] https://www.sternwarte.uni-erlangen.de/research/sixte/

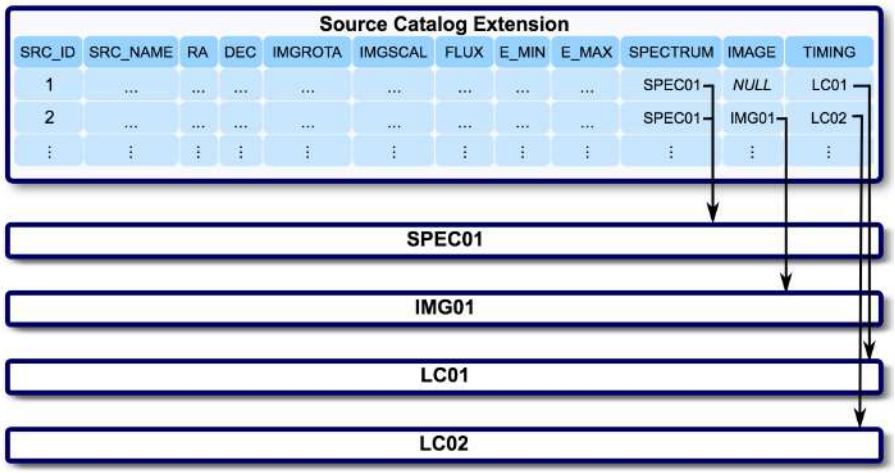

Figure 3.2: Schematic overview of a SIMPUT file. The file is organised as a catalogue of sources, each containing spatial, spectral and timing information (from SIXTE manual).

For each row of the SIMPUT file, the software performs a first verification to determine whether the source is within the simulated FoV. This criterion is satisfied if its angular separation with respect to the line-of-sight is within 1.5 times the equivalent angular radius of the detector. By default, the line-of-sight is fixed, though additional movements of the satellite (e.g. slewing or dithering) can be included using an attitude file (`FITS` file). For each visible source, the number of photons during the observation and their arrival time are computed assuming a Poisson distribution, with a λ-parameter depending on the flux of the source. In turn, the energy of the photons is determined using the spectrum of the source as a probability distribution function. To avoid generating unnecessary photons, the spectrum is convolved beforehand with the ancillary response file (ARF) of the instrument, which contains an energy-discretised approximation of the total effective area, i.e. the mirror effective area and instrumental quantum efficiency (QE). The full photon list is generated by concatenating, in chronological order, the photons from each source.

This first step can be skipped by providing a photon list generated using other programs. In this case, the photon list provided as input is sampled randomly using the overall flux value. To ensure a proper sampling of the input spectrum (i.e. to avoid selection effects), the photon list should contain at least an order of magnitude more photons than required. This can be interesting, for instance, when large-scale hydrodynamical simulations are used as inputs (see also Chapter 4), as such lists are much easier to produce in a parallelised way, especially for 3D simulation grids.

3.1.2 Imaging photons

Imaging is also shared between instrumental configurations, and simulates realistic geometrical effects of the telescope on the incoming photons. To maintain the modularity of the code, the instruments and the telescope are described using a `.xml` file (see Appendix C) which provides the spectrum of the instrumental background, a description of telescope effects (effective area, PSF, vignetting), and the detector spectral response, modelled using

[9] http://hea-www.harvard.edu/heasarc/formats/simput-1.1.0.pdf

a redistribution matrix file (RMF). Imaging uses the same template .xml files as inputs for multiple missions. For CCD/DEPFET applications, these files also specify the type of readout for each row, charge cloud mechanisms and background effects (Dauser et al., in prep.). For complex instruments, such as the X-IFU, a secondary .xml file is added to describe the detector array geometry (e.g. hexagonal) and its detection properties (e.g. pixel type, pixel pitch, grade-dependent RMFs). An ampler description of this modular approach can be found in the SIXTE simulator manual.[10]

For each incoming photon, vignetting and PSF effects are included through dedicated FITS files. Each contains the corresponding 2D probability distribution function, which are both functions of the energy and the angular position of the impact. Depending on the result from the vignetting randomisation, the photon is either transmitted or lost. If the photon is observed, its final spatial position on the focal plane is derived accordingly by randomly sampling the PSF distribution. Once all the geometric effects are taken into account, the photon list is reduced to an impact list, containing the position, the time stamp and the 'true' energy of the photons.

3.1.3 Processing the impact list

The final step of the simulations includes the spectral response of the instrument to obtain the detected energy of each event. For the X-IFU, this can be done in two ways,

- either by simulating the detection using a set of RMFs and interpolation tables to describe instrumental mechanisms (xifupipeline routine, see Section 3.2),
- or by simulating the TES pixel behaviour over time following a photon absorption (tessim/XIFUSIM routines, see Section 3.3).

3.2 xifupipeline as a performance simulator

The E2E simulator xifupipeline, within SIXTE, is designed to provide a full detector-scale analysis tool of the X-IFU starting from a given SIMPUT file. It includes the two previous simulation steps leading to an impact file. For each impact, the simulator assigns a grade depending on the time difference between the preceding and following pulse in the pixel. As shown in Chapter 2, the grade is related to the predicted spectral resolution of the event. The grading values considered in xifupipeline are reminded in Table 3.1; each is associated to a specific RMF in the secondary .xml file and corresponds to a specific energy resolution degradation due to finite record length (see Equation 2.4). After grading, the output energy of the photon is randomly sampled using the corresponding RMF, and saved in the event file. Events separated by less than a time sample are considered as pile-up and provided a grade of -2. Their energy is derived from the RMF using a sum of the energies of the simultaneous photons. Events which are neither limited-resolution nor pile-up are given a -1 grading ('invalid' events). This grading approach is a flexible way to flag events depending on their quality, and to mimic optimal filtering results. The final output is an event file (FITS file), which can then be post-processed using typical X-ray data analysis pipelines and spectral analysis tools (e.g. XSPEC, ISIS, SPEX).

An interesting feature of xifupipeline is the simplicity to simulate interactions between pixels. Using specific look-up tables (LUTs) or external files, the energy of an event

[10] https://www.sternwarte.uni-erlangen.de/research/sixte/data/simulator_manual_v1.3.8.pdf

Grade	Before the event ($t_{\rm pre}$)	After the event ($t_{\rm rec}$)
1: High resolution (2.5 eV)	>3.2 ms (494 samples)	>52.4 ms (8192 samples)
2: Medium resolution (3 eV)	>3.2 ms (494 samples)	>3.3 ms (512 samples)
3: Low resolution (7 eV)	>3.2 ms (494 samples)	>1.6 ms (256 samples)
4: Limited resolution (30 eV)	>3.2 ms (494 samples)	>25.6 µs (4 samples)

Table 3.1: Grade definitions and corresponding spectral resolution within `xifupipeline` in terms of time/number of samples before after the pulse (Peille et al., 2019).

can be modified to account, for instance, for crosstalk between pixels or changes in the background level. Thanks to the modular structure of the code, the LUTs can be modified or updated without complexities. Finally, the computational time needed to generate a synthetic observation of typical extended sources observed over 100 ks with the X-IFU does not exceed a few hours on a standard computer, which makes it interesting for routine studies of the instrument. `xifupipeline` is therefore a representative option to simulate the overall performances of the X-IFU, notably to test the feasibility of specific science cases (see Chapter 4). I actively contributed to the development and coding of `xifupipeline`, which I extensively used in the course of my work.

3.3 Detection chain analysis through `tessim` and `XIFUSIM`

A general overview of the instrument is useful to provide performance results and conduct scientific simulations of observations, but is insufficient to describe fine detector effects, such as the impact of noise on the spectral resolution, or changes in the energy scale due to TES operating parameters. A separate processing option of the impact files, `tessim`, was developed (Wilms et al., 2016) to provide a more physical approach of the readout. The core of the algorithm was developed by S. Smith (GSFC) and J. Wilms (ECAP), but is now an effort of the X-IFU E2E simulation team. More recently, `tessim` was detached from the SIXTE-based environment and improved to create a simulator of the entire X-IFU detection chain, `XIFUSIM` (see Section 3.3.3) tailored for an X-IFU application. I provide here a short description of the physical models implemented in `tessim` and `XIFUSIM` (inspired by Irwin & Hilton 2005), along with several additions included during my thesis.

3.3.1 Detailed TES simulations

The detection chain simulators `XIFUSIM` and `tessim` try to replicate, using physical models of the detectors, the behaviour of micro-calorimeters hit by incident photons. Starting from a simulated impact list, the result is a data stream of the current in each pixel. Post-processing occurs using triggering and by applying optimal filtering templates to the detected pulses. The output file is similar to an unprocessed X-IFU data file, which needs to be corrected for instrumental effects and converted into an event file using a calibrated energy scale function (see Chapter 5). This approach provides a more accurate description of the readout, including the effects of crosstalk and pile-up. However, the computational cost is high, and currently not more than a few pixels can be simulated over long exposures ($\geq$ 1 ks) using a standard machine without becoming cumbersome computationally.

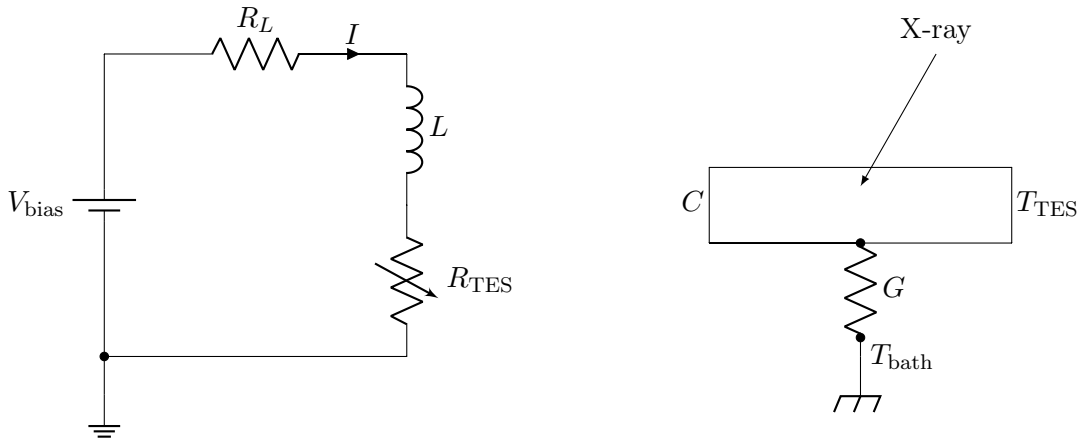

Figure 3.3: Electro-thermal model of the TES detector. (*Left*) Equivalent circuit of a voltage-biased TES. (*Right*) Equivalent thermal circuit of a TES micro-calorimeter.

Physical model

To model and understand TESs, Irwin & Hilton (2005) have formalised the detector behaviour. Electrically, a pixel readout is represented by a variable resistor $R_{\text{TES}}(T, I)$, which depends on the bias current running in the TES, I, and its temperature, T, placed in an inductive circuit of resistance R_L and inductance L, biased through a known voltage V_{bias} (Figure 3.3). Thermally, the detector (of heat capacity C) is connected to a stable thermal bath of temperature T_{bath} by a weak thermal link of thermal conductance G. Whenever an incident photon deposits heat on the absorber, the current and the temperature of the TES follow a coupled electro-thermal system of differential equations:

$$\begin{aligned} &\textit{(Thermal)} && C\frac{dT}{dt} = -P_{\text{bath}} + P_{\text{Joule}} + P_{\text{photon}} + P_{\text{noise}} + P_{\text{load}} \\ &\textit{(Electrical)} && L\frac{dI}{dt} = V_{\text{bias}} - R_L I - R_{\text{TES}}(T, I)I + V_{\text{noise}} \end{aligned} \tag{3.1}$$

The first term in the thermal equation represents the power flow from the pixel to the thermal bath. Using the notations in Irwin & Hilton (2005), $P_{\text{bath}} = K(T^n - T_{\text{bath}}^n)$, where n is the thermal conductance exponent (in general, $n \sim 3$) and $K = G/(nT^{n-1})$. The second term is $P_{\text{Joule}} = R_{\text{TES}}I^2$, the Joule power dissipated by the resistive part of the detector, and P_{photon} the instantaneous power deposited by a photon impact. An additional noise term, P_{noise}, can be added to the equation to account for phonon noise, as well as a constant excess load power P_{load} (see Chapter 5). Likewise, in the electrical equation V_{noise} is an additional electrical noise term (see below).

Small signal solution

Though Equation 3.1 cannot be solved analytically, it can be expanded using a small signal approach around the TES set point (T_0, I_0):

$$R_{\text{TES}} = R_0 + \frac{\partial R}{\partial T}\Big|_{I_0}\delta T + \frac{\partial R}{\partial I}\Big|_{T_0}\delta I \tag{3.2}$$

$$= R_0 + \alpha \frac{R_0}{T_0}\delta T + \beta \frac{R_0}{I_0}\delta I \tag{3.3}$$

where the logarithmic slopes α and β are defined as

$$\alpha = \frac{\partial \log(R)}{\partial \log(T)}\Big|_{I_0} = \frac{T_0}{R_0}\frac{\partial R}{\partial T}\Big|_{I_0} \qquad \beta = \frac{\partial \log(R)}{\partial \log(I)}\Big|_{T_0} = \frac{I_0}{R_0}\frac{\partial R}{\partial I}\Big|_{T_0} \tag{3.4}$$

By assuming a linear expansion of the other terms near the TES set point and by neglecting noise terms, the previous system (Equation 3.1) becomes

$$\frac{d}{dt}\begin{pmatrix}\delta T\\ \delta I\end{pmatrix} = -\begin{pmatrix}\frac{G(1-\mathcal{L}_I)}{C} & -\frac{R_0 I_0(2+\beta)}{C}\\ \frac{\mathcal{L}_I G}{L I_0} & \frac{R_L+R_0(1+\beta)}{L}\end{pmatrix}\begin{pmatrix}\delta T\\ \delta I\end{pmatrix} + \begin{pmatrix}\frac{P_{\text{photon}}}{C}\\ 0\end{pmatrix} \tag{3.5}$$

where $\tau_{\text{el}} = \frac{L}{R_L+R_0(1+\beta)}$ is the electrical time of the system, and $\mathcal{L}_I = \frac{R_0 I_0^2 \alpha}{G T_0}$ is the low-frequency loop gain under constant current. The homogeneous term of Equation 3.5 can be solved for a quasi-instantaneous deposition of energy onto the detector, i.e. $\delta T(t = 0) = E/C$, and $\delta I(t = 0) = 0$. The result can be expressed using the eigenvalues of the previous matrix (see Irwin & Hilton 2005 for the full development):

$$\frac{1}{\tau_\pm} = \frac{1}{2\tau_{\text{el}}} + \frac{G(1-\mathcal{L}_I)}{2C} \pm \frac{1}{2}\sqrt{\left(\frac{1}{\tau_{\text{el}}} - \frac{G(1-\mathcal{L}_I)}{C}\right)^2 - \frac{4R_0\mathcal{L}_I(2+\beta)G}{LC}} \tag{3.6}$$

such that the current pulse is given by $\delta I(t) \propto (e^{-t/\tau_+} - e^{-t/\tau_-})$. τ_+ and τ_- can be seen as the 'rise' and 'fall' time of the current pulse. The rise time τ_+ is dominated by the deposited energy and the electrical time of the circuit τ_{el}, whereas the fall time τ_- is dominated by the thermal part of the system, which dampens the energy through the heat sink (the thermal time of the system is $\tau_{\text{th}} = C/G$). In the case of the small signal solution for a low inductance, the amplitude (or pulse height) of the pulses is proportional to their energy (all other quantities being independent with the photon energy). Although valid for small energy excursions (up to 0.5 keV for the X-IFU), this solution breaks for higher energies, and more accurate or empirical models are required (see below).

Critical damping and pixel stability

The small signal solution approach is interesting to understand some of the TES main properties. The stability of the detector response, for instance, is related to the nature of the eigenvalues given by Equation 3.6, as in any second order linear problem (harmonic oscillator). Depending on the real/imaginary part of the eigenvalues, the pulse can be either over-, critically or under-damped. In the case of a voltage-biased TES detector, a critically damped or slightly over-damped system are advised to minimise the pixel speed (and therefore the required readout bandwidth), while ensuring the stability of the overall system. The system is critically damped if $\tau_+ = \tau_-$, which occurs when $L = L_\pm$, where

$$\begin{aligned} L_\pm = \Bigg[&\mathcal{L}_I\left(3+\beta-\frac{R_L}{R_0}\right) + \left(1+\beta+\frac{R_L}{R_0}\right) \\ &\pm 2\sqrt{\mathcal{L}_I(2+\beta)\left(\mathcal{L}_I\left(1-\frac{R_L}{R_0}\right) + \left(1+\beta+\frac{R_L}{R_0}\right)\right)}\Bigg]\frac{R_0 C}{G(1-\mathcal{L}_I)^2} \end{aligned} \tag{3.7}$$

Using the same notations, the system is under-damped when $L \in]L_-; L_+[$. In general, to avoid amplifier noise and increase the temperature-to-current responsivity, voltage-biased TESs are operated in critical damping configuration at low inductance values, i.e. $L \sim L_-$ (Irwin & Hilton, 2005). To ensure a stable system, the real part of the eigenvalues must be positive, which gives the following stability conditions for over-damped pixels

$$R_0 > \frac{\mathcal{L}_I - 1}{\mathcal{L}_I + 1 + \beta} R_L \tag{3.8}$$

which can always be satisfied in a voltage-biased circuit when $R_0 > R_L$ (as $\beta > 0$). This is related to the so-called negative electro-thermal feedback (ETF) of these circuits. Under these conditions, the Joule power of the TES $V_{\mathrm{bias}}^2/R_{\mathrm{TES}}$ decreases when the resistance increases (i.e. a photon is absorbed), thus naturally opposing the temperature increase and forcing the equilibrium at the initial set point. Voltage bias provides a good stability of the TES loop, even when high values of the loop gain $\mathcal{L}_I$ are considered, hence maximising the dynamic range of the pixels and linearising their response.

Noise terms and intrinsic energy resolution

To provide a realistic simulation of a TES detector, noise terms must be included when solving the system of coupled differential equations given by Equation 3.1. Four sources of noise are included in `tessim` and `XIFUSIM` through their power spectral density component in W^2/Hz (Irwin & Hilton, 2005):

- Load resistor, R_L, Johnson noise:

$$S_{\mathrm{P_{JN,R_L}}}(\omega) = 4k_B T_L R_L I_0^2 \frac{(\mathcal{L}_I - 1)^2}{\mathcal{L}_I^2} \left(1 + \omega^2 \left(\frac{C}{G(1-\mathcal{L}_I)}\right)^2\right) \tag{3.9}$$

  due to dissipative mechanisms in the load resistor of temperature T_L.

- TES Johnson noise:

$$S_{\mathrm{P_{JN,TES}}}(\omega) = 4k_B T_0 R_0 I_0^2 \frac{(1+2\beta)(1+M^2)}{\mathcal{L}_I^2} \left(1 + \omega^2 \left(\frac{C}{G}\right)^2\right) \tag{3.10}$$

  due to dissipative mechanisms in the TES resistor. Here, M is the 'unexplained' noise term, which appears in TES pixel characterizations and whose origins are unknown. Various assumptions exist and trace this component either to higher orders of the Johnson noise (Maul et al., 1969; Ullom et al., 2004; Smith et al., 2013), fluctuations of the magnetic field of the TES (Knoedler, 1983), fluctuations in superconducting order (Seidel & Beloborodov, 2004; Luukanen et al., 2003) or localised superconducting-to-normal changes in the pixel (Lindeman et al., 2004).

- Thermal fluctuation noise (TFN):

$$S_{\mathrm{P_{TFN}}}(\omega) = 4k_B T_0^2 G F(T_0, T_{\mathrm{bath}}) \tag{3.11}$$

related to the phonon noise between the TES and the thermal bath, where

$$F(T_0, T_{\text{bath}}) = \frac{1}{2}\left(1 + \left(\frac{T_{\text{bath}}}{T_0}\right)^{n+1}\right) \tag{3.12}$$

is a unitless factor between 0.5 and 1 related to the thermal conductance exponent, and due to phonon reflection in the absorber (Boyle & Rodgers, 1959; Mather, 1982). An additional source of noise, the internal thermal fluctuation noise (ITFN) is also present in the case of high normal resistance pixel, due to phonon noise at the transition between metals with two different heat capacities. It is added by multiplying Equation 3.11 with a $(1 + M_p^2)$ term (McCammon, 2005). This component can be neglected when TESs have low normal resistances (below the mΩ).

- Amplifier noise $S_{\text{P}_{\text{amp}}}(\omega)$ from the readout, assumed white.

Without noise, the intrinsic energy resolution of a TES is exclusively related to the measurement of the pulse height. Whenever the noise terms are included, it can be shown that the overall intrinsic energy resolution of the TES is given by (Moseley et al., 1984):

$$\begin{aligned}\Delta E &= \sqrt{8\log(2)}\left(\int_0^\infty \frac{4df}{\text{NEP}(f)^2}\right)^{-\frac{1}{2}} \\ &= \sqrt{8\log(2)}\left(\int_0^\infty \frac{4df}{S_{\text{P}_{\text{JN,R}_\text{L}}}(\omega)(f) + S_{\text{P}_{\text{JN,TES}}}(f) + S_{\text{P}_{\text{TFN}}}(f) + S_{\text{P}_{\text{amp}}}(f)}\right)^{-\frac{1}{2}}\end{aligned} \tag{3.13}$$

where the NEP represents the noise equivalent power of the various noise contributors. In the small signal limit, with $\mathcal{L}_I \gg 1$ and $R_L = 0$, when amplifier noises are neglected, Equation 3.13 at the TES set point becomes (see Irwin & Hilton 2005 for full development):

$$\Delta E = \sqrt{8\log(2)}\sqrt{\frac{4k_B T_0^2 C}{\alpha}\sqrt{\frac{n(1+2\beta)(1+M^2)F(T_0, T_{\text{bath}})}{1 - \left(\frac{T_{\text{bath}}}{T_0}\right)^n}}} \tag{3.14}$$

To achieve a high energy resolution, the pixel should have a low heat capacity C and a high temperature sensitivity α. This choice is however limited by either physical fabrication processes (e.g. deposition or etching of material) and by the desired bandpass, as a higher α and a lower C mean an earlier saturation of the pixel and higher demands on the readout. The current baseline of the pixel (used in the simulator) is given in Appendix D.

Classical and stochastic integrator

For high-energy photons, an analytical solution of Equation 3.1 is no longer possible. `XIFUSIM` and `tessim` implement a dedicated integrator based on a 4^{th} order Runge-Kutta (RK) solver with a constant step-size corresponding to the TES sampling (see Chapter 2). The main assumption is that the transition curves of the TES are linear, i.e. the derivatives of $R_{\text{TES}}(T, I)$ with respect to T and I along the superconducting transition are constant.[11] This approach provides excellent results for small energy pulses (consistent with the small signal solution) and ensures a better treatment at higher energies.

[11] This means, however, that α and β change in the simulation.

Constant	Value
C_R	0.7 + (T - T_c + 0.001)*100
C_I	0.75
n_1	1.8
n_2	0.85
$I_{c,0}$	10.25 mA
T_c	90 mK

Table 3.2: Two-fluid model constants for the large pixel array 2 (LPA2) pixel (Smith et al., 2016). Constants for the new baseline remain to be determined.

Whenever noise terms are included, an accurate solution of the stochastic system of differential equations is no longer possible through a RK4 scheme, and requires the implementation of a more accurate stochastic solver based on Itô integrals (Lorenz, 2017). Tests are ongoing to quantify the improvements made by this addition.

3.3.2 Additions to tessim and XIFUSIM

During my thesis, I helped expand the tessim and XIFUSIM simulators by implementing new features. I briefly introduce two of these additions.

Two-fluid model

The classical approximation of a fully linear transition made in the simulators has its limitations. Notably, it does not account for saturation of the pixel when large energies (e.g. 12 keV) are deposited onto the absorbers. More advanced models were investigated both numerically and experimentally to provide a more accurate description of the transition. Promising leads come from a modified 'two-fluid' model, based on a resistively shunted Johnson (RSJ) model (private communication, S. Smith, GSFC, L. Gottardi, SRON). Ignoring sources of noise, the resistance of the transition is given by

$$R_{\mathrm{TES}}(T,I) = \begin{cases} R_n C_R \left(1 - C_i \left(\frac{I_c(T)}{I_0}\right)^{n_2}\right)^{\frac{1}{n_2}} & \text{if } T \leq T_c. \\ 0.8 R_n & \text{otherwise.} \end{cases} \tag{3.15}$$

where R_n is the normal resistance of the TES, I_c the critical current of the TES is

$$I_c(T) = I_{c,0}\left(1 - \frac{T}{T_c}\right)^{n_1} \tag{3.16}$$

and T_c the critical temperature of the TES (~ 90 mK). The other parameters (C_R, C_i, n_1 and n_2) are constants, summarised in Table 3.2 for a LPA2 pixel configuration (Smith et al., 2016). This model was implemented by changing the solvers to account for Equation 3.15.

The addition of the two-fluid model goes a step further in approximating the behaviour of the detectors. It remains however a DC description and adds complexity related to the empirical aspect of the transition. The constants in Table 3.2 need to be tuned depending on the pixel type using experiments. Eventually, the option to have a fully experimental

table of the transition (e.g. derived from measurements) and a more accurate transition model for AC-biased pixels need to be investigated (Lorenz et al., in prep.).

Bath temperature fluctuations

Cosmic rays hitting the spacecraft can interact with the thin silicon wafer below the TES array, causing fluctuations in the thermal bath of the pixels (Hoevers et al., 2005). Measurements performed on recent cryogenic detectors (either for *SAFARI*/SPICA or on CMB bolometers, Stever et al. 2018) showed that the dissipation of this excess heat occurs through both a fast (athermal or 'ballistic') and a slow (thermal) phonon component, which create temperature spikes in the pixels. Physically, these result in small current pulses in the pixels. The understanding of these events presents multiple experimental challenges, as recreating a representative particle environment of flight-like detectors is complex in early phases of the instrumental design. Therefore, simulations are needed to understand the effect of these fluctuations on quantities such as the energy resolution.

To simulate these events within `XIFUSIM`, a time-dependent $T_{\mathrm{bath}}(t)$ was added in the previous system of coupled differential equations (Equation 3.1). At a given time of the solver, if a cosmic ray hits the wafer, T_{bath} is given a predefined pulse shape in time, which depends on the distance and the energy of the impact. These templates are so far derived from measurements performed for the instrument SPICA (courtesy SRON), but will eventually include more realistic shapes in later phases of the project. Due to the athermal component, the shape of these pulses on the detectors is different from that of typical X-ray photons, and can be excluded from data streams after optimal filtering. However, cosmic rays may change the pixel baseline, causing degradations in the detector performances. Current investigations show that these effects should be limited at a pixel scale. Additional measurements are however required to confirm this result.

3.3.3 Simulation of the full detection chain – `XIFUSIM`

To ensure a more realistic simulation of each readout chain block, the initial structure of `tessim` was modified and evolved into `XIFUSIM`, by using dedicated standalone blocks for each part or subsystem (e.g. SQUIDs, DRE, triggering). The code was changed from its initial *C* language, to a more versatile C^{++} code. Each block is described by a specific parameter file, contained in a single `.xml` which provides its characteristics, thus allowing the modification of subsections of the simulation at will (see Appendix C).

This approach is particularly useful for detailed performance studies of the readout chain, with or without noise, at subsystem level. The details of each building block are beyond the scope of this thesis, but can be found in the `XIFUSIM` manual. Most of this implementation was performed by the E2E simulation team over the course of my thesis.

3.4 Count rate capability of the X-IFU

The X-IFU is designed to provide spatially resolved high-resolution spectroscopy of point-like and extended sources. The need for high resolution (i.e. long record-lengths) drives its count rate capability. The instrument is optimised to target sources with low fluxes,

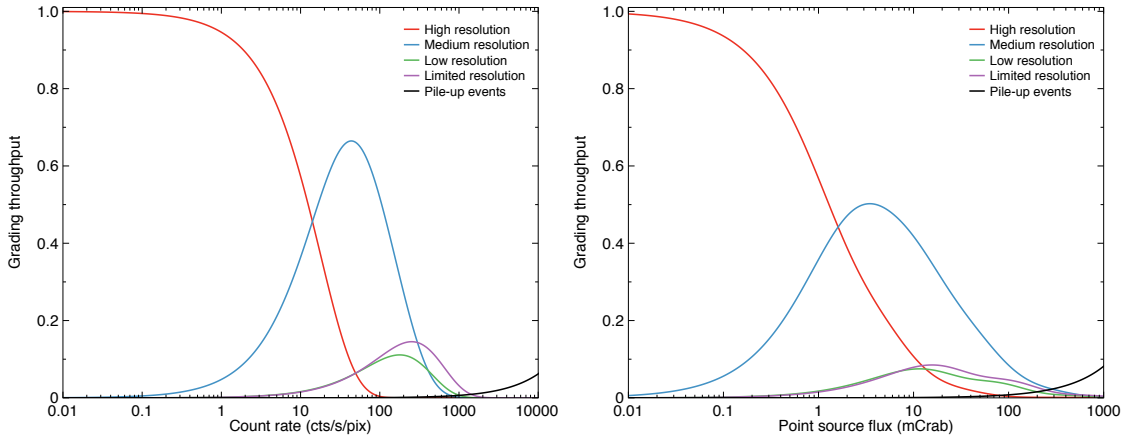

Figure 3.4: (*Left*) Throughput for extended sources as a function of the overall count rate on the pixels, assuming a uniform count rate on each pixel. (*Right*) Total throughput on the detector for point sources accounting for PSF effects as a function of the flux (in mCrab). Both plots show the fraction of events for each grade, along with pile-up effects.

ensuring a high throughput (ratio of the events used for scientific studies to the total detected events) for most of the observations. Above a certain flux, this throughput will naturally decrease, preventing spectroscopic analysis of bright sources. The main requirements derived from the science objectives are recalled in Chapter 2. I provide here a study of these requirements for extended sources. In this case, the throughput is the ratio of high-resolution events (2.5 eV energy resolution) to the total number of detected events.

3.4.1 Grading rejection

Assuming a count rate C of an observed source (in cts/s/pix for extended sources, or cts/s over the detector for point sources), a first effect on the total throughput is linked to the grading definitions, recalled in Table 3.1. As photons follow a Poisson distribution in time, the probability to have no photons k either before or after the event is given by

$$T = P(k = 0 \text{ during } t_{\text{pre}}) \times P(k = 0 \text{ during } t_{\text{rec}}) = e^{-C(t_{\text{rec}}+t_{\text{pre}})} \tag{3.17}$$

Since grades are mutually exclusive, for all grades above 1, the previous expression needs to be subtracted to the probability of being of a lower grade, thus:

$$\begin{aligned} T_1 &= e^{-C(t_{\text{rec},1}+t_{\text{pre},1})} \quad \text{for high resolution} \\ T_2 &= e^{-C(t_{\text{rec},2}+t_{\text{pre},2})} - T_1 \quad \text{for medium resolution} \\ T_3 &= e^{-C(t_{\text{rec},3}+t_{\text{pre},3})} - T_2 - T_1 \quad \text{for low resolution} \\ T_4 &= e^{-C(t_{\text{rec},4}+t_{\text{pre},4})} - T_3 - T_2 - T_1 \quad \text{for limited resolution} \end{aligned} \tag{3.18}$$

Likewise, the probability to have a piled-up event within a given sample of the DRE ($t_{\text{sample}} = 6.4\,\mu\text{s}$) is the probability to have two or more of events within t_{sample}, i.e.

$$T_{\text{pu}} = 1 - e^{-Ct_{\text{sample}}}(1 + Ct_{\text{sample}}) \tag{3.19}$$

All the events which do not satisfy a grading condition are considered invalid (see above). For extended sources with uniform count rates over the detector, the throughput is the same for each pixel (Figure 3.4 – *Left*). For point sources however, the pixel-to-pixel count rate will be determined by the PSF. A 1 mCrab flux is equivalent to 66 cts/s over the entire array, with a fraction $f_1 \sim 0.54$ on the central pixel (~ 29 cts/s) and lower fractions f_i in the neighbouring pixels ($\sum_i f_i = 1$) for the current PSF and pixel baseline. The high-resolution throughput is expressed on the overall array (Figure 3.4 – *Right*)

$$T_{\mathrm{point},1} = \sum_{i=1}^{N_{\mathrm{pix}}} f_i e^{-f_i C_{\mathrm{mCrab}}(t_{\mathrm{rec},1}+t_{\mathrm{pre},1})} \tag{3.20}$$

At high count rates, $T_{\mathrm{point},1}$ decreases, limiting spectral investigations of sources with fluxes above 10 mCrab. Two solutions are retained in the X-IFU design. The first is to use the defocussing capabilities of the MAM to distribute the counts over more pixels, as point sources do not require any spatial capabilities. The second, complementary to defocussing, is to screen the detectors from events below 4 keV using for instance a beryllium filter, thus reducing the count rates on the central pixel. This is interesting for hard X-ray sources, and enables a higher throughput of the detectors in the science-related energy bandpass (e.g. for Crab-like sources). For bright point sources, a lower spectral resolution is also accepted (e.g. 10 eV, see Table 2.1). Medium- and low-resolution events can thus be included in the spectral analysis, increasing the total throughput.

3.4.2 Crosstalk contribution

A second contribution to the overall count rate capability of the instrument is related to the crosstalk between pixels. Crosstalk is defined as a parasitic signal leak between two or more pixels, which may change the operational conditions of the detectors (i.e. create excess noise or small pulses in other pixels), and thus degrade the energy resolution and count rate capabilities of the instrument. Direct measurements of this effect are possible (Kilbourne et al., 2008; Eckart et al., 2012), but are in practice difficult on large arrays. For this reason, a dedicated analysis was performed using `xifupipeline` and `XIFUSIM`.

Crosstalk mechanisms

When discussing crosstalk, we define a 'perpetrator' pixel, in which a photon event is detected normally with an energy E_p, and a 'victim' pixel (or pixels), in which part of the energy E_v of this event is affected by E_p. For the X-IFU readout using FDM, three different mechanisms are expected, which are listed here and implemented in our simulations.

(1) Thermal crosstalk is due to the spatial proximity of pixels in the detector array and their heat sinking to the same thermal bath. An absorbed photon of initial energy E_p can thus leak a fraction of its energy to its immediate neighbours, creating local smaller versions of the perpetrator pulse in the victim pixels. Similarly to secondary events (see Section 2.3.3), the overall effect of thermal crosstalk will depend on the time difference between a photon pulse in the victim pixel, and the crosstalk pulse. For short separations, the thermal leakage will create an excess baseline current, modifying the noise spectrum.

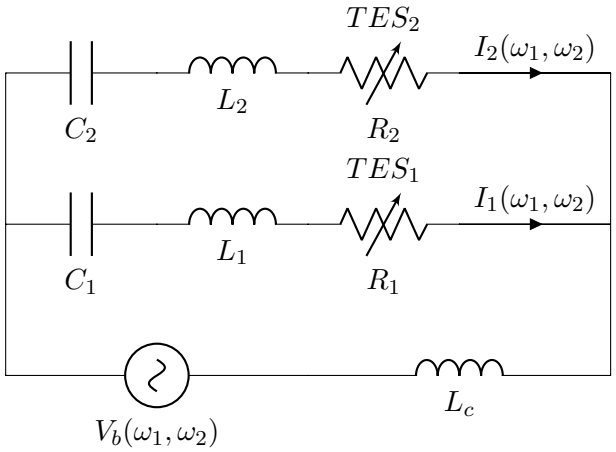

Figure 3.5: Simplified electrical circuit of a two-channel readout.

The use of predetermined optimal filtering templates (Szymkowiak et al., 1993) will bias the PHA estimation of the photon energy in the victim pixel, and degrade the energy resolution of the event. If the energy deposition is sufficiently high (equivalent heat deposition above 50 keV), a 'false' crosstalk pulse can be triggered in next-neighbour pixels. Using time correlation between events, crosstalk pulses should be identified and discarded.

The overall impact is also related to the geometry of the detectors and the heat sinking of the pixels. The addition of backside plated Cu is for instance one way to decrease the thermal coupling between pixels (Iyomoto et al., 2008), down to a 1×10^{-3} fraction for first neighbours (Kilbourne et al., 2008). This effect was implemented in the E2E simulator by creating, for each photon of energy E_p, a downscaled event in the neighbouring pixels with a fraction of E_p. The following conservative fractions are used in the simulator:

- $1 \times 10^{-3} E_p$ for first neighbours (275 µm) – four pixels
- $4 \times 10^{-4} E_p$ for diagonal neighbours (389 µm) – four pixels
- $8 \times 10^{-5} E_p$ for second next-neighbours (550 µm) – four pixels

In our simulations, thermal crosstalk is position-independent. Current measurements indicate that this may not be the case (Eckart et al., 2012). As the heat sinking is performed on the side of the array, power flows to the thermal bath can differ between central and side pixels. These spatial effects are considered for future implementation in the simulations.

(2) Electrical crosstalk is related to the FDM readout and namely to the non-perfect behaviour of TESs, which induce a frequency broadening near the characteristic frequency of the LC filters. Two main effects appear, even for the simplified two-channel readout shown in Figure 3.5, where TES are represented by resistances (Kirsch, 2016). Assuming that the second channel is the perpetrator, and the first is the victim, we have:

- **Carrier overlap**: despite the small bandpass of the first LC filter, part of the carrier that amplitude-modulates the perpetrator pixel 2 will be seen by channel 1. By using Kirchhoff's law, it can be shown that in a harmonic circuit, the perpetrator pixel causes an excess current at the frequency of the victim pixel ω_1 equal to

$$I_2(\omega_1) = \frac{(V_b(\omega_1)R_2 - Z_I(\omega_1)L_c\omega_1 I_1(\omega_1)) - j(V_b(\omega_1)Z_I(\omega_1) + \omega_1 R_2 L_c I_1(\omega_1))}{R_2^2 + Z_I(\omega_1)^2} \tag{3.21}$$

where $I_1(\omega_1)$ is the current in the victim channel and $Z_I(\omega_1) = L_2(\omega_1^2 - \omega_2^2)/\omega_1 + \omega_1 L_c$. For each pulse in TES_2, small currents leak in the frequency of TES_1, creating an additional parasitic signal under the shape of current pulses. This effect is significant only for frequency neighbours, and negligible for large differences in frequency.

- **Common impedance**: Similar equations for the carrier overlap can be found for the perpetrator pixel by a permutation of the indices in Equation 3.21. An additional current $I_1(\omega_2)$ thus circulates in the victim pixel, causing an additional Joule heating. The effective Joule power delivered to the first TES line over a period is

$$P_{\mathrm{Joule,eff}} = \frac{1}{2}\frac{V_b(\omega_1)^2 R_1 - V_b(\omega_1)\omega_2 Z_I(\omega_2)L_c I_2(\omega_2)}{R_1^2 + Z_I(\omega_2)^2} \tag{3.22}$$

  This effect changes the operating point of the victim TES similarly to thermal crosstalk. It can appear for any inductive coupling, but is expected to be most impacting on a readout channel level due to the input coil on the FE SQUID.

Electrical crosstalk sources are intrinsically related to the readout scheme. As explained in Appendix F, in the case of TDM readout, other types of crosstalk can appear.

(3) Intermodulation crosstalk is the third and final crosstalk mechanism considered in our simulations. It is related to the SQUID nonlinearity, which is compensated by BBFB. Given the sinusoidal shape of the transition (though linearised), when two current pulses arrive in the SQUID, part of the perpetrator pulse may leak to the other pixels. It was shown that this effect is significant only when the time separation between the pulses is short (a few µs) and the energies of the photons are high ($\geq$ 6 keV). The assumptions related the implementation of intermodulation crosstalk are given in Peille et al. (2019).

Crosstalk implementation in `xifupipeline`

To understand the effect of crosstalk on the relevant science cases, a dedicated mode of the simulator was created within `xifupipeline`, to which I actively contributed in the development and implementation. The accurate physical treatment of crosstalk pulses in the same readout channel can only be performed using `XIFUSIM`. However, for the limitations presented in Section 3.3, a detailed study would be computationally cumbersome. To simplify the approach, an interpolation using specific crosstalk LUTs within `xifupipeline` was preferred. This approach consists in creating dedicated tables for each crosstalk mechanism through `XIFUSIM`. LUTs can then be rapidly interpolated as a function of various parameters (e.g. arrival times separation, Δt, perpetrator and victim photon energies, E_p and E_v, or pixel frequencies, f_p and f_v) to determine the effect on the victim pulse. This energy contribution is then multiplied with a time-dependency weight, which accounts for the grade of the victim pulse and its time separation with the perpetrator. An example of the electrical crosstalk LUT and of the time-dependency weighting scheme are shown in Figure 3.6 (Kirsch, 2016; Peille et al., 2019). We assume that each crosstalk mechanism is independent, such that contributions of the LUTs can be linearly summed.

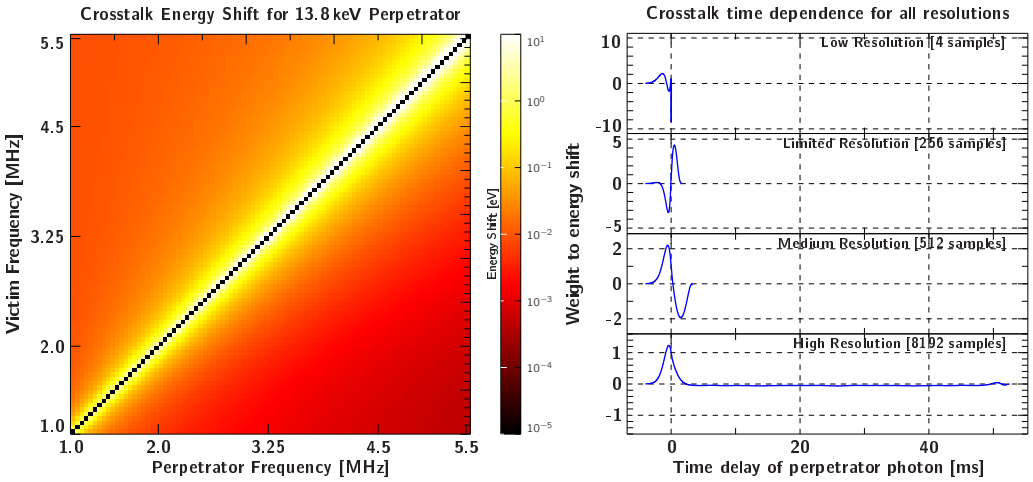

Figure 3.6: (*Left*) Example of a slice of the electrical crosstalk energy table for a perpetrator energy, $E_p = 13.8\,\mathrm{keV}$. The logarithmic colour code shows the effect of electrical crosstalk (in eV) in the frequency plane (f_p, f_v, in MHz). (*Right*) Time dependency weights for the different grades in `xifupipeline`. Courtesy: C. Kirsch (Peille et al., 2019)

Since the LUTs are grade-dependent (see Figure 3.6 – *Right*), one of my contributions to `xifupipeline` was to include this effect in the crosstalk computation using the outputs from `XIFUSIM`. The complexity is to derive the grade of each victim pulse first, and then compute the crosstalk effects on its energy. As crosstalk can trigger false events and change the grading, a linear approach in time is no longer valid. The overall scheme implemented in `xifupipeline` (accounting for pile-up, grade changes and triggers) is provided in Appendix E. The general principle can be summarised in four points:

1. For every impact find the next impact (if any) and grade the pulse accordingly.
2. Iterate through the buffer of all the perpetrator events of this pixel which may influence the pulse. For each compute the effect on the victim pulse using the LUTs.
3. If the effect is lower than the threshold energy (50 eV), no triggering occurs. The crosstalk effect computed in step 2 is added to the contribution on the victim pulse. Else, the perpetrator is removed from the buffer and the crosstalk impact is considered as a new event. The routine restarts from 1 using a new grade for the victim pulse and an updated crosstalk buffer.
4. The victim pulse energy and the contribution of crosstalk are saved.

3.4.3 Count rate capability of the X-IFU

In this section, I present and discuss the count rate capability studies performed using `xifupipeline` for extended sources (see Peille et al., 2018a, 2019, for point sources).

Driving science cases

To test the count rate requirement and the count rate goal set for the X-IFU in the observation of extended sources (reminded in Table 2.1), two science cases are identified:

- The Perseus cluster sets the requirement for extended sources, with a count rate of 0.34 cts/s/pix. Its spectrum can be simulated using an absorbed thermally-broadened plasma model `tbabs*apec`, based on the `APEC` code (Smith et al., 2001).
- The Cassiopeia A SNR sets the goal for extended sources, with a count rate of 2.1 cts/s/pix. Its spectrum can be simulated using an absorbed non-equilibrium ionization collisional plasma model `tbabs*vnei` (Mazzotta et al., 1998).

Each source is simulated through an associated SIMPUT file, created using the XSPEC models detailed in Table 3.3 as input models. To estimate the count rate capability of the X-IFU, each model is scaled (in normalisation) to change its total count rate on the detectors without changing its spectral shape. Although spectra of clusters and SNR may vary significantly with temperature or abundances (see Fig. 2 in Reiprich et al., 2013), it was verified using multiple models that such changes only have second-order effects, and that crosstalk results remain consistent with a simple scaling of the original model. Multiple SIMPUT files are generated for a discrete subset of normalisation values. When created, extended sources are assumed uniform over the FoV of the instrument (worst case). Finally, for each SIMPUT, simulations are performed using the standard `.xml` files for the X-IFU (regular PSF, and responses, no filters) adding one or all crosstalk mechanisms to see their relative contribution to the global throughput. The total simulated exposure in the runs is taken such that each event file has more than a million entries.

Crosstalk rejection

Once the event files are created, a first approach to determine the effect of crosstalk is to study the fraction of events which has a large energy deposition due to crosstalk. In our case, we estimate that events affected by more than 0.2 eV of crosstalk (Peille et al., 2018b) can be flagged and discarded from observations. The total throughput is given by:

$$T_{\mathrm{ctk},1} = \frac{\text{Events of grade 1 with crosstalk effects lower than } 0.2\,\mathrm{eV}}{\text{Total number of events}} \tag{3.23}$$

Results in the case of the extended sources can be seen in Figure 3.7 (*Left*) for the Perseus cluster spectrum. In the case of the Cas A SNR, no significant difference is found. We notice that in all cases, the main contributor to the performance is grading. Crosstalk rejection is dominated by the thermal component, but the electrical crosstalk is only slightly lower, as all pixels in the readout channels receive impacts uniformly (point sources show much lower rejection effects for electrical crosstalk, Peille et al. 2019). Non-linear crosstalk is negligible. Both the requirement and the goal are achieved, as the throughput reaches 80% for 2.13 cts/s/pix. This approach assumes however an *a priori* knowledge of the crosstalk effect on the pulses, which allows the rejection of contaminated events.

Degradation of the energy resolution

Another solution to estimate the count rate capability of the instrument is to determine the effect of crosstalk on its energy resolution. This option can be done quite simply with the simulator, by comparing the final value of the event generated by `xifupipeline` (which includes the crosstalk effect) to the input energy before the instrument (at impact file level).

Model	Parameter	Value
Perseus (`tbabs*apec`)	Column density n_H	0.136×10^{22} cm^{-2}
	Temperature k_BT	4 keV
	Z	0.3 $Z_\odot$
	Redshift z	0.0179
	Norm	0.01906 cts/s/keV/arcmin^2
Cas A (`tbabs*vnei`)	Column density n_H	1.20902×10^{22} cm^{-2}
	Temperature k_BT	1.64196 keV
	Z_H	1 $Z_\odot$
	Z_He	1 $Z_\odot$
	Z_C	1 $Z_\odot$
	Z_N	993.44 $Z_\odot$
	Z_O	46.8146 $Z_\odot$
	Z_Ne	5.13947×10^{-8} $Z_\odot$
	Z_Mg	3.28975 $Z_\odot$
	Z_Si	32.8867 $Z_\odot$
	Z_S	26.329 $Z_\odot$
	Z_Ar	1 $Z_\odot$
	Z_Ca	12.0033 $Z_\odot$
	Z_Fe	3.99307 $Z_\odot$
	Z_Ni	1 $Z_\odot$
	Ionisation time scale	5.42822e+10 s/cm^3
	Redshift z	-0.0133053
	Norm	0.000637178 cts/s/keV/arcmin^2

Table 3.3: Models and parameters used to simulate the astrophysical sources for the count rate studies. All abundances Z_X refer to Anders & Grevesse (1989) abundances, and the cosmology for XSPEC is set with $H_0 = 70$ km/s/Mpc, $\Omega_m = 0.3$ and $\Omega_\Lambda = 0.7$.

When no crosstalk is present, the energy resolution of the detectors should be Gaussian for each energy, with the intrinsic broadening provided in the RMF (e.g. $\Delta E_0 = 2.5$ eV FWHM below 7 keV for high-resolution events). When crosstalk is introduced, the energy resolution is degraded and the Gaussian is broadened (and skewed).

The data from the event file is compared to the one from the impact file to create a histogram. To reduce as much as possible sampling effects (limited statistics), event files were simulated for longer exposures ($\geq$ 10 millions counts) and the histogram was computed using all events between 0.2 and 7 keV, where the energy resolution of the RMF is constant (2.5 eV FWHM). The corresponding histogram is then fitted with a Gaussian function through a least-squares minimisation to compute its broadening ΔE. Due to a slight undersampling of the Gaussian response in the RMF used here, the energy resolution found without crosstalk is slightly higher than 2.5 eV and introduces $\sim$ 0.1 eV (FWHM) root-sum squared (RSS) error, which needs to be systematically removed.

Figure 3.7 (Right) shows the RSS excess broadening induced by the various crosstalk mechanisms ($\sqrt{\Delta E^2 - \Delta E_0^2}$), when events with a crosstalk contribution higher than 0.2 eV are discarded. As shown in Eckart et al. (2012), this degradation is well approximated by

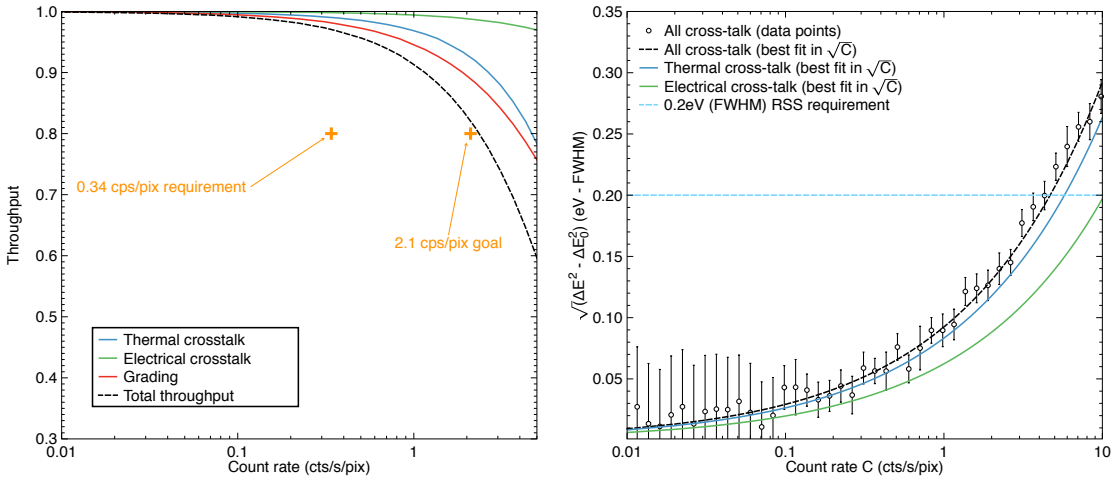

Figure 3.7: (*Left*) Total throughput for extended sources (blacked dashed line) as a function of the count rate (cts/s/pix). The throughput when only grading (red), thermal (blue) or electrical crosstalk (green) are rejected is also shown. (*Right*) Energy resolution degradation in eV RSS (FWHM) as a function of count rate C when all crosstalk mechanisms are considered, with best fit in $\sqrt{C}$ (black dashed line). The same curves are provided when only thermal (blue) or electrical (green) crosstalk are considered. The dashed light-blue horizontal line shows the requirement from the X-IFU energy resolution budget. In both plots, events with more than 0.2 eV of crosstalk influence are discarded.

a square-root function of the count rate, C. The degradation remains below 0.2 eV RSS (FWHM) as required in the X-IFU energy resolution budget (den Hartog et al., 2019) for count rates lower than ~ 4.5 cts/s/pix, consistently with the current goal and requirement.

Scaling relations

The implementation of the crosstalk in the simulator is based on early results, made in an effort to characterise its effect on the performances of the X-IFU. Despite a conservative approach in `xifupipeline` (thermal crosstalk fractions may be lower than those considered, private communication S. Bandler), our assumptions may not be entirely adequate. A sizeable effort has been started to compare our simulations through `XIFUSIM` with real data. First results are promising, and confirm that the LUTs give the proper order of magnitude of the amplitude of electrical crosstalk pulses and accurately describe its effect on the real events (den Hartog et al., 2018).

To cover any possible change that may arise, the previous count rate studies were extended by linearly scaling the LUT/energy fractions to consider worst-case scenarios (Figure 3.8). At the fixed count rate of the requirement, we notice that an order of magnitude change can be accepted without any mitigation. This is not as simple for the goal, where a factor 1.2 on thermal crosstalk fractions and 7 on electrical crosstalk LUTs provide a throughput lower than the required 80%. The difference between the current values of crosstalk and these upper boundaries provide an interesting margin for experimental teams to optimise their pixel geometry and readout schemes.

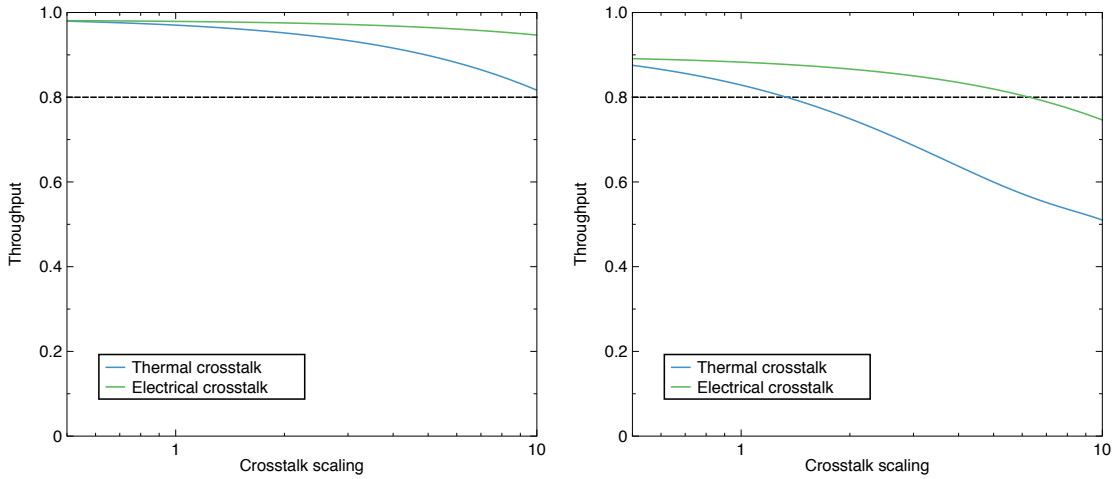

Figure 3.8: Total throughput obtained for the requirement count rate (0.34 cts/s/pix – *Left*) and for the goal count rate (2.1 cts/s/pix – *Right*) as a function of the linear scaling applied to thermal (blue) or electrical (green) crosstalk contributions.

Limitations and way forward

`xifupipeline` represents an excellent tool to test the count rate capability of the X-IFU in view of its phase B. However, multiple limitations of this approach need to be considered to consolidate the count rate budget in later phases of the instrument.

- The main question concerns the representativeness of our simulations, notably how these can be compared with real measurements. As mentioned in Section 3.4.3, first experimental tests are promising, and will help refine the simulator. However, only a dedicated experimental campaign can fully validate this approach.
- The current TES transition is based on DC-bias results. Though no major change is expected in the results, AC-biased TES have more complex transition shapes (Sakai et al., 2018; Gottardi et al., 2018). Efforts to model a more realistic transition shape using RSJ approximations are currently ongoing within the simulator team.
- Currently, the simulator treats crosstalk as a linear mechanism, summing the various contributions obtained through the LUTs. To account more accurately for a combination of the various crosstalk effects `XIFUSIM` should provide a fully representative simulation of a 40-pixel channel. A parallelised GPU version of `XIFUSIM` for crosstalk studies is currently under implementation (Lorenz et al., in prep.).

Aside from optimisations of the simulator, another point remains the *a priori* knowledge of the crosstalk effect (0.2 eV threshold), which remains to be assessed. Selections of the pulses in the χ^2 plane of the optimal filtering may be used,[12] but the level of accuracy achievable using such methods and their feasibility in flight remains to be determined. During my thesis, the same study was conducted for the TDM readout (current backup readout scheme for the X-IFU) and is given in Appendix F. Similarly to FDM, this approach was used to understand the impact of its crosstalk and to provide sizing figures for large arrays of TES pixels (Ullom et al., 2018).

[12] https://cloud2.neel.cnrs.fr/index.php/s/eb7HzDqtyKKXnyb

3.5 Line sensitivity analysis and scaling relations

The spectroscopic power of the X-IFU will give access to atomic lines hitherto noise-dominated. In low S/N ratio regimes, a good knowledge of errors is crucial. Recent observations performed by the SXS highlighted that our accuracy and knowledge on atomic physics and our data processing tools are insufficient for high-resolution X-ray spectroscopy (Hitomi Collaboration, 2018b). Current software (e.g. XSPEC, SPEX) leave however little possibility to study errors in a model-independent way. We thus return to simple cases to understand these effects. I provide here a study on the line sensitivity of the X-IFU starting from a single-line approach, and gradually increasing the line complexity to simulate realistic emission profiles. This work is introduced in Barret et al. (2018a), and will be summarised in a forthcoming paper (Lefkir et al., in prep.). This study is not a formal mathematical approach, unlike Hagen et al. (2007) or Minin & Kamalabadi (2009), but tries instead to provide simple tools and scaling laws for instrumental analysis.

3.5.1 Line sensitivity analysis

The sensitivity of a line is related to its S/N ratio, S, with respect to a (astrophysical) continuum. It will be one of the key performances to determine velocity broadening, velocity shifts or weak-line abundances with sufficient accuracy to answer several of the questions listed in Chapter 1. The final performances will be related to the effective area (i.e. photon collection capability), the energy resolution (line separation), the background level but also to the post-processing tools used. For a given line, S is defined as:

$$S = \frac{N_L}{\sqrt{N_L + N_C + N_B}} \tag{3.24}$$

where N_L, N_C, and N_B are the counts in the line, the continuum and the background respectively. For this definition to be valid when $N_C, N_B \geq 0$, S (hence the counts) must be defined on a specific energy interval.[13] For this study, the energy centroid, μ, and total width, $\sigma_{\rm W}$, of the observed lines is assumed to be known, and the S/N ratio is defined on $[\mu - 3\sigma_W; \mu + 3\sigma_{\rm W}]$ which contains $\sim 99.7\%$ of line counts for a Gaussian. A 'strong' line regime occurs when $N_L \gg N_C$ and a 'weak' line regime when $N_L \leq N_C$. We shall take a specific interest in the latter to constrain the X-IFU performances.

Line generation and fitting schemes

To investigate the sensitivity, a single line with a continuum is simulated to determine errors arising in its post-processing. The following assumptions are made:

- An astrophysical continuum can be well approximated by a power law. For a single line (a bandpass of a few tens of eV), power laws are slowly-varying. The continuum is therefore considered constant over the line bandpass (in cts/bin).
- Without loss of generality, the simulated line centroid is taken at an energy of 1 keV, with an instrumental spectral resolution of $\Delta E_0 = 2.5$ eV. Using the current response files, the channel binning is taken to be $\delta E = 0.4$ eV/channel. The response is assumed unitary and Gaussian on each channel.

[13] Otherwise S goes to 0 for a constant continuum integrated over the full bandpass.

- At the line level, background and astrophysical continuum have similar effects (see below). Both can be described by a constant spectrum. Their roles become permutable, and $N_B = 0$ without loss of generality.
- Finally, as discussed in previous chapters, the intrinsic Lorentzian profile of the atomic line will be broadened by instrumental and astrophysical effects. In our study, four possible sources of broadening are identified:
  - Thermal broadening $\sigma_{\rm th} = \sqrt{k_B T / A m_p}$ related to thermal Doppler effect along the line-of-sight.
  - Turbulent broadening $\sigma_{\rm turb}$ related to the velocity along the line-of-sight.
  - Energy scale accuracy broadening $\sigma_{\rm gain}$ related to the uncertainties expected on the energy scale of a given pixel (of the order of 0.4 eV FWHM for the X-IFU).
  - Instrumental spectral resolution $\sigma_0 = 1.06\,\text{eV}$ (i.e. 2.5 eV FWHM).

  Since Gaussians are the neutral element for convolution, the width of the total resulting broadening will be $\sigma^2 = \sigma_{\rm th}^2 + \sigma_{\rm turb}^2 + \sigma_{\rm gain}^2 + \sigma_0^2$. As such, the problem is simplified by taking a single excess Gaussian broadening σ for each line.

Although for previous X-ray instruments, with low spectral resolutions, the Lorentzian character of a line could be neglected, this is no longer the case for X-IFU-like instruments, whose energy resolution is of the same order (or lower) than the intrinsic broadening of the lines (typically 1 to 3 eV FWHM for lines above 4 keV). We thereby investigate two cases: the case of a purely Gaussian atomic line, G, or the case of a realistic Lorentzian line, L. Each can be modelled analytically as a function of energy by:

$$G(E, C, A, \mu, \sigma_G) = C + A e^{-\frac{(E-\mu)^2}{2\sigma_G^2}} \tag{3.25}$$

$$L(E, C, A, \mu, \gamma) = C + A \frac{1}{(E-\mu)^2 + \gamma^2} \tag{3.26}$$

where C is the continuum, A the amplitude, μ the centroid and σ_G its broadening. For the Lorentzian, γ is the half width at half maximum (HWHM) of the atomic line.

These profiles are then convolved with a Gaussian of broadening σ to include instrumental effects. In both cases, we call the total spectrum after convolution W, and its broadening $\sigma_{\rm W}$ (of FWHM $\Delta E_{\rm W}$). The resulting line is used as probability distribution function to extract N_L counts. Continuum is treated as a uniform distribution, with N_C count distributed over the $N_{\rm bins}$ bins of the bandpass. Once a realisation of W is simulated, we fit it to a line model using two minimization methods:

- A weighted least squares approach, where we minimize the cost function

$$K = \frac{(W - \text{Model})^2}{\omega^2} \tag{3.27}$$

  where $\omega_i = 1/\sqrt{N_i}$ for each bin (Gaussian error), with N_i the counts in channel i.

- A modified log-likelihood approach (C-statistics), inspired by Cash (1979), where the following function is minimised:

$$K' = 2\left(W \times \left(1 + \log\left(\frac{W}{\text{Model}}\right)\right) - \text{Model}\right) \tag{3.28}$$

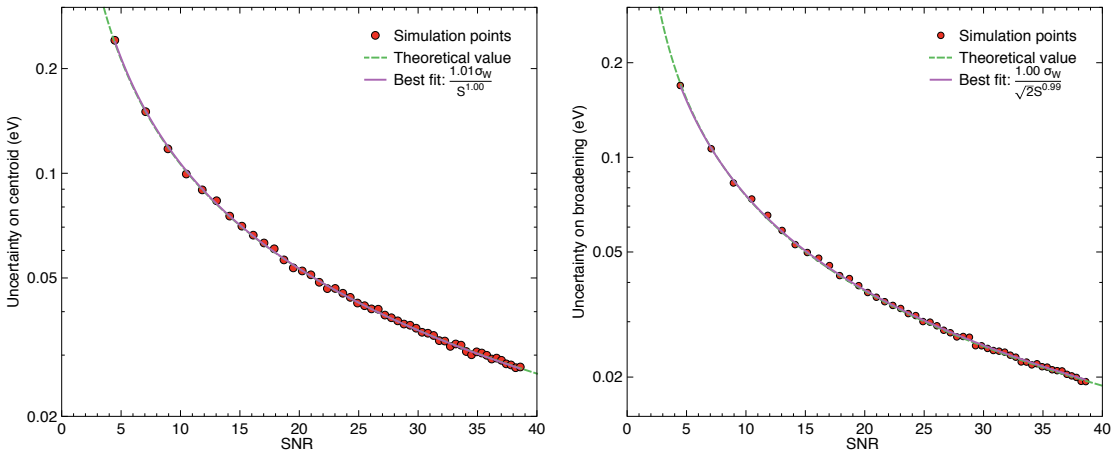

Figure 3.9: (*Left*) Error on the centroid, $\Delta\mu$, as a function of the S/N ratio of the line, S for a 2.5 eV (FWHM) Gaussian. The theoretical value is given by the green dashed line, the best fit is overlaid in purple. (*Right*) Likewise for $\Delta\sigma_W$.

To account for zero-value bins, a default truncation value of 10^{-25} cts is applied. Both approaches are implemented in current spectroscopic tools such as XSPEC and SPEX. We find (as recalled, e.g. in Kaastra & Bleeker 2016) that the second approach is more accurate for lines with low S/N ratios, and asymptotically converges towards the least squares method for high values of S (Barret et al., 2018a). We thereby limit our study to a C-statistics fit. The model function is either a Voigt or Gaussian profile, resulting from the convolution of G or L with a known Gaussian. The fit is performed over $[E_0 - 10\Delta E_W; E_0 + 10\Delta E_W]$ to ensure a correct evaluation of the continuum. For Voigt profiles, only the additional broadening σ is fitted, γ is considered known via theoretical physics.

To estimate the error made on the fitted parameters (C, μ, σ_W and A), simulations are repeated $N = 10\,000$ times to ensure a statistical convergence of the process. The dispersion of the parameters ($\Delta C, \Delta\mu, \Delta\sigma_W$ and ΔA) are computed by fitting their values using a Gaussian. Multiple other approaches are possible (covariance matrix, χ^2 computation) and all provide very similar results (Barret et al., 2018a). This approach uses as caveat that all the parameters can be considered as statistically independent. Finally, the error on the computed dispersion ($\epsilon_C, \epsilon_\mu, \epsilon_{\sigma_W}$ and ϵ_A) are estimated in two distinct ways, showing here again consistent values: either by taking the covariance matrix of the Gaussian fit of the distribution, or by sampling the minimisation potential well near the minimum to find the 1σ confidence region (68% confidence interval in all directions) for each iteration, then averaging over all results. For computational reasons, the former is retained.

Expected analytical results for Gaussian lines

In the case of Gaussian lines, the dispersion can be found analytically for both the centroid and the standard deviation (i.e. $\Delta\mu$ and $\Delta\sigma_W$) when $C = 0$.

The standard deviation on the centroid of a Gaussian line with N_L counts can be simply expressed (in a continuum-free or strong line regime) by $\Delta\mu = \sigma_W/\sqrt{N_L}$. In the

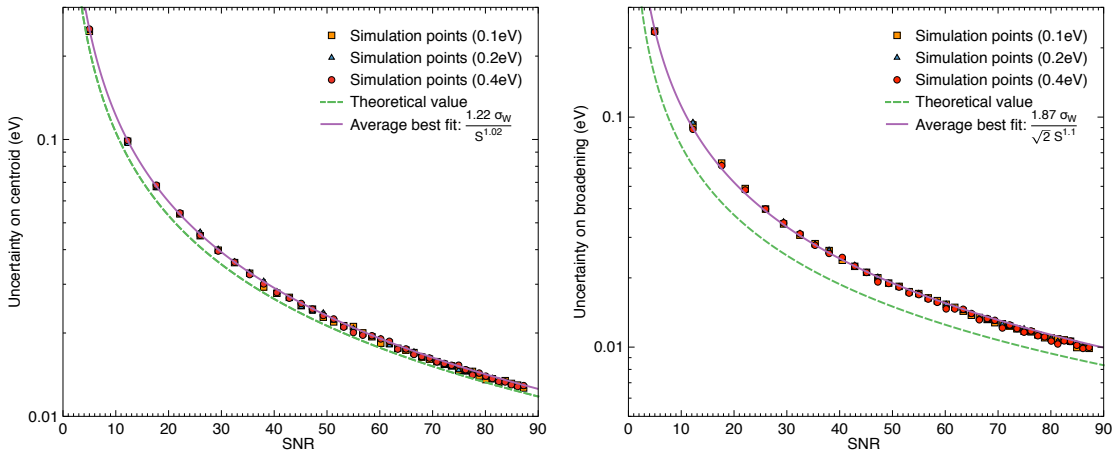

Figure 3.10: (*Left*) Error on the centroid, $\Delta\mu$, as a function of the S/N ratio of the line, S for a 2.5 eV (FWHM) Gaussian for different binning values (0.1, 0.2 and 0.4 eV). The theoretical value is given by the green dashed line, the best fit is overlaid in purple. (*Right*) Likewise for $\Delta\sigma_{\rm W}$.

case of a weak-line regime ($S < 10$), this formula becomes (Kaastra, 2008);

$$\Delta\mu = \frac{\sigma_{\rm W}}{S} \tag{3.29}$$

The variance on the variance of a Gaussian line with N_L counts can be expressed, using regular statistics, by $\Delta^2\sigma_{\rm W}^2 = 2\sigma_{\rm W}^4/N_L^2$. The standard deviation of the variance is then simply the square root of this expression, i.e. $\Delta\sigma_{\rm W}^2 = \sqrt{2}\sigma_{\rm W}^2/N_L$. Using differential calculus $\Delta\sigma_{\rm W}^2 \approx 2\sigma_{\rm W}\Delta\sigma_{\rm W}$, i.e. $\Delta\sigma_{\rm W} \approx \sigma_{\rm W}/\sqrt{2N_L}$. This estimator is nonetheless biased.[14] To provide a close-to-unbiased estimator of the deviation of the standard deviation, N_L can be replaced by $N_L - 1$, such that:

$$\Delta\sigma_{\rm W} \approx \frac{\sigma_{\rm W}}{\sqrt{2}S'} \tag{3.30}$$

where S' recalls the definitions of S replacing N_L with $N_L - 1$. These formulas are often used to estimate the errors of a given observation. Any departure from those will have a direct impact on the estimated performances of the instrument.

3.5.2 Results for a single line

The influence of continuum

As shown in Figure 3.9, for perfect Gaussian lines with $C = 0$, Equations 3.29 and 3.30 yield excellent results, regardless of the choice of $\sigma_{\rm W} \geq 1.06$ eV (1.06 eV corresponds to a mono-chromatic line seen by the instrument). This result holds as long as the binning oversamples the broadening of the Gaussian (Kaastra & Bleeker, 2016).

When a continuum value is added to the line, or simply when a continuum value is fitted (i.e. $N_C = 0$ but the model fits a potentially non-zero continuum to the data)

[14] As for a variable s, $d(\sqrt{s^2}) = ds \neq \sqrt{d(s^2)}$.

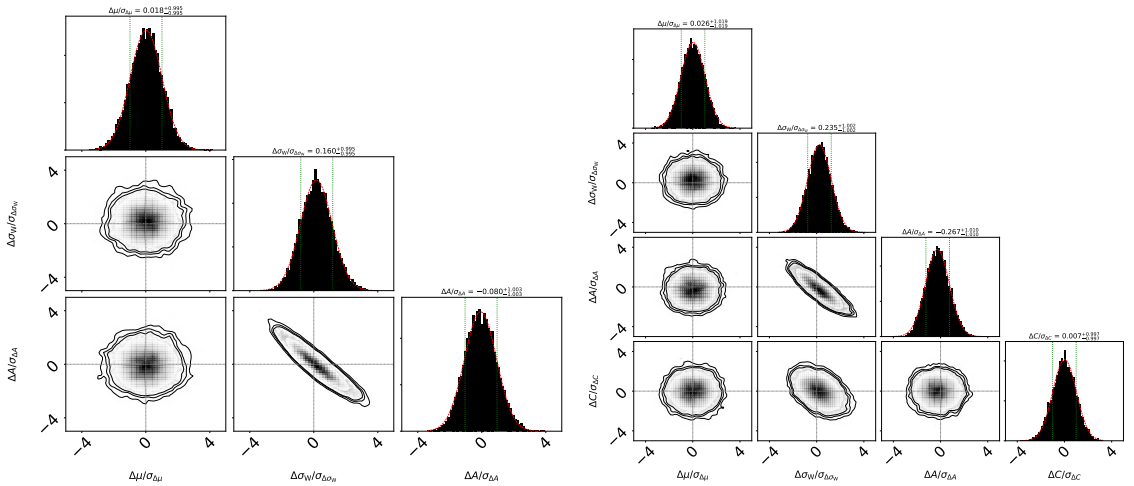

Figure 3.11: Correlation plots between fitted parameters in the case of Gaussian line ($\sigma_W = 3\,\mathrm{eV}$) without continuum (*Left*) or with continuum (*Right*) for $S \sim 17$. Contour plots are shown for each parameter (C, A, μ, or σ_W) divided by its dispersion.

Equations 3.29 and 3.30 break, even for moderately high values of S (e.g. 10 or 15), as shown in Figure 3.10. We find that the errors at a given S are always equal, regardless of the number of counts in the line or in the continuum considered. Similarly, no specific difference is found when the binning is changed, indicating that the fit converges, and that the bin size does not introduce a systematic error in the fit if sufficiently small (factor ≥ 5 at least between the bin size and the FWHM in our simulations). The previous formulas can no longer be applied in this case, but the simulated errors can be accurately recovered by including specific 'fudge' factors, f_μ, f_σ and β, such that:

$$\Delta\mu = f_\mu \frac{\sigma_W}{S} \qquad \Delta\sigma_W = f_\sigma \frac{\sigma_W}{\sqrt{2}S'^\beta} \tag{3.31}$$

We find that $f_\mu \sim 1.2$, $f_\sigma \sim 1.9$ and $\beta \sim 1.1$ provide good approximations of the errors for $S \leq 30$. When S asymptotically tends to infinity, the formulas presented in Section 3.5.1 become once again valid without correction.

Correlations between parameters

To understand the deviations of the errors from their analytical expression, a possibility is to review the assumption of independence between fitted parameters made in Section 3.5.1. To this end, we compute the correlations plots for all the parameters in both with and without continuum, for a 2.5 eV (FWHM) Gaussian line with $S \sim 17$, using $N_L = 500, N_C = 400$ and $N_L = 290, N_C = 0$ respectively. In the continuum-free case (Figure 3.11 – *Left*), an anti-correlation is present between the amplitude of the Gaussian and its broadening: the fit compensates a slightly higher value of σ_W by a slightly lower value of A. Intuitively, this can be explained by the finite, deterministic number N_L of counts used to generate the line, which correspond to its integral. Since $N_L = A\sigma_W\sqrt{2\pi}$, if one of the parameters is underestimated, the other is systematically overestimated.

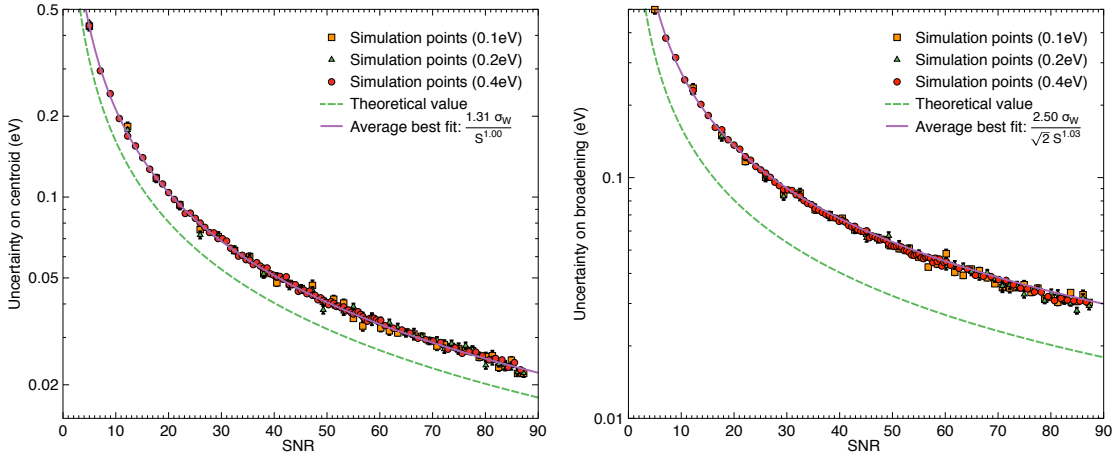

Figure 3.12: (*Left*) Error on the centroid, $\Delta\mu$, as a function of the S/N ratio of the line, S for a $\gamma = 1\,\mathrm{eV}$ Lorentzian line convolved with a $\sigma_0 = 2.5\,\mathrm{eV}$ (FWHM) Gaussian for different binning values (0.1, 0.2 and 0.4 eV). The theoretical value is given by the green dashed line, the best fit is overlaid in purple. (*Right*) Likewise for $\Delta\sigma_\mathrm{W}$.

When continuum is introduced (Figure 3.11 – *Right*), the anti-correlation between A and σ_W persists, but is less pronounced than in the previous case, as the fit has an additional degree of freedom due to the continuum. In this configuration, an additional anti-correlation between the continuum and σ_W appears. This connection can be explained with similar arguments as the σ_W/A anti-correlation: to maintain the overall integral value (continuum+line), an underestimation of sigma requires higher level of continuum.

These plots show that the numerical errors computed in the simulations cannot be considered as strictly independent, as the covariance matrix between the parameters is non-diagonal. Previous theoretical formulas can thus only be lower boundaries for these errors (Cramér-Rao boundary). In practice, a full computation of the Fisher matrix is possible provided semi-numerical approximations (Lenz & Ayres, 1992; Minin & Kamalabadi, 2009) and improves the results, but loses the convenience of a rule-of-thumb expression.

Gaussian and Voigt profiles

The assumption of a purely Gaussian emission line breaks when the intrinsic width of atomic lines is larger, or of the same order, as the spectral resolution of the detectors. The previous study was therefore extended to Voigt profiles. We mainly considered the case where the intrinsic FWHM of the Voigt line is similar to the Gaussian instrumental broadening ($2\gamma \sim \Delta E_0$), which should represent well typical X-IFU spectra. σ_W can be approximated to better than 0.02% using the empirical formula by Olivero (1977):

$$\Delta E_\mathrm{W} = \sqrt{8\log(2)}\sigma_\mathrm{W} \approx 1.0692\gamma + \sqrt{0.8664\gamma^2 + 8\log(2)\sigma^2} \tag{3.32}$$

For this configuration, the value of S remains defined over $[\mu - 3\sigma_W; \mu + 3\sigma_\mathrm{W}]$, but N_L needs to be rescaled, as the interval only contains $\sim 80\%$ of the line counts due the wider wings of the Lorentzian (which also increase the computational time of each fit). The conclusions

derived from the Gaussian case – notably on binning – remain valid (Figure 3.12). When no continuum is considered, the formulas from Section 3.5.1 are applicable, provided the use of the equivalent broadening (Equation 3.32). Similarly, these expressions need to be adapted at low S when a constant continuum is added. Slightly higher fudge factors of $f_\mu \sim 1.3$, $f_\sigma \sim 2.5$ and $\beta \sim 1$ provide accurate estimations of the errors for $S \leq 30$.

Interestingly, the convergence of errors toward their theoretical expression (without fudge factors) is much slower than for the Gaussian case, especially for high values of γ, with deviations still persisting at $S \sim 1\,000$. This effect is related to the shape of the Voigt profile, whose wings are much more prone to systematic errors in the fit. Finally, correlations between parameters remain comparable (A/σ_W and C/σ_W anti-correlations).

Whenever $2\gamma \gg \Delta E_0$, the previous formulas are no longer sufficient, and more complicated expressions are needed. These circumstances hardly occur during observations, since no intrinsic atomic line is much larger than the energy resolution (or at least not without being broadened by other Gaussian phenomena first, as, e.g. reflected iron lines of accretion disks near BH). This case was therefore not investigated.

3.5.3 The case of a line doublet

Physical motivation

Most of the lines observed with the X-IFU will not be single Lorentzian lines, but are likely to be composite (e.g. doublets as the Cu K_α of the MXS, Hölzer et al. 1997, or quadruplets for Fe, Hitomi Collaboration 2016). To investigate the errors of these complex lines, we extended the previous study to the case of a line doublet, with a fixed separation ΔE_L and with amplitudes verifying $A_1 = 2A_2$, imitating the case of natural K shell lines. We consider that the knowledge of the line centroid is perfect, or at least much more accurate than the channel width. We consider the case of a doublet of two Gaussian lines:

$$D(E, C, A1, A2, \mu_1, \mu_2, \sigma_G) = C + A_1 e^{-\frac{(E-\mu_1)^2}{2\sigma_G^2}} + A_2 e^{-\frac{(E-\mu_2-\Delta E_L)^2}{2\sigma_G^2}} \tag{3.33}$$

In the case of a doublet, the definition of S also needs to be modified to account for two lines. We considered shell lines as the same physical entity, and adapt the previous definition with N_L being the total number of counts in the main line (then rescaled to include $N_L/2$ counts in the secondary line), and N_C the counts beneath the main line ($\pm 3\sigma_\mathrm{W}$). We thus recover the case of a single line when $\Delta E_L \to \infty$.

Results and correlations

Similarly to the single-line case, results for line doublets can be approximated by the previous analytical formulas provided new numerical fudge factors. Due to spectral entangling, the minimisation problem becomes ill-constrained close to the blurring point (i.e. $\Delta E_L \sim \Delta E$). Fudge factors can no longer be considered constants, but need to be expressed as a function of ΔE_L (Figure 3.13 – *Left*).

When lines have large separations, the fudge factors converge towards the single-line values. Interestingly, the values reach a minimum for a separation of $\Delta E_L \sim 2\Delta E$, where parameters are recovered more accurately than in the single-line case. In fact, for low

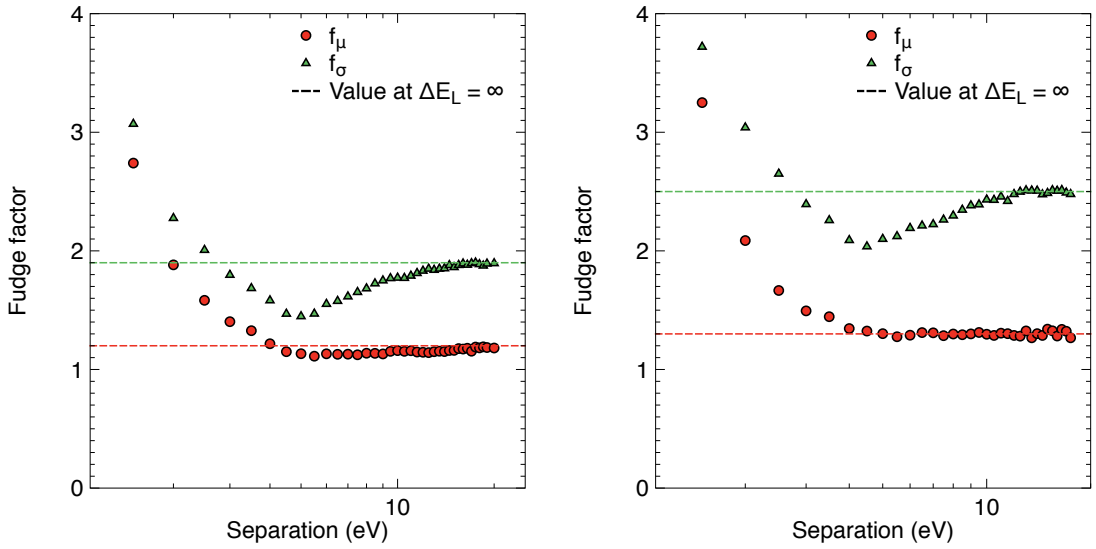

Figure 3.13: Fudge factors f_μ and f_σ for doublets as a function of separation for the Gaussian case (*Left*) or the Voigt case (*Right*). The values reached for an infinite separation (single line case) are given in dashed. β is fixed to the value when $\Delta E_L \to \infty$.

separations, more than N_L line counts are available in the $[\mu - 3\sigma_W; \mu + 3\sigma_W]$ interval under the main line which defines S (lines overlap). Thus, the fit sees a higher 'equivalent' value of the S/N ratio of the line, which improves its accuracy. When very low separations are considered ($\Delta E_L \leq 0.5\Delta E_0$), the line blur prevents a non-degenerate determination of the parameters, as single- or two-line models can be fitted to the same data set with comparable errors. Such narrow doublets exist, but require an *a priori* knowledge from spectral data. We thus force simulations to fit two lines to extend the previous fudge factors dependency plots to low-separation regimes. Consistency of the results however becomes questionable for separations similar to/smaller than the binning size.

Correlations between parameters remain comparable to the previous case, with the expected addition of an anti-correlation between both amplitudes. The latter decreases with ΔE_L, as the problem converges towards the case of two independent lines. As for the single-line case, the consideration of Voigt profiles instead of Gaussians provides comparable results as long as $2\gamma \lesssim \Delta E_0$, with slightly higher fudge factors (Figure 3.13 – *Right*).

3.5.4 Derivation of scaling relations

For low spectral resolution instruments, the approximation of Gaussian lines over a low continuum results in negligible biases in the estimation of the errors. For micro-calorimeter instruments, these simplifications are no longer possible. The spectral analysis of narrow lines in a low S/N regime exhibits number of complexities related to correlations between parameters. When realistic line profiles (Lorentzian doublets) are used, these deviations become even more significant, requiring the introduction of correction factors.

To reduce these effects, a solution is to ensure a systematic continuum subtraction before fitting. In this case, our simulations show that the errors related to the broadening

	Strong line	Continuum-dominated	Background dominated
S	$\frac{t_{\rm exp,2}}{t_{\rm exp,1}} = \frac{A_1}{A_2}$	$\frac{t_{\rm exp,2}}{t_{\rm exp,1}} = \frac{A_1}{A_2}\frac{\sigma_{\rm W,2}}{\sigma_{\rm W,1}}$	$\frac{t_{\rm exp,2}}{t_{\rm exp,1}} = \frac{A_1}{A_2}\frac{F_{B,2}}{F_{B,1}}\frac{\sigma_{\rm W,2}}{\sigma_{\rm W,1}}$
Δv_μ	$\frac{t_{\rm exp,2}}{t_{\rm exp,1}} = \frac{A_1}{A_2}\left(\frac{\sigma_{\rm W,2}}{\sigma_{\rm W,1}}\right)^2$	$\frac{t_{\rm exp,2}}{t_{\rm exp,1}} = \frac{A_1}{A_2}\left(\frac{\sigma_{\rm W,2}}{\sigma_{\rm W,1}}\right)^3$	$\frac{t_{\rm exp,2}}{t_{\rm exp,1}} = \frac{A_1}{A_2}\frac{F_{B,2}}{F_{B,1}}\left(\frac{\sigma_{\rm W,1}}{\sigma_{\rm W,2}}\right)^3$
$\Delta v_{\rm turb}$	$\frac{t_{\rm exp,2}}{t_{\rm exp,1}} = \frac{A_1}{A_2}\left(\frac{\sigma_{\rm W,2}}{\sigma_{\rm W,1}}\right)^{\frac{4}{\beta}}$	$\frac{t_{\rm exp,2}}{t_{\rm exp,1}} = \frac{A_1}{A_2}\left(\frac{\sigma_{\rm W,2}}{\sigma_{\rm W,1}}\right)^{\frac{4+\beta}{\beta}}$	$\frac{t_{\rm exp,2}}{t_{\rm exp,1}} = \frac{A_1}{A_2}\frac{F_{B,2}}{F_{B,1}}\left(\frac{\sigma_{\rm W,2}}{\sigma_{\rm W,1}}\right)^{\frac{4+\beta}{\beta}}$

Table 3.4: Scaling laws for line sensitivity, effect of a change in $A_{\rm eff}, \sigma_{\rm W}$, or F_B on the exposure time for the three main observation cases.

can be approximated, once again, by the formulas in Section 3.5.1 (fudge factors are still required for doublets). This approach is already current practice in the spectroscopic analysis over a reduced bandpass (de Plaa, 2013) and advised in the literature (Kaastra & Bleeker, 2016). However, for full spectra, an unbiased estimation of the continuum is extremely challenging, as it relies on quantities such as the column density n_H, or the temperature T, which are fitted. It also implies a quasi-perfect knowledge of the background level over time. In this case, only model-dependent studies can provide insight on the expected level of systematic errors. As shown in Chapter 4 or Cucchetti et al. 2018f; Roncarelli et al. 2018, interesting results can be achieved in this regard, but not without major simulation efforts. It becomes therefore crucial, when investigating the performances of an instrument in its early phases, to have simple scaling laws, giving rapid access to the order-of-magnitude of the expected errors on the science cases.

The knowledge of the error on the centroid and the broadening of the line provides a direct access to the centroid shift and velocity broadening errors (Kaastra, 2008):

$$\Delta v_\mu(E) = \frac{c}{E}\Delta\mu = \frac{c}{E}\frac{f_\mu \sigma_{\rm W}}{S} \tag{3.34}$$

$$\Delta v_{\rm turb}(E) = \frac{1}{\sigma_{\rm turb}}\frac{c}{E}\sigma_{\rm W}\Delta\sigma_{\rm W} = \frac{1}{\sigma_{\rm turb}}\frac{c^2}{E^2}\frac{f_\sigma \sigma_{\rm W}^2}{\sqrt{2}S'^\beta} \tag{3.35}$$

where we assume that $\frac{\sigma_{\rm turb}(E)}{E} = \frac{v_{\rm turb}}{c}$. The X-IFU shall verify $5\Delta v_{\rm turb}(E) < v_{\rm turb}(E)$, the second expression provides a minimal measurable value of $v_{\rm turb}$

$$v_{\rm turb,min}(E) = \frac{c}{E}\sqrt{\frac{5f_\sigma(\sigma_0^2 + \sigma_{\rm th}^2 + \sigma_{\rm line}^2 + \sigma_{\rm gain}^2)}{\sqrt{2}S^\beta - 5f_\sigma}} \tag{3.36}$$

which is achieved if $S \geq (5f_\sigma/\sqrt{2})^{\frac{1}{\beta}}$. By re-interpreting the value of S as a function of the line flux $\mathcal{F}_\ell$ (cts/s/m^2), the continuum flux, F_C (cts/s/m^2/keV), the background flux, F_B (cts/s/m^2/keV), the effective area A and exposure time $t_{\rm exp}$ (Barret et al., 2018a):

$$S \propto \sqrt{\frac{At_{\rm exp}}{1 + \frac{\Delta E_{\rm W}}{\mathcal{F}_\ell}(F_C + F_B)}} \tag{3.37}$$

and estimate the effect of key parameters on the performance of the instrument. To maintain the desired values of S, Δv_μ or $\Delta v_{\rm turb}$ required for a science objective, scaling relationships can be deduced (Table 3.4). We distinguish three observations cases:

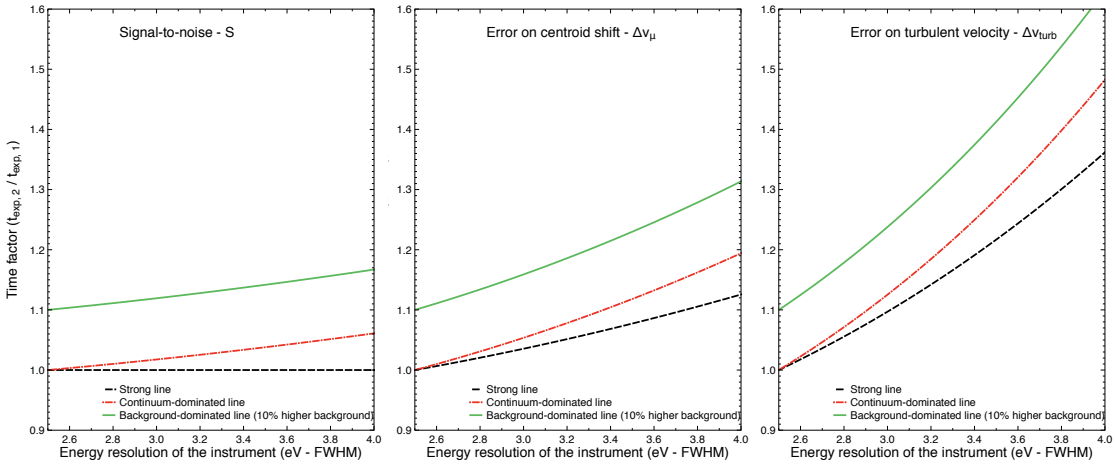

Figure 3.14: Exposure time penalty for the observation of a $T = 5\,\mathrm{keV}$ iron K_α line with a turbulent velocity of $v_{\mathrm{turb}} = 100\,\mathrm{km/s}$ and a gain accuracy $\sigma_{\mathrm{gain}} = 0.4\,\mathrm{eV}$ (FWHM) for the S/N ratio (*Left*), the centroid shift (*Middle*) and the turbulent velocity error (*Right*). In all cases, we plot the case of a strong line (black), a continuum-dominated line (red) and a background-dominated line with an additional 10% value of the background flux (green).

- Strong line ($\mathcal{F}_\ell \gg (F_B + F_C)\Delta E_{\mathrm{W}}$) $S \propto \sqrt{At_{\mathrm{exp}}}$
- Weak line dominated by continuum ($F_C \Delta E_{\mathrm{W}} \gg \mathcal{F}_\ell$) $S \propto \sqrt{\frac{At_{\mathrm{exp}}}{F_C \sigma_{\mathrm{W}}}}$
- Weak line dominated by background ($F_B \Delta E_{\mathrm{W}} \gg \mathcal{F}_\ell$) $S \propto \sqrt{\frac{At_{\mathrm{exp}}}{F_B \sigma_{\mathrm{W}}}}$

Using these formulas, we can deduce the penalty on time or on the errors due to, for instance, the effective area or the energy resolution of the instrument (Figure 3.14). More applications of these scaling relationships can be found in Barret et al. (2018a). This approach can be used to demonstrate, at first order, the feasibility of science objectives or to justify the need for spectral resolution/effective area for a specific observation.

3.6 Background reproducibility studies

The high sensitivity of the X-IFU TES detectors, coupled with the collective area of the *Athena* telescope, will undoubtedly provide information on currently statistically-dominated sources, such as high-redshift clusters or cluster outskirts. Yet, the intrinsic calorimetric nature of TESs also limits the instrumental performance. Any X-ray radiation falling in the soft X-ray bandpass, even unrelated to the observed X-ray sources, can contaminate the primary scientific data. To avoid introducing biases in the data analysis (Leccardi & Molendi, 2008b) or degrade the line sensitivity of the instrument (see Figure 3.14), an accurate and reproducible knowledge of this background is required.

In this section, I remind the main efforts conducted during my thesis to model the impact of the background on the detector, and derive a requirement on its reproducibility using the driving science case of background-dominated outskirts of galaxy clusters. The main results of this section are summarised in Cucchetti et al. (2018d).

3.6.1 Components of the X-ray background

Astrophysical foreground and background

Part of the background is related to the X-ray sources of the sky. Along the line-of-sight, multiple emission regions overlap with the observed target. X-ray components of astrophysical origin (dust, plasma, hot gas) will thus add to the science data. Two contributions are distinguished: one from the galactic X-ray sources between the observer and the target, the other from extra-galactic X-ray point sources near the line-of-sight.

The former is defined as the astrophysical foreground, related to the local environment of our Solar System (local plasma bubble emission) and to the halo of emitting gas within the Milky Way. As shown in Figure 1.5 (*Top*), this diffuse component is dominant in the soft X-ray band ≤ 1 keV. Its spectrum is the sum of an absorbed (galactic) and unabsorbed (stellar) thermal plasma component, whose average parameters are well determined (McCammon et al., 2002). This component is not likely to change over time, but can present substantial spatial variations (Kalberla et al., 2005).

The latter is defined as the cosmic X-ray background (CXB, Lehmer et al. 2012), related to high-energy photons from distant point-sources (e.g. AGNs) whose emission is redshifted in the soft X-ray band (De Luca & Molendi, 2004). Given the X-IFU angular resolution, $\sim 80\%$ of the log(N)-log(S) integrated flux of these sources should be resolved and subtracted from the observations (Moretti et al., 2003). For 100 ks X-IFU observations, this corresponds to removing all sources with fluxes $\gtrsim 3\times10^{-16}$ ergs/s/cm^2. The unresolved part of the CXB results in a diffuse absorbed power law component in the observations.

Both components are well understood and their spectra are well represented by combinations of power law or collisionless plasma models (Lotti et al., 2014). Their contribution should therefore be accurately removed from future X-IFU data. Though stable in time over the course of the mission, the main challenge remains the spatial anisotropy of these components (McCammon et al., 2002). Only a more detailed mapping of sky with upcoming missions such as eRosita, should improve this aspect. Otherwise, when possible, deep pointings of scarcely-populated regions near the targets of interest can be used to estimate the astrophysical background, at the expense of observing time.

Focused and unfocused particle background

The second part of X-ray background can be attributed to the environment of the instrument, and will depend on its configuration and the orbit of the spacecraft. We distinguish an unfocused (unrelated to the telescope attitude and mirror) and a focused component.

The former is associated to high-energy cosmic rays observed in our solar system. These particles, mainly protons, penetrate within the spacecraft and interact with its structures to create showers of secondary particles, which can deposit energies equivalent to soft X-rays. If these interactions occur sufficiently close to the detectors, they generate a background component, defined as the non-X-ray background (NXB). Cosmic rays have an isotropic distribution and their flux is anti-correlated with the solar cycle (11 years, Usoskin et al., 2005). The total value of the NXB thus changes along the mission. For the X-IFU most of the NXB is related to interactions with the Nb shield in the FPA. The CryoAC, coupled with passive shielding (e.g. Kapton and bismuth, D'Andrea et al. 2018), should lower this

level below 5×10^{-3} cts/s/keV/cm^2 at solar minimum (i.e. GCR maximum) over the 2 – 10 keV bandpass (Lotti et al., 2018a). The bulk of the NXB is composed of back-scattered secondary electrons. Because of its flat spectral distribution, the NXB will dominate on the high-energy bandpass (≥ 5 keV), where other background components are lower.

The focused particle background is related to the solar activity. During coronal mass ejections or solar flares, the Sun emits highly-variable bursts of charged soft protons. Depending on the attitude of the telescope, part of this emission can be focused onto the detectors. For the X-IFU a dedicated magnetic diverter (see Figure 2.1) will deflect most of these protons (Lotti et al., 2018b). A quiescent contribution should nonetheless persist ($\lesssim 5 \times 10^{-4}$ cts/s/keV/cm^2, Lotti et al. 2017). During solar activity, this component can become dominant, making data analysis noise-dominated for part of the observing time.

3.6.2 Simulating the instrumental background in SIXTE

State-of-the-art simulations using `GEANT4` (Agostinelli et al., 2003) can describe the expected particle background on any X-ray instrument. However, E2E simulations remain unavoidable to assess the impact of background on the performance. The addition of astrophysical background in simulations is done through representative models, as those detailed in Lotti et al. (2014). Since these contributions are convolved with the effective area of the instrument, they can be added to the SIXTE using specific SIMPUT files, generated from the `.xcm` file of their respective model.

As the NXB is an unfocused component, this solution no longer works. It was therefore included directly in the simulator from a `FITS` file derived from `GEANT4` simulations. This random implementation of the NXB does not account for physical features of GCR impacts (showers, streaks on the detectors). Modifications in SIXTE are in place to use direct `GEANT4` output files, whenever simulations with a more refined instrumental model are available (see Figure 5 of the SIXTE manual for an example on WFI). The resulting impact files can then be used in both `xifupipeline` or `XIFUSIM` simulations.

3.6.3 Derivation of the requirement on the NXB reproducibility

Decreasing the overall background level will be crucial for future X-IFU observations of faint sources. It is also important, however, to ensure its correct estimation over time – i.e. its reproducibility – to avoid systematic errors in the background subtraction. The astrophysical components detailed in the previous sections do not vary over an observation. They should therefore be negligible in the reproducibility budget. The soft proton components are assumed to be fully deviated by the magnetic diverter. Any excess emission can besides be correlated with the solar activity and discarded from the data in case of major solar events ($\leq 20\%$ of the total observing time). The NXB spectrum therefore drives the reproducibility. I investigate here the effect of an inaccurate estimation of the NXB level on the science, and derive a requirement on its reproducibility.

Driving science case of cluster outskirts

The NXB will dominate other background sources in the high-energy bandpass of the X-IFU spectra. Its knowledge will be particularly critical during the observation of faint,

Model	Parameter	Value
`wabs*bapec`	Column density n_H	0.136×10^{22} cm^{-2}
	Temperature k_BT	8 keV (at the centre)
	Z	$0.3\,Z_\odot$
	Redshift z	0.1
	Turbulent velocity	100 km/s
	Norm	given by Eckert et al. (2012)

Table 3.5: Model and parameters used to simulate the cluster used for the NXB studies. All abundances Z_X are as per Anders & Grevesse (1989), and the cosmology for XSPEC is set with $H_0 = 70$ km/s/Mpc, $\Omega_m = 0.3$ and $\Omega_\Lambda = 0.7$.

extended sources (e.g. cluster outskirts) to determine the features of iron lines and understand the turbulence and the abundances of these structures. Cluster outskirts are selected as driving science case to derive the requirement on the NXB reproducibility. For consistency with the complementary WFI study (Molendi et al., 2016), we simulate a 'toy' cluster using a velocity- and thermally-broadened plasma model (`bapec`, Smith et al. 2001) and an absorption model (`tbabs`, Wilms et al. 2000), with the parameters listed in Table 3.5. We use the universal emission-measure (EM) profile by Eckert et al. (2012) and the radial temperature distribution by Reiprich et al. (2013). We assume that clusters have a self-similar evolution, spherical symmetry and the radius/temperature scaling relation from Arnaud et al. (2005). Using these inputs and under a Λ-CDM cosmology ($\Omega_m = 0.3, \Omega_\Lambda = 0.7$), $R_{500} = 1.4$ Mpc ($\sim 12'$ on the sky).

Method and background models

To assess the reproducibility of the NXB, the cluster emission is divided into concentric circular annuli of different temperature and EM. To comply with the current specifications set for the X-IFU, the emission is assumed uniform over a 9 arcmin^2 area ($\sim$ half of the detector FoV). Though unrealistic in central parts of the cluster, this specification is driven by the observation of faint regions such as cluster outskirts, whose projected surface is much larger than a single X-IFU FoV. Thus variations of temperature and density over 9 arcmin^2 should be small. Furthermore, since vignetting effects on the X-IFU are negligible, any constant product of the detector area and the exposure time should provide similar results for a uniform emission model (i.e. the constant spectrum over 9 arcmin^2 during 100 ks will be equivalent to a 50 ks spectrum over 18 arcmin^2 FoV). Each annular spectrum is simulated using XSPEC with the various background contributions listed in Table 3.6. We assume that all astrophysical contributions are perfectly known and that no soft proton component is included. Two sets of simulations are conducted:

1. In the first case (simulations 'A'), a perfect background subtraction is performed for a typical observation time (100 ks and 1 Ms) and the spectrum is fitted to determine the main physical parameters of the cluster. This step determines the statistical error on the simulations, $\sigma_{\rm stat}(R, t_{\rm exp})$, of each parameter as a function of the radius and the exposure time. Numerically, we verified that these errors converge to zero whenever the exposure time is increased ($\ll 0.1\%$ for $t_{\rm exp} = 100$ Ms).

Model	Parameter	Value
Local bubble (`apec`)	Temperature k_BT	0.099 keV
	Abundance Z	$1\,Z_\odot$
	Redshift z	0
	Norm	1.7×10^{-6} cts/s/keV/arcmin^2
Galactic background (`tbabs*apec`)	Column density n_H	0.03×10^{22} cm^{-2}
	Temperature k_BT	0.225 keV
	Abundance Z	$1\,Z_\odot$
	Redshift z	0
	Norm	7.3×10^{-7} cts/s/keV/arcmin^2
CXB (`tbabs*powerlaw`) 20% unresolved	Column density n_H	0.03×10^{22} cm^{-2}
	Slope α	1.52
	Norm	$0.2 \times 1.0408 \times 10^{-6}$ cts/s/keV/arcmin^2
NXB (`powerlaw`)	Slope α	0
	Norm	6.0923×10^{-4} cts/s/keV/arcmin^2

Table 3.6: Model and parameters used to simulate the various background components. All abundances Z_X are as per Anders & Grevesse (1989), and the cosmology for XSPEC is set with $H_0 = 70$ km/s/Mpc, $\Omega_m = 0.3$ and $\Omega_\Lambda = 0.7$. See (Lotti et al., 2014)

2. In the second case (simulations 'B'), the background subtraction is perfect for all contributions except the NXB, which is systematically scaled by a factor $\Delta_{\rm norm}$. These runs are performed with very high unrealistic exposure times of 100 Ms to remove any statistical uncertainty and determine exclusively the systematic error on the simulations, $\sigma_{\rm sys}(R)$.

In both cases, fits are performed over the 0.2 – 12 keV bandpass using C-statistics leaving temperature, velocity, abundance and normalisation as free parameters. For simulations 'A', spectra are binned to a 5σ significance level. These simulations are performed more than 100 times each for reproducibility purposes and the values of $\sigma_{\rm stat}$ and $\sigma_{\rm sys}$ are averaged over the iterations.

Systematic effect

Starting from the data set of simulations 'B', we investigated the systematic effect of uncertainties in the knowledge of the NXB level (Figure 3.15). As expected, the error on the parameters increases with the radius, as the EM decreases. Assuming a spatial scale of R_{500} (resp. R_{200}), a reproducibility of 2% (resp. 1%) is needed to reduce the systematic errors below the required threshold. As this effect is purely systematic, we verified that these curves remain valid even for much lower exposure times, by subtracting the statistical errors from simulations 'A' (which add in quadrature as both effects are independent).

As shown in Figure 3.15, the effect of a systematic error is much greater on the temperature or on the abundances, for which the current requirement of 4% is reached before R_{500} for $\Delta_{\rm norm} = \pm 5\%$. Turbulent velocities are instead almost insensitive to these systematic uncertainties, with errors of ~ 5 km/s over the radial extension against the required 20 km/s for iron K_α lines. This discrepancy can be explained by the flat shape of the

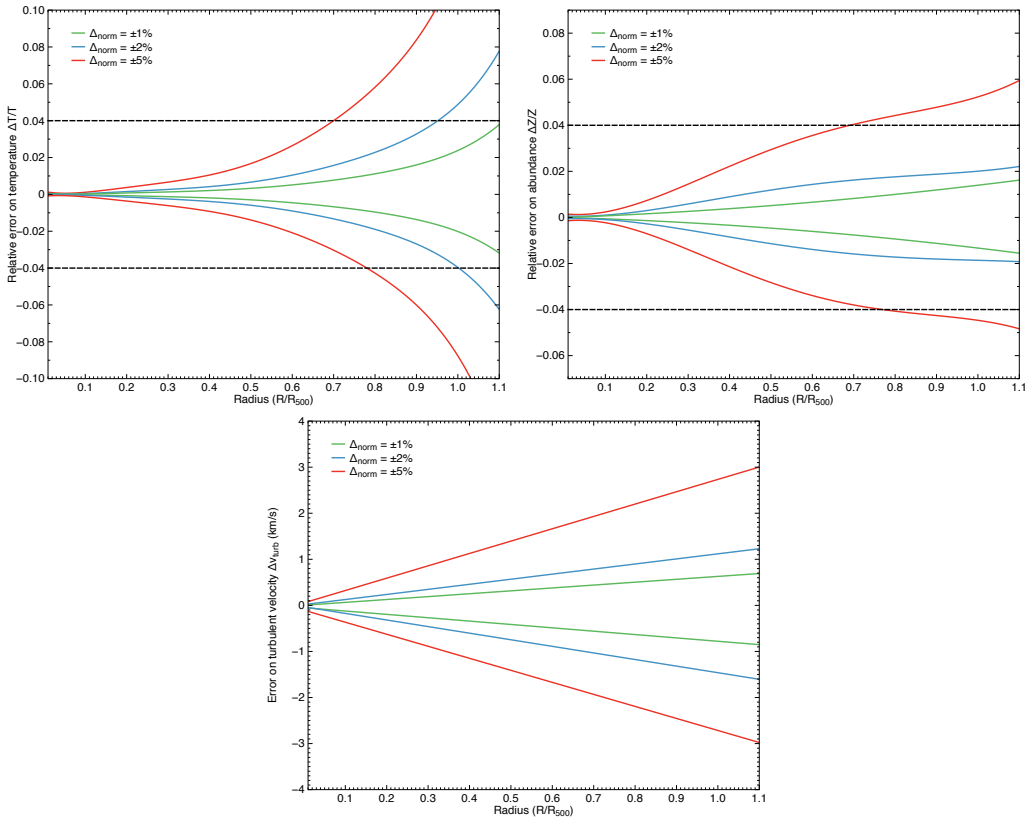

Figure 3.15: Systematic errors as a function of the radius (in units of R_{500}) for $\Delta_{\rm norm} = \pm\,1$ (green), 2 (blue) and 5% (red) for temperature (*Top left* - relative error), abundances (*Top right* - relative error) and turbulent velocity (*Bottom* - in km/s). Dashed lines indicate the current 4% requirement accuracy for temperature and abundances.

NXB. A wrong subtraction of the continuum will bias the estimation of the norm, which determines the overall integral of the line (abundance) and is related to the shape of the continuum (temperature), whereas it will not modify the estimation of the line broadening by much. The effect on turbulent velocity is therefore smaller than the other parameters. The residual errors on the turbulent velocity may in fact be related to degeneracies between the continuum and the line introduced by the fit, highlighted in Section 3.5.2.

Influence of statistics

In real observations, the influence of statistics cannot be neglected. Even for instruments such as the X-IFU, the observation of cluster outskirts will be predominately affected by the low count rates. The previous curves were recreated for typical 100 ks observations, and a 'deep' 1 Ms pointing. Results are summarised in Table 3.7. Statistics are largely dominant in the 100 ks observation case, with the systematic error often representing less than 10-20% of the total error on temperature or abundances, except when large systematic errors are considered ($\Delta_{\rm norm} = \pm 5\%$). This is no longer the case in the deep pointing, where

	$t_{\rm exp}$	100 ks				1 Ms			
	$\lvert\Delta_{\rm norm}\rvert$	0%	1%	2%	5%	0%	1%	2%	5%
T	$R_{\rm min}$ [†]	0.87	0.87	0.86	0.83	1.5	1.43	1.31	1.0
	$\Delta_{\rm S}$ [‡]	–	0.11	0.2	0.7	–	0.43	0.99	2.4
	$\Delta_{\rm T}$ [§]	–	0.12	0.27	0.57	–	0.41	0.67	0.93
Z	$R_{\rm min}$	0.5	0.5	0.49	0.45	1.10	1.09	1.07	0.72
	$\Delta_{\rm S}$	–	0.07	0.17	0.4	–	0.2	0.5	1.2
	$\Delta_{\rm T}$	–	0.07	0.15	0.4	–	0.2	0.45	0.8
$v_{\rm turb}$	$R_{\rm min}$	0.22	0.22	0.22	0.22	0.61	0.61	0.61	0.61
	$\Delta_{\rm S}$	–	0.0015	0.003	0.01	–	0.015	0.02	0.05
	$\Delta_{\rm T}$	–	0.0015	0.003	0.01	–	0.01	0.02	0.06

Table 3.7: Impact of an error in the relative knowledge of the NXB on the recovery of the temperature, T, abundance, Z, and the turbulent velocity, $v_{\rm turb}$ for realistic exposure times of 100ks and 1Ms. Contribution of statistics are included.

[†] $R_{\rm min}$ is the minimal radius at which the error on the parameter reaches the requirement in units of R_{500}.
[‡] $\Delta_{\rm S}$: ratio of the systematic to the statistical error. The maximum of $\sigma_{\rm sys}(R)$ is used for a given $\Delta_{\rm norm}$.
[§] $\Delta_{\rm T}$: ratio of the systematic to the total error, i.e. the systematic contribution to the total error budget.

systematic errors dominate for temperature and abundances as soon as $\Delta_{\rm norm} \geq 2\%$. In both cases, systematic errors can be neglected in the estimation of the turbulent speed.

Derivation of the requirement and discussion

The addition of statistics (Table 3.7) significantly degrades the capabilities of the instrument, and prevents an accurate measurement of the physical quantities at large radii ($\geq 0.8\,R_{500}$). This is especially the case for the turbulent speed, which is recovered only within $\sim 0.2\,R_{500}$. A few remarks need to be considered when interpreting these results. First, in this study, the observation of the outskirts was limited to spatial bins of half the detector FoV over 100 ks. Detailed investigations of outskirts will require much larger coverage and/or longer exposures. Furthermore, in spite of errors above the 4% requirements, temperature and abundances are already recovered at unprecedented levels through these observations ($\sim$ 10% above R_{200}). Finally, though measurements of line broadening are those most affected by statistics, we remind that the turbulent velocities will be preferentially investigated in central X-ray emission regions, where statistics are high. Turbulence measurements in the outskirts face other problems, including spatial mixing of turbulent scales due to large bins (see Section 4.1), and will require optimised observation strategies. The requirement on the reproducibility should therefore insist in minimizing systematic errors, even in low-statistics regimes. We derive two criteria for the reproducibility:

1. The level of systematic error induced by the NXB must be below the requirements at least up to a distance R_0 from the centre of the cluster. This ensures that for infinite statistics, the science objectives are always met.
2. Whenever statistics are the dominant term, the level of systematic error must be small compared to the statistical error ($5\sigma_{\rm sys} \leq \sigma_{\rm stat}$) at least up to $R = R_0$ from the

centre of the cluster. This ensures that the corresponding level of fitted NXB will be compatible, within statistical error bars, to the real value of the error.

R_0 is defined as the characteristic scale of the observation, where we request the instrument to be continuum-dominated. For the X-IFU, we chose $R_0 = R_{500}$ as stated in the afferent science case. The level verifying the previous criteria is $\Delta_{\mathrm{norm}} = \pm 2\%$ (Figure 3.15, Table 3.7). To satisfy the science objective, the requirement is set such that *the relative knowledge error of the NXB in the observation of clusters out to R_{500}, for an exposure of 100 ks over a solid angle of $9'^2$ shall be below 2% at 1σ*. When higher exposures are considered (typically 1 Ms), this requirement can be relaxed to 2.5%. The assumptions used in this study can nonetheless be discussed:

- Though identified as the limiting case for NXB reproducibility, the observation of clusters and cluster outskirts will be challenging for multiple other reasons (spatial mixing, systematic errors on the fits, extraction of CXB point-sources). Ideally, other toy models a should be investigated to draw a definitive conclusion.
- The choice of the characteristic spatial scale and the uniformity of the source over FoV can also be argued. Here the characteristic scale does not define the ultimate observable scale of the X-IFU, rather where the requirements apply. Beyond R_{500} it seems delicate to satisfy a 4% accuracy in temperature and abundances, nor does it seem justified for the overall instrument design. R_{500} is a compromise between accessible cluster volume and total observing time. As for uniformity of the annular sources over the FoV, no significant changes should arise in the previous results if other realistic models are used.
- The main assumption used in this study is the constant shape of the NXB. Though based on `GEANT4` numerical simulations, uncertainties related to the variability of this component and systematic errors in the models remain to be determined. In this regard, recent comparison of the in-flight NXB and `GEANT4` simulations in the case of the SXS showed a very good agreement ($\leq 10\%$), indicating that the `GEANT4` tool is representative of the background seen by X-ray missions. Additionally, multiple simulations performed for previous missions indicate that only minor changes in the overall normalisation of the NXB should be expected throughout the solar cycle (private discussion, S. Lotti), suggesting that the spectral shape shall indeed be flat.

We have derived here various results related to the reproducibility of the NXB in-flight. Under these assumptions, we found that a level of 2% is sufficient to comply, in general, with science requirements in the most driving case of galaxy cluster observation. To test the requirements in more accurate ways however, a simple approach is no longer sufficient. Model-dependent simulations using the E2E simulator SIXTE are needed.

3.7 Conclusions

Throughout this chapter, I have investigated several performance and science requirements related to the count rate, the line sensitivity and the particle background. These effects are challenging to measure through experiments, even more in the early phases of the X-IFU instrument. Numerical simulations, notably E2E simulations using SIXTE, are therefore a tool of choice for these investigations. The main results can be summarised as follows:

- Starting from experimental results, the simulator was improved, by adding more representative TES transition models, the capability to simulate background (cosmic and particle) and by improving the processing of crosstalk mechanisms.
- Using the E2E simulator, I have demonstrated that the X-IFU will be capable to observe bright extended sources (e.g. the Perseus cluster and the Cas A SNR) with a high-resolution throughput above 80% and with a degradation of the energy resolution due to crosstalk below 0.1 eV (FWHM RSS).
- Through a simple line fitting approach, I have demonstrated that the errors on the centroid and the broadening of line with low S/N ratios can be approximated by scaling laws, even for realistic line profiles (doublets of Voigt lines).
- Starting from the limiting case of outskirts of clusters, I derived the need to have a reproducible NXB level in-flight. For 100 ks observation, I have estimated that a 2% reproducibility (1σ) is required to achieve the *Athena* science objectives (under the assumptions made in the *Athena* science requirements document).

CHAPTER 4

Feasibility studies of the X-IFU using end-to-end simulations

The complexity of the high-resolution spatially resolved X-ray data collected by the X-IFU will be orders of magnitude above what current X-ray instruments can provide. A detailed analysis of its instrumental performances (Chapter 3) must therefore be completed with feasibility studies of the its core science objectives to understand the overall capabilities of the instrument. This is particularly true for observations of extended sources, which will use the full potential of the integral field unit. E2E simulations are once again a powerful option for these investigations. I present here three of these studies, related to the measurement of the chemical enrichment across cosmic time, the determination of enrichment mechanisms through abundance ratios and the estimation of errors on structure functions, which are key diagnostics to measure turbulence in the ICM. This chapter recalls the results published in Cucchetti et al. (2018f); Clerc et al. (2019); Cucchetti et al. (2019).

4.1 The study of the ICM enrichment through cosmic time

As recalled in Chapter 1, clusters of galaxies are the largest bound structures in the Universe, and the metallic content of the ICM represents a fossil record of the chemical enrichment across cosmic time. Though the enrichment is related to stellar processes (SN_e and AGB stars, see Werner et al. 2008; Nomoto et al. 2013 for reviews), the relative contributions and time scale of metal production mechanisms are still open questions.

The chemical enrichment of the Universe is one of the main science drivers for *Athena*, and more specifically for the X-IFU top-level instrumental performances, such as its energy scale or background. In this section, we analyse the capabilities of the X-IFU in measuring the metal content and physical parameters of the ICM (e.g. temperature, bulk motion).

4.1.1 Input cluster sample

The X-IFU is expected to provide new constraints on the processes governing the chemical enrichment of the Universe by observing the metal content of the ICM. Assessing the

Name		C1	C2	C3	C4
Type		CC	NCC	CC	NCC
$z = 0.105$	R_{500} (kpc h^{-1})	723	799	1027	1009
	M_{500} ($M_\odot$ h^{-1})	2.39×10^{14}	3.22×10^{14}	6.86×10^{14}	6.51×10^{14}
	T_{500} (keV)	3.22	4.20	6.47	6.36
$z = 0.5$	R_{500} (kpc h^{-1})	552	676	694	715
	M_{500} ($M_\odot$ h^{-1})	1.55×10^{14}	2.84×10^{14}	3.08×10^{14}	3.38×10^{14}
	T_{500} (keV)	2.88	4.06	4.58	4.84
$z = 1.0$	R_{500} (kpc h^{-1})	389	396	446	570
	M_{500} ($M_\odot$ h^{-1})	0.92×10^{14}	0.97×10^{14}	1.38×10^{14}	2.89×10^{14}
	T_{500} (keV)	2.41	2.47	3.12	4.41
$z = 1.48$	R_{500} (kpc h^{-1})	269	289	345	351
	M_{500} ($M_\odot$ h^{-1})	0.50×10^{14}	0.62×10^{14}	1.07×10^{14}	1.12×10^{14}
	T_{500} (keV)	1.76	2.10	3.07	3.08
$z = 2.0$	R_{500} (kpc h^{-1})	174	181	220	215
	M_{500} ($M_\odot$ h^{-1})	0.23×10^{14}	0.25×10^{14}	0.45×10^{14}	0.42×10^{14}
	T_{500} (keV)	1.19	1.55	2.24	1.86

Table 4.1: Properties of the simulated clusters at different redshift values in their evolution.

feasibility of this science objective requires, however, to model complex stellar mechanisms involving many atomic species over long periods of time. Simple toy models of galaxy clusters are unable to provide a representative picture for this study. Hydrodynamical simulations of galaxy clusters, implementing a wide range of physical mechanisms (see Biffi et al., 2018a, for a review) are instead promising candidates to conduct E2E simulations related to the evolution of galaxy clusters.

A total of four clusters, derived from Rasia et al. (2015); Biffi et al. (2018b), were used as inputs for this study. This sample includes two massive and two smaller systems (Table 4.1). Each mass bin contains one relaxed (CC) and one non-relaxed (NCC) cluster, defined according to their pseudo-entropy profiles, as described in Leccardi et al. (2010). This small set brackets the expected cluster population. The objects are part of a larger set of 29 Lagrangian regions extracted from a parent cosmological DM-only simulation and re-simulated at higher resolution including baryons (see Bonafede et al., 2011). The parent cosmological volume is 1 h^{-1} Gpc per side and adopts a Λ-CDM cosmological model with $\Omega_\mathrm{M} = 0.24$, $\Omega_\mathrm{b} = 0.04$, $H_0 = 72$ km s^{-1} Mpc^{-1} (i.e. $H_0 = h \times H_{100}$, where $h = 0.72$ and $H_{100} = 100$ km s^{-1} Mpc^{-1}), $\sigma_8 = 0.8$ and $n_s = 0.96$, consistent with WMAP-7 constraints given in Komatsu et al. (2011).

The magnification simulations were performed with the tree-PM smoothed particle hydrodynamics (SPH) code `GADGET-3` (Springel, 2005), including an improved hydrodynamical scheme (Beck et al., 2016) and various physical processes describing the evolution

of the baryonic component (see Rasia et al., 2015, for more details). These comprise metallicity-dependent radiative cooling (Wiersma et al., 2009), star formation and stellar feedback (thermal supernova feedback and galactic winds, see Springel & Hernquist 2003), cold and hot gas accretion onto the SMBH powering AGN thermal feedback (Steinborn et al., 2015; Gaspari & Sądowski, 2017). The metal enrichment is taken from Tornatore et al. (2004, 2007) for SN_{Ia}, SN_{cc}, and AGB stars. Specifically, the IMF by Chabrier (2003) is assumed, as well as the mass-dependent lifetimes by Padovani & Matteucci (1993) and stellar yields by Thielemann et al. (2003) for SN_{Ia}, by Woosley & Weaver (1995) and by Romano et al. (2010) for SN_{cc}, and by Karakas (2010) for AGB stars.

The model of chemical enrichment follows the production and evolution of 15 chemical species: H, He, C, Ca, O, N, Ne, Mg, S, Si, Fe, Na, Al, Ar, and Ni. Other elements are present, but regrouped under a residual metallic content, neglected here. Although these elements do not cover the full spectrum of interest (lacking e.g. Mn or Cr, which are important tracers of the enrichment, Hitomi Collaboration 2017; Simionescu et al. 2019a), this variety of abundances provides a good starting point for this study. Every gas particle traces the chemical composition and the fraction of each metal produced by the three enrichment sources (i.e. SN_{Ia}, SN_{cc}, AGB). Each object is analysed at $z = 0.105$, 0.5, 1, 1.48, and 2, to assess the enrichment through time. Table 4.1 provides the characteristic radii, R_{500}, masses, M_{500}, and mass-weighted temperatures, T_{500}, of the sample.

For each SPH particle, the output quantities provided by `GADGET-3` include the position of the particle, $\underline{\boldsymbol{x}}$, its 3D velocity in the observer's frame, $\underline{\boldsymbol{v}}$, its mass density, ρ, its mass, m, its temperature, T, and the individual masses and mass densities of the 15 individual chemical species X, μ_X, tracked in the simulations. The gas density n of each SPH particle is obtained by dividing ρ by m. The mass of each element of atomic mass number A_X is converted into abundances Z_X, expressed in solar metallicity units assuming the solar fractions $Z_{\odot,X}$ from Anders & Grevesse (1989):

$$Z_X = \frac{1}{Z_{\odot,X}} \times \frac{\mu_X}{\mu_H \times A_X} \tag{4.1}$$

4.1.2 Simulation set-up

These E2E simulations are performed using `xifupipeline` and XSPEC (Arnaud, 1996) version 12.9.1p, with the corresponding `ATOMDB v3.0.9.` version. Abundances refer to Anders & Grevesse (1989), with atomic cross-sections by Verner et al. (1996) tables. The X-IFU is modelled using the 2017 response files (`athena_xifu_rmf_v20171107.rmf` for the RMF and `athena_xifu_15row_onaxis_pitch249um_v20171107.arf` for the ARF).

Photon generation

For each cluster, the data set comes a list of $\geq 10^4$ SPH emitting particles with different parameters. As discussed in Chapter 3, for the photon generation, we chose here not to use a full SIMPUT associated with the particles to avoid handling large files. Instead, we generate the photons independently, which allows the parallelisation of this operation over the entire SPH table, thereby reducing the total computational time.

We assume that each particle has an isotropic emission spectrum, described by a collisionally-ionized diffuse plasma model derived from the `APEC` plasma code (Smith et al.,

2001). More specifically, to use all the different phyiscal properties listed above, we select the `vvapec` model, which provides individual characterisation of the all previous abundances. To describe the galactic absorption, we select the `wabs` model on XSPEC (Morrison & McCammon, 1983) for computational reasons, although more accurate (but slower) models exist, such as the `tbabs` model (Wilms et al., 2000). For all four clusters, regardless of redshift, the column density of galactic hydrogen is set to $n_H = 0.03 \times 10^{22}\,\mathrm{cm}^{-2}$, which is a typical value for a high galactic latitude (Kalberla et al., 2005).

The flux of the `vvapec` spectrum, F_i (in cts/s/cm^2), for a particle i is computed using the `apec` normalisation $\mathcal{N}_i$ (emission-measure weighted by the distance, in cm^{-5}):

$$\mathcal{N}_i = \frac{10^{-14}}{4\pi[D_A(1+z_i)]^2} \int_{V_i} n_{e,i} n_{H,i} dV \tag{4.2}$$

where D_A is the angular distance of the cluster, computed at the redshift z_0 of the simulation assuming the cosmology from Section 4.1.1, and z_i the redshift of particle. z_i is obtained using the speed $\underline{v}$ of the particle along the line of sight $\underline{e}_{\mathrm{los}}$ such that

$$z_{\mathrm{los},i} = \sqrt{\frac{1 + \frac{\underline{v}\cdot\underline{e}_{\mathrm{los}}}{c}}{1 - \frac{\underline{v}\cdot\underline{e}_{\mathrm{los}}}{c}}} \tag{4.3}$$

and $z_i = z_0 + z_{\mathrm{los},i} + z_{\mathrm{los},i}$. We assume a fully ionised plasma with $n_e = 1.2\,n_H$, where n_e, n_H are the densities of electrons and protons respectively. Finally, since the gas density is considered constant within the particle, the integration over its volume can be replaced by a simple multiplication.

The emission spectrum of each particle (or cell) is multiplied by the ARF and used as a probability distribution function, normalised over the instrumental energy bandpass (0.2 – 12 keV). For a fixed exposure time Δt, the number of photons emitted for a given particle is drawn from the afferent Poisson probability distribution of λ-parameter $F_i \Delta t A$, with A the total mirror area, while the corresponding energy is selected using the `vvapec` probability distribution. The generation of the emission spectrum and subsequent sampling is parallelised over ≥ 40 central processing units (CPUs) to increase the simulation speed.

In the hydrodynamical simulations, the smoothing length of the SPH particles is sufficiently small to neglect its effect compared to the PSF HEW of the *Athena* telescope (Roncarelli et al., 2012). Furthermore, the apparent size of each SPH particle ($\leq 1''$) is small with respect to an X-IFU pixel ($\sim 4.2''$). Hence, each generated photon can be associated with the spatial coordinates of its progenitor cell (right ascension and declination).

The output of this stage is gathered into a `FITS` file (photon list) containing the energy, right ascension and declination of each photon from the different gas particles as seen at the entrance of the telescope. This list is computed once for each cluster, and contains a large number of simulated photons (equivalent to a large exposure of$\geq$ 1 Ms) to avoid sampling effects. It is then sampled randomly to achieve smaller lists for typical exposures (e.g. 100 ks).

Observational set-up

For our simulations, we consider a fixed exposure time for each pointing of $\Delta t = 100$ ks over the FoV. The 2017 version of the detector array was used. It is made of 3832 LPA2 pixels,

as described in Smith et al. (2016). The previous photon list is used in `xifupipeline` to simulate the events including all the geometry effects presented in Chapter 3. To further increase computational speed, the photon list is divided into N sub-lists corresponding to the number of CPUs available. The sub-event files are then merged into a single event file. This approach prevents a realistic application of crosstalk in the simulations, however given the count rates observed here (≤ 0.1 cts/s/pix in the centre of the cluster), crosstalk can be safely neglected (see Section 3.4).

For each cluster, we simulate enough pointings to map the cluster spatially out to R_{500}, as required in the current X-IFU science objectives. This translates into seven pointings at $z = 0.105$. The event lists are merged during post-processing to obtain a single event file. Two simple sanity checks were performed to validate the photon generation process. First, we considered a single point source (e.g. a single SPH particle) observed with a high exposure time (≥ 1 Ms) to search for potential systematic errors. No specific bias was found in the reconstructed and fitted spectrum. A second test was conducted using a uniform source covering the entire FoV. In this case, after geometrical effects were accounted for (i.e. vignetting) all the parameters were also accurately recovered.

Background models

In addition to instrumental effects, we include three different foreground and background sources to ensure more realistic observations, notably of weak lines (e.g. Ne, Al):

- **An astrophysical foreground**, assumed uniform over the FoV and parametrised as per Table 3.6. An additional normalisation constant is used for versatility purposes. The total foreground model reads as `constant*(apec + phabs*apec)` in XSPEC. This component is folded into SIXTE using a SIMPUT file.
- **An instrumental particle background**, caused by interactions of high-energy cosmic rays with the instrument, and generated within SIXTE. It is modelled at the required level of 5×10^{-3} cts/s/keV/cm^2 over the entire bandpass (see Section 3.6.2).
- **A cosmic X-ray background** (CXB), due to AGNs, star forming galaxies and active stars along the line-of-sight. Given the expected spatial resolution of the X-IFU, 80% of the integrated log(N)/log(S) flux distribution of these sources should be resolved (Moretti et al., 2003). For 100 ks exposure times, this translates into fluxes above $\sim 3 \times 10^{-16}$ ergs/s/cm^2 (over 0.2 – 12 keV), using the log(N)/log(S) distribution from Lehmer et al. (2012). As the flux of star forming galaxies and active stars is an order of magnitude lower than this threshold, only the AGN contribution is considered here. To generate realistic CXB data, we draw a list of AGN sources and their corresponding X-ray spectra by sampling the luminosity function of Hasinger et al. (2005) in the luminosity-redshift space, given the boundary conditions $L_X \geq 10^{42}$ erg/s unabsorbed 0.5 – 2 keV rest-frame luminosity, $0 < z < 5$ and the size of the cosmological volume encompassed within a FoV. Each source is associated with a spectral energy distribution consistent with Gilli et al. (2007), according to a distribution of power law indices and intrinsic absorption column densities related to various levels of obscuration (see Gilli et al., 1999, 2007). Spatial distributions are fully random in the sky plane (no clustering). Further details about the procedure can be found in Clerc et al. (2018). This component is included using a SIMPUT file

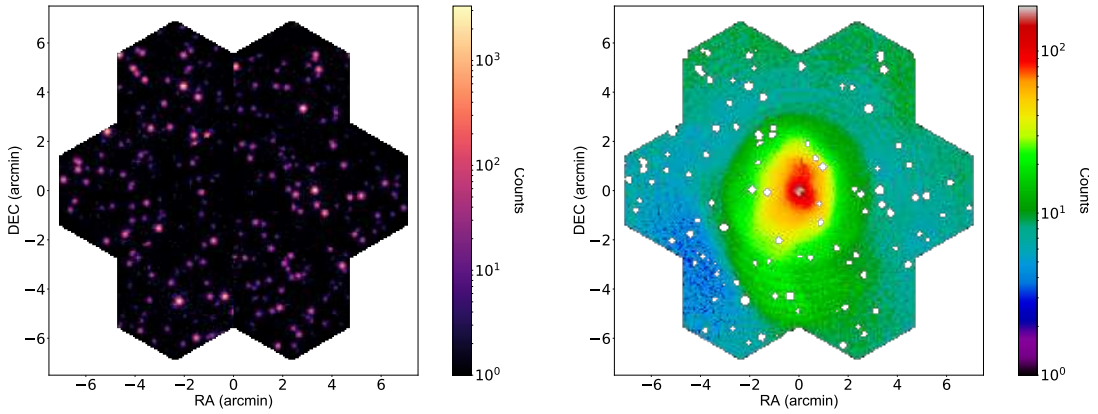

Figure 4.1: (*Left*) Example of seven 100 ks X-IFU pointings including exclusively the AGNs selected using the method from Clerc et al. (2018). The result is a CXB map, added here to the C2 simulation. (*Right*) Example of a continuum-subtracted count map for cluster C2 used for spatial binning. Each of the $\sim$ 27 000 pixels was rescaled as explained in Section 4.1.3 to enhance density contrasts in the cluster.

(see Figure 4.1 - *Left*). The resolved sources visible in the pointing can be excised, whereas the unresolved fraction, resulting in a diffuse component, is fitted with an absorbed power law (McCammon et al., 2002).

A specific flag is given to each background photon. They can thus be respectively masked to study background effects on the observations, or selected to generate background maps. Throughout this study, we assume that these background components have no systematic uncertainty. Systematic effects of the background knowledge on the observations are discussed in Section 4.1.3 and are also considered in Cucchetti et al. (2018e).

4.1.3 Data processing and pipeline validation

Point sources excision and binning

In the event list output file, we perform a selection based on the grading of the events. Only high-resolution events corresponding to $\Delta E = 2.5\,\mathrm{eV}$ are used. As the count rates of the clusters are low, no significant loss of throughput is observed ($\leq 1\%$). Using the selected events, we reconstruct raw brightness maps in counts as presented in Figure 4.2.

Beside the ICM, emission from other sources either present in the hydrodynamical simulations (i.e. strongly-emitting particles or clumps) or in the CXB can be observed. These sources need to be removed before any spectral interpretation. For this process, we use the *a priori* knowledge of the sources generated for the CXB. We start by simulating all sources with fluxes above $\sim 3 \times 10^{-16}\,\mathrm{ergs/s/cm^2}$ to find their exact coordinates on the detector with PSF effects. Then, these sources are excised automatically by finding all the corresponding pixels above a 2σ threshold in counts with respect to the average counts in neighbouring pixels (to account for the diffuse emission of the cluster). Although this process would not be possible for real event files, we adopt this strategy to avoid biases

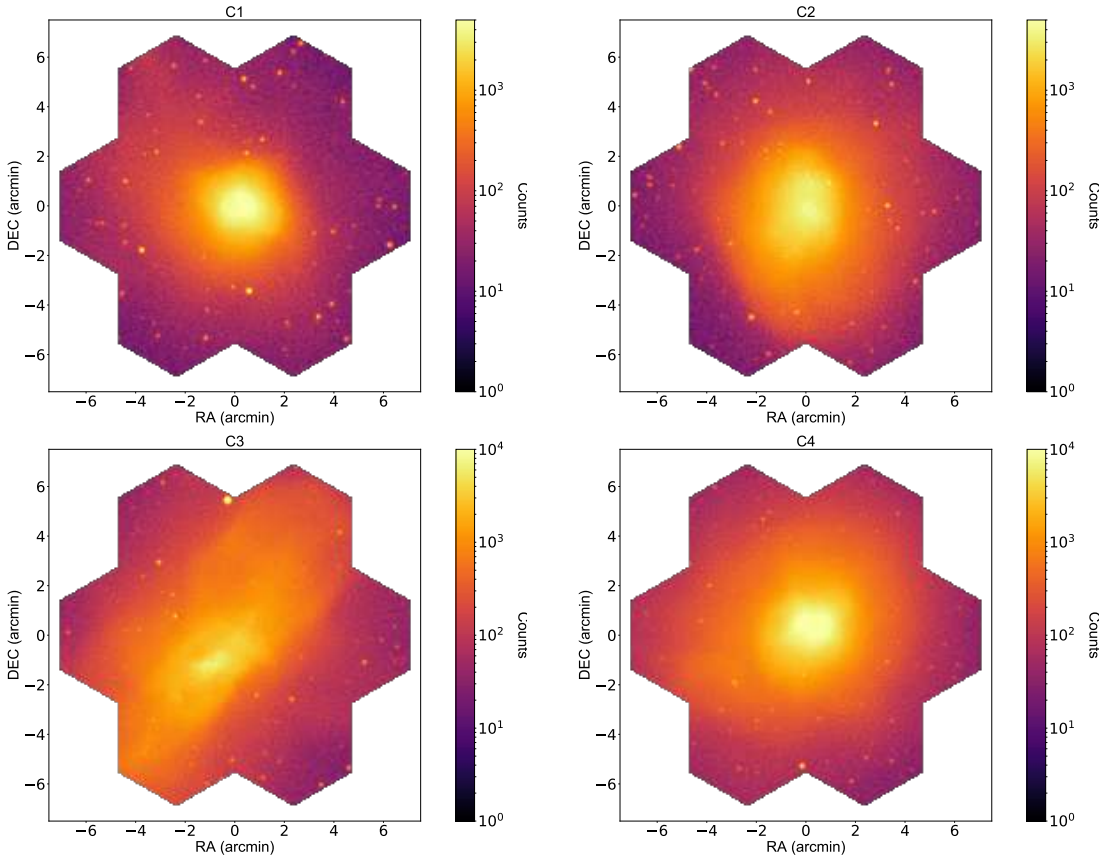

Figure 4.2: Maps in number of counts per X-IFU pixel for clusters 1 to 4 (see Table 4.1) at redshift $z = 0.105$. Each mosaic is made of seven X-IFU pointings of 100 ks each.

related to point-source detection algorithms. Once these sources are removed, a final visual inspection is performed to remove residual AGNs or remaining visible point-like source related to the hydrodynamical simulations.

Count rate maps are binned spatially to increase the S/N ratio of the spectral lines using the `contbin` tool (Sanders, 2006). An alternative method using a 2D Voronoï tessellation (Cappellari & Copin, 2003) was also investigated but not retained (see Sanders 2006 or Cucchetti et al. 2018f for a detailed comparison). The aspect-ratio of the binned regions is requested to be lower than two, to avoid artificially-created filamentary regions, which could mix spatially-uncorrelated structures (especially in low count rates areas, e.g. outskirts).

This binning procedure operates on the full count maps, dominated by the ICM Bremsstrahlung emission. As we aim to measure chemical abundances through X-ray emission lines, we further optimised our binning to account for local surface brightness variations atop the bulk of the cluster emission. To do so, we divided the count maps into annuli centred on the brightest part of the cluster and containing roughly the same number of events ($\sim 300\,000$). The spectrum of each annulus is fitted over the entire bandpass (0.2 – 12 keV) with a continuum-only `vvapec` model (abundances set to zero) to estimate the number of counts in the continuum $C_{\rm cont}$. Although slightly overestimating the con-

tinuum counts, this approach converges quickly. A more accurate solution is to perform fits by leaving abundances as free parameters first, then setting abundances to zero after convergence. In this case however, the algorithms converge on local minima or not at all, as strong lines in the spectrum can be separated by more than an energy resolution bin (due to bulk motions). Even after convergence, differences between both methods do not exceed $\leq 3\%$. The number of counts on a pixel i, C_i, in the annulus is then rescaled by:

$$\overline{C_i} = \left(1 - \frac{C_{\rm cont}}{C_{\rm total}}\right) \times C_i \tag{4.4}$$

The resulting template image for cluster C2 can be seen in Figure 4.1 (*Right*) and is used exclusively for spatial binning. This approach defines regions over a continuum subtracted image, enhancing the brightness fluctuations with respect to the azimuthal continuum model due to the emission of atomic lines. Accounting for statistics, we request a S/N ratio of 30 (900 counts in regions). Given a count ratio of ~ 100 between the template map and the full surface brightness map, we ensure that each spectrum has a S/N ratio of ~ 300. This represents a total of at least 90 000 counts per region, i.e. an average of three counts in each instrumental channel. The resulting spatial regions are used over the full count maps to compute the corresponding spectra.

This binning approach is used in the case of local clusters ($z \leq 0.5$). For high-redshift clusters, count rates are insufficient to ensure statistically independent regions with a high-enough S/N ratio. In this case, we followed the formulation of the *Athena* science objectives and considered two radial annular regions, $0 - 0.3\,R_{500}$ and $0.3 - 1\,R_{500}$.

Fitting procedure and input maps

The unbinned spectra for each region are post-processed with XSPEC using C-statistics. Spectra are fitted to an absorbed single-temperature thermal plasma model including a velocity broadening component of the lines to account for variability and mixing along the line-of-sight (i.e. `wabs*bvvapec`). The column density n_H is fixed to its input value, while temperature, abundances of metals traced in the input numerical simulations, redshift and normalisation are fitted. The background components are accounted as an additional model. Their spectral shapes is assumed to be perfectly known, whilst the normalisation of each component is set free (either the model norm for the CXB and instrumental background, or the multiplicative constant factor for the foreground, see Section 4.1.2). Vignetting effects are included by creating a specific ARF for each binned region. To do so, the response of each pixel is multiplied over the energy bandpass by the vignetting function implemented in SIXTE. The new ARF is obtained by averaging, in each energy channel, the response of each pixel weighted by their respective number of counts.

As an initial fitting strategy, we attempted a 'naive' approach and fitted all parameters simultaneously over the $0.2 - 12$ keV energy band (broadband fit). To estimate the goodness of the fit, the outputs are compared to input maps, projected along the line-of-sight. These maps are constructed from the hydrodynamical simulation tables using the same spatial binning regions, j, than the outputs. Since the parameter distribution along the line-of-sight cannot be perfectly integrated (we measure a discrete number of counts, affected by statistics and background), the parameters need to be weighted to match the

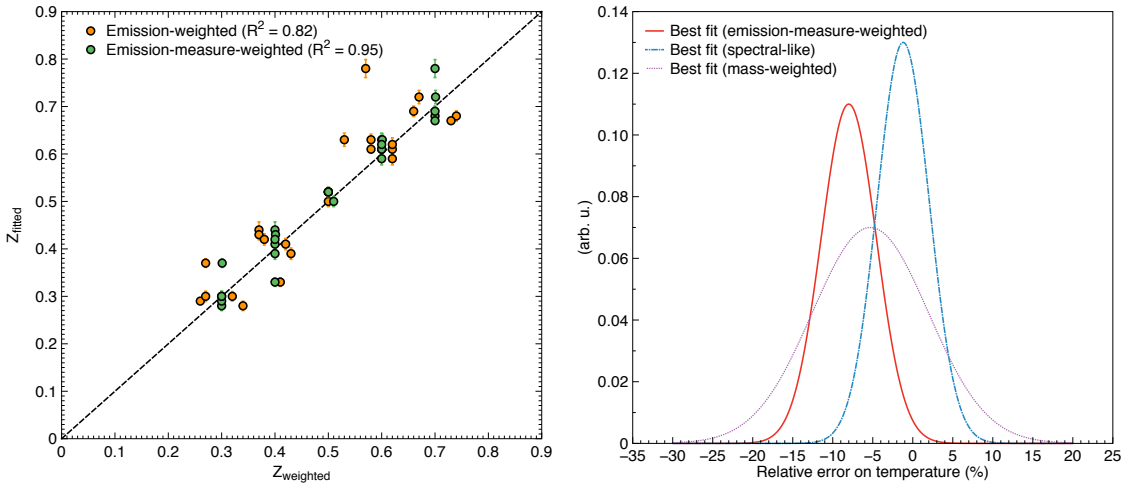

Figure 4.3: (*Left*) Test-case of a two-temperature, two-abundance `apec` model on XSPEC. Fitted abundance as a function of the weighted abundance for EW (orange) and EMW (green) schemes. The R^2 values of the linear fit are given. (*Right*) Gaussian best fits of the normalised relative error distribution of the temperature of cluster C4 for EW (red solid - $\mu_{\Delta T} = -8.0\%$, $\sigma_{\Delta T} = 3.4\%$), spectroscopic (blue dash-dotted - $\mu_{\Delta T} = -1.2\%$, $\sigma_{\Delta T} = 2.2\%$) and MW (violet dotted - $\mu_{\Delta T} = -5.2\%$, $\sigma_{\Delta T} = 7.2\%$) schemes.

measurements. For a parameter P in the region j, the weighted input reads

$$P_j = \frac{\Sigma_i P_i \mathcal{W}_i}{\Sigma_i \mathcal{W}_i} \tag{4.5}$$

where the sum includes each SPH particle i contributing to the spatial region j, and $\mathcal{W}$ is the weighting coefficient. The weighting scheme depends on the considered parameters. Multiple schemes exist to compare inputs and outputs depending on the physical quantity under investigation. Among those most widely used in the literature we find:

- Emission-weighted (EW) projection, $\mathcal{W}_i = \rho_i^2 \sqrt{T_i}$.
- Emission-measure-weighted (EMW) projection, $\mathcal{W}_i = \mathcal{N}_i \propto \rho_i^2$.
- Mass-weighted (MW) projection, $\mathcal{W}_i = m_i$.

EMW or EW schemes are expected to be more representative than MW schemes for abundances (Biffi et al., 2013). To test which of these two schemes is most suited, we performed a simple test case: we generated through XSPEC two `apec` spectra of temperatures T_1, T_2 and abundances Z_1, Z_2, and compared the fitted result using a single-temperature model with the weighted value for both schemes. As shown in Figure 4.3 (*Left*), the EMW scheme seems here more accurate than the EW scheme for various choices of T_1, T_2 and Z_1, Z_2, and was thus retained as baseline to compare output abundances to their inputs.

For temperatures, the previous schemes do not match fitted quantities very accurately, as shown by the biases in the relative error distribution of the temperatures in Figure 4.3 (*Right*). This discrepancy, demonstrated throughout the literature (Gardini et al., 2004; Rasia et al., 2006, 2008) can be related to mixing effects along the line-of-sight and complexities to disentangle multi-temperature plasma with a single plasma model. A solution is to

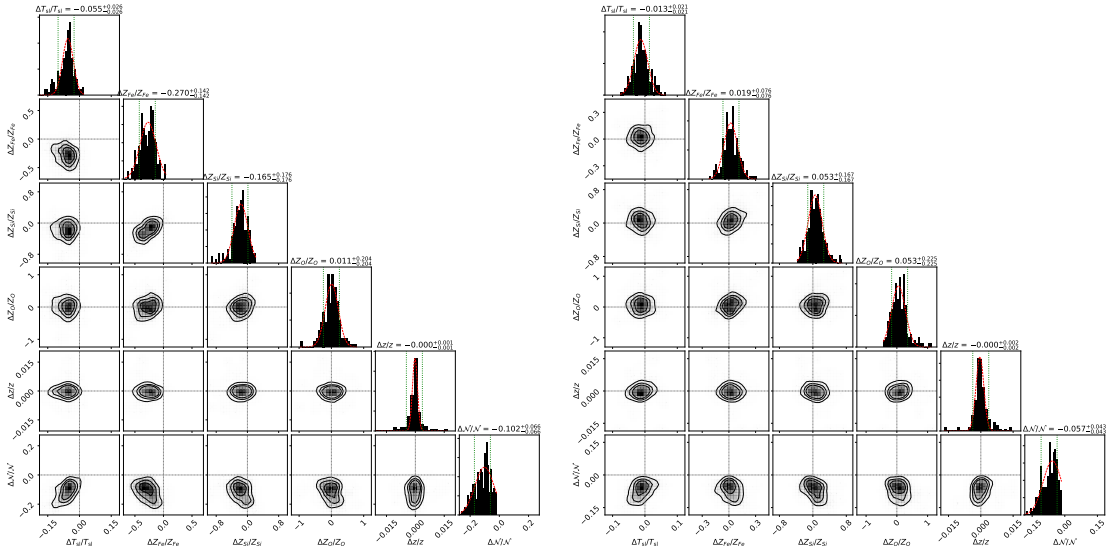

Figure 4.4: Corner plots of the relative error on parameter X, $(X_{fit} - X_{inp})/X_{inp} = \Delta X/X_{inp}$ as a function of the error on parameter Y, $(Y_{fit} - Y_{inp})/Y_{inp} = \Delta Y/Y_{inp}$, for a broadband (*Top*) and multi-band (*Bottom*) fit of cluster C4. $T_{\rm sl}$, $Z_{\rm O}$, $Z_{\rm Si}$, $Z_{\rm Fe}$ z, and the normalisation $\mathcal{N}$ are shown. The diagonal panels are the relative error distributions. The red solid line indicates the Gaussian best fit and the dotted line is the value of $\mu_{\Delta P} \pm \mu_{\rm fit}$.

correct the temperature maps using the 'spectroscopic' temperature weighting, introduced by Mazzotta et al. (2004), where $\mathcal{W}_i = \mathcal{N}_i\, T_i^{-0.75}$. This translates here into

$$T_j = \frac{\Sigma_i\, \mathcal{N}_i\, T_i^{+0.25}}{\Sigma_i\, \mathcal{N}_i\, T_i^{-0.75}} \tag{4.6}$$

This method is particularly suited to high-temperature regions (≥ 3 keV), well represented in the central parts of our clusters (see Figure 4.5 – *Upper central panel*), but may be limited towards the outskirts or for cooler systems. A more elaborate technique to account for low-temperature regions exists (Vikhlinin et al., 2006), however, since our outer regions are large (small number of counts per pixel) and results remain within statistical error bars of the XSPEC fit, spectroscopic temperature weighting is maintained for simplicity.

The use of the simultaneous broadband fit induces visible biases in the fitted parameters ($\sim 10\%$), notably between abundances (O, Si, and Fe) and temperature (Figure 4.4 – *Left*). These values underline degeneracies in the fitting procedure itself. For our data analysis, we moved to a multi-band fit of the spectrum instead (inspired by Rasia et al., 2008):

I. As a first step, since the cluster sample is relatively hot (≥ 4 keV in the centre) the temperature is recovered from the high-energy band (3.5 – 12 keV), then fixed.

II. Iron metallicity, $Z_{\rm Fe}$, is recovered by a subsequent broadband fit (i.e. 0.2 – 12 keV) to estimate the contribution from both the K and the L complex, then fixed.

III. Metallicities of other elements are computed by fitting specific energy bands (for redshift $z \leq 0.1$):

i. Abundances for C, N, O, Ne and Na are fitted over the 0.2 - 1.2 keV bandpass.
ii. Abundances for Mg, Si, Ar and Ca are fitted over the 1.2 – 3.5 keV bandpass.
iii. Abundance of Ni is finally fitted over the 3.5 – 12 keV bandpass.

IV. With all other parameters fixed, redshift, velocity broadening and normalisation are recovered with a broadband fit.

This strategy significantly reduces these biases (Figure 4.4 – *Right*) within the statistical variations of the parameters. Only small correlations remain between abundances and temperature, and between the normalisation and the other parameters. An exploration of the χ^2 parameter space with a Monte Carlo (MC) approach was tested on several ill-fitted regions in an attempt to improve the fit. The accuracy of the fit in these cases in only marginally improved (χ^2 is reduced by $\leq 5\%$), but requires longer fitting times for each spectrum, thereby lengthening the simulations of an order of magnitude (one fit takes a few hours without MC, up to a day using a MC approach). This test was performed on various regions of different clusters showing minor changes, the multi-band approach retained.

This technique is used under the caveat that despite fitted parameters are fixed, errors are propagated correctly throughout the fit. Although not perfectly true, this effect remains limited with respect to our level of statistics, ensuring a safe application of this method.

Validation and assessment of overall systematic errors

The accuracy of the reconstructed parameter P is evaluated using three different tests. Each region being much larger than the telescope PSF, they are considered spatially independent on a strict statistical term. For simplicity, we limit this investigation to the four local clusters, and assume that high-redshift cluster will show no additional bias. Using as baseline for comparison the EMW input and the output distributions obtained with the multi-band fit, let us take as null hypothesis to confirm or reject, with a threshold $p_\alpha = 5\%$ (i.e. 97.5% of the Gaussian distribution, or $2.5\,\sigma$):

- (H_0): "The measurements obtained with the pipeline are consistent with the statistical errors for a given exposure time"
- (H_1): "The measurements are not biased"

As a first test, we investigate the relative error distribution of the fitted parameter P with respect to the weighted input value, i.e. we compute the distribution of

$$\Delta P_j = \frac{P_j - P_{\mathrm{in},j}}{P_{\mathrm{in},j}} \tag{4.7}$$

over the regions j. If no systematic effect is present in the pipeline, the relative error distribution for P should follow a Gaussian distribution (given the high number of regions ≥ 80), with a mean $\mu_{\Delta P} = 0$ (if no biases are present) and a standard deviation $\sigma_{\Delta P}$ The fitting error returned by XSPEC should also be Gaussian, and centred on μ_{fit} which depends on the exposure time and the emission model parameters. For an accurate measurement, μ_{fit} should be comparable to $\sigma_{\Delta P}$. For some parameters – e.g, rare metals such as Na or Al – fits are in some regions ($\lesssim 5$) inaccurate with very large error bars, causing relative errors above 100%. To avoid biases in the Gaussian fits, these outliers are not considered.

	$\mu_{\Delta P}$ (%)	$\sigma_{\Delta P}$ (%)	$\mu_{\rm fit}$ (%)	$\chi^2_{\rm red}$	$\tilde{\chi}^2_{\rm red}$	$N_{\rm bad}$
$T_{\rm sl}$	-0.71	2.60	1.64	3.93	1.38	4
z	0.00	0.04	0.05	1.54	1.09	3
O	4.23	16.0	13.4	1.50	1.50	2
Mg	5.22	20.7	18.4	2.84	1.01	1
Si	3.22	11.4	10.6	1.78	1.37	3
S	4.48	16.3	14.6	1.52	1.41	1
Ca	-1.42	8.27	8.62	2.69	1.06	3
Fe	0.94	5.73	5.22	2.71	1.49	2
Ni	0.39	25.3	26.6	0.99	0.92	1
$\mathcal{N}$	-6.5	3.68	3.74	4.11	2.83	7

Table 4.2: Values of $\mu_{\Delta P}$ and $\sigma_{\Delta P}$ of the best fit of the relative error distributions for the main physical parameters in cluster C2, over 80 spatial regions, with the average XSPEC error of the fits $\mu_{\rm fit}$. The corresponding values of $\chi^2_{\rm red}$ and the corrected $\tilde{\chi}^2_{\rm red}$ are also given, along with the number of outliers regions $N_{\rm bad}$ removed to compute $\tilde{\chi}^2_{\rm red}$.

The results from these tests can be seen in Figure 4.5 (*Right panels*) for cluster C2, and the corresponding values of the Gaussian distributions are reminded in Table 4.2. In all cases, the mean fit error is consistent with the standard deviation of the error distribution $\sigma_{\Delta P}$, thus excluding large systematic effects. Small biases of the order of a few percent ($\lesssim 5\%$) are however still visible. This is particularly true for the normalisation (similarly to what was found in Roncarelli et al., 2018) and the abundances of low mass elements (e.g. O, Si), in which an underestimation of the normalisation directly results in an overestimation of abundances (see also Figure 4.4). All these systematic errors are however well inside the statistical deviations at $\pm 3\sigma_{\Delta P}$ indicating that results are consistent with (H_0). The average values show instead a good agreement with (H_1).

A second test can be performed using as estimator the ratio between the relative difference and the XSPEC error $\sigma_{\rm fit}$ for each region, i.e.

$$\chi_j = \frac{P_j - P_{{\rm in},j}}{\sigma_{{\rm fit},j}} \tag{4.8}$$

which shows the goodness of the fits. By computing the reduced chi-squared, $\chi^2_{\rm red}$, we can estimate the overall accuracy of the fit with respect to the XSPEC errors. As shown in Table 4.2, some of the $\chi^2_{\rm red}$ are not well recovered, especially for the normalisation. This can be partially explained by outlier regions in the fit, which affect this computation. When $N_{\rm bad}$ outliers regions ($\chi_j \geq 5\sigma_{\rm fit,j}$) are removed, the new reduced chi-squared, $\tilde{\chi}^2_{\rm red}$, shows more consistency, indicating a good agreement between the fitted maps and the input distributions. Furthermore, as shown in Figure 4.5 (*Central panels*), χ distributions generally remain below 2.5, in agreement with (H_0). Only the normalisation shows a consistent deviation, as also found in Roncarelli et al. (2018). This error is likely related to the fitting process and degeneracies with the background components (see below).

The previous tests are valid when the error distributions are Gaussian, which may not strictly be the case. The accuracy of our method was thus tested in the sense of the

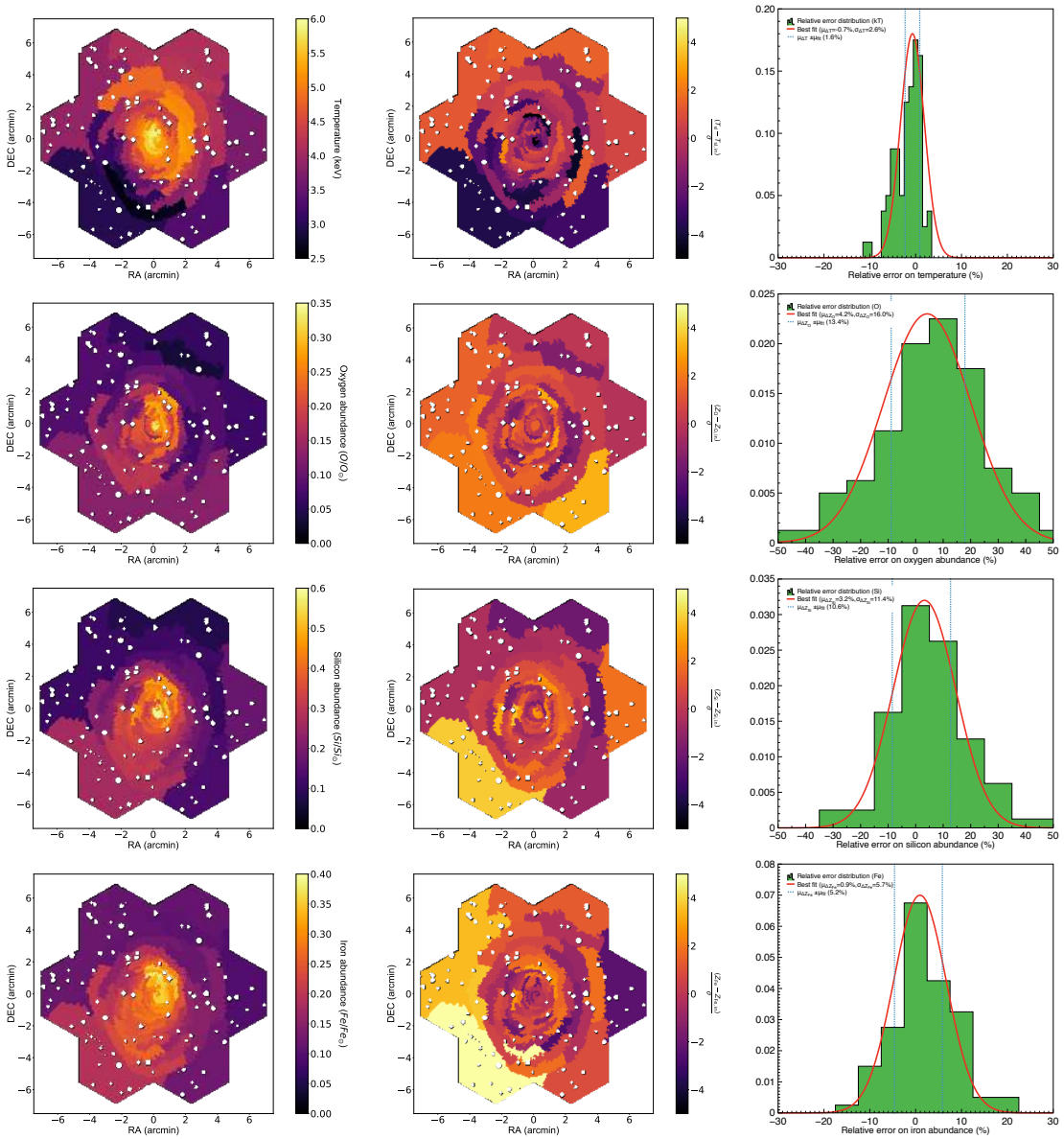

Figure 4.5: *(Left)* Reconstructed ICM parameters maps for C2 at $z \sim 0.105$. *(Middle)* Distribution of χ_j indicating the goodness of the fit in terms of the XSPEC error σ_j for each region j. *(Right)* Relative error distribution across all spectral regions (green histogram). The red solid line indicates the Gaussian best fit. The vertical blue dashed lines are the mean value of the fit errors. *(From top to bottom)* spectroscopic temperature $T_{\rm sl}$ (in keV), EWM abundances of oxygen (O), silicon (Si) and iron (Fe).

distributions, performing a simplified Kolmogorov-Smirnov (KS) test over the output and input distributions. The KS test compares the probability p_{KS} for two random variables to be drawn from the same probability density. Using both the input and output distribution, this test showed p_{KS} values between 0.6 and 1. Statistically speaking, no real conclusion

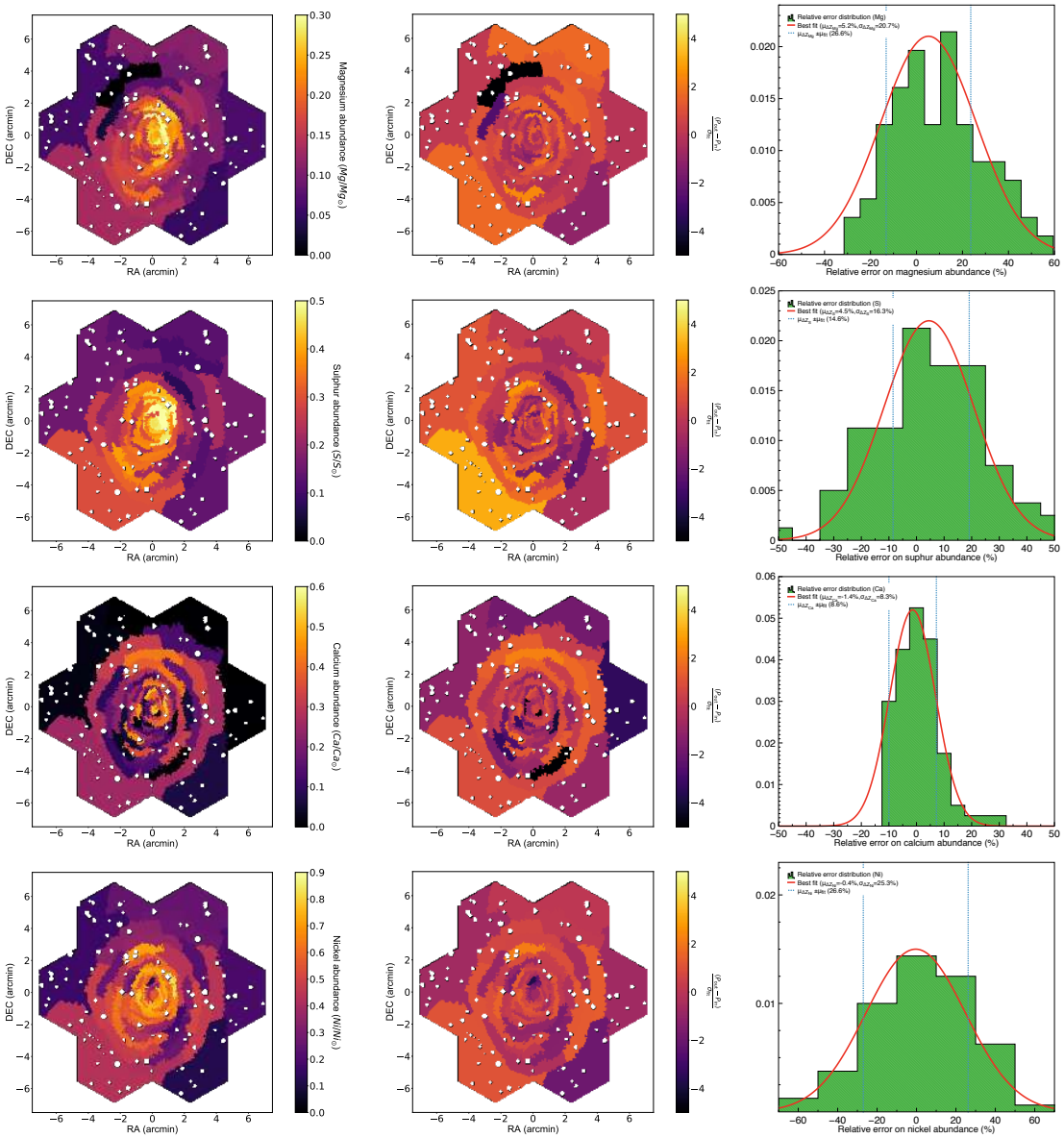

Figure 4.6: Same as Figure 4.5 *(From top to bottom)* EMW abundances of magnesium (Mg), sulphur (S), calcium (Ca), and nickel (Ni).

can be achieved with a single realization. A large number of observations of the same cluster is needed for a meaningful comparison using a KS method. Unfortunately, the duration of one full simulation of the order of a day, making it computationally cumbersome to carry out this test. For simplicity, a higher exposure observation was performed instead (≥ 1 Ms). Using the same binning regions as the 100 ks case. Most of the remaining biases decrease below 2% and create distributions which much more alike ($p_{KS} \sim 0.8/1$), suggesting that the residual errors are essentially related to statistics.

Overall, the previous tests show the robustness of the pipeline. Although small sys-

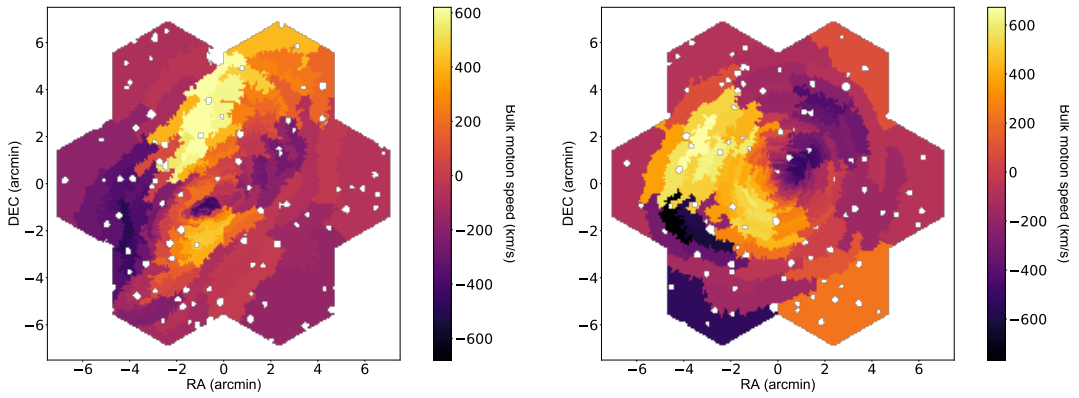

Figure 4.7: Reconstructed bulk motion velocity maps (in km/s) for cluster C3 (*Left*) and C4 (*Right*). Velocities are normalised with respect to the average redshift of the cluster.

tematic errors remain, both null hypothesis (H_0) and (H_1) cannot be rejected based on these studies. The remaining systematic effects seen here can be attributed to other features, such as degeneracy between fitted parameters ($\geq$ 15 here) or the spatial binning, which regroups in a large region (a few arcmin^2 in the outskirts) different physical structures. The choice of a single temperature model could also introduce some biases. Two- or multi-temperature models were investigated over single regions but showed no significant improvement over the entire observation mosaic.

The effect of background

Background causes additional uncertainties in the parameter estimation. To investigate these effects we performed two different tests. First, using the flags on the event list, we generated and fitted spectra without any background component. In this case, the biases listed in Table 4.2 are reduced, notably for $\mathcal{N}$, due to smaller degeneracies between the normalisation of the background spectra and that of the particle emission.

A second comparison was performed by generating and fitting spectra with all background components fixed to their input values, with and without leaving normalisations as free parameters. In both cases, the background increased the statistical errors of $\sim 5\%$ for the main parameters (e.g. T, $Z_{\rm O}$, $Z_{\rm Si}$ or $Z_{\rm Fe}$) and up to 15% for other abundances (e.g. $Z_{\rm Ni}$ or $Z_{\rm Ca}$) with respect to the first test. Fixing the normalisation also introduced additional biases in the recovery of abundances, which disappeared when the normalisations were thawed. This effect is likely related to degeneracies between the various normalisations, which stiffen the algorithm descent when fixed, and cause convergence on local minima. Background normalisations are therefore left free in the multi-band fit.

4.1.4 Physical parameters of the cluster sample

Physical parameters

Under the previous fitting assumption, we can recover for each of the four clusters the spatial maps of the ICM physical parameters. Examples of these maps is provided in

Figure 4.5 (*Left panels*) for the cluster C2 at $z = 0.105$. The maps are shown for the spectroscopic temperature $T_{\rm sl}$ and the abundances of Fe, Si, and O. Those for Mg, S, Ca, and Ni are shown in Figure 4.6. Similar maps for the other three clusters are provided in Cucchetti et al. (2018f). On the same figures, we also show the χ distribution of the fitted parameter as defined in the previous section (*Central panels*), and the distribution of the relative error (*Right panels*) to demonstrate the accuracy of the pipeline.

The redshift of each region can be converted into bulk motion velocities to estimate the overall movement of the cluster (Figure 4.7). For C3, the velocity profile highlights the ongoing merging activity, while for C4, we notice a rotational movement of the ICM, possibly resulting of a previous merger (visible in the sample at higher redshift). The velocity broadening along the line-of-sight is also recovered in the fit. However, no turbulence was included in these simulations. A study of the ICM turbulence was therefore not conducted here, as it requires dedicated inputs from either toy models (see Section 4.3) or hydrodynamical inputs (see Roncarelli et al., 2018, for an illustration).

Radial profiles

The previous simulations can also be used to investigate the radial metallicity profiles of the cluster sample. In the hierarchical formation of these structures, profiles should be self-similar and demonstrate similar behaviours for the different atomic species (Planelles et al., 2015). The values of the abundances around R_{500} can also provide a view of the early enrichment of the cluster, and whether or not it preceded the halo formation.

We computed the radial profiles on the local clusters for the main chemical elements (O, Mg, Si, and Fe). As shown in Figure 4.8, the values are consistent across the sample, showing a peak near the centre (i.e. up to $0.1\,R_{500}$) and a decrease towards a constant value between $\sim 0.1/0.2\,Z_{\odot}$ at R_{500}. Cluster C3 shows metallicities systematically higher than the other objects in the sample, which could be caused by the ongoing merger, visible in Figure 4.2 (*Bottom left*), or by AGN activity. This movement also creates a more complicated line-of-sight distribution of the parameters, hence less accurate fits. This is particularly the case in the outskirts, where background contributions become relevant, thus increasing the deviations between our simulations and the weighted input values (especially for iron). The constant metallicity in the outskirts suggests, as discussed in Biffi et al. (2017); Truong et al. (2018), that the enrichment of the sample pre-dates the infall of gas towards the central object, and is mainly related by the early enrichment mechanisms of the Universe. Other hydrodynamical simulations (Vogelsberger et al., 2018) and recent observational results (e.g. Ezer et al., 2017; Simionescu et al., 2017) also argue in favour of this paradigm. This analysis can be compared to a similar study performed by simulating 200 ks cluster observations with *XMM-Newton*/EPIC MOS1 and MOS2 for the same chemical species (see Figure 4 in Rasia et al. 2008), or to current observational data using the `CHEERS` catalogue (Mernier et al., 2017). For typical 100 ks exposure times, the X-IFU will provide measurements of the main metallic content of the ICM, with sufficient accuracy to reduce the uncertainties on abundances even for rare elements and therefore clearly constrain the scheme for the chemical evolution of the ICM.

The overall dispersion across the sample found in our simulations is consistent with the average EMW input distribution within 1σ. However, the sample considered here

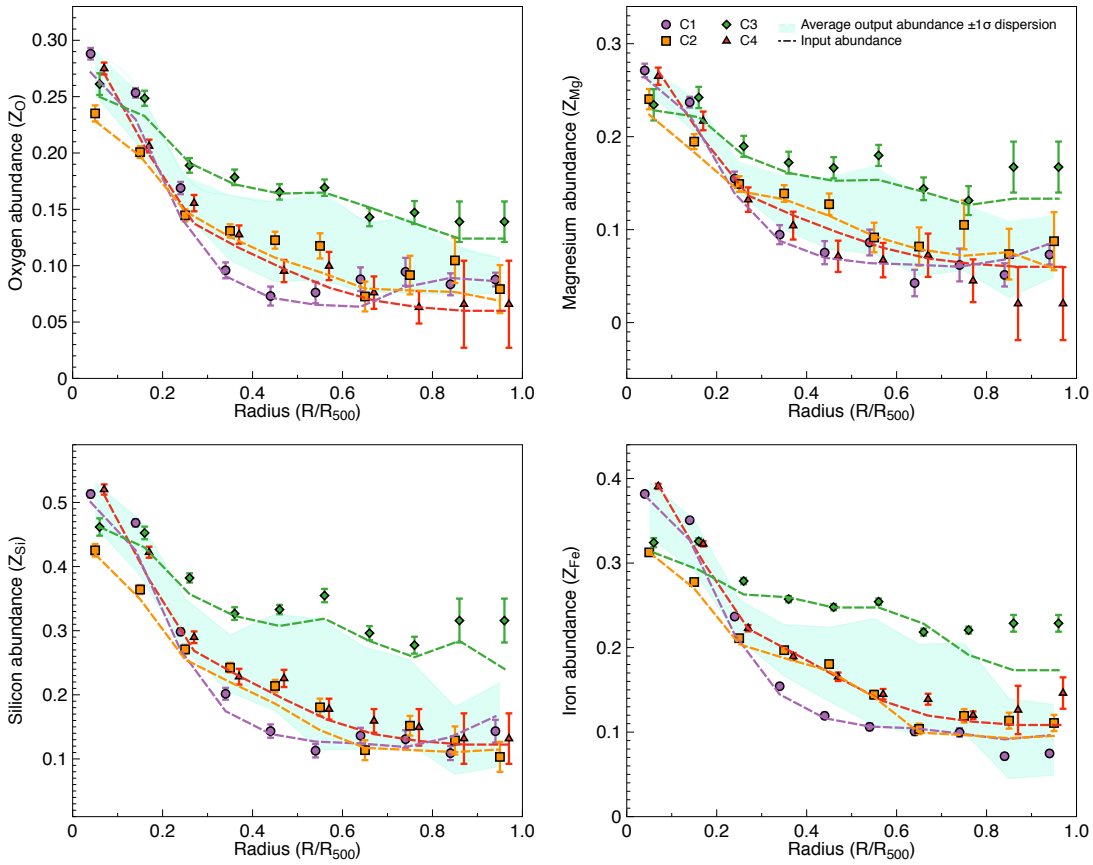

Figure 4.8: Best-fit values of the metallicity as a function of radius, up to R_{500} (0.1 R_{500} bins) for the entire sample (C1 - purple dots, C2 - orange squares, C3 - green diamonds, C4 - red triangles). *(From top left to bottom right)* $Z_{\rm O}$, $Z_{\rm Mg}$, $Z_{\rm Si}$ and $Z_{\rm Fe}$ with respect to solar. The dashed lines represent the profile of the EMW input abundances using the same colours. The cyan shaded envelope represents the $\pm1\sigma$ dispersion of the recovered output metallicity for the entire sample. Points are slightly shifted for clarity.

is relatively small, and the scatter of our results remains significant. Namely, we see that the dynamic behaviour of C3 affects the overall scatter of the sample, otherwise similar for the other three objects (C1, C2, and C4). A more accurately constrained scatter will provide important information on the metallicity distribution of the ICM and firm observational confirmation of the nature of the enrichment scenario during the early phases of the Universe. Once in orbit, the X-IFU will probe a much larger number of galaxy clusters (≥ 10 per mass and redshift bins), therefore reducing the sample variance of these profiles even further, especially near the outskirts of the clusters.

Finally, the values of iron abundance in the outskirts ($0.1/0.2\,Z_{\odot}$) are lower than those derived from observations, which range around $0.2\,Z_{\odot}$ (Werner et al., 2013; Mantz et al., 2017; Urban et al., 2017). This effect may be related to the EMW projection scheme, as it was shown to provide lower results than EW schemes (used e.g. in Biffi et al., 2017).

4.1.5 The enrichment through cosmic time

To understand how and when the ICM was enriched, we extended our previous study by observing the same clusters at different stages of their evolution, considering five redshift values up to $z = 2$. An exposure time of 100 ks was used for these simulations, regardless of the redshift (see Figure 7 in Cucchetti et al. 2018f). For the highest redshift clusters, we complied with the definition of the *Athena* science case and performed measurements in two distinct spatial regions only: between $0 - 0.3\,R_{500}$ and between $0.3 - 1\,R_{500}$.

Figure 4.9 shows the evolution of the mean cluster abundances, $Z_{\rm O}$, $Z_{\rm Mg}$, $Z_{\rm Si}$, and $Z_{\rm Fe}$, over the sample as a function of the redshift in the two annular regions. Despite the lower source-to-background level, input metallicity values are recovered accurately within the statistical uncertainties, even for high-redshift clusters. In the case of low-mass elements, abundances are not measurable up to a redshift of $z = 2$, as lines are shifted outside the instrument energy band (e.g. O and Mg for $z \geq 1.5$) or are too weak to be disentangled from the continuum and the background emissions (e.g. Si at $z = 2$). As expected, measurements in the central parts of the cluster are more accurate, due to the higher signal-to-background level than in the outskirts, especially for $z \geq 1.5$.

Through these simulations, we demonstrated that the X-IFU will provide strong constraints on the chemical enrichment across time. We recover for instance that in the central parts of the cluster metallicity hardly changes across time, even at a redshift of $z = 2$, consistently with the analysis by Biffi et al. (2017). This concurs with an early enrichment of the cluster in the simulations. Interestingly, iron abundance in the central parts slightly decreases with redshift, which could be connected to an increase in time of iron production mechanisms (e.g. $\rm SN_{Ia}$) or to the time delay before which long-lived $\rm SN_{Ia}$ progenitors create Fe. Similar results are found in the outskirts, with near-constant values of metallicities up to local redshift values, in agreement with recent observations (Ettori et al., 2015). These results show that even with moderate exposures, the X-IFU will provide an unprecedented view of the early days of clusters. The spectral capabilities of the X-IFU will also give a glimpse of the dynamic history of the clusters (mergers, shocks), as we notice here local peaks of abundance, for example, C3 at $z = 1$ or C4 at $z = 0.5$ indicating merger events. Given the sparse number of redshift points, turbulence or mixing within the cluster (whose eddy turnover time scale is of the order of a few Gyr over scales of ~ 1 Mpc for ~ 500 km/s velocities) creates over time a more homogeneous distribution of metals, returning abundances to typical values after mergers.

4.1.6 Abundance ratios and underlying enrichment model

Strong constraints on the relative contribution of the enrichment mechanisms (notably $\rm SN_{cc}$ and $\rm SN_{Ia}$) can be found through the ICM abundance ratios. Table 4.3 shows the consistency between the recovered ratios within R_{500}, confirming a self-similar behaviour in the simulations. A small fraction of outlier regions ($\lesssim 5\%$) was however excluded in the comparison, as results clearly showed incompatible values with respect to EMW inputs for rare elements (N, Na, and Al). The average abundance ratio profile can then be compared to the true average abundance ratio derived from the input maps. As shown in Table 4.3, all the elements present in the simulations are consistent within their statistical error bars to their inputs (courtesy V. Biffi, L. Tornatore – see Section 4.1.1 for references). Most of

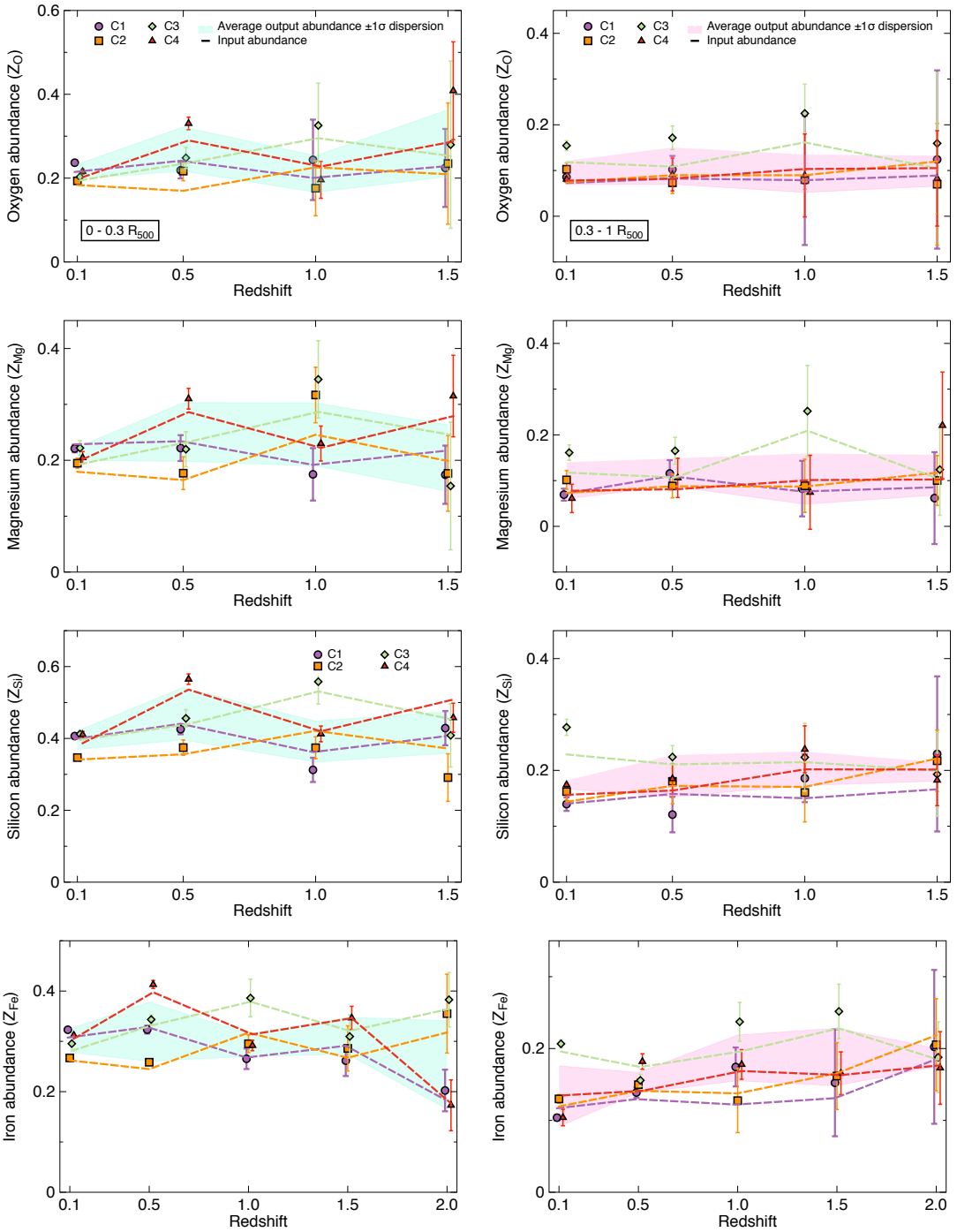

Figure 4.9: Evolution of the average abundance of the cluster sample as a function of the redshift between 0 – 0.3 R_{500} (*Left*) and 0.3 – 1 R_{500} (*Right*). (*From top to bottom*) $Z_{\rm O}$, $Z_{\rm Mg}$, $Z_{\rm Si}$ and $Z_{\rm Fe}$ abundances with respect to solar. The dashed lines represent the profile of the emission-measure-weighted input abundances using the same colours. The cyan (resp. magenta) shaded envelope represents the $\pm 1\sigma$ dispersion of the output metallicity over the sample. Points are slightly shifted for clarity.

	C1	C2	C3	C4	Average	Input (average)
C/Fe	0.48 ± 0.34	0.35 ± 0.24	0.43 ± 0.28	0.48 ± 0.31	0.39 ± 0.15	0.50
N/Fe	0.32 ± 0.12	0.40 ± 0.15	0.52 ± 0.30	0.57 ± 0.20	0.41± 0.08	0.39
O/Fe	0.73 ± 0.04	0.68 ± 0.04	0.67 ± 0.06	0.69 ± 0.06	0.69 ± 0.02	0.68
Ne/Fe	0.10 ± 0.03	0.12 ± 0.04	0.14 ± 0.06	0.20 ± 0.06	0.12 ± 0.02	0.12
Na/Fe	0.17 ± 0.12	0.34 ± 0.24	0.20 ± 0.13	0.21 ± 0.17	0.21 ± 0.08	0.13
Mg/Fe	0.63 ± 0.05	0.58 ± 0.06	0.59 ± 0.08	0.53 ± 0.08	0.59 ± 0.03	0.61
Al/Fe	0.16 ± 0.08	0.18 ± 0.10	0.21 ± 0.18	0.20 ± 0.13	0.18 ± 0.06	0.13
Si/Fe	1.24 ± 0.06	1.18 ± 0.05	1.27 ± 0.08	1.27 ± 0.09	1.23 ± 0.03	1.21
S/Fe	1.33 ± 0.08	1.30 ± 0.08	1.26 ± 0.12	1.18 ± 0.12	1.28 ± 0.05	1.26
Ar/Fe	0.19 ± 0.09	0.22 ± 0.11	0.20 ± 0.15	0.30 ± 0.17	0.22 ± 0.06	0.23
Ca/Fe	0.94 ± 0.20	0.71 ± 0.16	0.71 ± 0.24	0.99 ± 0.25	0.82 ± 0.10	0.93
Ni/Fe	2.12 ± 0.20	1.91 ± 0.21	2.11 ± 0.29	2.12 ± 0.32	2.05 ± 0.12	2.17

Table 4.3: Recovered abundance ratios within R_{500} at $z \sim 0.1$ for each cluster in the sample, and average over the entire sample. The last column indicates the true input ratio measured in the hydrodynamical simulations averaged over the same sample.

all, the ratios of the main elements of the ICM (e.g. O/Fe, Mg/Fe, and Si/Fe) are very accurately recovered with a significance of the detection above 10 (i.e. the ratio between the value and the error). Less abundant elements (Na and Al) have looser constraints in the fitted regions due to the considered exposure time and are slightly overestimated in their reconstruction. Ni tends on the other hand to be underestimated, likely due to the low S/N ratio of the line with respect to the high-energy background.

These results demonstrate that the X-IFU can provide robust estimations of the abundance ratios. With a larger sample of cluster (40 clusters are planned to be observed) and using adapted exposure times, the X-IFU will thus give access to the enrichment of the ICM. Using rare elements produced by single mechanisms (e.g. Ne, Na for AGB, or Ar, Ni for SN_{Ia}), accurate measurements of abundance ratios will provide strong constraints on the IMF and the contribution of each production mechanism over cosmic time.

4.2 Constraints on the enrichment mechanisms

Measurements of the ICM abundance ratios are a powerful tool to analyse the evolution of metal production mechanisms across time. As discussed in Chapter 1, SN_e events populate the ISM with heavy metals, later circulated to the ICM, where they remain trapped in the gravitational potential of the cluster. A common assumption is to consider that the resulting ICM metallicity is representative of the chemical enrichment history of the Universe, though the metal distribution between the ICM and the galaxies within the cluster may differ (Kirkpatrick et al., 2011). The enrichment is then treated as a self-similar mechanism. A star of mass M will populate the ISM with a given amount of metals (referred to as abundance 'yields') either through SN_e or AGB winds. Despite significant steps forward, the physics of these events remains questioned, and multiple models coexist to predict metal production yields (see Mernier et al., 2016b). Breakthroughs require instruments with spatially resolved high-resolution spectroscopy, such as the X-IFU. In this section, we investigate the capabilities of the X-IFU in constraining these models.

4.2.1 Constraining the chemical enrichment models

Principle of the comparison

The origin of metals in the ICM can be traced to stellar mechanisms such as SN_e or AGB winds. Classically, the number of atoms, N_X, of a species X produced by a given number M of mechanisms m can be expressed by (Gastaldello & Molendi, 2002):

$$N_{X,\mathrm{tot}} = \sum_{m=1}^{M} a_m N_{X,m} \tag{4.9}$$

where $\forall m \in [1, M],\ a_m \in \mathbb{R}$ are multiplicative constants representing the total number of such mechanisms needed to obtain the observed enrichment (i.e. number of SN_e or AGB stars) and $N_{X,m}$ the atoms produced in each case. The corresponding formula over the abundance ratios can be derived from the previous expression, and compared to actual measurements, D, by fitting a linear combination of the abundance yields, y_m, derived from the theoretical models of stellar dynamics:

$$\chi^2 = \sum_X \frac{(D_X - \sum_{m=1}^{M} a_m y_{X,m})^2}{\sigma^2_{\mathrm{stat},X}} \tag{4.10}$$

The sum is performed over the total number of available elements (of cardinal O), and σ_{stat} is the statistical uncertainty of the measurements D. This equation is in theory only valid for an integrated study of the abundances (total production in stars, galaxies and the ICM, Matteucci & Chiappini 2005) as it does not include the time scale of circulation of the metals from the galaxies to the ICM (see also de Grandi & Molendi, 2009). It can nonetheless be applied under the caveat that the fractions a_m are representative of the number of events enriching the ICM rather than the Universe (equivalence if and only if the metal distribution is the same in galaxies and the ICM, Humphrey & Buote 2006).

A generic way of assessing the accuracy of a model is to compute the reduced chi-squared of the fit, $\chi^2_{\mathrm{red}} = \chi^2/(O - M)$. If large values are obtained, the predicted yields are not likely to be representative of the reality of the chemical enrichment (at least at ICM level). Efforts provided in previous studies (Werner et al., 2006; de Plaa et al., 2006, 2007) already discarded multiple models, yet a finer understanding is required. Additional constraints can also be derived from the ratio of SN_{Ia}/SN_e (Mernier et al., 2015).

A way to quantify the capabilities of the X-IFU in recovering the underlying enrichment models is to compare the results of a typical observation with a significant number of available models and determine the fraction which can be excluded. Ideally, a given combination of theoretical models (SN_{Ia}, SN_{cc} and AGB) should provide an accurate match, and reject all other models. As no real observation can be used at the moment, data sets derived from E2E simulations remain the only way to test the feasibility of this science case. We therefore assume that the previous study of the ICM in a representative cluster sample (Section 4.1.6) can be treated as an idealised observation obtained in flight. Using the theoretical models at our disposal, we blindly derive which combination matches the ratios in the most statistically-accurate way, hoping to recover the models (or family of models) used in our sample of four clusters extracted from numerical simulations.

In the rest of this study, we assume that metals are produced by three mechanisms: SN_{Ia}, SN_{cc} and AGB winds. Each is considered independent from the other. We also consider that the bulk of the enrichment is completed at $z = 0.105$ (supported by both numerical and observational results, see Section 4.1.5). The simulated X-IFU measurements of abundance ratios are taken from Table 4.3, while the list of theoretical models used for the comparison is detailed in Table ii (Appendix G), with the corresponding specificity of each model (courtesy F. Mernier). In some cases, models are tested various times, depending on the initial metallicities used for the numerical integration with the IMF. Although the data set is obtained using an IMF by Chabrier (2003), all the yields are integrated with a Salpeter-like IMF to ease the comparison. Finally, to simplify notations, we include both supernovæ mechanisms in the generic 'SN_e' notation (i.e. SN_e means SN_{Ia} + SN_{cc}).

The yields derived from the models, y_m, are fitted to the data points recovered in the synthetic X-IFU measurements using the `abunfit` package,[15] which solves the following minimisation problem on $a_{SN_{Ia}}$, $a_{SN_{cc}}$, $a_{AGB} \in \mathbb{R}$:

$$\chi^2 = \sum_X \frac{(D_X - a_{SN_{Ia}} y_{SN_{Ia},X} - a_{SN_{cc}} y_{SN_{cc},X} - a_{AGB} y_{AGB,X})^2}{\sigma^2_{stat,X}} \tag{4.11}$$

The sum is performed over all the elements X present in the simulation (Section 4.1.1) except iron. Since the iron abundance ratio is used as normalising figure, the fit adds the constraint $a_{SN_{Ia}} y_{SN_{Ia},Fe} + a_{SN_{cc}} y_{SN_{cc},Fe} + a_{AGB} y_{AGB,Fe} = 1$.

Results

For each combination of models, we computed the reduced chi-squared of the fit with 9 degrees of freedom. The corresponding distribution of χ^2_{red} is shown in Figure 4.10 (*Left*). We define a model as 'statistically acceptable' if it verifies $\chi^2_{red} \lesssim 5$. This corresponds to models complying with the null hypothesis (H_0): "The models represent the data", with a p-value of 3×10^{-7}. For our number of degrees of freedom, realistic models are in general found whenever $\chi^2_{red} \lesssim 1.87$ (corresponding to a p-value of 0.05). The distribution indicates that, in most of the cases, the fit does not provide a good description of the (simulated) measurements. The first peak ($\chi^2_{red} \sim 10$), corresponds to a fit in which one out of three fitted models is not compatible. The second peak ($\chi^2_{red} \sim 100$), corresponds to the case where two or more models are not consistent with the data set.

For the list of models presented in Table ii, only $\sim$ 80 combinations (over $\sim$ 2000) provide statistically-acceptable results. The X-IFU is therefore able to reject more than $\geq 95\%$ of the theoretical model combinations. A further refinement can be performed by analysing the results of the fit, in particular the relative contribution of each mechanism. From observations, we know that the observed fraction $SN_{Ia}/(SN_{Ia}+SN_{cc})$ is likely to be comprised between 0.1 and 0.6 (see Table 5 and 6 in de Grandi & Molendi, 2009), due to the late character of SN_{Ia} enrichment. As such, we can constrain the number of statistically-accurate fits even further by requesting that $a_{SN_{Ia}}/(a_{SN_{Ia}} + a_{SN_{cc}})$ remains within these bounds (Figure 4.10 – *Right*). Following this second selection, only five combinations satisfy $\chi^2_{red} < 5$ (Table 4.4), with the most credible results corresponding to combinations of enrichment models used in the numerical simulations. The best fit is achieved with $Z_{init} = 2 \times 10^{-4}\, Z_\odot$ for SN_{cc} yields and $Z_{init} = 0.02\, Z_\odot$ for AGB yields ($\chi^2_{red} = 1.49$).

[15] http://mernier.web.elte.hu/#scripts

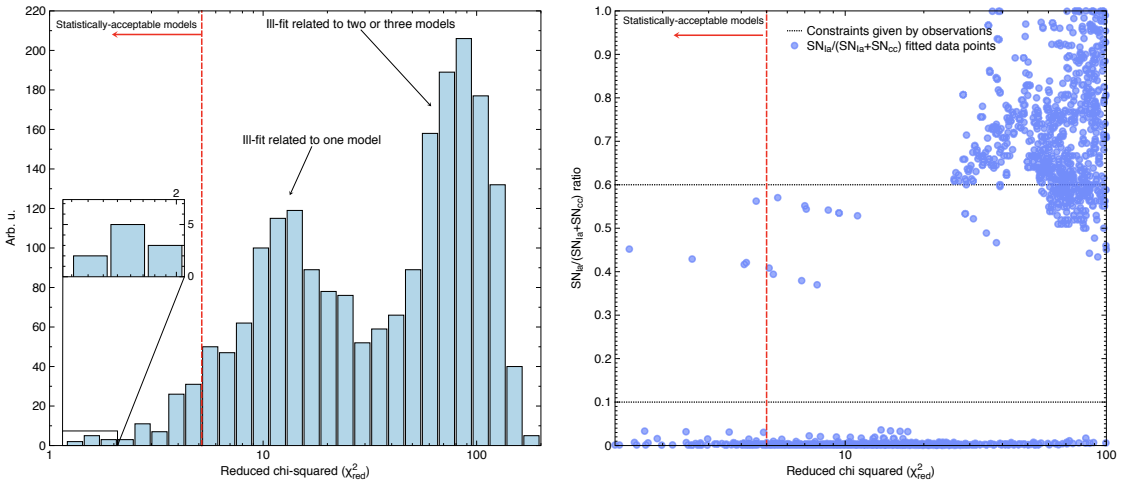

Figure 4.10: (*Left*) χ^2_{red} distribution obtained by fitting all the combinations of models listed in Appendix G to the data set derived from the E2E simulation (Table 4.3). The plot is truncated at $\chi^2_{\text{red}} = 200$. The sub-panel shows the models having $\chi^2_{\text{red}} \leq 5$. (*Right*) Same distribution in the $\text{SN}_{\text{Ia}}/(\text{SN}_{\text{Ia}}+\text{SN}_{\text{cc}})$ plane. The horizontal black dashed line represents a boundary for realistic models derived from observations (de Grandi & Molendi, 2009).

In theory, multiple models may exist to represent the same phenomenon. This is notably the case for SN_{Ia}, whose end of life can be significantly different depending on single-degenerate/double-degenerate scenarios and/or deflagration/delayed-detonation thermonuclear explosions. We thus extended the previous work to include an additional SN_{Ia} model to the fit, to represent a more complex stellar reality. The same method is applied, considering two scalars, $a_{\text{SN}_{\text{Ia}},1}$ and $a_{\text{SN}_{\text{Ia}},2}$ in the fit. Similarly to Figure 4.10 (*Left*), only a certain combinations offer χ^2_{red} values below 5 ($\sim 8\,000$ over $\sim 72\,000$ combinations). After a second selection using the ratio $(\text{SN}_{\text{Ia},1}+\text{SN}_{\text{Ia},2})/\text{SN}_{\text{e}}$ however, many models remain compatible due to degeneracies (~ 280 models). To reduce this number, other refinements can be applied, notably by requesting that $\text{SN}_{\text{Ia},1}/\text{SN}_{\text{Ia},2}$ ratio and the AGB fraction remain consistent with expected physical results, i.e. between 0.01 and 100 for the former (neither mechanism is sub-dominant), and lower than 0.5 for the latter (expected sub-dominant with respect to SN_{Ia} and SN_{cc}). Only three model combinations satisfy these criteria and $\chi^2_{\text{red}} < 5$ (Table 4.4). We notice these combinations coincide with a previous (single SN_{Ia}) accurate combination plus a sub-dominant SN_{Ia} model. Such combinations should likely be discarded during analysis, especially given the low $\text{SN}_{\text{Ia}}/\text{SN}_{\text{e}}$ ratios, and the high $\text{SN}_{\text{Ia},1}/\text{SN}_{\text{Ia},2}$ ratio. With these considerations, double SN_{Ia} models seem less accurate than single SN_{Ia} models to describe this data set.

Discussion

Previous results show encouraging perspectives for the X-IFU. Through a simple linear fit and physical considerations, we are capable of accurately recovering the enrichment models implemented in the numerical simulations (Tornatore et al., 2007). In our case, the enrichment within these simulations uses an entire family of models, yet a single combination

χ^2_{red}	SN_{Ia}/SN_e	$SN_{Ia,1}/SN_{Ia,2}$	AGB frac.	$SN_{Ia,1}$	$SN_{Ia,2}$	SN_{cc}	AGB
Input models family – SN_{Ia}: Th03 – SN_{cc}: Ro10 – AGB:K10							
Single SN_{Ia} model							
1.490	0.451	/	0.318	Th03	/	Ro10_2E-4	K10_2E-2
2.593	0.428	/	0.377	Th03	/	Ro10_2E-4	K10_8E-3
4.105	0.417	/	0.357	Th03	/	Ro10_2E-4	K10_4E-3
4.182	0.421	/	0.332	Th03	/	Ro10_2E-3	K10_2E-2
4.561	0.562	/	0.317	Th03	/	Ro10_2E-6	K10_2E-2
5.112	0.408	/	0.356	Th03	/	Ro10_2E-4	K10_1E-4
5.306	0.393	/	0.390	Th03	/	Ro10_2E-3	K10_8E-3
Two SN_{Ia} models							
1.491	0.264	11.031	0.376	Th03	N1def	Ro10_2E-6	K10_2E-2
1.529	0.191	37.218	0.394	Th03	N5def	Ro10_2E-6	K10_2E-2
2.872	0.184	54.906	0.389	Th03	N20def	Ro10_2E-6	K10_2E-2
5.607	0.194	98.160	0.366	Th03	N100def	Ro10_2E-6	K10_4E-3

Table 4.4: List of SN_e models deemed statistically-acceptable with the data set (see text for criteria). The model names are explained in Appendix G.

provides already very accurate results. As shown in Table 4.4, the best fit is obtained for the models with $Z_{init} = 2 \times 10^{-4}\, Z_\odot$ for SN_{cc} yields and of $Z_{init} = 0.02\, Z_\odot$ for AGB yields. The different Z_{init} suggest that AGB and SN_{cc} enrichment mechanisms act at different time scales within the simulation, the former occurring earlier, when low-metallicity stars dominate. This specific combination is therefore the most accurate to describe this feature.

The same approach was also tested for $z = 1$ (see Fig. 4.11 – *Right*) with similar results. We find that the X-IFU is still capable of recovering the underlying input enrichment model with excellent accuracy ($\chi^2 = 1.53$). Yields of the main elements have no significant changes between both redshift values, consistently with our previous conclusions. In the case of high-redshift objects, low-mass elements such as carbon and nitrogen can no longer be detected (lines outside the energy bandpass) and rarer elements (e.g. Ne, Na, and Al) have larger uncertainties due to the low S/N ratio of the observations (100 ks). More accurate results call for better exposure strategies.

This investigation shows that the X-IFU will be an excellent tool to investigate chemical enrichment models. It also demonstrate promising results in breaking model-to-model degeneracies, which so far impeded a statistically-accurate distinction between models. Several limitations can however be highlighted:

- The full integration of the yields is performed using a Salpeter-like power-slope of the IMF (i.e. power law with slope $\alpha = -2.35$). Though representative at the first order, more advanced models (e.g. Chabrier-like) which provide a low-mass cut-off in the integration need to be tested. However, since all models are integrated using the same IMF (for consistency) no significant change is expected.
- The X-IFU 'observation' used here is related to a specific family of enrichment models used in the numerical simulations (as described in Section 4.1.1 and references

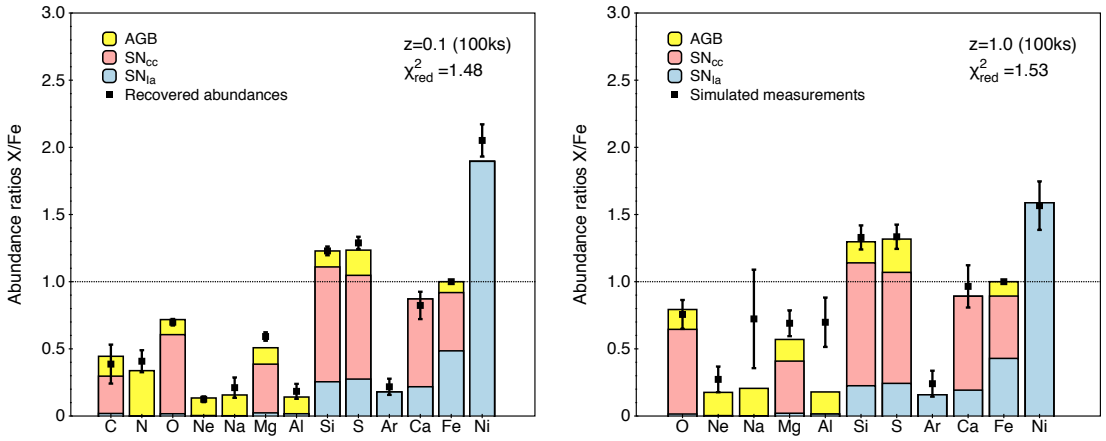

Figure 4.11: Average abundance ratio with respect to iron within R_{500} over the cluster sample for $z = 0.1$ (*Left*) and $z = 1$ (*Right*) recovered using 100 ks observations. These values are fitted using the hydrodynamical enrichment yields derived from the references provided in Section 4.1.1. The corresponding fitted contributions of SN_{Ia} (blue), SN_{cc} (magenta) and AGB stars (yellow) are shown as histograms. For $z = 1$, carbon (C) and nitrogen (N) are not shown as the lines are outside the energy bandpass of the instrument.

therein). This initial condition may be a source of bias if this specific set of input models is significantly different from other current SN_e models. Though this is in practice not the case, a proper validation would require tests with other input models. This is nonetheless challenging computationally, as it implies running new hydrodynamic simulations with different input models (weeks of computation), and perform new synthetic X-IFU observations (two weeks of computational time). This validation will thus be addressed in future studies. The χ^2_{red} test itself can be questioned. In real observations, more details will be provided by rare elements (e.g, Mn, Cu), which will give targeted information on a specific set of models.

Though effects related to the initial model may remain, the observations of large cluster samples with the X-IFU should provide a sufficiently accurate view of the ICM physics to improve our current knowledge of the underlying chemical enrichment models. The exclusion of classes and families of models is important to provide constraints in theoretical physics and improve our understanding of metal production processes in the Universe.

4.3 The challenges of measuring turbulence in the ICM

4.3.1 Turbulence and non-thermal pressure support

Dynamics induced by constant 3D accretion from the medium surrounding the cluster, by internal shocks or by the central AGN drive powerful mechanical and radiative motions, which stir the ICM at every spatial scale (Gaspari & Sądowski, 2017; Morganti, 2017), and severely question the assumption of hydrostatic equilibrium of the cluster (see Pratt et al., 2019). The infall of the ICM towards the central parts of the clusters must therefore

be compensated by other non-thermal and thermal pressure support mechanisms. The dynamics of the hot gas (Lau et al., 2009) and the dissipation of its kinetic energy through turbulent motions (Voit, 2018) are likely candidates (see Chapter 1).

Seemingly random motions of gas particles create line shifts, induce further broadening of the line, and can add skewness in the projection of the natural line profile along the line-of-sight. The observation of these turbulence-related features requires specific diagnostics, such as the measurement of the centroid shift and the broadening of spectral lines, or the computation of structure functions (Inogamov & Sunyaev, 2003). The mapping of turbulence over the full cluster scale drives the need to resolve velocities spatially with accuracies of a few tens of km/s. This can only be achieved through new-generation instruments like the X-IFU. However, even for such high-precision spectrometers, measurement of line diagnostics will be limited by statistical uncertainties and by the sampling variance (or 'cosmic' variance) of the observation, which is the intrinsic variation of a diagnostic related to the small number of observations of a random process.

Current ways to estimate the cosmic variance use MC approaches, and derive errors from a large number of simulated observations. We describe in this section an analytical approach to provide fast estimates of this uncertainty for any X-ray instrument, using the formalism started by ZuHone et al. (2016), hereby Z16. The formulas are then extended by accounting for measurement uncertainties related to finite statistics in the observations. This work is summarised in Clerc et al. (2019, hereby CL19), and Cucchetti et al. (2019, hereby CU19). We assume a Λ-CDM cosmology, with $h = 0.72$, $\Omega_m = 0.24$ and $\Omega_\Lambda = 0.76$. Bold, underlined letters $\underline{\boldsymbol{x}}$ indicate 3D vectors, arrowed letters $\vec{x}$ indicate 2D vectors. In a 3D space mapped by a (x, y, z) orthonormal frame, x is the line-of-sight direction and $(y, z) = \vec{\theta}$ the plane-of-sky coordinates. The 3D wave-vector associated with $\underline{\boldsymbol{x}}$ is $\underline{\boldsymbol{k}} = (k_x, k_y, k_z)$, with $(k_y, k_z) = \vec{\xi}$. $\langle\cdot\rangle$ is the average operator, $||\cdot||_2$ the Euclidean norm and $\overline{X}$ an estimator of the quantity X.

4.3.2 Line diagnostics for turbulence in X-ray astrophysics

We distinguish three diagnostics to study turbulence through X-ray emission lines: the shift of the line with respect to its rest frame value, its broadening, and the estimated structure function over the FoV. We assume here that the bulk motion is perfectly known, and its contribution is systematically subtracted from the measurements. Any line-of-sight component of the turbulent velocity field is thus centred, with a dispersion $\sigma_{\rm turb}$.

Line shift or centroid shift C: Line shift is defined as the difference between the energy of the line in the inertial frame of the emitting source at redshift z, E_z, and the measured value. By noting $I_l(E)$ the line profile (e.g. Gaussian or Voigt profile multiplied by the emissivity ϵ) the energy shift δE along a given line-of-sight $\vec{\theta}$ is defined as:

$$\delta E(\vec{\theta}) = F^{-1}(\vec{\theta}) \int (E - E_z) I_l(E, \vec{\theta}) dE \tag{4.12}$$

where $F(\vec{\theta}) = \int I_l(E, \vec{\theta}) dE$ is the integrated flux of the line. δE can be expressed as a centroid velocity shift C of the projected line-of-sight component of the velocity field:

$$C(\vec{\theta}) = \frac{\delta E(\vec{\theta})}{E_z} c \tag{4.13}$$

Line broadening S: The line broadening is the dispersion of the line around its centroid value, and can be expressed as follows:

$$\Sigma^2(\vec{\theta}) = F^{-1}(\vec{\theta}) \int (E - \delta E - E_z)^2 I_l(E, \vec{\theta}) dE \tag{4.14}$$

Small turbulent motions create shifts in the line centroids of the gas particles. Integrated over along the line-of-sight, these result in a broadening of the observed line. The velocity broadening is thus defined by

$$\tilde{S}^2(\vec{\theta}) = \frac{\tilde{\Sigma}^2(\vec{\theta})}{E_z^2} c^2 \tag{4.15}$$

where $\tilde{\Sigma}$ is the broadening after subtraction of the instrument spectral resolution and other physical broadening effects (e.g. thermal or natural broadening), assumed perfectly known here. The measurement of $\tilde{S}$ provides insight on the velocity distribution along the line-of-sight, making it a tool widely used to study turbulence (Hitomi Collaboration, 2018a).

Second-order structure function $\mathcal{SF}$: Its use originates from the early studies of turbulent motions in fluid dynamics (Kolmogorov, 1941) before its extension to other branches of science (e.g. Earth sciences under the name of 'variogram'), and later to astrophysics (Miville-Deschenes et al. 1995 in studies of the interstellar medium, Roelens et al. 2017 in stellar variability, Martínez et al. 2010 for galaxy clustering, or Inogamov & Sunyaev 2003 in the case of ICM turbulence). The structure function appears when observing the dispersion σ of the line-of-sight component v of the velocity field over all the points in space $\underline{\boldsymbol{x}} \in \mathbb{R}^3$

$$\sigma^2 = \langle v^2(\underline{\boldsymbol{x}}) - \langle v(\underline{\boldsymbol{x}}) \rangle_x^2 \rangle_x = K_v(\underline{\mathbf{0}}) \tag{4.16}$$

which is a particular case of the auto-covariance function of the velocity field, K_v. Under the assumption of an isotropic velocity field, the second-order structure function of the 3D line-of-sight component of the turbulent velocity field v, $\mathcal{SF}_2$, can be expressed exclusively as a function of spatial separation s between two points in space, and is related to K_v by

$$\begin{aligned} \mathcal{SF}_2(s) &= 2(K_v(\underline{\mathbf{0}}) - K_v(\underline{\boldsymbol{r}})) \\ &= \langle (v(\underline{\boldsymbol{x}} + \underline{\boldsymbol{r}}) - v(\underline{\boldsymbol{x}}))^2 \rangle_x \end{aligned} \tag{4.17}$$

where we average over all points $\underline{\boldsymbol{x}} \in \mathbb{R}^3$ separated by a distance $||\underline{\boldsymbol{r}}||_2 = s$. The measurement of $\mathcal{SF}_2$ provides a view of the underlying turbulent velocity power spectrum through a 'modified' second order moment of the velocity field. Although the properties of a turbulent field are not fully characterised by its power spectrum, the properties of structure functions and their simple estimation in fluid dynamics explains the success of this approach in all turbulence-related subjects. Notably, $\mathcal{SF}_2$ can be used to estimate the characteristic lengths of the turbulence (Miniati, 2015). More generally, we can define the n^{th} moment of the structure function ($n \in \mathbb{N}$) as

$$\mathcal{SF}_n(s) = \langle (v(\underline{\boldsymbol{x}} + \underline{\boldsymbol{r}}) - v(\underline{\boldsymbol{x}}))^n \rangle_x \tag{4.18}$$

for a separation $||\underline{\boldsymbol{r}}||_2 = s$. In the following sections, $\mathcal{SF}$ indicates the second-order structure function, and $\mathcal{D}$ the first-order structure function, or incremental function.

In astrophysical observations, velocities can only be measured in the 2D space of the detector. Per pixel, the result will be the projection of the line-of-sight component of the velocity field modulated by emissivity effects. We define the subset $\mathbf{S}_s \subset \mathbb{R}^4$, which contains all the doublets $(\vec{x}, \vec{y})$ separated by exactly s in the sense of the Euclidean norm. By convention, $\mathbf{S}_0 = \varnothing$. We also define $\tilde{\mathbf{S}}_s$ as the 'halved' subset, not counting for $\vec{x} \leftrightarrow \vec{y}$ permutations. The cardinal of $\tilde{\mathbf{S}}_s$ is named $N_p(s)$ and represents the number of evaluations of the spatial average at a separation s. $\mathcal{SF}$ and $\mathcal{D}$ can be transposed to their 2D projected equivalents, SF and D, using the centroid shift C:

$$\mathrm{SF}(s) = \langle (C(\vec{x}) - C(\vec{y}))^2 \rangle_{\tilde{\mathbf{S}}_s} \tag{4.19}$$

$$\mathrm{D}(s) = \langle C(\vec{x}) - C(\vec{y}) \rangle_{\tilde{\mathbf{S}}_s} \tag{4.20}$$

where $\langle \cdot \rangle_{\tilde{\mathbf{S}}_s}$ is the average over the data points in $\tilde{\mathbf{S}}_s$.

4.3.3 Intrinsic cosmic variance

We assume ergodicity and isotropy of the turbulence processes. For a given $\underline{\boldsymbol{x}} \in \mathbb{R}^3$ and a turbulent velocity field $\underline{\boldsymbol{v}}$ in the frame of the observer, we only consider the line-of-sight component, i.e. $\underline{\boldsymbol{v}}(\underline{\boldsymbol{x}}) \cdot \underline{\boldsymbol{e}}_x = v(\underline{\boldsymbol{x}})$, with no loss of generality.

Centroid shift and line broadening

As pixels never correspond to a single punctual line-of-sight, Equations 4.13 and 4.15 must be integrated accounting for the finite size of the detector. This is modelled in the computations by a window function $\mathcal{W}$ of value 1 in the region or 0 otherwise. Assuming an optically-thin plasma of emissivity ϵ and a Gaussian or Voigt line profile I_l, we can write the previous equations expressing F, C and $\tilde{S}^2$ as (CL19):

$$F_{\mathcal{W}}(\vec{\theta}) = \int F(\vec{\theta}) \mathcal{W}(\vec{\theta}) d\vec{\theta} \tag{4.21}$$

$$C_{\mathcal{W}}(\vec{\theta}) = F_{\mathcal{W}}(\vec{\theta})^{-1} \int F(\vec{\theta}) \mathcal{W}(\vec{\theta}) C(\vec{\theta}) d\vec{\theta} \tag{4.22}$$

$$\tilde{S}^2_{\mathcal{W}}(\vec{\theta}) = F_{\mathcal{W}}(\vec{\theta})^{-1} \int F(\vec{\theta}) \mathcal{W}(\vec{\theta}) (\tilde{S}^2(\vec{\theta})^2 + C(\vec{\theta})^2) d\vec{\theta} - C_{\mathcal{W}}(\vec{\theta})^2 \tag{4.23}$$

To simplify notations in the rest of the study, we take $C_{\mathcal{W}} \equiv C$ and $\tilde{S}^2_{\mathcal{W}} \equiv \tilde{S}^2$ for a given detector of centre $\vec{x}$. By averaging over multiple realisations of a turbulent velocity field, characterised by its turbulent velocity power spectrum $P_{3\mathrm{D}}$, we find using the Fourier decomposition of the velocity field $v(\underline{\boldsymbol{x}}) = \sum_{\underline{\boldsymbol{k}}} V_{\underline{\boldsymbol{k}}} \exp(i\omega \underline{\boldsymbol{k}} \cdot \underline{\boldsymbol{x}})$:

$$\mathbb{E}[C(\vec{x})] = 0 \tag{4.24}$$

$$\mathrm{Var}[C(\vec{x})] = \sum_{\underline{\boldsymbol{k}}} P_{3\mathrm{D}}(||\underline{\boldsymbol{k}}||_2) ||c_{\epsilon,\mathcal{W}}(||\underline{\boldsymbol{k}}||_2)||_2^2 \tag{4.25}$$

where $c_{\epsilon,\mathcal{W}}$ is 3D the Fourier transform coefficient of $\epsilon(\underline{\boldsymbol{x}})\mathcal{W}(\vec{\theta})$. This formula is different from the one presented in Z16 as emissivity is assumed to be variable in space. If we

assume that $\epsilon(\underline{\boldsymbol{x}}) = \epsilon(x)$, the previous formula becomes

$$\mathrm{Var}[C(\vec{x})] = \int P_{\mathrm{3D}}(||\underline{\boldsymbol{k}}||_2) P_{\mathcal{W}}(\vec{\xi}) P_{\epsilon}(k_x) dk x d\vec{\xi} \tag{4.26}$$

where $P_{\mathcal{W}}$ is the 2D power spectrum of the window function and P_{ϵ} the emissivity power spectrum along the line-of-sight. We recover the formula from Z16 when the emissivity is constant and when we consider a single line-of-sight. Similarly, for $\tilde{S}^2$, in the case of a Rayleigh distribution the velocity field moduli (see CL19 otherwise):

$$\mathbb{E}[\tilde{S}^2(\vec{x})] = \sigma^2_{\mathrm{turb}} - \mathrm{Var}[C(\vec{x})] \tag{4.27}$$

$$\mathrm{Var}[\tilde{S}^2(\vec{x})] = 2 \sum_{\underline{\boldsymbol{k}}, \underline{\boldsymbol{k'}}} P_{\mathrm{3D}}(||\underline{\boldsymbol{k}}||_2) P_{\mathrm{3D}}(||\underline{\boldsymbol{k'}}||_2) || \frac{c_{\epsilon,\mathcal{W}}(||\underline{\boldsymbol{k}} + \underline{\boldsymbol{k'}}||_2)}{F} - \frac{c_{\epsilon,\mathcal{W}}(||\underline{\boldsymbol{k}}||_2) c_{\epsilon,\mathcal{W}}(||\underline{\boldsymbol{k'}}||_2)}{F^2} ||^2_2 \tag{4.28}$$

Structure function

Under the same assumptions, the expected value of the 2D projected structure function, SF, can be expressed (for an isotropic velocity field) using $\xi = ||\vec{\xi}||_2$ as

$$\mathrm{SF}(s) = 4\pi \int (1 - J_0(\omega \xi s)) P_{\mathrm{2D}}(\xi) d\xi \tag{4.29}$$

Here, P_{2D} is the 2D power spectrum of the centroid shift, which depends notably on the choice of the spatial domain of analysis $\mathcal{A}$ (i.e. the FoV) and its surface $\mathcal{S}_{\mathcal{A}}$:

$$P_{\mathrm{2D}}(\xi) = \left(\frac{\omega}{2\pi}\right)^2 \frac{1}{\mathcal{S}_{\mathcal{A}}} \sum_{k_x, \xi'} P_{\mathrm{3D}}(\sqrt{\xi'^2 + k_x^2}) P_{\rho}(k_x, \xi - \xi') \tag{4.30}$$

This equation resembles that by Z16, but involves the power spectrum of the emissivity normalised by the line flux over a given line-of-sight $\vec{\theta}$:

$$\rho(\underline{\boldsymbol{x}}) = \frac{\epsilon(\underline{\boldsymbol{x}})}{F(\vec{\theta})} \tag{4.31}$$

Hence, the value of the structure function is modulated by the emissivity and may vary across the FoV. Since the structure function is computed over a given spatial domain, border effects also affect the numerical estimation of SF. Furthermore the spatial binning of the pixels adds a convolution of the 2D power spectrum of the shape of the binned region to the projected P_{3D}. As shown in CL19, both these features can be corrected for in the computation. In the case of Var[SF], computations become more cumbersome, and we refer to CL19 for a full formal approach and an expression of the formula.

4.3.4 Estimators and value: the influence of finite statistics

The measurement of a velocity shift or a velocity broadening is related to a particular choice of the line-of-sight. Similarly, the definition of the structure function is related to a spatial average, such that an exact value can only be accessed either by averaging over a large number of spatial data points, or – if we assume ergodicity – by averaging over the same area for a large number of realisation of the turbulent velocity field. When observing astrophysical sources only a finite number of pointings and a limited exposure time are possible. Hence, it is essential *to distinguish between the physical value and its estimation.*

Estimators of the structure function

The estimators of the centroid shift $\overline{C}(\vec{x})$ and of the line broadening $\overline{\tilde{S}}(\vec{x})$ within a pixel (or region) $\vec{x}$ are the measurements of these quantities on the spectrum of each detector. They will however be affected by sources of statistical and systematic errors, such that

$$\overline{C}(\vec{x}) = C(\vec{x}) + \delta C(\vec{x})_{\text{stat}} + \delta C(\vec{x})_{\text{syst}} \tag{4.32}$$

$$\overline{\tilde{S}}(\vec{x}) = \tilde{S}(\vec{x}) + \delta \tilde{S}(\vec{x})_{\text{stat}} + \delta \tilde{S}(\vec{x})_{\text{syst}} \tag{4.33}$$

The former is related to the exposure time of the observation, the latter to uncertainties in the calibration or in the fit. We assume no systematic error is present in the observations. The statistical error on each point is represented as a random variable, normally distributed and centred. We define $\sigma_{\text{stat},C}$ and $\sigma_{\text{stat},\tilde{S}}$ the standard deviation of the statistical error for C and $\tilde{S}$ respectively (not necessarily equal). This distribution is considered spatially-independent (i.e. valid on any subset of pixels). In practice, in an observation, SF and D for a given separation s are computed using the following estimators:

$$\overline{\text{SF}}(s) = \frac{1}{N_p(s)} \sum_{(\vec{x},\vec{y})\in\tilde{\mathbf{S}}_s} (\overline{C}(\vec{x}) - \overline{C}(\vec{y}))^2 \tag{4.34}$$

$$\overline{\text{D}}(s) = \frac{1}{N_p(s)} \sum_{(\vec{x},\vec{y})\in\tilde{\mathbf{S}}_s} (\overline{C}(\vec{x}) - \overline{C}(\vec{y})) \tag{4.35}$$

In real data sets, only one, or a few realisations of these quantities will be computed. To determine whether these estimators are biased, one has to compute their expected value (in the statistical sense) and compare it to the real value.

Expected value of the velocity shift and broadening

The expected value and the variance of the centroid shift of the projected line-of-sight component of the velocity field for a pixel (or region) $\vec{x}$ over multiple realisations of the same random process are (CU19):

$$\mathbb{E}[\overline{C}(\vec{x})] = 0 \tag{4.36}$$

$$\text{Var}[\overline{C}(\vec{x})] = \text{Var}[C(\vec{x})] + \sigma^2_{\text{stat},C} \tag{4.37}$$

where $\text{Var}[C(\vec{x})]$ is given in Equation 4.25. Similarly, for the velocity broadening of the projected line-of-sight component of the velocity field over multiple realisations we obtain (see CU19):

$$\mathbb{E}[\overline{\tilde{S}^2}(\vec{x})] = \mathbb{E}[\tilde{S}^2(\vec{x})] + \sigma^2_{\text{stat},\tilde{S}} \tag{4.38}$$

$$\text{Var}[\overline{\tilde{S}^2}(\vec{x})] = \text{Var}[\tilde{S}^2(\vec{x})] + 4\sigma^2_{\text{stat},\tilde{S}}\mathbb{E}[\tilde{S}^2(\vec{x})] + 2\sigma^4_{\text{stat},\tilde{S}} \tag{4.39}$$

where $\mathbb{E}[\tilde{S}^2(\vec{x})], \text{Var}[\tilde{S}^2(\vec{x})]$ are the expected value and intrinsic variance of $\tilde{S}^2$ (Equation 4.28). Statistics induce an additional term in the estimation of the total broadening, which adds to the intrinsic variance of the turbulent velocity field through purely statistical terms and cross products.

Expected value of the structure function

In the case of the structure function, an ampler analytical approach is needed to quantify the effect of limited statistics in the measurements. For a large number of observations of the same random turbulent process, the expected value of $\overline{\mathrm{SF}}(s)$ is (Z16, CU19):

$$\mathbb{E}[\overline{\mathrm{SF}}(s)] = \mathrm{SF}(s) + 2\sigma^2_{\mathrm{stat},C} \tag{4.40}$$

The measurement of SF using a statistically inaccurate measurement of C is thus systematically biased, regardless of the number of points used to derive the structure function.

Variance of the structure function

The same approach is applied to Var[SF]. Under the previous assumptions, we find:

$$\mathrm{Var}[\overline{\mathrm{SF}}(s)] = \mathrm{Var}[\mathrm{SF}(s)] + \underbrace{4\mathrm{Var}[\mathrm{D}(s)]\sigma^2_{\mathrm{stat},C}}_{(1)} + \underbrace{\frac{4}{N_p(s)}\mathrm{SF}(s)\sigma^2_{\mathrm{stat},C}}_{(2)} + \underbrace{\frac{4(N_{nei}(s)+1)}{N_p(s)}\sigma^4_{\mathrm{stat},C}}_{(3)} \tag{4.41}$$

where $N_{nei}(s)$ is the number of neighbouring regions/pixels at a distance s of any given point (see CU19 for a mathematical definition). When $\sigma_{\mathrm{stat},C} = 0$, we recover the intrinsic variance of the structure function, which can be determined using the approach from CL19. With statistics, we distinguish between three different additional terms:

(1) **Velocity field fluctuation term:** The first term is related to the variance of the incremental function D. This term provides a sense of the velocity fluctuations over the observational filed-of-view (FoV). If fluctuations are small (i.e. nearby pixels have similar velocities), the effect of a statistical error will be small. On the contrary, when pixel-to-pixel fluctuations are large, statistics will affect the computation of the estimator for a given observation of the turbulent velocity power spectrum. This term will therefore be small for dissipation scales larger than the pixel (or binned region) size, or large otherwise.

(2) **Structure function fluctuation term:** This term can be related to the uncertainty with which the structure function is computed when using turbulent velocities affected by statistical errors. Its value follows closely the shape of the 'true' structure function (i.e. not positively biased, as in Section 4.3.4) and is therefore negligible at low spatial separations (where SF is small), but increases with s. This term becomes negligible when a large number of pairs is used to estimate the structure function.

(3) **Statistical fluctuations term:** This term is the sheer contribution of the statistics to the overall variance of the structure function estimator. It appears from the covariance terms of the velocity field and is associated to the topology of the detector through the neighbour term $N_{nei}(s)$. Its contribution is most important at low spatial separations, where velocities are similar, and large statistical errors may introduce biases in the structure function estimation.

Alternatively, the first two terms can be written under a single term (1)+(2), related to the intrinsic nature of the line-of-sight component of the velocity field (both scale with $\sigma^2_{\mathrm{stat},C}$). Formally, Var[D] is linked to SF (see CU19) and both show similar properties,

notably at large spatial scales. Whenever N_p is large, terms (2) and (3), related to the number of regions used to evaluate SF, go to zero. The first term however, is intrinsically linked to the number of observations of the turbulent process, and remains non-zero, even for large N_p. It can be interpreted as a cross product between the cosmic variance of the field and the statistics, which can only be determined through multiple observations of the random process. For this reason, in the case of a Gaussian field, we made the choice to separate it from the sheer contribution of SF (2). A verification of these formulas on simple test cases (e.g. constant velocity fields, Gaussian fields) yields excellent results.

4.3.5 Validation on typical X-IFU observations

Emission profile and turbulent power spectrum

The typical measurable scales of turbulence span from the size of the FoV – or the mapped area in case of multiple pointings – to the size of the pixel. A study of the turbulent cascade with X-ray instruments is therefore limited to nearby clusters, where kpc to Mpc scales are accessible with arcmin-like FoV and arcsec-like pixels (provided a sufficient angular resolution). As such, forecasted targets to investigate the ICM turbulence with the X-IFU are local and massive clusters, such as the Perseus and the Coma clusters.

To test the previous error formulas, we consider Coma-like clusters. We assume that their emission profile is described by a β-model (see Equation 1.7) with an electron density at the core, $n_{e,0}$, and a core radius, r_c. In particular, we take $n_{e,0} = 3 \times 10^{-3}\,\mathrm{cm}^{-3}$, $r_c = 400\,\mathrm{kpc}$, $\beta = 2/3$, and $n_e = 1.2\,n_H$. We only perform observations of the core of the cluster, where emissivity varies but slightly ($\sim 2\%$) over an X-IFU FoV (i.e. $5'$ in equivalent diameter). At the redshift of Coma ($z_0 = 0.023$), 1 kpc corresponds to $2.21''$ on the sky. For simplicity, we assume an isothermal cluster at $k_B T = 7\,\mathrm{keV}$, with a constant metallicity $Z = 0.7\,Z_\odot$ (see Ettori et al. 2015, abundances are given with respect to Anders & Grevesse 1989). Each gas particle is simulated with a line-of-sight component of the turbulent velocity $v(\underline{\boldsymbol{x}})$. A full description of turbulence requires hydrodynamical treatments (Gaspari & Churazov, 2013; Gaspari et al., 2014). We simplify here this approach by assuming that $v(\underline{\boldsymbol{x}})$ follows an isotropic Kolmogorov 3D power spectrum

$$P_{3\mathrm{D}}(\underline{\boldsymbol{k}}) = ||\tilde{v}(\underline{\boldsymbol{k}})||_2^2 = C_n k^\alpha e^{-(k/k_{\mathrm{dis}})^2} e^{-(k_{\mathrm{inj}}/k)^2} \tag{4.42}$$

where $\tilde{v}$ is the 3D Fourier transform of v, C_n is a normalisation factor of the power spectrum and $k = ||\underline{\boldsymbol{k}}||_2$. We note k_{dis}, k_{inj} the dissipation and injection scale respectively, and α the turbulent power-slope (Figure 4.12 – *Left*).

Normalisation of the power spectrum

The expected value of $\tilde{S}^2$ along $\vec{\theta}$ is related to the turbulent power spectrum by (CL19):

$$\mathbb{E}[\tilde{S}^2(\vec{\theta})] = \int P_{3\mathrm{D}}(\underline{\boldsymbol{k}})[1 - P_\rho^{\vec{\theta}}(k_x)]dk_x dk_y dk_z \tag{4.43}$$

where we remind that $P_\rho^{\vec{\theta}}$ is computed for a fixed $\vec{\theta}$ (depends on the selected line-of-sight, see Figure 4.12 – *Left*). The normalisation is chosen to satisfy $\mathbb{E}[\tilde{S}^2(\vec{0})] = (\mathcal{M} c_{\mathrm{sound}})^2$,

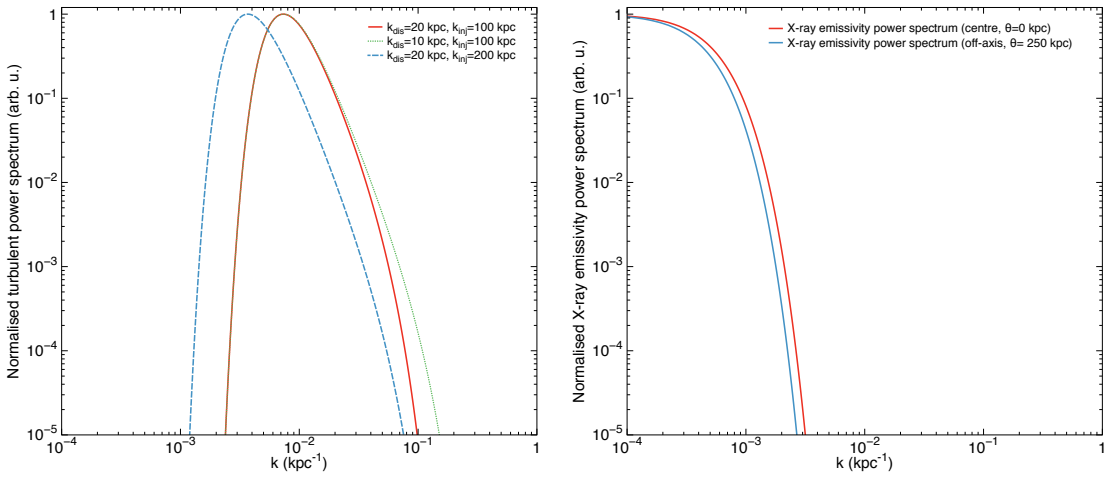

Figure 4.12: (*Left*) Turbulent power spectra used in the simulation for different injections and dissipation scales. (*Right*) Normalised X-ray emissivity power spectrum of the toy model at the centre ($||\vec{\theta}||_2 = 0\,\mathrm{kpc}$, red) and off-axis ($||\vec{\theta}||_2 = 250\,\mathrm{kpc}$, blue).

where $\mathbb{E}[\tilde{S}^2(\vec{0})]$ is the expected velocity broadening of the projected turbulent field v at the centre of the cluster, $\mathcal{M}$ the Mach number and c_{sound} the sound celerity in the ICM. We use here $\mathcal{M} = 0.3$ and $c_{\mathrm{sound}} = 1460\,\mathrm{km/s}$ (Z16). The normalisation C_n is computed through numerical integration of Equation 4.43 for $\vec{\theta} = \vec{0}$, using a uniform 8192×8192×8192 grid of a length $k_\ell = 0.50\,\mathrm{kpc}^{-1}$, corresponding to the spatial scale ℓ of pixel. To accurately compute the small scales in the centre of the cluster (notably for $P_\rho^{\vec{\theta}}$), the smallest integration scale is $k_{\mathrm{min}} = (50 r_c)^{-1}\,\mathrm{kpc}^{-1}$ (Figure 4.12 – *Right*). This approach yields excellent results (analytical comparison is possible with a β-model) with accuracies better than 0.1%.

Generation of the turbulent velocity field

One realisation of the turbulent velocity field is generated under the previous assumptions using the 3D turbulent power spectrum. We operate with a uniform area on the sky of $8.5' \times 8.5'$ (i.e. $230\,\mathrm{kpc} \times 230\,\mathrm{kpc}$) and 1.84 Mpc along the line-of-sight. The $\vec{\theta}$ plane size is chosen to include more than 1.5 times the X-IFU FoV to avoid finite box-size effects of the simulation, while the grid is extended over the line-of-sight (8 times larger) to account more accurately for projection effects and ensure a smoother cut-off of the emissivity at the edges of the grid in the simulation. For each run, we take a $2048 \times 256 \times 256$ mesh, with a step size of $\ell/2 = 2.14''$ (0.97 kpc), which corresponds to the half-width of the X-IFU pixel to avoid aliasing (Shannon criterion), and offers a good computational speed compromise.

Each grid point is given a turbulent velocity in Fourier space $\tilde{v}(\underline{\boldsymbol{k}}) = |V_k| e^{i\psi}$, with $|V_k|$ the modulus, and ψ the phase, assumed without spatial correlation. As in Z16, we use a Rayleigh distribution of parameter $\Sigma_{V_k} = P_{3\mathrm{D}}(\underline{\boldsymbol{k}})/2$ for the modulus, and a spatially-independent uniform distribution of the phase ψ, i.e.:

$$\mathcal{P}(V_k, \psi) dV_k d\psi = \frac{V_k}{\Sigma_{V_k}^2} e^{-\frac{V_k^2}{2\Sigma_{V_k}^2}} dV_k \, \frac{d\psi}{2\pi} \tag{4.44}$$

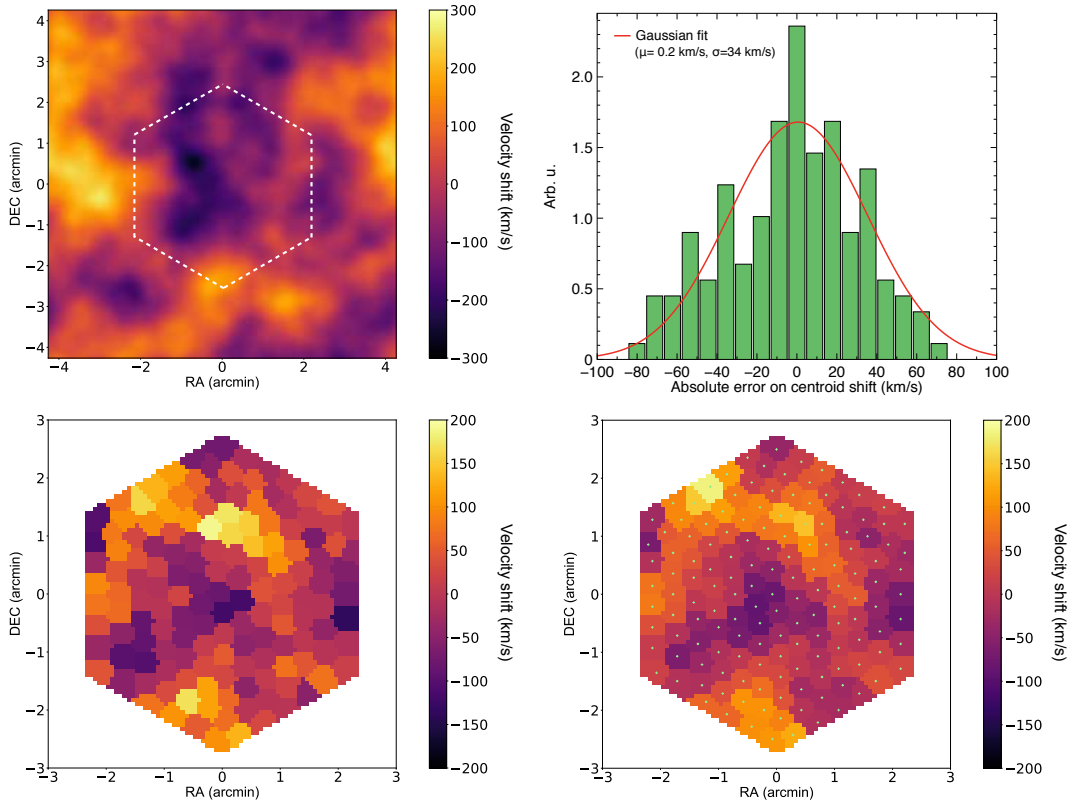

Figure 4.13: (*Top left*) Example of an EMW projection of the simulated turbulent velocity field for $k_{\rm inj} = 1/150\,{\rm kpc}^{-1}$ and $k_{\rm dis} = 1/20\,{\rm kpc}^{-1}$. The extent of the X-IFU FoV is shown as a white dashed line (*Top right*) Absolute error distribution between the recovered centroid in one simulation and the corresponding EMW input velocity. The statistical error follows a centred Gaussian distribution where the best fit (in red) is found for $\mu_{\rm stat} = 0.2\,{\rm km/s}$ and $\sigma_{{\rm stat},C} = 34\,{\rm km/s}$. (*Bottom left*) Example of a synthetic X-IFU observation of bulk motion for $k_{\rm inj} = 1/200\,{\rm kpc}^{-1}$ and $k_{\rm dis} = 1/10\,{\rm kpc}^{-1}$ and (*Bottom right*) EMW input map (binned). The green crosses indicate the centres of the Voronoï regions.

Without loss of generality, nor influence on the power spectrum, phases are computed on the lower triangular matrix of the velocity field, and transposed to the upper triangular matrix to obtain a Hermitian field. The grid is then transformed into the physical space to obtain the line-of-sight component of the velocity field $v(\underline{\boldsymbol{x}})$. Given the size of the arrays, the inverse Fourier transform is performed through `2DECOMP&FFT` (Li & Laizet, 2010),[16] which is memory-optimised for large matrices. An example of the emission-weighted projection of a simulated velocity grid of $v(\underline{\boldsymbol{x}})$ is provided in Figure 4.13 (*Top left*).

Particle emission model

Each gas particle is associated with a grid point and an element of volume. Since particle volumes are four times smaller than the X-IFU pixel area, and given the *Athena* telescope

[16] http://www.2decomp.org/

required angular resolution of 5″ half-energy width, we consider them as point-like sources on the sky. Each particle is assumed to emit isotropically following an unabsorbed thermally broadened collisionless plasma, modelled through XSPEC using `wabs*apec` with a constant temperature of 7 keV, a metallicity of $0.7\,Z\odot$ and a column density of $0.03 \times 10^{22}\,\mathrm{cm}^{-2}$. The turbulent motions of the gas are included by converting the line-of-sight component of the velocity field for each grid point into an additional redshift. No excess broadening is considered locally due to, for instance, microscopic turbulent motions. The total redshift z_i of the i^{th} cell is computed using the classical composition, $z_i = z_0 + z_{v,i} + z_0 z_{v,i}$, where $z_{v,i}$ is the shift induced by the velocity of the cell along the line-of-sight (Equation 4.3). The `apec` normalisation $\mathcal{N}_i$ is used for each cell (Equation 4.2).

The photon generation and E2E simulation follow the same process detailed in Section 4.1, with the same instrumental responses. Since the main objective is the estimation of turbulent velocities and the velocity power spectrum, no background nor crosstalk are included in the simulation to avoid introducing additional systematic errors. However, as shown above, an accurate knowledge of the background components should not bias the following results. Additionally, since the observations are focused on the centre of a bright Coma-like cluster, the astrophysical and instrumental background levels are expected to be sub-dominant with respect to the cluster emission. A typical exposure time of 100 ks is considered for any of the following observations.

Post-processing of the data

Due to limited statistics of the observation, pixels are binned into regions of equal S/N ratio of 200 (i.e. $\sim 40\,000$ counts per region) to reduce the uncertainty on the parameter estimation. Binning is performed using an adapted Voronoï tessellation of the plane (Cappellari & Copin, 2003), which provides here ~ 150 regions over the X-IFU detector area (~ 20 pixels per region, Figure 4.13 – *Bottom*). This choice is motivated by the will to remain generic in our approach (this binning can be applied to any detector) and to provide round-shaped regions of constant S/N ratio, which ensure a faster convergence than square regions for the cosmic variance computation presented in CL19.

Spectra are fitted using the input XSPEC model with an additional broadening component (`bapec`) to account for turbulent velocities. A simultaneous fit of all the free parameters (temperature, abundance, redshift, velocity broadening, and norm) is performed. Results from the fits are excellent. No bias is visible on both parameters, and the statistical error distribution of the measured velocity shift, δC_{stat}, is consistent with a centred Gaussian, of standard deviation $\sigma_{\mathrm{stat},C} = 34\,\mathrm{km/s}$ (Figure 4.13 – *Top right*). An example of binned input velocity map and the recovered output is provided Figure 4.13 (*Bottom*).

Validation of error formulas

The E2E simulations are used as a test case to verify Equations 4.40 and 4.41. A computation of the structure function and its variance over a very large FoV requires simulations with large spatial grids and refined meshes, which are computationally cumbersome (memory- and time-wise). Instead, we take advantage of the ergodicity assumption to simulate a large number of independent velocity fields over the previous $2048 \times 256 \times 256$ mesh, and average over these iterations to derive an estimation of SF. In practice, for a

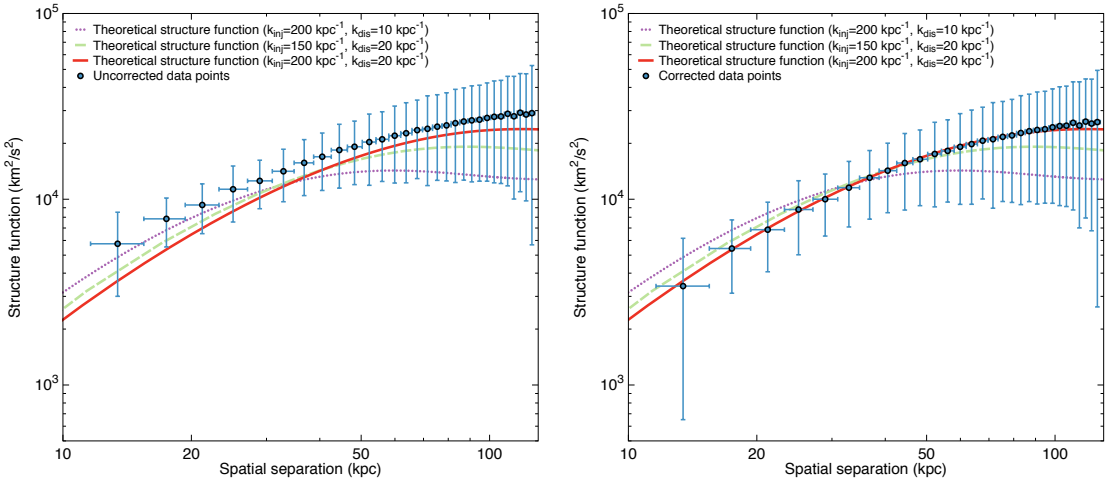

Figure 4.14: Estimated structure function ($\mathrm{km}^2/\mathrm{s}^2$) averaged over 100 different observations of a velocity field generated with the same underlying turbulent velocity power spectrum as a function of the separation s (kpc). (*Left*) Raw structure function recovered for $k_{\mathrm{inj}} = 1/200\,\mathrm{kpc}^{-1}$ and $k_{\mathrm{dis}} = 1/20\,\mathrm{kpc}^{-1}$. Different theoretical structure functions are also shown, the one associated to the run is given by red solid line. (*Right*) Same as left panel but the data points are corrected for the statistical bias and the binning projection effects (see CL19 for more information on the latter). In both cases, error bars indicate the $\pm 1\sigma$ deviation within the 100 iterations.

given choice of the turbulent velocity power spectrum (i.e. a subset of α, k_{inj} and k_{dis}), we create 100 different velocity fields, which are then observed using the previous E2E pipeline assuming a 100 ks exposure time. We thus obtain – for one choice of P_{3D} – 100 independent synthetic velocity maps of the same random process.

In the case of the Coma cluster, we use as minimal dissipation scale of the turbulent velocity power spectrum 10 kpc, which represents a good compromise between current observational expectations (Gaspari & Churazov, 2013) and future capabilities of the X-IFU (a pixel size represents $\ell \sim 2\,\mathrm{kpc}$ at the Coma cluster redshift). Given the binned regions of our map (~ 5 pixels of diameter) any scale larger than 10 kpc should be resolved. We know that large injection scales, a few hundred kpc up to 1 Mpc, can occur due to merger events or subgroup accretion (e.g. Khatri & Gaspari, 2016). As we aim here to verify our analytical formulation of the statistical error, we consider injection scales $\leq 200\,\mathrm{kpc}$, which provide a likely description of the scale at which turbulence may be injected and keep the velocity field size within range of our available computation power. The slope of the turbulent power spectrum is fixed at $\alpha = -11/3$.

Structure function estimation: For a given P_{3D}, $\overline{\mathrm{SF}}$ can be estimated for each recovered velocity field using as separation s the distances between the centres of binned regions $\mathcal{R}$. For a Voronoï tessellation, the centres are found by taking the weighted barycentre with respect to the number of counts in each region $\mathcal{R}$. Given the homogeneous emission of the cluster toy model over the FoV, these points coincide in most of the cases with the geometrical centre of $\mathcal{R}$ (se Figure 4.13 – *Bottom right*).

Though the emission profile of the cluster is the same, the non-constant region shape provided by the Voronoï tessellation creates slightly different bins from one observation to the other. Hence, separations between regions do not follow a discrete mesh of values in each of the 100 observations of a given turbulent power spectrum. To compare the structure functions between the runs, we estimate SF on a *a priori* grid of spatial separations, equal for each iteration, and with a step size of $\sim 5\,\mathrm{kpc}$, which corresponds approximately to the (equivalent) radius of a Voronoï region. The expected value of SF in the bin is then recovered by averaging over the 100 observations. The 'true' value of spatial separation in the bin is taken by averaging all the real distances contained in the bin.

Examples of the estimated structure function for a given $P_{3\mathrm{D}}$ are shown Figure 4.14, along with the 1σ deviation of each separation bin. The theoretical structure function associated with each 3D power spectrum is recovered through numerical integration of Equation 4.29. As the emissivity is not constant (see Figure 4.12 – *Right*), the structure function also varies depending on the regions considered to compute it (except in annular regions as the emission satisfies a spherical symmetry here). However, since ϵ is slowly-varying over the detector FoV, only minor changes of the SF are expected ($\leq 5\%$ over the FoV). A good approximation can be obtained by evaluating Equation 4.29 (in particular $P_{2\mathrm{D}}$) on the annular radius corresponding to half of the equivalent radius of the detector. For the X-IFU this corresponds to $\theta_{\mathrm{eff}} \sim 34\,\mathrm{kpc}$ ($1.24'$).

As expected, the uncorrected values of the structure function are positively biased due to the statistical uncertainties in the measurements (Figure 4.14 – *Left*). This bias can be corrected by subtracting $2\sigma^2_{\mathrm{stat},C}$. Even with this correction, slight discrepancies of the order of 5% remain, which can be related to binning effects (see CL19). After subsequent correction (Figure 4.14 – *Right*), the average value of the structure function matches very accurately the analytical structure function ($\leq 3\%$ in average on the relative difference between the simulations and the computed structure function over all separations). Remaining sources of error may be related to the number of iterations (100) used here to recover the expected value of the structure function. Small numerical effects related to the integration, the choice of θ_{eff} and the binning may also create small deviations.

Structure function variance: The variance of the structure function over the runs can be compared to the theoretical formulas. The geometrical terms, $N_{nei}(s)$ and $N_p(s)$, are derived from the binning map. D can be computed through $\overline{\mathrm{D}}$, unbiased for a centred Gaussian statistical noise. Its variance however, is biased (see CU19):

$$\mathrm{Var}[\overline{\mathrm{D}}(s)] = \mathrm{Var}[\mathrm{D}(s)] + \frac{2\sigma^2_{\mathrm{stat},C} N_{nei}(s)}{N_p(s)} \tag{4.45}$$

$\mathrm{Var}[\mathrm{D}(s)]$ is therefore estimated through $\mathrm{Var}[\overline{\mathrm{D}}(s)]$ over the 100 simulations, and corrected of its bias. The intrinsic cosmic variance is obtained using the formulas provided in CL19. To do so, a specific circular FoV of the instrument and a pixel size (or bin size) are needed. We consider here that bins are well described by disks of the same diameter as the Voronoï regions. Similarly the hexagonal detector is approximated by an equivalent disk. Three different options were considered for its radius R:

- 'Equivalent' radius R_{eq}. $R_{\mathrm{eq}} = \sqrt{\mathcal{S}_{\mathcal{A}}/\pi} = 67.6\,\mathrm{kpc} = 149.4''$.

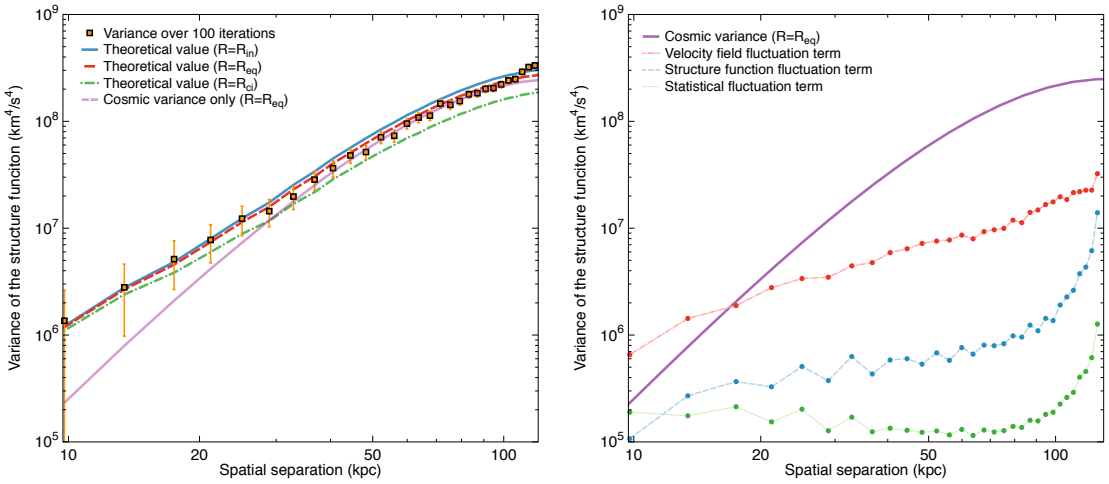

Figure 4.15: (*Left*) Structure function variance ($\mathrm{km}^4/\mathrm{s}^4$) averaged over 100 observations of a velocity field generated with the same underlying turbulent power spectrum ($k_{\mathrm{inj}} = 1/200\,\mathrm{kpc}^{-1}$, $k_{\mathrm{dis}} = 1/20\,\mathrm{kpc}^{-1}$) and corresponding $\pm 1\sigma$ error bars as a function of the separation s (kpc). The comparison to the theoretical models derived from the simulation and the formulas by CL19 is shown for a circular FoV of R_{in} (blue solid), R_{eq} (red dashed) or R_{ci} (green dash-dotted). The sheer contribution of the cosmic variance without statistical terms for $R = R_{\mathrm{eq}}$ is given in light purple. (*Right*). Error contributions in the total variance for the previous case for $R = R_{\mathrm{eq}}$ when $\sigma_{\mathrm{stat},C} = 34\,\mathrm{km/s}$. The data points for the statistical and structure function fluctuation term are derived from analytical formulas, while the velocity field fluctuation term is computed using the 100 iterations (see text).

- Radius of the inscribed circle, $R_{\mathrm{in}} = 63.9\,\mathrm{kpc} = 141.2''$.
- Radius of the circumscribed circle, $R_{\mathrm{ci}} = 82.1\,\mathrm{kpc} = 181.4''$.

Figure 4.15 (*Left*) shows the comparison for different values of R, and the case without statistical corrections. For large s, the statistical terms presented in Equation 4.41 have little effect, but must be accounted for when considering smaller separations. Also, despite the slight differences between the considered radii, changes in the analytical values of the variance up to a factor 2 are observed when statistics are included. Simulation points are comprised between the $R = R_{\mathrm{ci}}$ and $R = R_{\mathrm{in}}$ curves, and all three curves show a good agreement within error bars. Deviations between the simulated data and predicted errors is lower than 20% for all separations (i.e. less than 10% in standard deviation) with R_{eq} providing the best results (10% in variance, hence $\leq 5\%$ in standard deviation).

These curves accurately recover the shape of the expected variance, but show a consistent deviation at large separations, which can be related to two distinct effects. On the one hand, these separations are sampled only a handful of times within a single X-IFU pointing (i.e. one or two regions per iteration are separated by a detector diameter), thus creating a simulation-related sample variance in the data. On the other hand, the circular FoV approximation reaches a limit for separations of the same order (or higher) than R_{eq}. Smaller deviations could also be caused by box-size effects of the turbulent velocity grid.

Other factors can explain the remaining deviations between the theoretical curves and

the simulations:

- The computation of the analytical error formulas involve complex numerical integrals, which can account for errors in the variance around 1 to 2%.
- The E2E simulation sample used in the simulations (100) is sufficiently large to have a good estimate of the average, but may be insufficient for an accurate value of the variance, up to a level of 10%. Results with 250 iterations indicate a better agreement with the theoretical error formulas (improvement of a few %), suggesting that part of the deviations are consistent with a small size of the sample. To reduce this contribution within numerical errors (i.e. below the 2% threshold) at least 2500 iterations are required. Such an increase would however render the computational time unreasonable ($\sim$ 1 week of computational time for 250 iterations for a given $P_{\rm 3D}$ with our current set-up).
- The approximation of the X-IFU FoV with a disk. A better description of the detector geometry in the computation of the intrinsic variance component could reduce this component, especially for separations larger than the detector equivalent diameter.
- The bin shape used for the numerical computation, which assumes a uniform tessellation of the detector. Voronoï binning was chosen to represent a more generic case than simple square regions. It does not, however, verify a uniform tessellation. Test runs performed using square groups of pixels show similar results in the comparison, suggesting little impact of this particular effect on our previous results.

The previous analysis was extended to several other turbulent velocity power spectra, with $k_{\rm inj}$ within 100 and 200 kpc, and $k_{\rm dis}$ from 10 kpc to 30 kpc, showing similar results.

4.3.6 Implication of error formulas

Relative contribution and verification

Figure 4.15 (*Right*) shows the contribution of the sources of error for a given $P_{\rm 3D}$. Among the statistical error contributions, computed in each bin, the velocity field fluctuation term dominates the other two and shows a monotonous trend. The structure function fluctuation term is lower than the previous contributor, but becomes comparable at high s, where the number of regions used to compute SF is small. Finally, as expected, the purely statistical term is the smallest and can in most cases be neglected. Its contribution is mostly on small separations and minimal on average separations, where N_p is highest. We note however that its value becomes comparable to the cosmic variance for small s.

For $\sigma_{{\rm stat},C} = 34\,{\rm km/s}$, used here, the contribution of the intrinsic cosmic variance dominates over most of the separations ($s \geq 30/40\,{\rm kpc}$). This result holds for all the tested $P_{\rm 3D}$. As suggested by Figure 4.15 (*Left*), the addition of the statistical terms in the estimation of the total variance is mainly visible at small separations, validating the formulas out to $\sim 50\,{\rm kpc}$. To test the previous formulas more accurately over high separations requires instead to decrease the contribution of the cosmic variance or to increase the other statistical contributors to enhance error terms for high s. All things being equal, these terms scale with $\sigma^2_{{\rm stat},C}$ and $\sigma^4_{{\rm stat},C}$ respectively. They become dominant when $\sigma_{{\rm stat},C} \geq 100\,{\rm km/s}$. This can be achieved using larger pointings with a similar binning and exposure (to reduce

the cosmic variance), or by artificially increasing the statistical error, by for instance considering shallower exposures. The latter was considered. Results obtained after reducing the exposure to 20 ks are once again in agreement with the theoretical formulas (see CU19).

Practical estimation of errors

As shown in CL19, an estimation of the cosmic variance can be obtained numerically with several approximations on the detector geometry. The statistical terms however are intrinsically related to the observational set-up. We provide here some solutions to estimate the quantities involved in Equations 4.40 and 4.41 for a specific instrumental configuration.

The values of $N_p(s)$ and $N_{nei}(s)$ are related to the binning and geometry of the detector, and can be determined analytically with high accuracy. $\sigma_{\mathrm{stat},C}$ will be a direct output of the observation. However, an *a priori* estimation of the statistical error of an observation, which could be used to forecast structure function errors before an observation (e.g. to optimise the exposure strategy) is more challenging. Crude estimations can be derived using a simple Poissonian approach using the flux of the source and the exposure time. Provided E2E simulations of the instrument become sufficiently representative, a promising solution could be to derive $\sigma_{\mathrm{stat},C}$ numerically (a single pointing is required).

The variance of D is by far the most challenging term to estimate, as it requires multiple observations. In our simulations, the ergodicity assumption simplifies these computations, as accurate estimations of the previous terms can be obtained by averaging over a large number of iterations. This approach does not hold in flight, as multiple realisations of the same turbulent field are unlikely to be met (statistically speaking), even assuming a self-similar behaviour of the turbulence between clusters. Even if multiple pointings in a larger mapping of the same object are performed, an accurate computation of the variance cannot be achieved unless the emission profile does not vary across the entire observed area, which only concerns a handful of clusters (at a zeroth order approximation). A solution is once again to use numerical simulations. An idea is to find analytical formulas, similarly to CL19, and use them to obtain a fast numerical estimation of $\mathrm{Var}[\mathrm{D}(s)]$ for a given power spectrum assumption. As this remains to be investigated, dedicated MC simulations remain at the moment the other possible solution. Although relying once again on an iterative method, these simulations do not require a full E2E approach, and can be performed without any prior on the instrument except its geometry (implying large gains in computational time).

Towards optimising observation strategies

Under the current assumption of 100 ks pointings, we expect statistical errors on X-IFU observations to be low and well constrained. Over a single pointing, an accurate knowledge of the intrinsic cosmic variance will be sufficient to provide an error estimation of the SF at large separations (Figure 4.15), and thereby to investigate turbulence at large scales (i.e. injection scale). Statistical terms can in this case be neglected in the error computation. On the contrary, when measuring the structure function for small separations (i.e. to probe dissipation scales), a good estimation of all the statistical terms is paramount to ensure a proper error description. Depending on the science objectives of the X-IFU (large- or small-scale turbulence investigations), the observational strategy can therefore be optimised.

For a constant exposure time, several options can be explored. Deep pointings would provide a constant value of the cosmic variance, but significantly reduce $\sigma_{\mathrm{stat},C}$, which may be interesting to explore small separations. On the contrary, since statistical errors are negligible at high s, multiple shallower pointings could be used to explore larger separations (notably larger than the detector) while reducing the cosmic variance. An optimal point where all errors are comparable across the separations could also be used. The formulas derived here in CL19 and CU19 demonstrate that accurate error estimations of the SF can be found by numerical integration. This approach is complementary to studies of turbulence limited through an iterative approach (e.g. 100 simulations of very large grids), which can now be reduced to a handful of simulations (mostly to evaluate Var[D]).

4.4 Conclusions

E2E simulations are a tool of choice to test the scientific performances of the X-IFU. They provide a closed environment, with a well defined framework, which can be used to forecast typical results and assess the feasibility of science objectives. In this chapter, I applied this approach to the observation of clusters of galaxies. The main results can be summarised as follows:

- I have developed a full E2E pipeline, which covers all the steps of a typical X-ray observation from the photon generation using realistic astrophysical sources (either from other simulations or toy models), to its post-processing, including all the perturbative effects of the instrument (geometry, instrumental effects, noise, background).
- Using this pipeline I have demonstrated that the X-IFU will provide an unprecedented view of the ICM properties, both at local redshift and across time, even using 100 ks observations. In particular, the X-IFU will provide a picture of the chemical enrichment of the Universe through accurate measurements of abundance ratios.
- By using E2E results as a toy observation of a cluster sample, I have shown that the X-IFU will be capable of constraining the underlying enrichment models of the ICM (related to $\mathrm{SN_e}$ and AGB winds) and break model degeneracies.
- I have demonstrated that the cosmic variance related to the observation of turbulence in the ICM can be characterised using a direct approach, even in the case of an imperfect instrument, limited by the finite statistics of the observations. This method shows that cosmic variance can be estimated through semi-numerical formulas, instead of using iterative approaches. The formalism introduced here was tested on typical X-IFU observations and showed an excellent agreement, hence opening the window for optimisations in future observations of the ICM turbulence.

CHAPTER 5

Calibration studies of the X-IFU

The challenging observations performed by the X-IFU will provide astronomers with raw data, in detector units. Scientific breakthroughs will be possible by transforming these quantities (currents, voltages, temperatures) into meaningful physical parameters (e.g. abundances, velocities), provided a thorough calibration of the instrument. For high-energy missions (and even more for high spectral resolution instruments), in-flight calibration is a challenging task due to the few known standard candles in the sky (Kirsch et al., 2005). This makes ground calibration essential. Although calibration data can only be obtained through measurements on flight-like hardware, numerical simulations remain a powerful tool early in the mission, when prototypes are still under development.

A significant effort to design the calibration of the instrument was started by the X-IFU calibration team (XCaT). As a member of the XCaT, I performed various investigation to understand the calibration of some of the X-IFU most important instrumental parameters. I provide here a summary of these studies regarding the energy scale, the instrumental quantum efficiency, the MXS dead time or the monitoring in flight of the NXB. The referential lines considered for spectral calibration and their corresponding uncertainties are listed in Appendix H. The following results are summarised in Cucchetti et al. (2018a,b,c,d).

5.1 Energy scale drift correction studies

Calorimetric detection of X-ray photons is based on the absorption of an incoming photon on the pixels. As explained in Chapter 2, the absorbed energy will create an increase in temperature, detected as a current pulse by the TES. This pulse retains the information on the initial energy of the photon, which is recovered in two steps. First, the signal is filtered using, for instance, optimal filtering (Szymkowiak et al., 1993) to derive its pulse height PHA (e.g. in µA). Then, the PHA converted into energy units using the energy scale (or gain scale) function, $f_{\rm es}$, such that $E = f_{\rm es}(\mathrm{PHA})$.

Micro-calorimeters are extremely sensitive to their environment, and a small change in their operating conditions (e.g. thermal bath, magnetic field) may result in large changes in

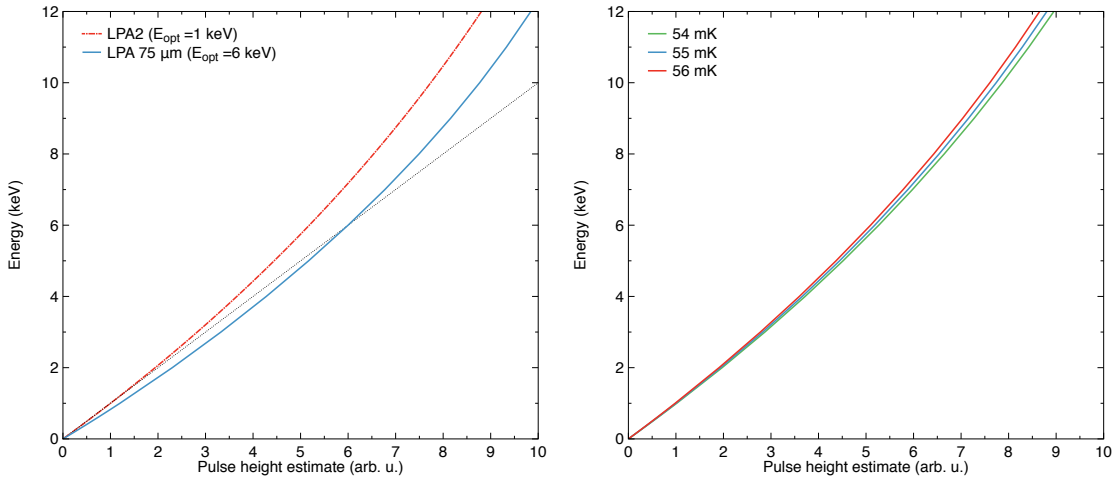

Figure 5.1: Simulated energy scale functions using `XIFUSIM`. (*Left*) Effect of the TES model and the optimal filtering energy E_{opt} on the shape of the function for a former LPA2 pixel (red dash-dotted) and the current baseline (blue solid). The dashed line represents a purely linear case. (*Right*) Example of three energy scale functions for different T_{bath} set points.

their intrinsic value of f_{es}. On short time scales, these changes will result in a degradation of the instantaneous energy resolution. Integrated over time, these drifts result instead into systematic errors in the energy scale of the instrument. Currently, a mean knowledge error of 0.4 eV ($\pm 1\sigma$) on 0.2 – 7 keV is specified for the X-IFU high-resolution events. These requirements are driven by the need to measure bulk-motion velocities of 100 km/s with uncertainties of 20 km/s (at 6 keV). In flight, these changes will be monitored per pixel using housekeeping data and through dedicated reference lines provided by MXS. The energy scale will then be corrected accordingly during post-processing. In this section, I investigate ways of performing this correction using the MXS data, and compare their accuracy in light of the current requirements.

5.1.1 Sensitivity of the energy scale function

The energy scale function is related to the physics of the TES superconducting transition. Different pixels will thus provide different shapes of f_{es} (Figure 5.1 – *Left*). Since TESs are intrinsically nonlinear, so is their energy scale function. When using optimal filtering, linearity can be forced at one specific energy of the bandpass, E_{opt}, which verifies $\mathrm{PHA}_{\mathrm{opt}} \equiv E_{\mathrm{opt}}$. Since a single optimal filtering template (per grade) is assumed, its choice – and the choice of E_{opt} – also influences the shape of the energy scale (Figure 5.1 – *Left*).

As of today, no physically justified functional formula exists to match f_{es}. The function is therefore measured on the ground using a set of fiducial lines (see Eckart et al., 2018), interpolated using polynomials and used as such in flight. To understand changes on the energy scale function related to the TES environment, data from flight-like pixels under different operating points is required. As the X-IFU pixels are still undergoing an optimisation, no representative measurement is available for this study. Insight on the sensitivity of the gain scale can therefore only be obtained numerically.

In our simulations, AC-biased TESs are modelled using the current pixel baseline (LPA 75µm AR0.5), reminded in Appendix D. At electro-thermal equilibrium, these detectors have a bath temperature, T_{bath}, of 55 mK, and a bias voltage, V_{bias}, of 112.65 $\mathrm{nV_{rms}}$. For simplicity, this study is reduced to a single equivalent pixel, as correction on a pool of pixels is strictly equal.[17] For a given operating set point, the impact of an X-ray of energy E can be simulated using `XIFUSIM`. As we investigate systematic effects only, pulses are simulated without noise. The recovered event is filtered using a 6 keV optimal filtering template to determine the corresponding PHA (courtesy P. Peille). By repeating this process over the entire bandpass (0.2 – 12 keV) we can derive, for that particular set point, the energy scale function f_{es} and its inverse f_{es}^{-1}. Finally, by changing the set point, we can recover the energy scale function at any other set point (Figure 5.1 – *Right*).

In theory, many parameters can influence the energy scale function. Assuming the TES transition models implemented in `XIFUSIM`, only four are considered: T_{bath}, V_{bias}, a linear amplification in the gain of the onboard electronics, G_{amp} (which multiplies linearly the energy scale function, Prêle et al. 2016), and a constant additional power load on the TES, P_{load}, included in the electro-thermal equations of `XIFUSIM` (Equation 3.1).

5.1.2 Modulated X-ray sources

In-flight monitoring of the energy scale can be performed using the housekeeping data of the subsystems (temperature, electronic gains) to compensate for changes over the observations. An additional ^{55}Fe source with a count rate of 2 cts/s/pix in beginning of life is planned on the FW for verifications. To satisfy the challenging 0.4 eV requirement, the energy scale will also be monitored and corrected using a MXS developed by SRON, similar to the one flown on *Hitomi*/SXS (de Vries et al., 2010). The MXS is a high-voltage cathode, which creates flashes of electrons towards its anode, where a fine metallic layer is deposited. Electrons interact with the layer to generate stable, referential lines on the detectors. The layer itself can be adapted to generate different fluorescence lines, depending on the calibration needs. Currently, two types of MXSs are considered:

- Two high-energy MXSs to monitor the gain (high count rates), the high energies allowing a more accurate correction over the bandpass.
- Two low-energy indirect MXSs for occasional verification or in-flight recalibration.

Various configurations of the MXS were tested through `GEANT4` by varying the anode layers. The accuracy of these simulations was compared to measurements performed during *Hitomi*/SXS ground calibration, with excellent results (de Vries et al., 2018). We investigate four different types of high-energy MXSs to test gain drift correction techniques. As per-pixel monitoring is currently excluded due to dead time considerations (Section 5.2), we assume that the correction occurs on a pool of N_{pool} (see Appendix H for line energies):

- Single-line MXS (Cu K_α) with 2.25 cts/s/pool.
- *Hitomi*-like MXS (Cr/Cu K_α) with 1.125 and 1.125 cts/s/pool per line.
- Titanium MXS (Ti/Cr/Cu K_α) with 0.5, 0.85 and 0.9 cts/s/pool per line.
- Broadband MXS (Si/Ti/Cr/Cu K_α) with 0.25, 0.5, 0.75 and 0.77 cts/s/pool per line.

The baseline design for the X-IFU remains to be determined, but will likely be similar to either the second or the third configuration. Monitoring will occur on 1 ks time scales,

[17] Neighbouring pixels will likely see similar drifts, and will have similar corrections.

which is deemed a good compromise between instantaneous degradation of the energy resolution and sufficient statistics for the energy scale correction. Count rates for the MXS are chosen to verify 0.2 eV (FWHM) accuracy of the line centroids measured on a pool of N_{pixel} over 1 ks (see Appendix H) while remaining low in term cathode fluxes (to increase lifetime). The corresponding K_β lines will also be observed, but the low count rates only allow a verification of the energy scale rather than an accurate monitoring.

5.1.3 Linear and nonlinear correction techniques

Different techniques exist to monitor the gain drifts over time. To investigate purely systematic effects, we first neglect the statistics of the MXS, which are assumed with an infinite count rate (see Section 5.1.5 otherwise), and we consider a single-line configuration (Cu K_α of energy $E_{\text{cal}} = 8.04\,\text{keV}$) for simplicity. For each correction technique, we compare the 'true' energy scale function derived with `XIFUSIM` and the one corrected using the MXS lines to estimate its overall accuracy.

Linear correction

The simplest assumption is to consider any deviation from the reference energy scale function f_{es} as linear. At the time t of the correction, the measurement of the pulse height of the referential line $\text{PHA}_{\text{cal}}(t)$ gives access to the new energy scale function $f'_{\text{es}}(t)$ by considering it a homothetic transformation of f_{es}, i.e.:

$$f'_{\text{es}}(t) = \frac{f_{\text{es}}(\text{PHA}_{\text{cal}}(t))}{f_{\text{es}}(\text{PHA}_{\text{cal}}(0))} \times f_{\text{es}}(t) \tag{5.1}$$

where $f_{\text{es}}(\text{PHA}_{\text{cal}}(0)) = E_{\text{cal}}$, by definition of a well-calibrated energy scale function measured on the ground or set after the previous correction.

This type of correction is limited for nonlinear detectors such as micro-calorimeters, and notably TESs (Porter et al., 2016). This can be demonstrated by simulating a change of $\pm 0.5\,\text{mK}$ in T_{bath} and by correcting it with a linear stretch. Knowing that X-IFU bath temperature shall be controlled to better than 0.5 mK over the mission lifetime (even as good as $\sim 1\,\mu\text{K}_{\text{rms}}/\text{ks}$, Charles et al. 2016), this sets a conservative upper boundary. Figure 5.2 (*Left*) shows that even with a perfect knowledge of the calibration line, the new gain function is recovered with residuals greater than 0.4 eV. The linear correction can in fact compensate changes up to 0.17 mK in T_{bath}. Although this may be sufficient for T_{bath} over regular observations, this technique is limited in correcting changes in any of the other operating parameters, and is hence unsuited to meet the X-IFU challenging requirements.

Nonlinear correction

More advanced techniques (so called 'nonlinear techniques') were introduced to increase the accuracy of the correction. They extend the concept of the previous technique and considering multiple values of the energy scale for different TES set points (e.g. different operating bath temperatures), therefore allowing a more accurate interpolation of the new energy scale function (see Porter et al., 2016, for more details). As an example, we consider

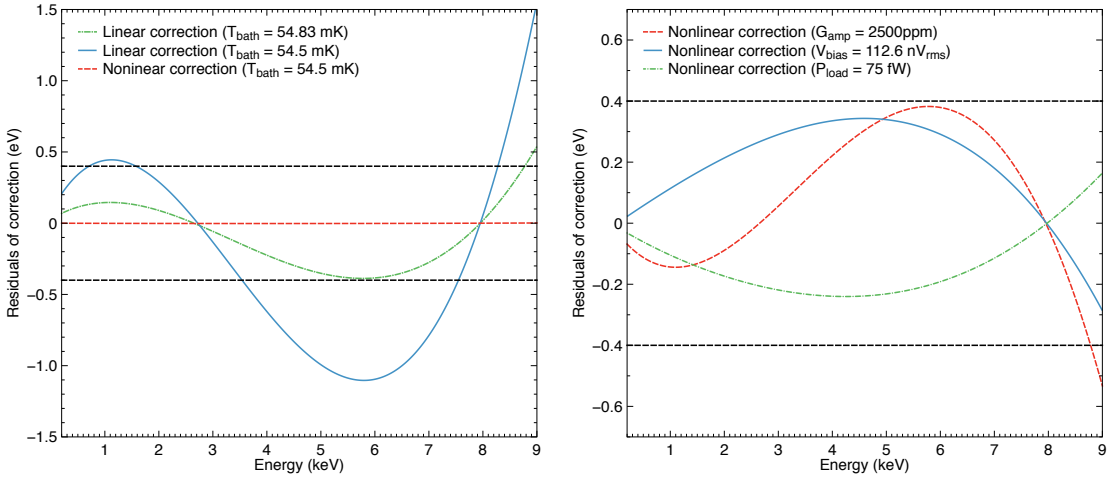

Figure 5.2: Correction residuals (eV) along the energy band (keV). In both cases, the horizontal black dashed lines represent the 0.4 eV requirement. (*Left*) Residuals for a -0.17 mK (green dash-dotted) and a -0.5 mK (blue solid) change in T_{bath} corrected with a linear technique, or with the nonlinear technique (red dashed). (*Right*) Residuals for a -0.05 $\mathrm{nV_{rms}}$ change in V_{bias} (blue solid), 2500 ppm in G_{amp} (red dashed), and +75 fW in P_{load} (green dash-dotted) corrected using the nonlinear technique.

as calibration data the gain functions $f_{\mathrm{es},54}$, $f_{\mathrm{es},55}$ and $f_{\mathrm{es},56}$ computed for a value of $T_{\mathrm{bath}} = 54$, 55 and 56 mK respectively (Figure 5.1 – *Right*).

The principle is to use the information of the three calibration energy scale functions to interpolate a new function through a second-degree polynomial. We consider a variation in T_{bath}. Via the three calibration curves and notably the value of the referential lines at the various calibration set points (i.e. the values of $\mathrm{PHA}_{\mathrm{cal},54}(0)$ and $\mathrm{PHA}_{\mathrm{cal},56}(0)$), we can interpolate a second degree polynomial p_{cal} between the bath temperature, T_{bath}, and the calibration pulse heights, $\mathrm{PHA}_{\mathrm{cal}}$. At a given time t, from $\mathrm{PHA}_{\mathrm{cal}}(t)$ and by inverting p_{cal}, we derive an effective bath temperature $T_{\mathrm{bath,eff}}$ related to this change such that:

$$p_{\mathrm{cal}}(T_{\mathrm{bath,eff}}) = \mathrm{PHA}_{\mathrm{cal}}(t) \tag{5.2}$$

To determine the new energy scale function f'_{es}, we compute a polynomial p_E at each energy E using the calibrated values of PHA. Using $T_{\mathrm{bath,eff}}$, the associated PHA is:

$$\mathrm{PHA}(E) = p_E(T_{\mathrm{bath,eff}}) \tag{5.3}$$

The corrected gain function can thus be recovered by repeating this process over the bandpass. The nonlinear technique is very efficient and achieves low correction residuals (Figure 5.2 – *Left*). Even for large temperature variations (~ 1 mK), the algorithm is able to recover the original gain curve with excellent accuracy. This approach is however based on the assumption that all changes in the TES operating conditions can be described by changes in T_{bath}. This is unfortunately not always the case, and changes in V_{bias} or G_{amp} still cause substantial drifts in the correction (see Figure 5.2 – *Right*).

5.1.4 Towards more advanced correction techniques

The nonlinear correction technique offers promising results but is nevertheless not fully satisfactory as: (1) most of the parameters will vary simultaneously creating larger errors, (2) the gain drift error is only a part of the total contribution to the total energy scale budget of 0.4 eV. For these two reasons, these techniques must be improved.

Improving the nonlinear technique

To improve the correction accuracy, a first solution is to change the number of calibration curves used to interpolate the data. Despite slight improvements for the effective parameter, no significant improvement is seen using this approach.

A second idea is to verify which optimal effective parameter can be used for the reconstruction. After changing between T_{bath}, V_{bias}, G_{amp} and P_{load}, we estimate that for a single-parameter correction, T_{bath} remains the best option. When V_{bias} or P_{load} are used, results show a more nonlinear behaviour, which degrades the overall correction.

The most promising solution is to take advantage of the multiple lines available in the MXS. We consider for instance a MXS with a Cr and Cu K_α lines. As previously, we can compute for each of these lines two separate values of the effective parameters. Two options were explored: either use the average of the two effective parameters as one single effective parameter for the nonlinear correction, or interpolate the effective parameter over the bandpass to obtain $T_{\mathrm{bath,eff}}(E)$ and use this energy dependent value of the parameter during the interpolations. The first approach was discarded as it showed less accurate results than a single-line approach. The second one however, showed promising results. When multiple lines are considered, the result is highly improved, notably for a drift in V_{bias} or a linear change G_{amp} (Figure 5.3). Even better results can be expected with more lines. This concerns all parameters, and is the best improvement found for the nonlinear correction (Table 5.1). This technique is also attractive as – for a given MXS – it implies no additional technical complexities, moderate trade-offs, and more leverage in the correction. The use of multiple lines requires however a closer investigation of the statistics involved, as the overall count rate of the MXS is limited (Section 5.1.5).

Multi-parameter correction

If the previous improvements are insufficient for an accurate correction, new techniques need to be put forward. For DC-coupled detectors such as TESs, the correction can be improved by using, in addition to the PHA, the value of the pixel's baseline Ba (i.e. its set point current in µA) which depends on the operating conditions of the TES (Cucchetti et al., 2018b). This allows the extension of the nonlinear technique into a two-dimensional space, significantly improving the energy scale correction for larger parameter excursions.

During the calibration phase we measure both these physical quantities for different sets of TES parameters P_1, P_2, e.g, $T_{\mathrm{bath}}, V_{\mathrm{bias}}$. Via these calibration curves, we interpolate the two-parameter function $\underline{h}_{2D,\mathrm{cal}} : \mathbb{R}^2 \to \mathbb{R}^2$ with the calibration line such that

$$(\mathrm{PHA}_{\mathrm{cal}}(0), \mathrm{Ba}_{\mathrm{cal}}(0)) = \underline{h}_{2D,\mathrm{cal}}(T_{\mathrm{bath}}, V_{\mathrm{bias}}) \tag{5.4}$$

using a two-dimensional second order polynomial interpolation. To do so, six curves for different sets of P_1, P_2 are required. Using in-flight measurements of the calibration pulse (both its pulse height $\mathrm{PHA_{cal}}$ and baseline $\mathrm{Ba_{cal}}$), we can derive the set of effective parameters for the drift $(P_{1,\mathrm{eff}}, P_{2,\mathrm{eff}})$ by inverting the previous function. As no analytical inversion is possible, this amounts to solving the following inverse problem:

$$(P_{1,\mathrm{eff}}, P_{2,\mathrm{eff}}) = \min_{P_1,P_2}(||(\mathrm{PHA_{cal}}(t); \mathrm{Ba_{cal}}(t)) - \underline{h}_{2D,\mathrm{cal}}(P_1, P_2)||_2) \tag{5.5}$$

where $||\cdot||_2$ is Euclidean norm. The minimisation is performed using a robust least squares approach. Using the effective parameters found in Equation 5.5, the corrected value of the PHA for an energy E can be obtained using:

$$\mathrm{PHA}(E) = \underline{h}_{2D,E}(P_{1,\mathrm{eff}}, P_{2,\mathrm{eff}}) \cdot \underline{e}_1 \tag{5.6}$$

where $\underline{h}_{2D,E}$ is interpolated from the ground calibration energy scale functions (as done for $\underline{h}_{2D,\mathrm{cal}}$ in Equation 5.4) at the value of energy E, projected along its first dimension.

Different sets of parameters were compared to determine an optimal choice for the calibration curves. Overall, the sets (PHA, Ba) $\Leftrightarrow$ $(T_{\mathrm{bath}}, V_{\mathrm{bias}})$ and (PHA, Ba) $\Leftrightarrow$ $(T_{\mathrm{bath}}, G_{\mathrm{amp}})$ are the ones providing the best results (Cucchetti et al., 2018b). Here, we select as effective parameters the second set, i.e. $(T_{\mathrm{bath}}, G_{\mathrm{amp}})$. This combination provides both a linear and nonlinear degree of freedom in the correction, and is expected to well represent most of the drifts encountered by the TES. An example of the correction is shown in Figure 5.3 (*Left*). The same improvements considered previously for the nonlinear technique can also be applied here, notably the use of multiple lines. Depending on the nature of the drifts, this technique also provides a leverage on the set of effective parameters to provide more accurate results.

The previous techniques are compared by finding the maximal corrected excursion for each parameter (Table 5.1). Results for the multi-parameter technique are obtained using as calibration set points $\{T_{\mathrm{bath}}, G_{\mathrm{amp}}\}$: {55 mK, 0 ppm}, {56 mK, 250 ppm}, {55 mK, 500 ppm}, {54 mK, 1000 ppm}, {54.5 mK, 250 ppm}, {55.5 mK, 100 ppm}, which ensure a high stability of the algorithm (different set as the one from Cucchetti et al. 2018b).

As expected, under the caveat that lines are known perfectly, the multi-parameter multi-line technique provides the best correction of the energy scale. The presence of multiple lines comes however at a cost at high energies. As shown also in Table 5.1, when a larger correction band is considered (0.2 – 12 keV) the absence of high-energy referential lines and the simplistic polynomial interpolation of the parameters reduces the efficiency of the correction in the extrapolated parts (blue and green curves in Figure 5.3 – *Right*). Although such an accurate correction may not be required for the upper part of the bandpass, the final choice of the MXS configuration shall be pondered by the scientific needs driving the absolute knowledge of the energy scale over the high-energy band.

5.1.5 The effect of statistics

In flight, changes in the operating conditions will be seen as slow-moving drifts over the TES operating conditions. To correct them, MXS counts will be integrated over 1 ks. However, this introduces statistical uncertainties on the referential line centroids, which

Technique	Nonlinear correction [RD8]		Multi-parameter nonlinear correction (T_{bath}, G_{amp})			
Configuration Line(s) used	Single-line Cu	Two-line Cr, Cu	Single-line Cu	High-energy Cr, Cu	Titanium layer Ti, Cr, Cu	Low-energy Si, Ti, Cr, Cu
Bandpass: 0.2 – 7 keV (< 0.4 eV)						
ΔT_{bath} (mK)	≥ 3	≥ 3	≥ 3	≥ 3	≥ 3	≥ 3
ΔV_{bias} ($\mathrm{nV_{rms}}$)	$\pm$ 0.07	$\pm$ 0.30	$\pm$ 0.07	$\pm$ 1.15	$\pm$ 1.35	$\pm$ 1.55
ΔG_{amp} (%)	$\pm$ 0.25	$\pm$ 0.23	$\pm$ 0.53	$\pm$ 0.93	$\pm$ 1.02	$\pm$ 1.05
ΔP_{load} (fW)	+80	+175	+100	+180	+200	+225
Bandpass: 0.2 – 12 keV (< 2 eV)						
ΔT_{bath} (mK)	≥ 3	≥ 3	≥ 3	≥ 3	≥ 3	≥ 3
ΔV_{bias} ($\mathrm{nV_{rms}}$)	$\pm$ 0.07	$\pm$ 0.24	$\pm$ 0.09	$\pm$ 0.55	$\pm$ 0.35	$\pm$ 0.30
ΔG_{amp} (%)	$\pm$ 0.13	$\pm$ 0.23	$\pm$ 1.17	$\pm$ 0.65	$\pm$ 0.62	$\pm$ 0.57
ΔP_{load} (fW)	+134	+190	+165	+140	+130	+121

Table 5.1: Maximal change in TES operating conditions recovered within 0.4 eV over 0.2 – 7 keV and within 2 eV over 0.2 – 12 keV using various correction techniques and different MXS configurations. A perfect knowledge of the correction lines is assumed. Parameters considered here are T_{bath} (in mK), V_{bias} (in $\mathrm{nV_{rms}}$), G_{amp} (in % of multiplicative factor) and P_{load} (in pW - always positive). Deviations are given with respect to the TES equilibrium set point, i.e, $T_{\mathrm{bath}} = 55\,\mathrm{mK}$, $V_{\mathrm{bias}} = 112.65\,\mathrm{nV_{rms}}$, $G_{\mathrm{amp}} = 0\,\mathrm{ppm}$ and $P_{\mathrm{load}} = 0\,\mathrm{pW}$.

could degrade the accuracy of the correction. To include statistics, we generate the MXS lines using a random Poisson sampling of the corresponding line profile (see Appendix H) convolved with the energy resolution of the instrument. The line is generated in PHA-space and fitted using C-statistics. The profile-weighted value of the line is then used as a calibration point for the previous techniques. By performing the correction over the same drift multiple times, the associated statistical error can thus be computed (see Figure 5.3 – *Right* and the corresponding $\pm 1\sigma$ envelopes). In average, results obtained with statistics remain consistent with the results presented in the previous sections, but are individually less accurate (see Cucchetti et al., 2018a, for a comparison on LPA2 pixels).

The introduction of statistics is used to test the efficiency of the multi-line corrections for a fixed MXS configuration. In this case, each line will take part of the overall count rate, causing centroid errors affecting the correction accuracy. We find that results depend on the drift (Cucchetti et al., 2018b). For simple drifts (e.g. small changes in T_{bath} or G_{amp}), a single line provides an excellent correction while limiting statistical errors. For more complex changes however (e.g. simultaneous changes in various TES parameters), the use of a single line is not sufficient to decrease the residual systematic errors to an acceptable level, and multi-line schemes are more accurate. This effect is related to the interpolation error made on the effective parameters when the statistics of the lines are low. When the drift is sufficiently simple, the correction is always good. On the other hand, individual interpolation errors are larger when multiple lines are used, causing a slightly less accurate correction. On the contrary, when multiple parameters vary, the information brought by multiple lines provides a stronger lever to reduce the systematic residuals of the correction, despite the larger statistical errors.

In flight, simultaneous drifts are likely to occur in all parameters. The extra information provided by two or three lines (coupled with housekeeping data) will provide a more robust

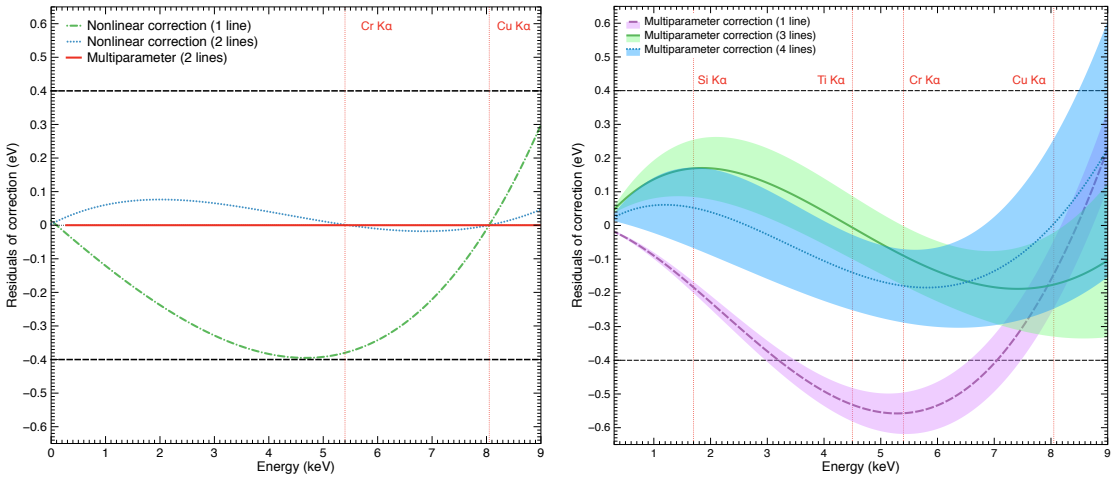

Figure 5.3: Same as Figure 5.2. The vertical red dotted lines remind the calibration lines. (*Left*) Residuals for a $+0.07\ \mathrm{nV_{rms}}$ change in V_{bias} corrected using the nonlinear correction with one (green dash-dotted) or two calibration lines (blue dotted), or the multi-parameter correction with two calibration lines (red solid). (*Right*) Residuals and $\pm 1\sigma$ envelope for a $+120\,\mathrm{fW}$ change in P_{load} corrected using the multi-parameter correction technique with one (purple dashed), three (green solid) and four calibration lines (blue dotted). The horizontal black dashed lines represent the 0.4 eV requirement.

correction of the drifts than a single-line case. For the considered count rate of the MXS and the number of pixels in a correction group, a high number of lines (≥ 4) can however degrade the correction, as the interpolation of the gain function becomes increasingly affected by the low statistics of each line. An optimal correction strategy will thus be a compromise between correction time, number of lines and total count rate.

5.1.6 Other contributors and way forward

Multiple solutions exist to meet the challenging requirement on the knowledge of the energy scale. Various assumptions were made for this study and can be questioned:

- We assumed that the curves computed using `XIFUSIM` are perfectly known. In practice, all energy scale curves calibrated on the ground will possess an uncertainty, which needs to be included in the overall error. Provided enough calibration time ($\sim 100\,\mathrm{ks}$), this component can be reduced below $\leq 0.1\,\mathrm{eV}$ (Cucchetti et al., 2018b).
- Residuals from different parameters were assumed independent. Yet, T_{bath} and P_{load} affect the pixels similarly. Although no significant correlation has been observed between any of the parameters in our models, experimental investigations are required.
- Only four parameters were investigated as part of the current `XIFUSIM` models. Although these include some main contributors, important physical quantities affecting the energy scale were not addressed here, namely the magnetic field, B. Preliminary results obtained at NASA GSFC and SRON show levels of sensitivity to B of $\sim 8\,\mathrm{eV/nT}$ (worst-case). Even assuming that the magnetic field becomes the main

contributor (with uncorrected drifts of a few eVs), the margin derived from the previous correction techniques should be sufficient to recover these drifts within 0.4 eV. The lack of a representative numerical model prevents nonetheless any further analysis. A more accurate approach will be performed as soon as models become available.
- The correction was performed here using exclusively the MXS. In flight, housekeeping data and the use of the resistive pixel in each readout channel (see Chapter 2) will provide additional layers of correction, notably for the electronic gains. The balance between all these correction possibilities remains to be determined.

All the results obtained here were derived from numerical simulations. Though they represent a promising result for the X-IFU, real conclusions can only be drawn from physical measurements, with representative pixels. Such measurements are planned in phase B, either at GSFC or within the IRAP test bench facility (see Chapter 6). They will also provide a preliminary validation of the previous techniques.

5.2 MXS dead time analysis

The count rate of the MXS will play an important role in the accuracy of the energy scale correction. Over a 1 ks correction time, the source will emit n flashes of duration δt, during which referential photons can be detected and used to monitor drifts in the gain of the instrument. To increase the statistical accuracy of the lines, a large number of MXS flashes is required. Yet, time used to monitor the gain is inevitably lost during an observation, thus creating 'dead time'. Currently, three main sources of dead time are identified: the CryoAC veto procedure, the cosmic ray hits on the wafer and the MXS flashes. Each is apportioned with a 1% contribution. In this section, I take a specific interest to the third contributor and investigate the impact of its dead time on the MXS design.

5.2.1 MXS dead time analysis: an analytical approach

Energy scale monitoring will be performed over 1 ks intervals. For a given MXS configuration (see Section 5.1.2), 0.2 eV (FWHM) are allocated as statistical uncertainty on each referential line centroid. Without loss of generality, we use here the case of a *Hitomi*-like MXS, made of a combination of Cu and Cr K_α, K_β lines.[18] To achieve this level of accuracy, a total of 945 cts and 735 cts are required for the Cu K_α and Cr K_α line respectively (see Table iv in Appendix H). Accounting for K_β lines and that two thirds of the total MXS emission falls outside the referential lines due to Bremsstrahlung, the MXS must deliver a total of 6300 cts for the correction, i.e. satisfy a count rate $M_0 = 6.3$ cts/s (Table v) within a correction pool of N_{pool} pixels ($N_{\text{pool}} \geq 10$, see below). A MXS flash creates two sources of dead time:

1. Since MXS photons are undistinguishable from sky photons, each time the MXS is turned on a dead time δt is induced.

2. Before and after each calibration pulse, a given time Δt_d and Δt_{hr} respectively is required to reconstruct MXS pulses with the highest resolution. For the baseline LPA 75µm AR0.5 pixels, $\Delta t_d = 3.16$ ms and $\Delta t_{hr} = 52.4$ ms.

[18] The reasoning being the same for any configuration, only M_0 slightly changes.

The arrival of X-ray photons follows Poisson statistics. The probability to get exactly one count per MXS flash, assuming an instantaneous MXS count rate C is

$$P(N=1) = C\delta t e^{-C\delta t} \tag{5.7}$$

If pulses are sufficiently spaced in time, the expected number of high-resolution MXS events in a second, M, is given by $M = nC\delta t e^{-C\delta t}$. For the current pixels, this implies that the number of flashes n during a second does not exceed $n_{\max} = 1/\Delta t_{hr} \sim 20$. Otherwise, if a photon is observed during one flash, the following flashes should not yield photons to obtain a high-resolution calibration pulse. The probability to have no photons on a given flash is given by $P(N=0) = e^{-C\delta t}$. The number of flashes to exclude after an event is given by $\lfloor n\Delta t_{\rm hr} \rfloor$, where $\lfloor \cdot \rfloor$ is the integer floor of the number. Likewise, if flashes become very short spaced, the previous $\lfloor n\Delta t_{\rm d} \rfloor$ flashes also need to receive zero photons to ensure high-resolution events. Thus, the probability to have M high-resolution events is

$$M = nC\delta t e^{-C\delta t(1+\lfloor n\Delta t_{\rm hr}\rfloor + \lfloor n\Delta t_{\rm d}\rfloor)} \tag{5.8}$$

The MXS will be used during sky observations. Any photon impacting the pixel in the $[t_0 - \Delta t_{\rm d},\ t_0 + \Delta t_{\rm hr}]$ time interval around a flash at t_0 will prevent its use. The sky photons also follow Poisson statistics and being statistically independent from the MXS, the probability for such an impact not to occur on the pixel is $P_{\rm sky}(N=0) = e^{-C_{\rm sky}\cdot(\Delta t_{\rm d}+\Delta t_{\rm hr})}$. Accounting for $C_{\rm sky}$, the previous equation becomes:

$$M = nC\delta t e^{-C\delta t(1+\lfloor n\Delta t_{\rm hr}\rfloor + \lfloor n\Delta t_{\rm d}\rfloor)} e^{-C_{\rm sky}(\Delta t_{\rm d}+\Delta t_{\rm hr})} \tag{5.9}$$

Finally, we also need to take into account crosstalk between pixels. We consider the three sources of crosstalk seen in Chapter 3. Each affects the MXS pulses in differently.

- The intermodulation crosstalk will affect all the pulses in the same channel during a flash. If the readout chain multiplexes $N_{\rm MUX}$ pixels, we can set a strong crosstalk constraint by requiring that a calibration event is only usable when no other MXS events is detected in the channel. Let us call $N_{\rm ctk,int}$ the number of neighbouring pixels to be excluded in the readout chain to avoid intermodulation crosstalk. The probability to have a calibration pulse on one of the pixels and strictly none on the others is $P_{\rm ctk,int} = e^{-N_{\rm ctk,int}C\delta t}$, where $N_{\rm ctk,int} = N_{\rm MUX} - 1$.
- The electrical crosstalk will affect a victim pixel over a time scale of $\Delta t_{\rm el}$ (assumed symmetric between $[t_0 - \Delta t_{\rm el}/2;\ t_0 + \Delta t_{\rm el}/2]$). This concerns frequency neighbours only, hence $N_{\rm ctk,el} = 2$. Since these neighbours are also in the same readout channel, this probability is included in the intermodulation crosstalk. If the flash frequency is very high, preceding/succeeding flashes should also be excluded to avoid crosstalk effects. The probability to have no electrical crosstalk on the $N_{\rm ctk,el}$ neighbours is therefore $P_{\rm ctk,el} = e^{-2C\Delta t N_{\rm ctk,el}\lfloor n\Delta t_{\rm el}/2\rfloor}$. We note that for the intermodulation crosstalk, as it only happens when the error signal on the SQUID is non-negligible (few tens of µs), this second rejection does not need to be taken into account.
- The thermal crosstalk works very similarly to the electrical crosstalk with a different time constant $\Delta t_{\rm th}$ after the pulse. However, the pixels to exclude are the spatial next-neighbours ($N_{\rm ctk,th}$=4), which are not (in the worst case) in the same readout channel as the considered pixel. Thus $P_{\rm ctk,th} = e^{-C\delta t N_{\rm ctk,th}(1+2\lfloor n\Delta t_{\rm th}/2\rfloor)}$.

The total number of high-resolution counts thus becomes (including crosstalk related to sky counts):

$$M = nC\delta t e^{-C\delta t(1+\lfloor n\Delta t_{\mathrm{hr}}\rfloor+\lfloor n\Delta t_{\mathrm{d}}\rfloor+N_{\mathrm{ctk,int}}+2N_{\mathrm{ctk,el}}\lfloor n\Delta t_{\mathrm{el}}/2\rfloor+N_{\mathrm{ctk,th}}(1+2\lfloor n\Delta t_{\mathrm{th}}/2\rfloor))} \times e^{-C_{\mathrm{sky}}(\Delta t_{\mathrm{d}}+\Delta t_{\mathrm{hr}}+N_{\mathrm{ctk,th}}\Delta t_{\mathrm{th}}+N_{\mathrm{ctk,el}}\Delta t_{\mathrm{el}}+N_{\mathrm{ctk,int}}\delta t)} \tag{5.10}$$

If n flashes are emitted per second, the first dead time contribution described amounts to $n\delta t$, while the second reaches $nP(N \geqslant 1)(\Delta t_d - \frac{\delta t}{2})$, as the pulse issued by the flash has a uniform probability of happening over the interval δt, hence an additional expected dead time proportional to $\Delta t_d - \frac{\delta t}{2}$. In total, the induced dead time f amounts to:

$$f = n\left[\delta t + \left(1 - e^{-C\delta t}\right)\left(\Delta t_d - \frac{\delta t}{2}\right)\right] \tag{5.11}$$

This gives a limit on the maximal number of calibration flashes per second of $n \leqslant f/\delta t = 200$ (for $f \leqslant 1\%$). Combining both equations, the overall problem can be summarized in:

$$M = \frac{fC\delta t e^{-C\delta t(1+\lfloor n\Delta t_{\mathrm{hr}}\rfloor+\lfloor n\Delta t_{\mathrm{d}}\rfloor+N_{\mathrm{ctk,int}}+2N_{\mathrm{ctk,el}}\lfloor n\Delta t_{\mathrm{el}}/2\rfloor+N_{\mathrm{ctk,th}}(1+2\lfloor n\Delta t_{\mathrm{th}}/2\rfloor))}}{\delta t + (1 - e^{-C\delta t})(\Delta t_d - \frac{\delta t}{2})} \times e^{-C_{\mathrm{sky}}(\Delta t_{\mathrm{d}}+\Delta t_{\mathrm{hr}}+N_{\mathrm{ctk,th}}\Delta t_{th}+N_{\mathrm{ctk,el}}\Delta t_{el}+N_{\mathrm{ctk,int}}\delta t)} \tag{5.12}$$

Considering the required count rate M_0, the dead time fraction f and the flash duration δt (Δt_{d} and Δt_{hr} being fixed by the pixel choice), a set of optimal calibration parameters exists when the previous equation has solutions in C. To increase as much as possible our solution space, we adopt the lowest possible value for the flash duration, $\delta t = 50\,\mu\mathrm{s}$.

5.2.2 Parametric study

For fixed f and M, we determine the boundaries of the solution space of Equation 5.12 for different values of C_{sky} (0, 0.35 and 2.1 cts/s/pix, see Chapter 3) with and without crosstalk considerations. We assume $N_{\mathrm{MUX}} = 34$, $N_{\mathrm{ctk,int}} = 33$, $N_{\mathrm{ctk,el}} = 2$ and $N_{\mathrm{ctk,th}} = 4$. All the parameters below the curves are a set of possible solutions for a single pixel.

As shown in Figure 5.4, without sky contributions nor crosstalk, working solutions exist as soon as $M \leqslant 2.62\,\mathrm{cts/s/pix}$, at which point the instantaneous count rate is $C \sim 3280\,\mathrm{cts/s/pix}$ and $n \sim 19$. For the required sky count rate due to extended sources (0.35 cts/s/pix for Perseus), solutions can still be found if $M \leqslant 2.60\,\mathrm{cts/s/pix}$ (C $\sim 3260\,\mathrm{cts/s/pix}$, $n \sim 19$). However, for the specified set of parameters ($f_0 = 0.01$, $M_0 = 6.3\,\mathrm{cts/s}$), no solution exists. To achieve the required M_0, a dead time relaxation up to 2.81% (resp. 2.90%) is needed when $C_{\mathrm{sky}} = 0\,\mathrm{cts/s/pix}$ (resp. $C_{\mathrm{sky}} = 0.35\,\mathrm{cts/s/pix}$). In the case of the highest sky count rate considered (goal of $C_{\mathrm{sky}} = 2.1\,\mathrm{cts/s/pix}$ for Cassiopeia A), solutions only exist below $M \leqslant 2.35\,\mathrm{cts/s/pix}$. Furthermore, no dead time relaxations can be found in this case: the required M_0 cannot be achieved even with a dead time of 100%. Once crosstalk rejection is considered, the solution space is further reduced. We see for instance that no solutions exist to achieve M_0, even without sky counts. Reciprocally, whenever the dead time fraction remains at 1%, a count rate of 0.82 cts/pix/s can be tolerated without sky counts (resp. 0.80 cts/s/pix for $C_{\mathrm{sky}} = 0.35\,\mathrm{cts/s/pix}$ and 0.68 cts/s/pix for $C_{\mathrm{sky}} = 2.1\,\mathrm{cts/s/pix}$). In this case, $C = 244\,\mathrm{cts/s/pix}$ and $n = 113.6\,\mathrm{Hz}$.

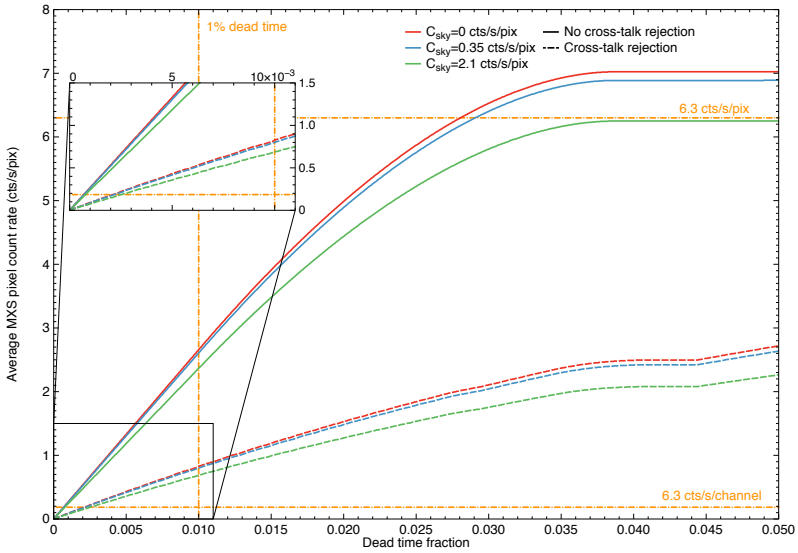

Figure 5.4: Borders of the solution space in the (f,M) plane for different values of $C_{\rm sky}$ with (dashed lines) and without (solid lines) crosstalk rejection for $N_{\rm MUX} = 34$. All sets (f,M) below the curve are a possible set of solutions. The horizontal dash-dotted lines represent the $M_0 = 6.3\,{\rm cts/s}$ requirement for a non-monochromatic MXS either per pixel or per channel. The vertical dashed and dotted line reminds the 1% dead time requirement.

A solution is to pool pixels from the same readout channel, thus substantially reducing the required count rate per pixel by a factor up to $N_{\rm MUX}$ (here 34), i.e. down to $M_0' = 0.185\,{\rm cts/s/pix}$ for the *Hitomi*-like MXS. When pixels are pooled together by multiplexing channels (Figure 5.4 – sub panel), solutions exist for as soon as $f \geq 0.3\%$. A minimal number of $N_{\rm pool} = 10$ pixels is needed within the same group to verify the 1% dead time requirement and is chosen as the current baseline for the correction (300 pools over the array).

5.2.3 Contribution of SQUID unlock

Due to the instantaneous count rate of the MXS, multiple high-energy photons can be detected almost simultaneously in the same readout channel. If the total energy of these photons exceeds $\sim 24\,{\rm keV}$, the FE SQUID unlocks. Currently as many as $t_{\rm lock} = 10\,{\rm ms}$ are needed to 're-lock' the SQUID (worst-case, Peille et al., 2019). This effect may create additional dead time if the instantaneous count rate C of the MXS is too large.

To verify whether $t_{\rm lock}$ is a significant contributor to the MXS-induced dead time, we evaluated the probability, in a given flash of duration δt, to have a BBFB unlock for a given count rate C. We assume $N_{\rm MUX} = 34$. The MXS spectrum is simulated as follows:

- The Bremsstrahlung spectrum represents 2/3 of the total counts. It is assumed to follow an absorbed Kramer law with a 12 keV cut-off:

$$I(E) = \left(\frac{12}{E} - 1\right) T_{\rm Be}(E) \tag{5.13}$$

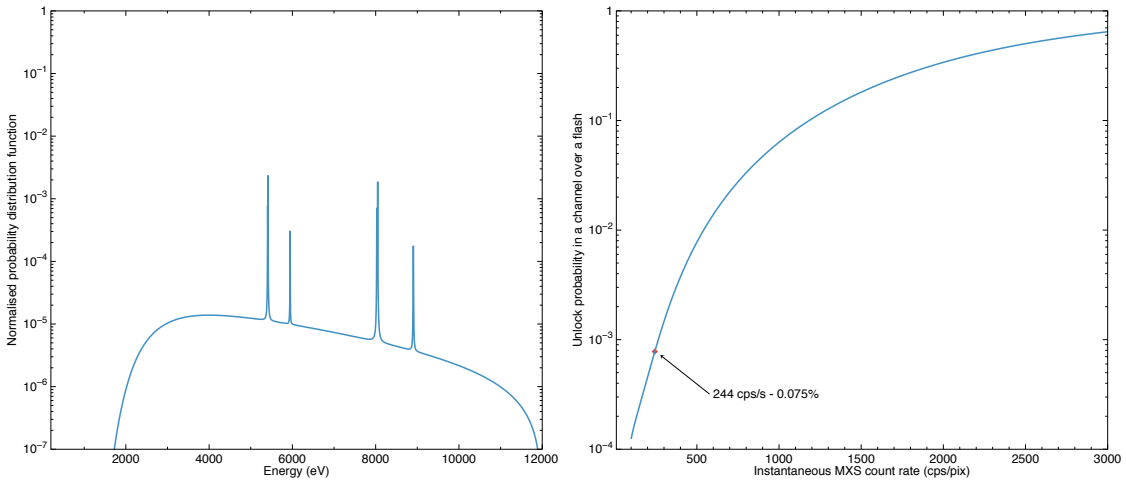

Figure 5.5: (*Left*) Probability distribution function of the MXS photons generated using 2/3 of Bremsstrahlung and a *Hitomi*-like MXS configuration. (*Right*) Unlock probability in a channel during a flash as a function of the instantaneous MXS count rate (cts/s/pix). The red diamond shows the $C = 244$ cts/s/pix configuration (see Section 5.2.2).

where E is the energy in keV and $T_{\mathrm{Be}}(E)$ is the transmission of the beryllium window placed in front of the MXS anode. This window is assumed to be 300 µm thick, and $T_{\mathrm{Be}}(E)$ is computed using the CXRO database.[19] This spectral shape neglects the additional low-energy cut-off by the instrument thermal filters, but should not change the results (filter transmission is constant above 3 keV, see Section 5.3.1).

- The MXS K- shell lines represent 1/3 of the total counts. Each doublet is taken from Hölzer et al. (1997), and convolved with the instrumental energy resolution at the given energy. Within the lines, counts are distributed in a *Hitomi*-like MXS configuration (45% for Cr K_α, 5% for Cr K_β, 45% for Cu K_α, and 5% for Cu K_β).

The overall MXS spectrum is shown in Figure 5.5 (*Left*). For a given count rate C, the photons detected during a flash follow a Poisson law of parameter $\lambda = C\delta t N_{\mathrm{MUX}}$. The probability to have an unlock during a flash can be computed by repeating the process multiple times and finding the number of flashes for which the total energy seen by the SQUID exceeds 24 keV (see Figure 5.5 – *Right* for values of the instantaneous count rate between 100 cts/s/pix and 3000 cts/s/pix). The probability for a SQUID unlock of a readout chain during a flash remains below 1% if $C \leq 541$ cts/s/pix, and below 0.1% if $C \leq 265$ cts/s/pix. Assuming the MXS configuration presented in Section 5.2.2 ($C = 244$ cts/s/pix and $n = 113.6$ Hz), the unlock probability is $p_{\mathrm{unlock}} \sim 0.075\%$. The corresponding number of unlocks per second is given by $p_{\mathrm{unlock}} n = 0.085$ unlocks/s. If $t_{\mathrm{lock}} = 10$ ms, the dead time fraction due to BBFB unlock is below 0.1% and thereby negligible with respect to the dead time induced by the MXS flashes themselves.

5.2.4 Impact on MXS design and energy scale monitoring

Through this study, two conclusions can be drawn:

[19] http://henke.lbl.gov/optical_constants/

- The core of the MXS-induced dead time is related to the flashes.
- Considering a single-pixel strategy to monitor the energy scale, the 1% dead time allocation cannot be met over 1000 s with the current MXS design (Figure 5.4).

Although the stability of the instrument in L2 may allow longer integration periods to monitor the energy scale, a promising solution is to group pixels for the correction. To satisfy the dead time requirement for a *Hitomi*-like MXS, pools of 10 pixels or more (i.e. $\sim$ 300 monitoring pools over the array) are required. Using the highest count rate acceptable on a single pixel, ($M = 0.68$ cts/s/pix) and the MXS properties verifying the 1% dead time fraction ($C = 244\,\mathrm{cts/s/pix}$, $n = 113.6\,\mathrm{Hz}$), the total count rate over the array amounts to $\sim 4400\,\mathrm{cts/s}$ ($= n \times C \times \delta t \times N_{\mathrm{pixel}}$). Assuming a baseline pixel pitch of 275 µm, a current maximal distance between the MXS and the detectors of 536 mm, the fact that two sources are used to illuminate the detector, as well as an instrumental QE of 0.66 at 8 keV (energy of the Cu K_α line), this translates into an instantaneous flux of $0.5 \times \frac{244}{0.66} \times 2\pi \times \left(\frac{536}{0.275}\right)^2 \sim 44 \times 10^8\,\mathrm{cts/s/(2\pi\,sr)}$ for a single source. Once MXS parameters will be set in phase B (notably δt) the numerical approach used here will provide an accurate estimation of the required MXS flux and expected dead time.

5.3 Knowledge of the instrumental response

The instrumental response of the X-IFU depends on both the effective area of the mirror and the quantum efficiency of individual detectors. Its knowledge at a single-pixel scale is crucial for accurate spectroscopic measurements, as it influences the S/N ratio of the lines or their equivalent width (e.g. related to abundances or broadening measurements).

The calibration of the response is planned on the ground using a synchrotron beam-line, and should not change once in-flight (except in case of contamination). However, per-pixel measurements are challenging (beam-line PSF needs to be small) and time consuming (need to sweep the bandpass with a sub-eV steps). Similarly to the energy scale, calibration will thus be performed on parts of the array and a 'mean' calibrated response will be applied to each subset of pixels. For integration issues, these measurements will occur at subsystem level, and only verifications on the full instrument will be performed. Small uncertainties in its knowledge may therefore remain even after calibration. In this section, I investigate the effect of such uncertainties on the science performances. Specifically, using a numerical approach, I studied the uncertainties related to TES absorber thickness and their effect on the observation of iron K lines in clusters of galaxies.

5.3.1 Sources of variations

The total effective area of the X-IFU is related to four distinct contributors in the beginning of life of the instrument:

- The effective area of the mirror (Chapter 2), which depends on the MMs layout.
- The transmission of the filters on the aperture cylinder and (if not open) on the FW.
- The geometrical filling factor of the detectors.
- The stopping power of the TES absorber.

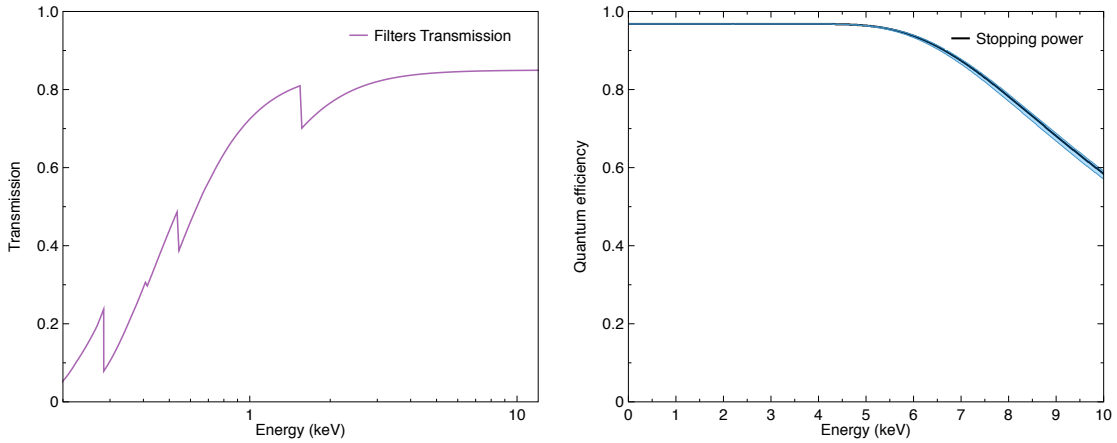

Figure 5.6: (*Left*) Total transmission of the thermal filters of the instrument (courtesy M. Barbera). (*Right*) Total stopping power of the absorber with 1.7 µm Au and 4.2 µm Bi, with a geometrical filling factor of 96.8% (Smith et al., 2016). The blue envelope represents the effect of a 1.5% change in Au and in Bi ($\pm 1\sigma$) used to generate new responses.

Over the mission lifetime, contamination deposited on the filters may also modify the overall response. This effect is neglected here. At instrumental level, the absolute knowledge of the effective area (i.e. overall normalisation at 1 keV) is expected to be better than 4%. Correspondingly, the relative knowledge (i.e. deviations from the absolute level) is required to be below 3% over 0.2 – 10 keV, with higher uncertainties allowed near the main atomic edges (e.g. C, Si). We remain here strictly at X-IFU level, and consider the effective area of the telescope as fixed. The size of the pixel being well determined, the geometrical filling factor is considered constant (e.g. $\sim$ 97.11% for 271 µm pitch pixels with a 2 µm pixel spacing on each side, as in the current baseline).

Sources of variations at instrumental level are therefore linked to variations in the filters transmission or in the stopping power of the TES absorber. The former can be related to the hexagonal-shaped supporting meshes (Barbera et al., 2018b), the fabrication, or to wrinkling. The latter is essentially due to fabrication processes, which can provide granularity or gradients in the deposited absorber. We assume that filters are made of (cumulatively) 225 nm of polyimide, 120 nm of Al and 30 nm of Al_2O_3, with one 60µm-thick gold-plated stainless steel mesh (2 mm pitch, 4% blocking factor), and four 130µm-thick stainless steel meshes (5 mm pitch, 3% blocking factor).[20] TES absorbers are considered as a bi-layer of 4.2 µm layer of Bi deposited over 1.7 µm of Au (Smith et al., 2016). LPA2 pixels are used, although no significant difference is expected in the results as long as the absorbers remain similar. Both filters and absorbers transmissions are shown in Figure 5.6.

Changes in either contributor will provide uncertainties in the knowledge of the response. The impact will however differ depending on the considered bandpass. For the filters (Figure 5.6 – *Left*, courtesy M. Barbera), changes in thickness will e.g. only modify the low-energy part of the spectrum ($\leq$ 4 keV), where the transmission is low and the curve presents several edges, with no effect on higher energies. On the contrary, the absorber stopping power (Figure 5.6 - *Right*) decreases only at high energies ($\geq$ 5 keV).

[20] 2018 filter configuration, see Chapter 2 for current configuration.

5.3.2 Calibration pipeline

The instrument response is expected to be calibrated at subsystem level using synchrotron beam-lines for both filters and TES absorbers. However, given programmatic constraints and technological limitations, an accurate per-pixel calibration is excluded, and only an average response will be used. In many cases, pixels will be binned together for scientific studies. If changes follow a Gaussian distribution, the local response will thus converge towards the total average response. A per-pixel knowledge of the response may nonetheless be needed to investigate bright extended sources (each pixel will be a statistically-independent region) or to measure turbulence through structure functions (see Chapter 4), where small pools of pixels are used. Simulations provide an excellent tool to estimate the systematic errors introduced by these uncertainties in future X-IFU observations.

One method is to use a MC approach based on modified instrumental response functions (e.g. Drake et al., 2006), i.e. based on modified ARF and RMF files, which contain the discretised effective area as a function of energy and the spectral response over the bandpass respectively (see Chapter 3). The first step of these simulations is to determine, for a specific energy band, the science case(s) most affected by a change in one of the physical parameters (e.g. the absorber stopping power above 6 keV). Then, using a realistic range of variations (assumed Gaussian), the simulation can be conducted as follows:

1. Assuming Gaussian changes in the corresponding parameter (e.g. TES Bi thickness), we generate randomly modified responses starting from the baseline response files.
2. The input spectrum of the retained science case is simulated with XSPEC using the previous response. To investigate purely systematic effects, spectra are generated with a very high statistical significance (unrealistically high exposure times).
3. The spectrum is fitted (using C-statistics) with the same input model used to generate the spectrum but assuming the baseline response files.

By repeating this process many times, we can assess the effect of systematic errors in the instrumental response on a specific science case. This approach differs from Drake et al. (2006) as the spectra are simulated with different responses (instead of one) and fitted exclusively with their baseline (instead of many responses). We believe it provides a better description of the systematic errors seen by the instrument, as deviations correspond to actual systematic errors with respect to the single (expected) set of calibration files. To simplify the interpretation of the results, only changes in one of the contributors will be considered. Individual effects can be summed quadratically at the first order.

5.3.3 An application to changes in TES absorber thickness

The previous pipeline was applied to a change in the TES absorber thickness.

Realistic changes in absorber thickness

The TES stopping power represents the main variation of the instrumental response at high energies. For this study, we consider that absorbers are composed by a gold/bismuth bi-layer. The gold layer is deposited first and is expected to be homogeneous within a pixel, with low gradients over the full array (estimated $\leq 5\%$). Bismuth is deposited on top of

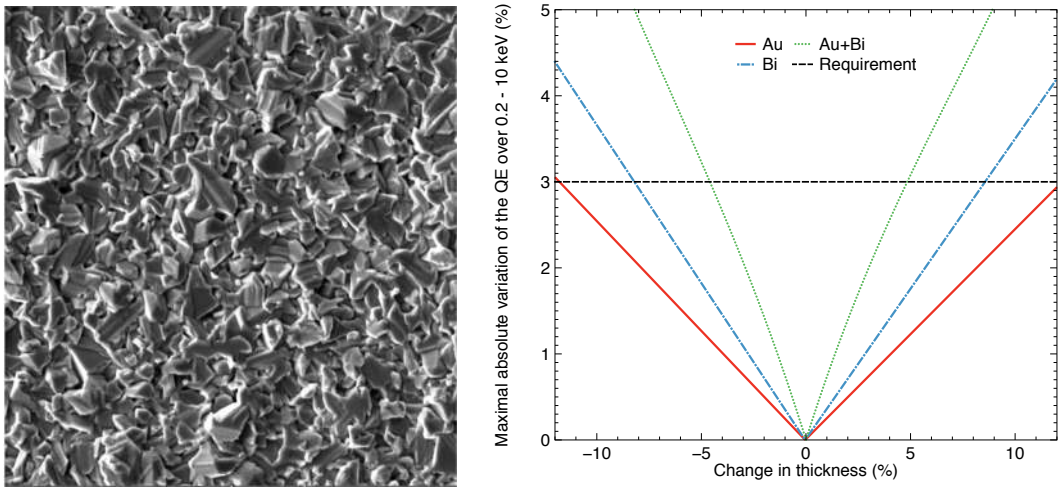

Figure 5.7: (*Left*) Example of a Bi absorber layer without grain refiner observed through electronic microscope (courtesy SRON, NASA). (*Right*) Maximal absolute change in the absorber quantum efficiency over the 0.2 – 10 keV bandpass as a function of the change (in %) in the absorber thickness for Au (red solid line), Bi (blue dash-dotted line) and both in Au and in Bi (green dotted line). The horizontal dashed line recalls the 3% requirement.

gold, and exhibits a much more heterogeneous aspect, with granularity visible at tenths of µm scales within a pixel, creating 'valleys' and 'craters' in the deposition (Figure 5.7 – *Left*). Although large efforts are conducted to decrease Bi roughness (by e.g, changing the fabrication process or depositing an additional thin Au layer on top of Bi), currently differences up to 5% can be expected within a pixel (M. Eckart, private communication) .

Using the CXRO database, we computed the variation of the Bi stopping power for absolute changes in thickness up to 10% starting from the nominal 4.2 µm value. The largest variations are found at high energy. Considering 10 keV as the upper boundary for this study, we find that as long as changes remain within ±10% (i.e. ±0.42 µm), variations in the response can be considered as linear. A similar result can be shown for gold. Hence, we can assume that the average pixel stopping power can be approximated by the stopping power obtained using an average Bi and Au thickness. In other words, despite intra-pixel heterogeneities, we can accurately determine an 'effective' thickness of the layers which accurately represents the full stopping power of the pixel.

For both materials, changes in absorber thickness mainly affect the response above 6 keV (see also Figure 5.6 – *Right*). To remain below the 3% variation over the 0.2 – 10 keV bandpass specified in the current instrumental requirements ($\pm 1\sigma$), per-pixel variations in absorber thickness should not exceed ±0.20 µm ($\pm 1\sigma$) for gold and ±0.33 µm for bismuth ($\pm 1\sigma$), i.e. respectively 12% and 8% of their original value (Figure 5.7 – *Right*). We notice that Bi has a much larger effect than gold for the same relative contribution. Although Bi is more likely to have higher absolute thickness variations, we assume that these changes are comparable on a relative scale. Hence, in the rest of this study we assume that ΔAu/Au $\equiv$ ΔBi/Bi. A similar study for comparable variations in absolute thickness (ΔAu = ΔBi in µm) is given in Cucchetti et al. (2018c) and provides equivalent conclusions.

Science case and results

The largest effect of uncertainties in the absorbers concerns single pixels, observing at high energies ($\geq 6\,\mathrm{keV}$). Given the X-IFU science objectives, this will affect in particular the observation of extended sources and their physical parameters (temperature, velocities, abundances) using the Fe K line ($\sim 6.4\,\mathrm{keV}$). Hard point-like sources may also be concerned, although the defocussing capabilities of the MAM should spread counts on larger pools of pixels, naturally mitigating any QE uncertainty. In the current requirements, temperatures and abundances shall be recovered within 4% of their values, while velocity broadening should be known to better than 5σ (i.e. $20\,\mathrm{km/s}$ for $100\,\mathrm{km/s}$ velocities).

A typical emission spectrum of the ICM thermal plasma is generated through XSPEC `bapec` model for a local cluster ($z \sim 0.1$) with an iron abundance of 0.3 $Z_\odot$ (solar abundances follow Anders & Grevesse 1989) and a turbulent velocity of $100\,\mathrm{km/s}$. This spectrum is used as input of the previous MC pipeline. The responses are modified by randomly selecting a thickness change in the absorber (in relative scale) assuming a normal distribution centred on the 'true' response and with a standard deviation of $\pm X\%$. To speed up computation, the new response is interpolated using 5 different stopping power curves.

To cover a wider range of objects, the cluster temperature is varied between 4, 6 and 8 keV. The fit is performed on the 5 – 10 keV energy band of Fe K, with temperature, abundance and turbulent velocity as free parameters. The 3% requirement is met when both layers remain below a $\sim 3\%$ change over the pixel (i.e. $0.126\,\mu\mathrm{m}$ for Bi and $0.051\,\mu\mathrm{m}$ for Au respectively, see also Figure 5.7 – *Right*). Results for each of the three parameters are given in Figure 5.8. Temperature and abundances are the most affected, although systematic errors remain $\leq 1\%$ for variations of 3% in absorber thickness. Systematic errors on the velocity broadening are minimal, well below $1\,\mathrm{km/s}$ in most cases. This can be related to the nature of the changes in the stopping power, which locally affect the S/N ratio of the line rather than its broadening, causing larger effects on parameters such as temperature or abundances (see also the NXB study for a similar feature, Section 3.6.3).

Overall, these effects are well below the current requirements even for significant changes in the stopping power of the TES. The current results obtained in manufacturing foresee that changes in thickness of the absorbers should be low, notably for gold layers, whose residual gradients are expected below the percent level. Likewise, new processes in Bi deposition already show significant effects in reducing the granularity of the deposition (down to a %) within a pixel. These changes, averaged within a pixel itself should also be below the percent level. Thereby, the systematic errors in the measurement of Fe K lines is expected to be negligible, even per pixel, especially compared to other sources of error (mainly statistics). Experimental verifications of the gold layer gradients and bismuth granularity are nevertheless planned in phase B (private discussion, XCaT).

5.3.4 Limitation and perspectives

The previous study shows that – for the specific science cases using Fe K lines – systematic errors related to changes in TES absorber thickness can safely be neglected, even at pixel level. However, the choice of the input model in the MC pipeline and the top-level science case drive this result. The main complexity of this approach is to determine the representative science case(s) needed as input. Multiple studies on other science objectives

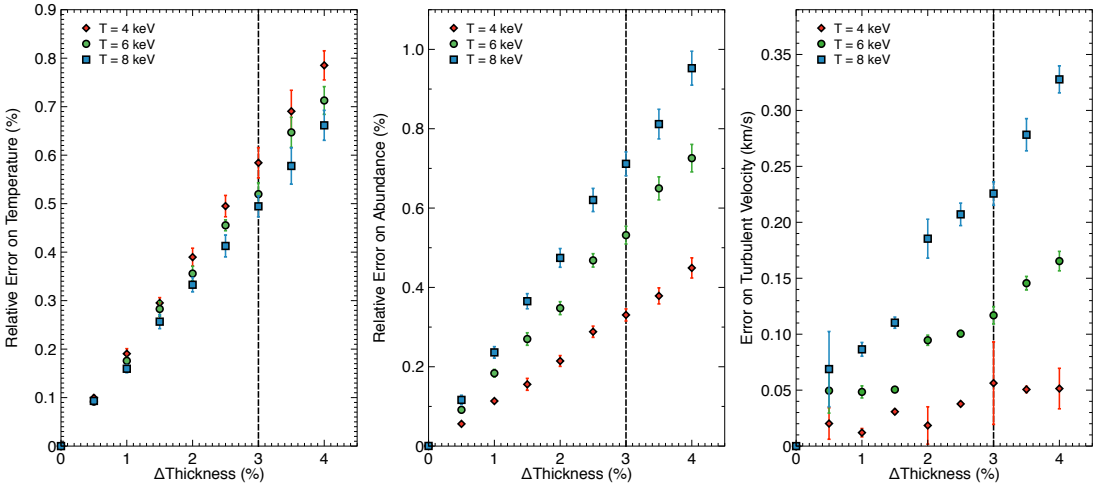

Figure 5.8: Effect of a change in detector thickness (in % in Au and Bi) on the recovery of different physical parameters in terms of relative error (%) for temperature (*Left*) and iron abundance (*Middle*), and in km/s for the turbulent velocity (*Right*). Simulations are done for a cluster temperature of 4 (red diamonds), 6 (green circles) and 8 keV (blue squares) using 10 000 iterations of the pipeline. The vertical dashed line indicates the change in Au and in Bi (µm) such that the maximal change in the instrumental response reaches 3% over 0.2 – 10 keV. Error bars indicate the $\pm 1\sigma$ deviation over the iterations.

are therefore advised to draw a definitive conclusion on these systematic errors.

The versatility of this approach can provide a generic tool to test calibration requirements before launch for any quantity affecting the ARF and the RMF (see Cucchetti et al., 2018c, for another example), including contamination effects. At the time of the study, the optimisation of the filter layers and of the mesh structures prevented a combined approach with TES absorbers and filters transmission. Following new results and using the new baseline of the filter configuration, this approach was for instance implemented in Barret et al. (2019, submitted) in the study of black holes and their spins.

5.4 Monitoring the NXB

A ground calibration of the instrumental background is unlikely, due to the lack of representative conditions. Simulations are therefore the only way to predict and control this effect. A design lowering the background and ways to ensure its reproducibility are equally important to minimise systematic errors related to the NXB. As shown in Section 3.6.3, a relative knowledge of ±2% of the NXB over 2 – 10 keV and over an area of $9'^2$, for 80% of the observing time is needed to maintain these errors compatible with the current science requirements. This translates into a knowledge of $\pm\,1 \times 10^{-4}$ cts/s/keV/cm^2 ($\pm 1\sigma$) for the current requirement of $\pm\,5 \times 10^{-3}$ cts/s/keV/cm^2. In this section, we investigate different ways of monitoring the NXB using the available equipment on *Athena* and the latest results on the variability in L2.

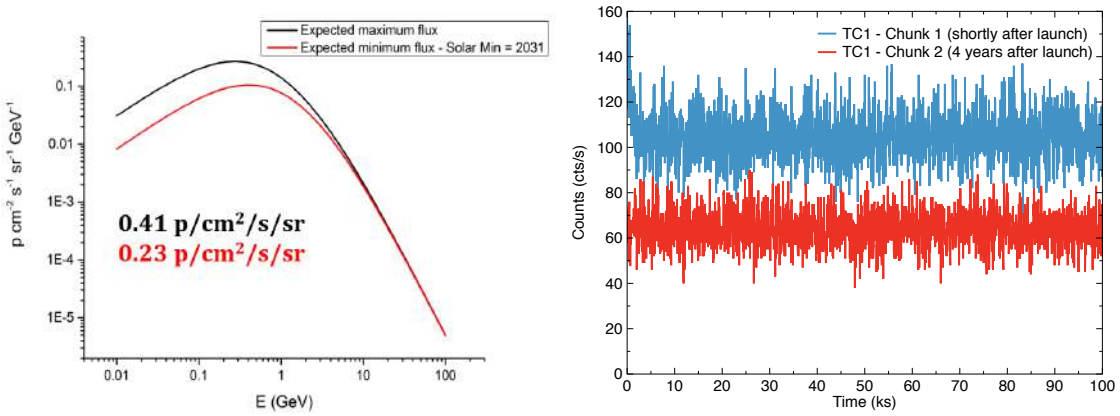

Figure 5.9: (*Left*) Best fit of the GCR flux expected at solar minimum (black) and maximum (red) in cts/s/GeV/sr as a function of energy (GeV) derived from the data measured on *SOHO*, *PAMELA* and using the `CREME96` models (courtesy S. Lotti, C. Macculi). (*Right*) Example of a 100 ks chunk used to estimate the variability in L2 of the *Planck* mission (see text). Data sets are taken either in the beginning (blue) or end of the mission (red) four years later showing almost a factor two in flux.

5.4.1 Variability of the NXB

Long time scale variability - current results in L2

The instrumental particle background is related to the GCRs spectrum near the spacecraft, assumed to be isotropic and anti-correlated with the activity of the Sun (Usoskin et al., 2005). Unlike previous X-ray missions, the orbit of *Athena* in a Lagrange point should provide a more stable environment than for observatories in low Earth orbit (which periodically go through the South Atlantic anomaly or the Van Allen belts).[21] Over the course of its mission, *Athena* should experience this modulation of the GCR, which flows down directly onto the variability of the NXB. Given the current results provided by missions such as the solar and heliospheric observatory (*SOHO*, Kühl et al. 2016) and payload for antimatter/matter exploration and light-nuclei astrophysics (*PAMELA*, Martucci et al. 2018), the variability of the solar cycle should not exceed a factor two in flux (Figure 5.9 – *Left*). These results are also confirmed numerically with the cosmic ray effect on microelectronics code (`CREME96`, Tylka et al. 1997). On typical 100 ks observations, a variability of ~ 290 ppm of the overall flux is expected, which is safely below the required 2%.

Short time scale variability - return of experience from *Planck*

Shorter time scale variability is also expected due to the structure of the tail of the magnetosphere in L2 (Duldig, 1994) or to small solar events (large solar flares or eruptions will be discarded from the data sets $\sim 20\%$ of the time). As no X-ray mission has so far measured the background variability in L2, no representative data can be used. Nevertheless, measurements from other X-ray satellites were used to gain insight on the topic. Studies conducted on the apogee periods of *XMM-Newton* for instance showed that the

[21] A more stable environment does not necessarily imply less cosmic rays, rather lower variations over time.

variability is well below 5% (at the 3σ upper level) over times scales of a few ks (private communication F. Gastaldello, S. Molendi). Aside from X-ray data, interesting information on the short time scale variability can be determined using the standard radiation and environment monitors (SREMs) onboard other missions positioned in L2, such as *Planck* (Mohammadzadeh et al., 2003). Though conducted in an *Athena*-representative environment, this comparison should be analysed with caution since:

- The SREM only provides data of protons above 40 MeV and electrons above 20 MeV. This only shows the high-energy part of the GCR spectrum, which is also the one varying the least between solar maximum and minimum (Figure 5.9 – *Left*). However, since most of the primaries creating the NXB should in principle be within this energy band (see below), this data remains very interesting to analyse.
- SREM data accounts for particles hitting the *Planck* satellite, which may not be entirely representative (spectrally) to the future X-IFU background particles (mass models of the two satellites differ).
- The SREM provides no knowledge of the energy of the particles, hence variability can only be studied as a flux (in terms of number of counts).

Data reduction: the full stream from *Planck* SREM was extracted from the level 1 ancillary data stored in the high frequency instrument (HFI) database. The data comprises three columns: time (Julian date with respect to 01/01/1904 00:00 UTC in s), TC1 (counter ≥ 20 MeV) and TC2 (counter ≥ 40 MeV). Counts are derived from the raw data by dividing TC1 and TC2 by the 16-bit conversion factor 65536. Unless otherwise specified, the time reference is taken as the first data point, i.e. 3325158611.380493 s JD.

After analysis, several intervals were excluded due to solar flares and other significant peaks in the flux. These include (with respect to the time origin): 0 to 5.04 10^4 s, 3.90 10^7 to 4.00 10^7 s, 5.72 10^7 to 5.76 10^7 s, 5.82 10^7 to 5.88 10^7 s, 6.45 10^7 to 6.65 10^7 s, 6.95 10^7 to 7.15 10^7 s, 7.25 10^7 to 7.35 10^7 s, 7.40 10^7 to 7.50 10^7 s, 7.80 10^7 to 7.85 10^7 s, 7.92 10^7 to 7.95 10^7 s, 7.99 10^7 to 8.06 10^7 s, 8,49 10^7 to 8.58 10^7 s, 8.87 10^7 to 8.95 10^7 s, 9.49 10^7 to 9.52 10^7 s, 9.75 10^7 to 9.77 10^7 s, 9.90 10^7 to 1.02 10^8 s, 1.03 10^8 to 1.05 10^8 s, 1.06 10^8 to 1.08 10^8 s, 1.09 10^8 to 1.11 10^8 s. This extracted data represents 16% of the total SREM data (compatible with the 20% required for the X-IFU).

Data analysis: the extracted data was divided in chunks of 100 ks to recreate a typical X-IFU observation of a faint source, over which we plan to monitor the NXB (Figure 5.9 – *Right*). For each chunk, we compute the relative excess variance of the distribution with respect to a Poisson distribution as follows (see also Nandra et al., 1997):

$$\tilde{\sigma}_{\rm exc} = \frac{\sigma_{\rm exc}}{\sigma_{\rm poiss}} = \sqrt{\frac{1}{N\mu^2\sigma^2_{\rm poiss}} \sum_i ((X_i - \mu)^2 - \sigma_i^2)} \tag{5.14}$$

for each bin i in the 100 ks sample. Assuming data in a bin follows Poissonian error bars ($X_i = \sigma_i^2$) and knowing that $\mu = \sigma^2_{\rm poiss}$ by definition, the previous formula reduces to

$$\tilde{\sigma}_{\rm exc} = \sqrt{\frac{1}{N\mu^3} \sum_i ((X_i - \mu)^2 - X_i)} \tag{5.15}$$

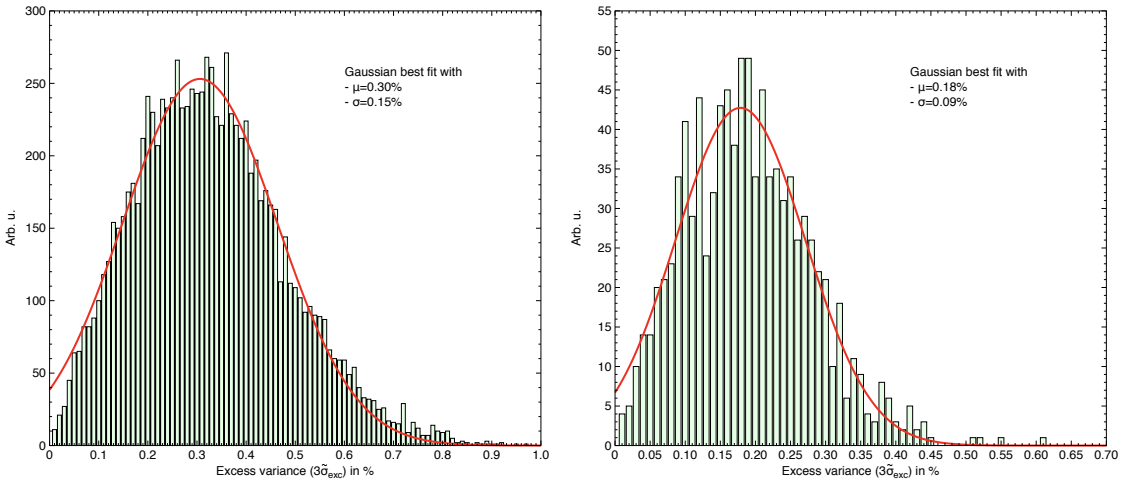

Figure 5.10: Relative level of excess variance found for detector TC1 ($3\tilde{\sigma}_{\rm exc}$ level in %) for two observation times, either 10 ks (*Left*) or 100 ks (*Right*). The Gaussian best fit is provided in red with the fitted mean and standard deviation parameters.

To estimate the variability of the GCR, we take the $3\tilde{\sigma}_{\rm exc}$ level for each interval and plot the associated histogram (in %) as shown in Figure 5.10 for either long (100 ks) or short (10 ks) observations. In our case, since data points are taken with a frequency of 0.02 Hz, time scale lower than 5 ks were not considered to avoid having less than 100 data points in the dataset (potentially introducing limited sample size errors). As the TC1 detector shows systematically higher variability than TC2, we use it as a worst-case reference.

On *Planck*'s results, the variability with respect to a purely Poisson level of background is minor. Even for small time scales, the variability remains systematically below 0.3% ($\pm$0.15% at 1σ) and well below the required 2%. This indicates that most of the high-energy part of the GCR spectrum shows little evidence of variability on typical time scales of the observations, supporting the results found for *XMM-Newton*. However, no detail on the low-energy part of the spectrum (most susceptible to change) can be given using this approach. Additionally, these results only provide insight in terms of a scalar (number of counts) but give no information on potential changes in the GCR spectral shape.

Changes in spectral shape - predictions using `GEANT4`

Though representative measurements in L2 are lacking, insight on the spectral shape variability can be obtained using numerical simulation tools such as `GEANT4`, which shows a good agreement with measured data (private discussion, V. Fioretti). Current simulations show that the level of GCR seen by the CryoAC will scale of a factor ~ 2 over the course of the mission, causing a rescaling of the same order in the NXB (Figure 5.11 – *Top*). Even though short time scale variability is not simulated, the spectral shape of the NXB is not expected to vary significantly over time, excluding large spectral changes. This can be explained by the distribution of the primary particles contributing to the NXB, which is uniform over the bandpass (Figure 5.11 – *Bottom right*) and whose energies are above 100 MeV (slow varying part of the GCR spectrum). Due to long computational times, these

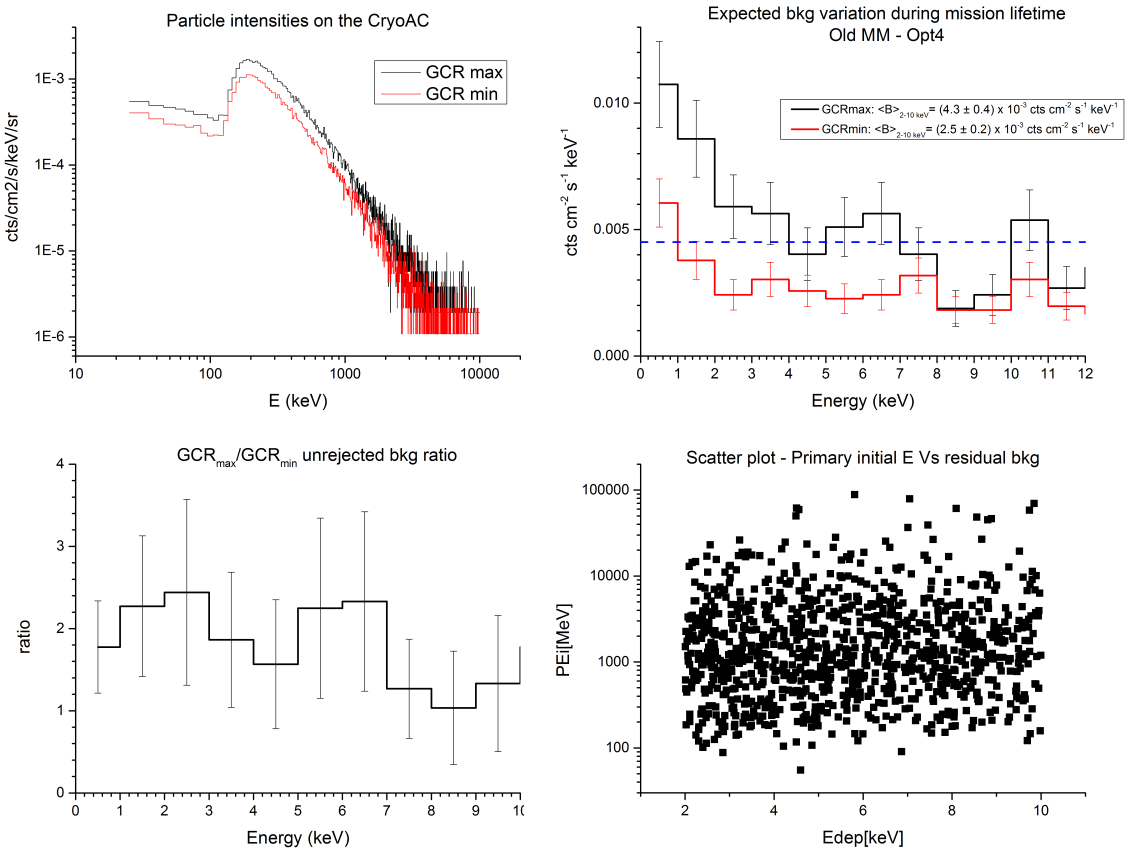

Figure 5.11: (*Top left*) Expected changes in the GCR spectrum seen by the CryoAC over the solar cycle. (*Top right*) Corresponding impact on the unrejected background level. (*Bottom left*) Ratio between the unrejected background at solar minimum and maximum. (*Bottom right*) Distribution of the energy of the primaries (MeV) causing unrejected background over the bandpass (keV). Courtesy S. Lotti, C. Macculi.

results are obtained with large statistical uncertainties. Activities in phase B will aim to decrease these contributions (to investigate systematic errors) and improve the simulations with more representative mass and physical models.

5.4.2 Instrumental solutions

In the rest of this study we assume the NXB as a Poisson process (outside solar events). The X-IFU is expected to comply with its 2% requirement without external contribution, although several ways of monitoring the NXB are possible using the *Athena* equipment (see below). During my thesis, I investigated three different solutions for this monitoring. Unless otherwise specified, these techniques take advantage of the full detector, assuming that the overall NXB distribution is not spatially dependent over the pixels, or that such variations are well characterised. In this case, the NXB level can be estimated with the same accuracy over a pool of pixels (in particular the required $9'^2$ – Section 3.6.3).

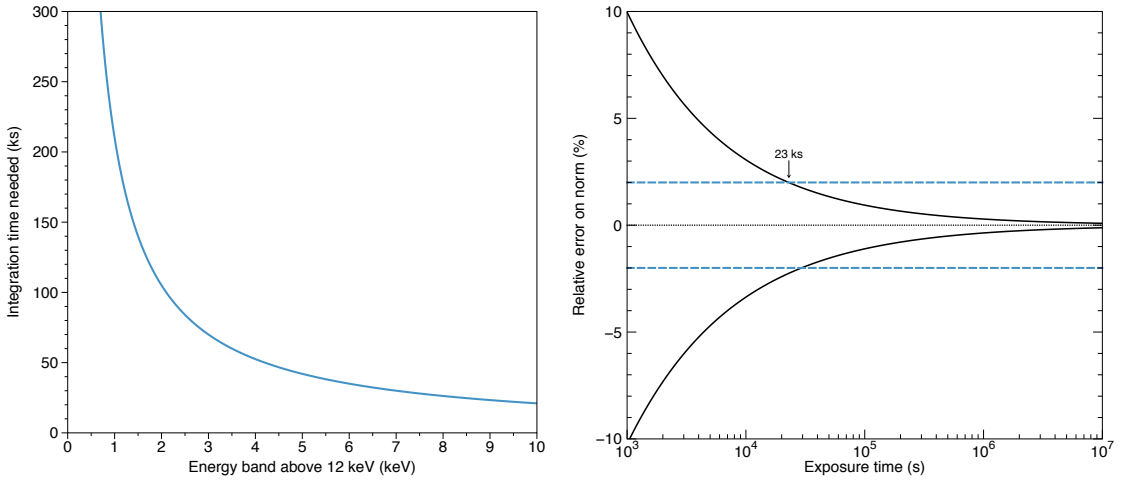

Figure 5.12: (*Left*) Exposure time needed (in ks) to achieve a relative error on the NXB normalisation of 2% ($\pm 1\sigma$) as a function of the energy band considered above 12 keV, assuming a constant NXB level (e.g. 2 keV stands for the 12 – 14 keV energy band).(*Right*) Relative error (in %) on the NXB normalisation ($\pm 1\sigma$) as a function of the exposure time (in s) used for a closed observation.

High-energy bandpass

A first solution is to use the high-energy band of the instrument (e.g. above $\geq$ 12 keV) as a proxy of the NXB level and variability. The main assumption is that counts in that bandpass are exclusively due to NXB. This solution has the immediate advantage of using no dedicated exposure time, nor interruptions in the observations. However, count rates in the band are low, requiring long integration times to achieve the 2% level of accuracy. Assuming the current calibration of the effective area up to 15 keV, a 2% reproducibility is achieved after $\geq$ 62 ks observations (Figure 5.12 – *Left*). In practice, for background-dominated observations, little to no spectral feature is expected above 9/10 keV, implying that this technique could in principle be extended to the 10 – 15 keV energy band, thus reducing the integration time to 37 ks. Higher energy bands could eventually be considered (e.g. up to 20 keV) provided a sufficient calibration (to investigate in later phases).

This solution requires high exposure times, and cannot measure the short time scale variability of the NXB. It remains however the preferred approach for its simplicity and its legacy, as it is routinely used in current X-ray missions with excellent results.

Closed observations

A second option is to use obscured observations of the detectors. These can be done in two ways, either by having part of the pixels outside the FoV or by simply switching the FW into closed position. For the X-IFU, the latter is retained, as the former was discarded during design. Since the NXB is assumed Poissonian, we can estimate the number of counts (and the time) required to obtain the required 2% level. To do so, we can either use an analytical approach or simulate a constant spectrum using XSPEC and fit it to estimate

the error as a function of the exposure time. Both approaches provide equal results and show that ≥ 23 ks are needed to achieve the required precision over the 2 – 10 keV energy band, which corresponds to ≥ 2500 NXB counts (Figure 5.12 – *Left*).

This approach has the main advantage of directly measuring the NXB without any other underlying assumption. However, such long measurements in closed position require planning and do not give access to variations with time scales lower than ~ 20 ks. Additionally, as measurements will occur beside the actual observation, observers must either assume that the NXB level does not change significantly after the closed observation, or renormalise the level measured during closed time to the level of background measured in the high-energy, thus potentially introducing additional errors.

The CryoAC as monitor for the NXB?

During observations, the CryoAC will be used to monitor and flag background events on the detector array. Unlike the TES array, its large area gathers a significant number of counts over short time periods (~ 40 cts/s). An idea is to investigate whether the CryoAC could be used to monitor the NXB while in flight. In the rest of this study we assume a configuration of the CryoAC which provides measurements over the 20 – 800 keV bandpass. Though not required in the current baseline of the instrument, the CryoAC may possess spectral capabilities across the bandpass (as also investigated in D'Andrea et al. 2017). To perform this exercise, we assume the CryoAC will have such capabilities, with a resolving power $R \sim 10$, sampled with increasing $\Delta E/5$ steps across the bandpass. For the NXB spectrum, a sampling in 0.4 eV steps (as in the current X-IFU responses) is considered.

Principle: Given an isotropic distribution of the GCR spectrum, a proportional relationship can be demonstrated between the number of primaries going through the anti-coincidence detector and the primaries seen by the TES. Using purely geometrical arguments, the corresponding number of unrejected primaries can thus be related to the primaries on the CryoAC. Additionally, since the detector array is placed near the CryoAC, the detector "shadows" part of the distribution of the particles, notably of back-scattered secondary electrons, which compose the bulk of the NXB. A similar correlation can therefore be assumed for secondaries. In this case, we can derive a transfer function $\mathcal{H}$ between the GCR spectrum on the CryoAC and the level of unrejected background, which could be used to monitor the NXB over short time scales (Figure 5.13). By noting f_{CryoAC} the CryoAC spectrum and f_{NXB} the residual particle background, $\mathcal{H}$ is, at a given time t:

$$f_{\mathrm{NXB}}(t) = \mathcal{H}(f_{\mathrm{CryoAC}}(t)) \tag{5.16}$$

As spectra measured by the instrument are discrete (with sizes corresponding to the number of spectral channels of the instrument), $\mathcal{H}$ will be approximated by a rectangular matrix H, and its accuracy will depend on the accumulation time t_{acc} used to estimate it. Since f_{NXB} and f_{CryoAC} only take positive values, H is given by the pseudo-inverse,

$$H(t_{\mathrm{acc}}) = \frac{f_{\mathrm{NXB}}(t_{\mathrm{acc}}) \times f_{\mathrm{CryoAC}}(t_{\mathrm{acc}})^T}{||f_{\mathrm{CryoAC}}(t_{\mathrm{acc}})||^2} \tag{5.17}$$

and used to determine the NXB level, as illustrated in Figure 5.13.

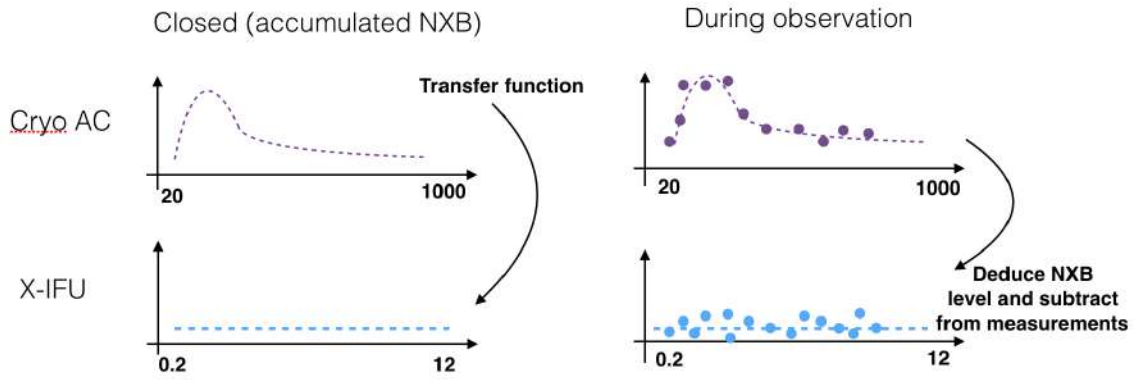

Figure 5.13: Cartoon illustration of NXB monitoring using the CryoAC. (*Left*) During dedicated phases, the NXB and the CryoAC spectra are used to estimate a transfer function between the two quantities. (*Right*) During observations, the large number of counts on the CryoAC is used to estimate the NXB and subtract it from the observed spectrum.

Results: This technique can be tested by computing an estimation of the matrix H for a given accumulation time $t_{\rm acc}$. The accumulated NXB counts are drawn randomly at the required level of 5×10^{-3} cts/s/cm^2/keV. Likewise, CryoAC counts are sampled using a toy model of the CryoAC spectrum, generated from the outputs of `GEANT4` simulations with the latest mass models (courtesy S. Lotti).

$H(t_{\rm acc})$ is then used to derive the level of NXB during an observation time $t_{\rm exp}$, $f_{\rm NXB}(t_{\rm exp})$. After generating a typical CryoAC spectrum over $t_{\rm exp}$ by sampling once again the `GEANT4` toy model spectrum, $f_{\rm NXB}(t_{\rm exp})$ is simply provided by $H(t_{\rm acc}) \times f_{\rm CryoAC}(t_{\rm exp})$. The average value and the standard deviation of the estimated NXB are computed by repeating this process 1000 times. As shown in Figure 5.14 (*Left*) for $t_{\rm acc} = 100$ ks, this method is very accurate, even over short time scales (≤ 1000 s).

Systematic effects in the correction can appear if the matrix H is estimated with a short accumulation time (see the shift with respect to zero in Figure 5.14 – *Left*). To quantify this average systematic error for a fixed value of $t_{\rm acc}$, we repeated the previous simulations for ≥ 100 different estimations of $H(t_{\rm acc})$. In each case, ≥ 1000 NXB estimations are performed using unrealistically long exposure times $t_{\rm exp}$, to reduce statistical errors at negligible levels. The evolution of the bias with $t_{\rm acc}$ is derived by extending the previous analysis for different values of the accumulation time (Figure 5.14 – *Right*). To achieve a sufficiently accurate value of $\mathcal{H}$, we find that an accumulation time $t_{\rm acc}$ of the order of ~ 20 ks is required, which is comparable to the result found in Section 5.4.2.

Discussion and limitations: Similarly to the closed observation technique presented above, the use of the CryoAC requires dedicated closed phases to estimate $\mathcal{H}$. However, this option presents several advantages with respect to its counterpart. First of all, once computed, the transfer function can be used in parallel with observations, thus giving access to short-time variability of the NXB. Furthermore, as shown by the previous equations, this technique is robust to changes in the overall normalisation of the CryoAC spectrum, which are predicted by current `GEANT4` results. Finally, if simulations become sufficiently

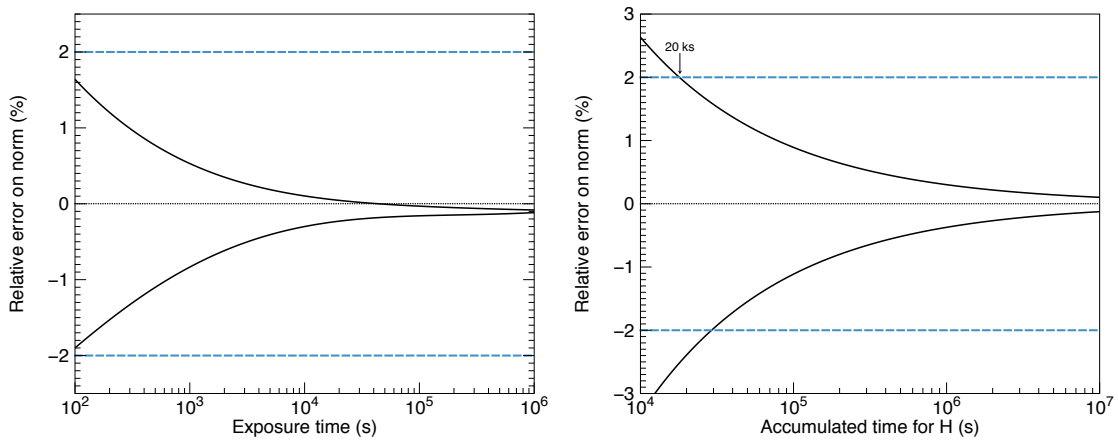

Figure 5.14: (*Left*) Best fit over 1000 corrections of the relative error (in %) on the value of the NXB normalisation ($\pm 1\sigma$) as a function of exposure time (in s) when using the CryoAC technique with an accumulation time of 100 ks. The bias on the correction is related to the finite time used to estimate $\mathcal{H}$. (Right) Relative systematic error made on the CryoAC correction as a function of the accumulation time (in s) used to estimate the transfer function matrix H. Dashed lines represent the 2% requirement.

representative, a valid estimation of $\mathcal{H}$ could also be obtained numerically.

Previous results show that – in theory – this technique can be used for NXB monitoring in-flight, and is complementary to the previous two options. This entire study relies nonetheless on two strong assumptions on the CryoAC:

- The first assumption is that $\mathcal{H}$ does indeed exist, which remains to be confirmed. Current `GEANT4` results provide hints validating this assumption. As shown in Figure 5.11 (*Top*) the overall level of GCR and NXB only changes in normalisation over the solar cycle. The uniform contribution in energy of the primaries generating NXB (Figure 5.11 – *Bottom left*) also suggests that the NXB spectral shape is not dependent on the CryoAC spectrum (i.e. a primary of energy E_p can cause a NXB event over the entire bandpass). Measurements and new `GEANT4` simulations performed in phase B will provide new results to validate this approach.
- Indirectly, we also made the hypothesis that the CryoAC will have some spectral capabilities over its bandpass. Currently no such capability is required nor quantified in the baseline of the instrument. As long as the NXB shape remains flat, this correction approach can in fact be reduced to a scalar form (where f_{CryoAC} is the total number of counts on the CryoAC) with similar results. However, if spectral features are present in the NXB, the presence or not of these capabilities will ultimately determine the overall feasibility of this option.

5.4.3 Additional monitoring solutions

Other ways of monitoring the NXB are possible without involving the X-IFU. Though the instrument is expected to monitor this background component by itself, these solutions

can be seen as additional proxies to improve the knowledge of the NXB even further:

- The main disadvantage of using closed X-IFU observations is the small FoV of the instrument, which implies a substantial integration time to decrease the statistical uncertainty on the NXB. Assuming the particle environment will be the same for the X-IFU and the WFI (including secondary electrons), an idea is to take advantage of the large FoV of the WFI. If used in parallel to X-IFU observations, integration times $\leq 500\,\mathrm{s}$ could achieve a 2% accuracy level at $\pm 1\sigma$. Due to the out-of-focus position of the WFI during X-IFU observations, this solution also ensures a limited contamination by the variable focused soft proton component. However, this solution relies on strong assumptions which remain to be confirmed (notably the inter-calibration between instruments), and also implies a simultaneous operation of both the X-IFU and the WFI, whose feasibility is yet to be assessed.
- Similarly to previous missions, *Athena* will carry an onboard radiation monitor, which will provide insight on the particle environment of the spacecraft, thus decreasing the statistical uncertainty on the level of NXB. By improving the radiation monitor, an accuracy better than 2% is theoretically achievable even over short time scales (i.e. below $\sim 10\,\mathrm{ks}$). This new-generation particle radiation monitor (S. Molendi, F. Gastaldello, in prep.) represents a very good option to achieve the 2% requirement during observations, even on short time scales.

5.5 Conclusions

In this chapter, I have investigated the calibration and monitoring of some of the crucial quantities needed to maximise the science return of the X-IFU. These studies were conducted in the framework of the XCaT. The main findings can be summarised as follows:

- The challenging energy scale requirement set for the X-IFU (0.4 eV FWHM) needs a continuous monitoring of the drifts in flight using housekeeping data and the MXS. Different techniques exist to satisfy this requirement, showing that a reasonable margin can be achieved provided an accurate ground calibration.
- The MXS design and count rate requires that pixels are pooled together for the energy scale correction to avoid a significant dead time in the data (at least 10 pixels per pool). The count rate however remains driven by the need to have a centroid accuracy of the lines below 0.2 eV (FWHM).
- To test calibration requirements, I have developed a MC based pipeline. When applied to changes in the instrumental response (more specifically to TES absorber thickness) results show that physical information derived from Fe K lines present negligible systematic errors, even for conservative changes in the TES stopping power. The same approach can be applied for any other parameter affecting the effective area.
- The reproducibility of the NXB will be as important as ensuring its lowest possible level. I have presented two classical ways to monitor the NXB over long ($\geq 20\,\mathrm{ks}$) time scale variations, and posited a third using the CryoAC, which could provide access to short ($\leq 1\,\mathrm{ks}$) time scale variations (if its practical use can be demonstrated).

CHAPTER 6

Development of a cryogenic test bench for the X-IFU

Within the X-IFU consortium, several cryogenic experiments were developed to study the TESs and their readout, to qualify the overall X-IFU cryogenic system, and to characterise some of the background effects on the detectors. The specifications set for the X-IFU require an additional understanding of every subsystem, and a careful validation of the ground calibration procedures. Early 2016, IRAP and CNES decided to develop a dedicated cryogenic experiment to perform these tests during the phase B of the instrument. In this chapter, I detail the design of this test facility, and provide a brief summary of the early results. These include the characterisation of the cryostat in temperature and magnetic field. I refer to this experiment as the "cryogenic test bench' or by its nickname, "*Elsa*".

6.1 Motivation of the cryogenic test bench

Most of the simulations characterising the X-IFU readout chain use assumptions on the TES pixels, their noise or their design. Though most are plausible or verified, a fully representative knowledge of the hardware is only possible after final integration. Also, most of the simulations make approximations on the TES transition (linear or two-fluid), on the pixel readout (FDM, TDM) or on the MXS design, which will be confirmed at later stages of the project (see Chapter 3 and 5). As of 2016, the main cryogenic facilities at GSFC and SRON investigated the critical subsystems of the mission, i.e. the TES fabrication and the FDM readout respectively. An additional demonstrator for the cryogenic chain (the detector cooling system, or DCS) was also created to demonstrate a cooling chain reaching 55 mK (namely hold time, recycling strategies and lifetime of the components) and its compatibility with flight-like detectors. However, no representative set up was planned for other subsystems before the demonstration model (in late phase B). To complete this set of experiments, CNES and IRAP have decided to set up, in 2016, a cryogenic bench. Its role is threefold:

- **Testing the DRE and WFEE electronics** – Part of the warm electronics (notably

the DRE) are developed at IRAP. A stringent knowledge of their performances (e.g. noise and spurious effects) is needed before integration in the demonstration model. Currently, performance tests make use of simulators, which provide representative data streams as inputs (e.g. generated through `XIFUSIM` for the DRE, Ravera et al. 2018). With the test bench, using flight-like detectors and cold-stage electronics (provided by GSFC and SRON respectively), we aim to characterise the DRE and the WFEE with real pulses, under some of the most demanding regimes (e.g. high count rate sources). Cryogenic operations are also a possibility to develop routines to test individual pixels, to create diagnostics, and to determine the stability of each sub-element (e.g. measure typical values of drifts in V_{bias} and G_{amp}).

- **Preparing the ground calibration** – The ground calibration of the X-IFU will determine some of its main performance-related quantities, which will otherwise be challenging to measure in flight (e.g. energy scale, quantum efficiency). To do so, various X-ray sources are required: radioactive sources, rotating target sources, MXS-like equipment, channel-cut crystal monochromators (CCCMs) or even electron-beam ion traps (EBITs). Part of this ground support equipment (GSE) can be reused from previous missions (typically *XRISM*) but the rest requires in-house development and testing. Furthermore, some of the calibration techniques put forward for the X-IFU, namely the multi-parameter gain drift correction, need to be validated before launch. *Elsa* will be an adequate set up to prepare these ground calibration activities.
- **Expertise and analysis** – CNES will handle the integration of the instrument, but so far lacks expertise in X-ray cryogenic experiments. This facility located at IRAP will improve the understanding of the instrument and will represent an important set-up during later phases of the project, to characterise for instance micro-vibrations or to test specific equipment before integration.

The procurement of the bench started in 2017, with a delivery and commissioning in 2018. First steps towards a full integration started in 2019 within an ISO8 clean room at IRAP. First light is expected in early 2020.

6.2 Overall design of the test bench

The cryogenic test bench was designed to provide a sufficiently stable 55 mK environment to operate a representative X-IFU focal plane. I develop here the specificities of the design, and the main differences/common points with the X-IFU.

6.2.1 Cryogenic chain and mechanical design

Requirements and specificities

Much like the X-IFU, the test bench is designed to provide cooling power at 55 mK. Several differences can nonetheless be highlighted:

- In the case of the X-IFU, reliability drives the need for a robust cryogenic chain with redounded elements. In the case of the test bench, no redundancy is planned.
- The use of commercial cryogenic systems ensures a smaller number of cold stages, simplifying the cryostat at the expense a higher level of noise and of customisation.

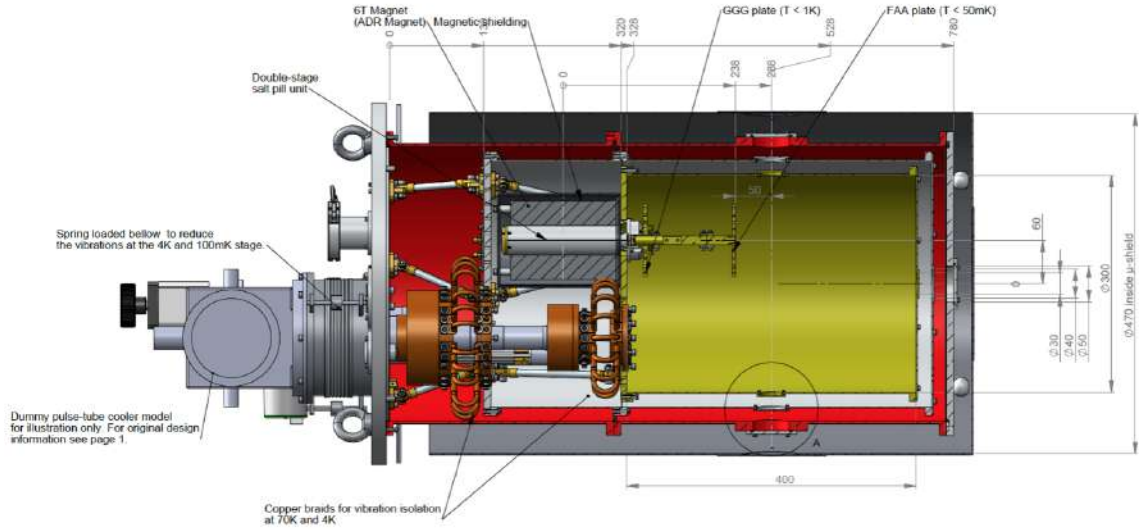

Figure 6.1: Mechanical and thermal design of the cryogenic test bench as proposed by Entropy GmbH^{TM}.

- The stringent level of noise and micro-vibration specified for the X-IFU requires a very complex system of dampeners, suspensions and shielding. Since the objective of the bench is not to demonstrate the feasibility of a multiplexed readout of TESs with a 2.5 eV energy resolution (ongoing at SRON), a higher apportionment for the temperature fluctuations and energy resolution are specified (see below and Appendix I). In particular, a stability better than 5 μK_{rms} at 55 mK over 1 ks, and an energy resolution below 3.5 eV (FWHM) at 6 keV are required.

Design of the cryogenic chain

The cryogenic chain retained for *Elsa* was provided by Entropy GmbH^{TM,22} (see Figure 6.1). The dewar is divided into four temperature stages. A PT (Sumimoto F70) provides two layers of thermalisation: a first refrigeration stage provides cooling around 35 K ("70 K stage" in the rest of this manuscript) and a second stage around 2.5 K ("4K stage"). The sub-Kelvin cooler is formed by a two-stage ADR: a first pill made of gadolinium-gallium garnet (GGG, $Gd_3Ga_5O_{12}$) provides cooling power down to $\sim$ 500 mK, while a second stage ferric ammonium alum (FAA, $Fe_2(NH_4)_2(SO_4)_4{+}24H_2O$) pill completes the cool-down to $\leq$ 55 mK (minimal temperature achieved of 32 mK). The salt pills are mounted using Vespel stems to provide enough thermal isolation at low temperatures.

Each stage is equipped with a feedthrough to the cold harnesses. Thermalisation on the cold stages is ensured by a heat switch, based on a stepping piezoelectric actuator coupled with a synchronous motor, which can be manually opened or closed during cool-down and ADR recharge. The superconducting magnet associated with the ADR is made of a solenoidal 6 T niobium coil, encased in a double *Cryoperm* shield and completed by an *Hyperco* disk on the 4 K stage side to avoid magnetic field contamination of the cryogenic

[22] www.entropy-cryogenics.com

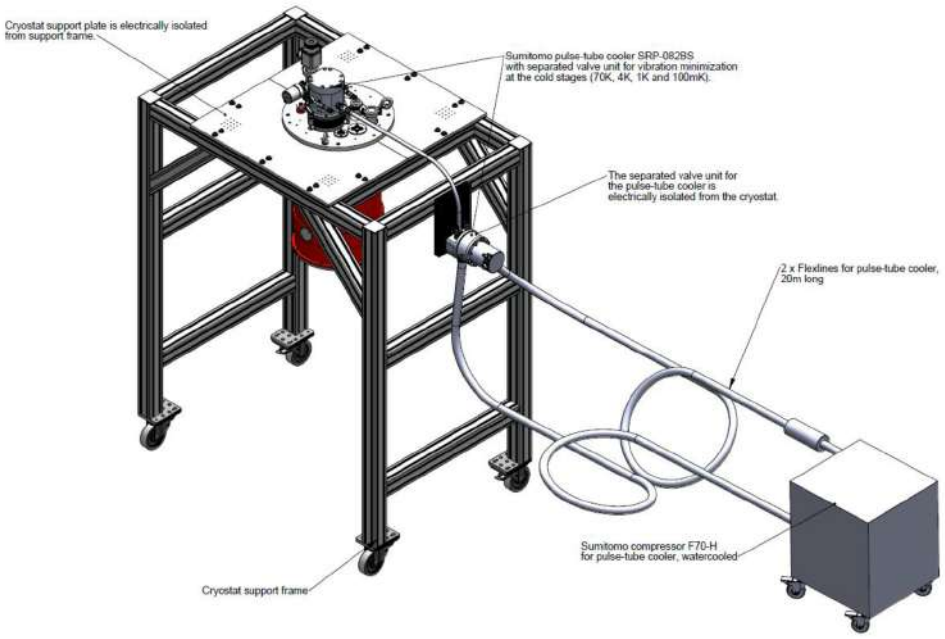

Figure 6.2: Set up of the test bench provided by Entropy GmbH^{TM}.

stages. The magnet current goes up to 40 A during recycling. Cooling time to 4 K is typically around 20 hours, with an additional 2 hours to reach 55 mK through the ADR recycling. The cryogenic chain was designed to provide more than 6 hours of cold time at 55 mK with a 1 µW load power at the FAA stage and 15 µW at the GGG stage.

Mechanical design

The dewar is mounted on a specific structure (see Figure 6.2), with pipes towards the PT Helium compressor (placed outside the clean room in our case). The mechanical design follows the cryogenic chain, with three aluminium shields (300 K, 70 K and 4 K). The 4K shield is layered with gold to ensure a proper thermalisation, and equipped with a hole allowing the crossing of the GGG and FAA cold fingers of the ADR. Each of these fingers carries a gold-layered copper plate (named the "500 mK plate" and the "55 mK plate" respectively). The FPA will be placed on the 55 mK plate. An additional external µ-metal shield is added to avoid contamination from the Earth's magnetic field.

The dewar is equipped with a total of three windows: two on each side of the cylindrical body, and one underneath. In our case, only the side windows will be used. To avoid shot noise and infra-red loads on the detectors, each shield will have an opening equipped with an aluminised Mylar filter, made of 200 nm Al deposited on a 6 µm of $(C_{10}H_8O_4)_n$. An additional vacuum-tight light-element X-ray transmission window provided by Luxel[23] will be mounted on the 300 K stage to remove any excess soft X-ray emission. Finally, an in-house dedicated structure will support the X-ray radioactive source, with slots for X-ray dampening filters to modulate the count rate on the detectors.

[23] https://luxel.com/

6.2.2 Focal plane array and readout

The test bench will provide a verification of the readout chain. It will include:

- An array of representative TES detectors provided by GSFC (see Appendix D).
- The corresponding LC filter chip and transformer chip, provided by SRON.
- A cold electronic and amplification based on SQUIDs, provided by SRON and VTT.
- The warm electronics with a representative ASIC of the WFEE stage provided by APC (Paris), coupled to the digital electronics developed at IRAP.

Design of the focal plane array

The current design on the focal plane array presents similarities with the one retained for the X-IFU. It has however two notable differences. First, to perform functional tests of the readout chain, a full array of detectors is not necessary. Hence, we limit ourselves to smaller arrays, which can provide a few multiplexing channels of 18 pixels each to test the DRE under FDM. This provides a smaller integration complexity at 55 mK than for the X-IFU. Secondly, due to the compactness of the set-up, the 500 mK/4K stages will not be used for signal amplification. Hence, both SQUIDs will be placed on the printed circuit board (PCB) at 55 mK containing the readout electronics. This causes a higher power dissipation at FAA stage than in the baseline X-IFU configuration.

The FPA is based on the equivalent design by NASA (see Figure 6.3 – *Left*). The pixel array will be placed on the farthest side a copper plate, aligned with the dewar windows. Sufficient spacing has been planned to include a 32×32 pixel array. Wire-bonds will connect the TESs to the transformer chip, and the transformer chip to the rest of the circuit on the PCB. The full cold readout circuit, notably the SQUIDs, will be integrated at 55 mK. To have the lowest power consumption a low-power model L6 SQUID by VTT is planned for the amplifier SQUID ($\leq 0.5\,\mu$W at maximal consumption), while a K4 model will be used for the FE SQUID. The electrical connections to warmer stages will be ensured at the end of the FPA by two 21-pin MDM connectors.

The TES detector array will be placed under a NbTi alloy Helmholtz coil, which will tune the pixel operating point or heat pixels stuck in hybrid-normal superconducting phases. The FPA will be bolted to the 55 mK plate. To avoid contamination from the external magnetic field (parasitic and from the ADR magnet), an in-house niobium shield will cover the PCB. X-ray photons will pass through a dedicated 'chimney' (Figure 6.3 – *Right*). Thermalisation of the PCB will be ensured by additional copper rods between the 55 mK and the Nb, which needs to remain superconducting (≤ 9.2 K).

Readout chain and harnesses

The harness design is provided in Appendix I. The entire readout chain is designed to be operated under differential readout for compatibility with the WFEE and the DRE. The connections will be ensured by NbTi looms in the cold stages, and by copper looms at higher temperatures. Only the bias line will be separated from the rest for crosstalk reasons. Feedthroughs between the dewar and the outside will use multi-pin LEMO connectors. The warm electronics will be composed of the AwaXe v2.5 ASIC from APC, coupled with the DRE demonstration model developed at IRAP.

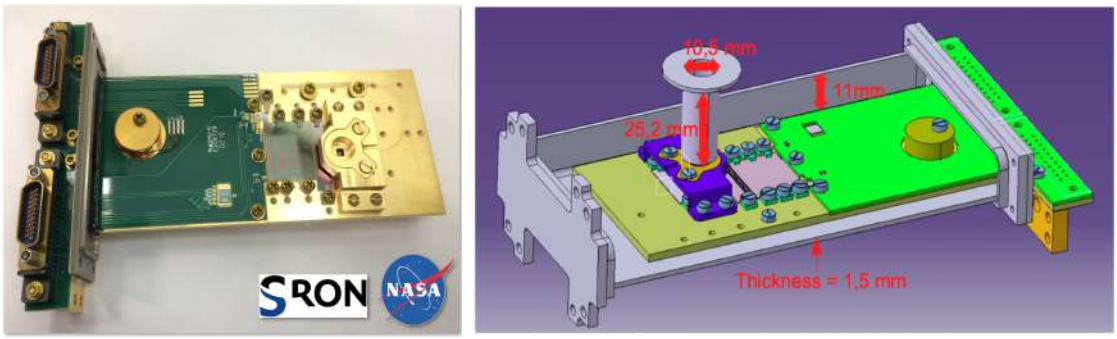

Figure 6.3: (*Left*) Design of the FPA used at NASA GSFC (courtesy NASA, SRON). (*Right*) CAD cutaway of the Nb box used to shield the FPA (courtesy T. Delecroix).

6.2.3 Estimated energy resolution budget

The estimated energy resolution budget for the test bench is provided Appendix I (Table vi). As the main objective of the bench is to perform a demonstration the readout electronics, a higher energy resolution than for flight-like pixels is targeted (3.5 eV).

This budget is inspired from the energy resolution budget (ERB) of the FPA demonstration model and from the X-IFU ERB. Values in this budget were adapted to the test bench application where possible. For a number of contributors however, this exercise is pending new measurements or detailed analysis of e.g. the noise levels at various points in the readout chain. In this case, we defaulted to the values in the flight ERB. I detail here some of the main points of this budget, and refer to the project documentation for more information. Each contributor is given an apportionment which contributes to the total noise, to a drift in operating set point (gain drift correction will be performed on a 1 ks time scale, see Chapter 5) or to "other" when the effect falls in neither of the previous categories (e.g. crosstalk). All contributions are summed by taking the RSS of the apportionments. The finite record length effect presented in Chapter 2 only affects noise terms.

Detector – The energy resolution of the TES is estimated from NEP measurements performed at NASA GSFC (S. Smith, private communication). It includes the intrinsic energy resolution of the detector (~ 2.5 eV FWHM), along with degradations from a non-optimal set point, from the AC readout (AC losses, weak-link effects) and from shot noise. As our set-up should be comparable to NASA's, the same apportionments are used.

Cables noise – Cables and harness noise are referenced to a noise level at SQUID input using the same values as in the X-IFU ERB (in $\mathrm{pA}/\sqrt{\mathrm{Hz}}$). The effect of noise on the energy resolution is estimated through `XIFUSIM` simulations for 7 keV pulses, using the test bench pixel characteristics (Figure 6.4). We notice that noise on the bias line has a lower effect than on the amplifier line (factor $\sim 2/3$), due notably to the LC filters, whose bandwidth limits the noise. A single apportionment of 0.5 eV (FWHM) is given to the conducted susceptibility as a worst case (using the X-IFU noise levels, a total of 0.2 eV FWHM would be expected). These figures will be verified experimentally in the coming months. The same apportionments as those specified in the FPA DM ERB are used for crosstalk. These are derived from current estimates measured at SRON (den Hartog et al., 2019).

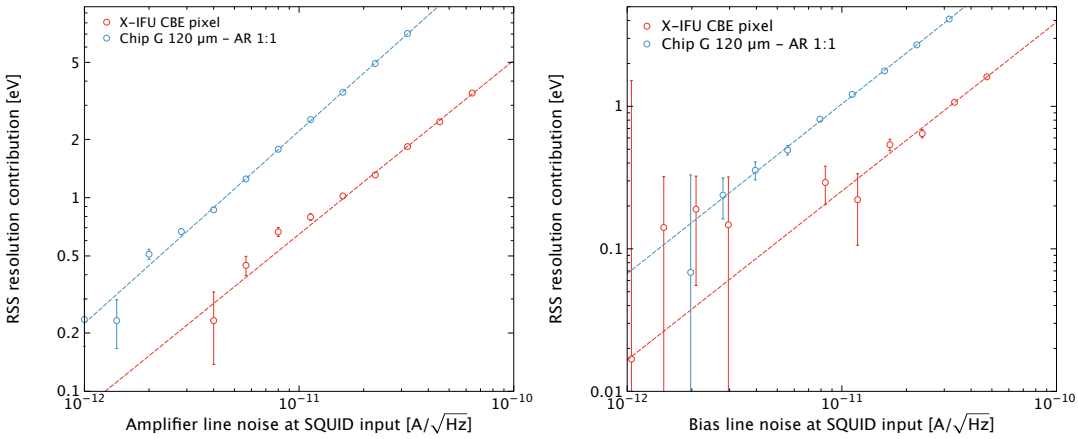

Figure 6.4: Quadratic degradation of the energy resolution (in eV RSS) as a function of the noise in the amplifier (*Left*) and bias line (*Right*). The blue points show the test bench pixel results, the red one those for the baseline X-IFU pixel. The best power law fit is shown in dashed lines. These figures were obtained using a Monte Carlo simulation of 7 keV pulses using `XIFUSIM`. (courtesy P. Peille).

SQUID and shunt resistor – The noise level of the SQUIDs was measured at SRON for similar devices (J .Van der Kuur, M. Kiviranta, private communication). Over the FDM readout bandpass it is expected to be $\sim 5\,\mathrm{pA}/\sqrt{\mathrm{Hz}}$. The Johnson noise on the shunt resistor ($R_{\mathrm{shunt}} = 0.1\,\Omega$) is derived using Equation 3.9 assuming $T_{\mathrm{bath}} = 55\,\mathrm{mK}$ and a current at FPA level $I_0 = 5.64\,\mu\mathrm{A_{rms}}$ (see Appendix D). Using Figure 6.4, these contributors cause a $\sim 1.1\,\mathrm{eV}$ (FWHM) and $\sim 2.86\,\mathrm{meV}$ (FHWM) RSS degradation of the energy resolution.

WFEE and DRE – The degradation of the energy resolution is derived using Figure 6.4 using the same noise levels as the X-IFU ERB. The only difference is on the DAC lines, whose current noise should be reduced by a factor ~ 2.63 due to the lower current before TTR ($5.64\,\mu\mathrm{A_{rms}}$ versus $14.82\,\mu\mathrm{A_{rms}}$ in flight). For the WFEE an experimental verification is planned. Similarly, the degradation induced by the DRE will be measured in the demonstration hardware using a simulated pulse shape derived from `XIFUSIM` with the test bench pixel characteristics. Apportionments will be updated correspondingly.

Thermal stability and micro-vibrations – The thermal stability of the test bench is better than $4\,\mu\mathrm{K_{rms}}$ over a 24-hour period (see below). Using the sensitivity expected for the test bench TESs (simulated at $45.8\,\mathrm{meV}/\mu\mathrm{K_{rms}}$, courtesy P. Peille), we can derive the corresponding value of the degradation of the energy resolution. Micro-vibrations were divided into two components: a micro-phonics component and a micro-vibration drift. Both are allocated a 0.5 eV (FWHM) RSS contribution, which represents a worst-case.

Magnetic field – For the magnetic field drifts, the ADR drifts should be the largest contributor. In our set up, the total drift in norm is expected around $\sim 52.5\,\mathrm{nT}/15\,\mathrm{min}$ (see below). Including 30% margins (due to hysteresis, see below), this should result into a $\sim 12.64\,\mathrm{pT}/15\,\mathrm{min}$ change (radiated susceptibility) and an equivalent $\sim 3.65\,\mathrm{pT_{rms}}$ noise on

the detectors, assuming a worst-case Nb rejection of 5400 (SRON, private communication – results will be updated after actual measurements, see below). Using the sensitivity levels measured at GSFC ($\sim 8\,\mathrm{eV/nT}$ worst-case), the influence of these contributors is of 0.24 eV (FWHM) and 0.07 eV (FWHM) RSS respectively. For high-frequency E-fields ($\geq 1\,\mathrm{MHz}$), an allocation of 0.5 eV (FWHM RSS) is used.

The current energy resolution budget achieves 3.5 eV (FWHM) accounting for additional (25) 0.1 eV (FWHM) RSS engineering margin contributions. New measurements on the test bench will provide bottom-up values to verify these allocations.

6.2.4 Designing an adequate X-ray source for validation

Limiting case and assumptions

To achieve the objectives of the test bench (e.g. DRE tests under high count rates, validation of calibration sources), the detectors need to observe up to 2 cts/s/pix (see also Chapter 3 and 5). The design of the baseline source should therefore satisfy this count rate requirement. Our current choice is to use a ^{55}Fe radioactive source, which emits Mn K_α and K_β photons. These sources have the advantage of being easy to manipulate (low doses), of providing high-energy counts and of having a strong heritage in other X-ray experiments (thus good availability). Their half-life is of $\lambda_{\mathrm{hl}} \sim 2.7$ years.

Source design

The source will be placed on the side window of the dewar using a specific mount, at a distance of $\sim 20\,\mathrm{cm}$ from the detectors. Along the optical axis, the photons emitted by the source will see the Luxel window and the Al/Mylar filters on each of the cold stages. The source will be at less than 3 cm from the outer window, and the rest of the optical axis is considered under vacuum (the pressure inside the dewar is $\sim 10^{-7}\,\mathrm{mbar}$). It should be capable of delivering a count rate $C_0 = 2\,\mathrm{cts/s/pix}$ for at least 4 years with the use of thin filters on the mount during the first years to attenuate the flux. The transmission at 5.88 keV (Mn K_α) over line-of-sight will be affected by (CXRO database):

- The transmission of the $\leq 3\,\mathrm{cm}$ of air between the source and the window: $\tau_{\mathrm{air}} = 0.951$.
- The transmission of the window and the frame: $\tau_{\mathrm{window}} = 0.771$.
- The transmission of each Al/Mylar filter (200 nm/6 µm): $\tau_{\mathrm{Al/Mylar}} = 0.965$.
- The quantum efficiency of the detectors at the Mn K_α energy: $\rho_{\mathrm{QE}} = 0.937$.
- The half-life factor for a four-year operation: $\Lambda = e^{-\ln(2)\times 4\times \lambda_{\mathrm{hl}}^{-1}} \sim 0.358$.

The total number of counts emitted by the source should therefore be $C_0 = C_{\mathrm{tot}} \times \tau_{\mathrm{air}} \times \tau_{\mathrm{window}} \times \tau_{\mathrm{Al/Mylar}}^3 \times \rho_{\mathrm{QE}} \times \Lambda$ which makes a count rate of the source $C_{\mathrm{tot}} = 9.049\,\mathrm{cts/s/pix}$ without attenuation. The solid angle of the square detectors of side $x = 275\,\mu\mathrm{m}$ at a distance d is given by (Figure 6.5 – *Left*):

$$\Omega = 4 \arccos\left(\frac{\sqrt{1+\frac{x^2}{2d^2}}}{1+\frac{x^2}{4d^2}}\right)$$

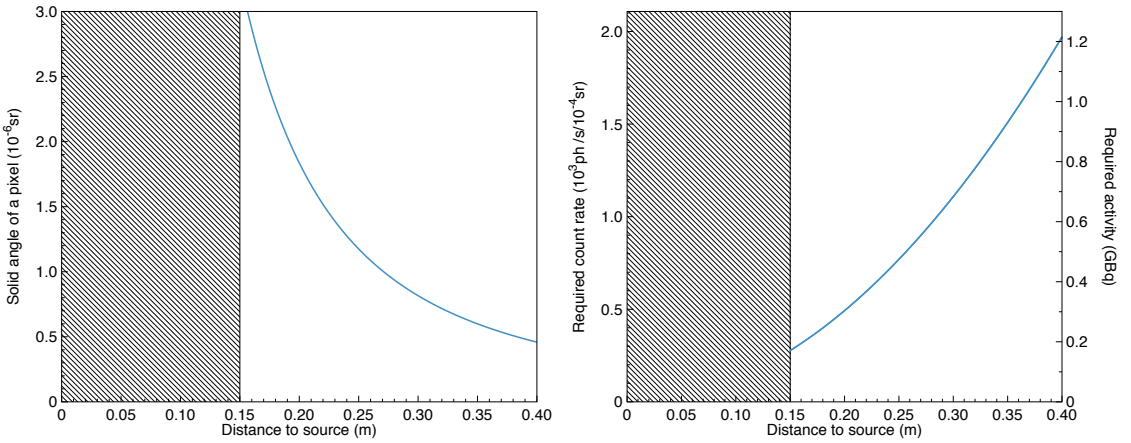

Figure 6.5: (*Left*) Solid angle of a typical 271 µm pixel (in 10^{-6} sr) as a function of distance between the source and the detectors for a detector side $x = 275\,\mu$m (m). Regions below 15 cm are not considered (inside the dewar). (*Right*) Count rate needed from the source (10^3 ph/s/10^{-4} sr) and corresponding activity for a ^{55}Fe (Gbq) as a function of distance between the source of count rate $C_{\text{tot}} = 9.049$ cts/s/pix and the detectors (m).

For a given d, C_{tot} can be expressed in terms of cts/s/10^{-4} sr or as an activity knowing it will only emit over 2π sr (Figure 6.5 – *Right*). For $d = 20$ cm, the corresponding activity of the source is around 300 MBq. A commercial source of 370 MBq is available[24] and will likely be selected for the purpose.

6.3 Characterisation of the test bench: first results

We present here the first results obtained on the test bench. As no representative FPA was implemented during my thesis, these results are related to the characterisation of the cryostat in temperature stability and magnetic field.

6.3.1 Hold time tests

We performed tests to obtain the hold time of the cryostat at a targeted sub-Kelvin temperature, under different load power conditions applied to the GGG and/or FAA stage. The cryogenic chain should provide sufficient cooling power to comply with the FPA power consumption, i.e. remain at a stable temperature of 55 mK with 1 µW load power at FAA level, and 15 µW load power at GGG level, for more than 6 hours. To test this requirement, an excess power is injected using two resistors of 1 kΩ and 5.6 kΩ (including cable resistance) placed at the FAA and GGG stages respectively (Figure 6.6). These resistors can be used individually to study the load power on one of the stages, or simultaneously to simulate a typical FPA power consumption. Results are summarised in Table 6.1. For these tests, the FAA resistor is placed on the cold finger of the sub-Kelvin stage (see Figure 6.6).

The hold time is compliant with the specifications when no 55 mK plate is included. When the plate is included, the hold time drops significantly (25%). This is likely related

[24] https://www.ezag.com

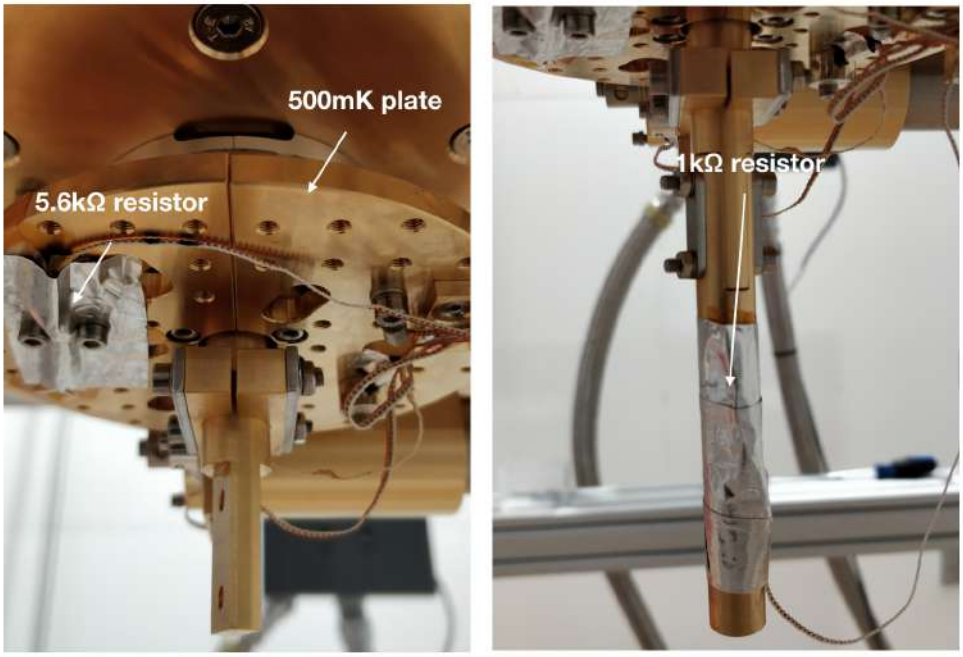

Figure 6.6: Heat load tests set-up during integration. Resistors are fixed on the 500 mK and 55 mK stages respectively, and fixed with Kapton and aluminium tape.

Temperature (mK)	P_{load} on FAA (µW)	P_{load} on GGG (µW)	Hold Time
50	0	0	20 h 32 min
	0.5	0	8 h 35 min
	1	0	5 h 15 min
	1	15	5 h 00 min
55	0	0	23 h 00 min
	0.5	0	11 h 10 min
	1	0	6 h 50 min
	1	15	6 h 05 min
100	0	0	48h 10 min
	0.5	0	31 h 30 min
	1	0	20 h 50 min
	1	15	17 h 30 min

Table 6.1: Hold time measurements performed on the test bench

to the clamping of the plate, which creates a bad thermal conductivity, thus reducing the cooling power. This hypothesis will be investigated by including an additional thermometry on the 55 mK plate. The clamping is also planned to be changed for future experiments. For all measurements, the temperature stability is found to be better than 4 μK_{rms} over the cool-down (and even as low as 3 μK_{rms} for certain runs).

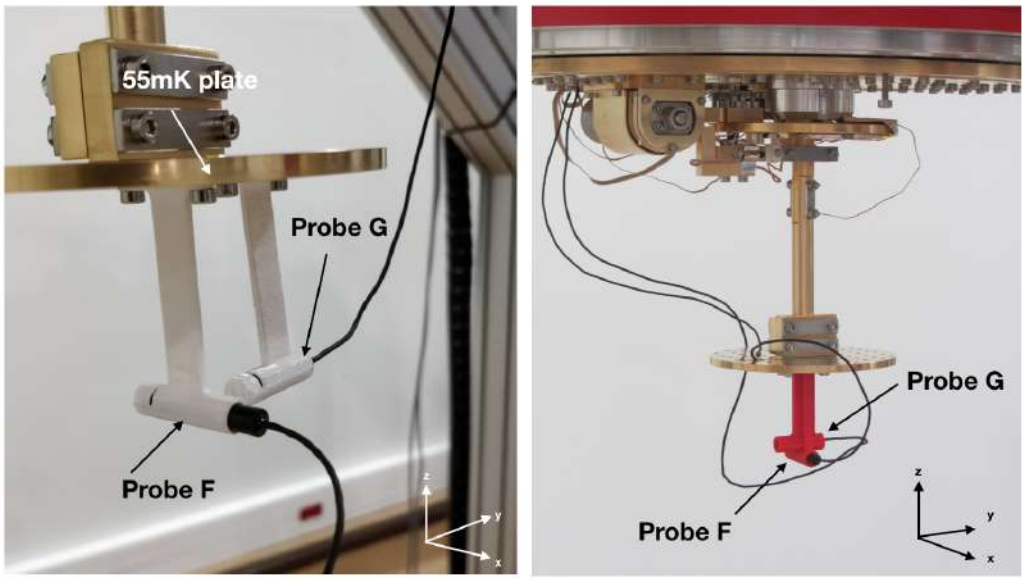

Figure 6.7: Magnetic field measurements set-up at room temperature (*Left*) and for cryogenic measurements (*Right*). The orthonormal frame used for the measurements is reminded in the lower right corner.

6.3.2 Magnetic field characterisation

The second campaign performed on the test bench focused on determining the level of residual magnetic field at the FPA level. To do so, we used two Bartigton cryogenic probes (type F and G), coupled with a Mag-01H readout electronic.[25] The former (type F) provides a cryogenic measurement with a resolution of 0.1 nT and a maximal specified power consumption of 26 mW ($\sim$ 11 mW measured), while the latter (type G), provides a measurement with a resolution of 1 nT and a maximal specified power consumption of 16 mW ($\sim$ 5 mW measured). The probes are placed on the 55 mK plate using two dedicated 3D printed mounting structures (for room temperature and for cold operations), as shown in Figure 6.7. Both mounts are placed at the location of the detectors within the FPA and orthogonal to measure B in two directions: normal to the detector surface (called axis x) or in the perpendicular horizontal direction (called axis y). The vertical direction (axis z) was measured using another similar support.

Given the high power usage of these probes, a sub-Kelvin operation of the cryostat is excluded. Hence, to estimate the magnetic field generated by the magnet in operation (e.g. during ADR recycling), we chose to manually increase/decrease the magnet current to achieve the desired magnetic field at 4 K.

µ-metal shielding factor – The first test aimed at characterising the shielding factor, S, of the external µ-metal shield. S is required to be above 30 in the normal direction of the pixel array (axis x), which is most sensitive to the magnetic field. The total normalisation of the Earth magnetic field (along the three axes x, y and z) is measured around $\sim 43\,\mu$T, consistently with the latest magnetic field models.[26] Six different measurements were

[25] https://www.bartington.com

µ-metal	Shields	Window	x axis	y axis	z axis
No	No	/	-16.522 ± 0.05 µT	-19.915 ± 0.19 µT	-34.058 ± 0.33 µT
No	Yes	Closed	-16.480 ± 0.05 µT	-20,090 ± 0.19 µT	-33.776 ± 0.33 µT
Yes	No	Closed	91.0 ± 0.34 nT	1.126 ± 0.01 µT	-0.740 ± 0.01 µT
Yes	No	Open	-108.6 ± 0.40 nT	1.097 ± 0.01 µT	-0.961 ± 0.01 µT
Yes	Yes	Closed	161.7 ± 0.55 nT	1.125 ± 0.01 µT	-1.003 ± 0.01 µT
Yes	Yes	Open	-179.8 ± 0.61 nT	1.096 ± 0.01 µT	-0.985 ± 0.01 µT

Table 6.2: Worst-case magnetic shielding measurements obtained on *Elsa*

also performed and are summarised in Table 6.2. In the configuration closest to future operations (i.e. µ-metal shield and dewar shields in place, with windows opened), we find shielding factors of $S_x \sim 92$, $S_y \sim 18$ and $S_z \sim 35$. Inside the dewar, the Earth's magnetic field along the axis x is thus attenuated as required.

Characterising the ADR magnetic field – The second test measured the value of B as a function of the current, I_{mag}, circulating in the magnet coil. I_{mag} is changed manually once a 4 K temperature is reached on the cold stages. A settling time of a few minutes is considered between each measurement, and each probe is turned on individually to avoid eddy current contamination of the measurements. Turning on the probes induces only slight temperature changes at the 4 K stage ($\leq$ 100 mK), which can be neglected with respect to changes in the salt pill temperature when the magnet is turned on ($\leq$ 1 K).

Results are shown in Figure 6.8 when the µ-metal shield window is closed (*Left*) or opened (*Right*). All curves are shown for a decreasing magnet current from 6 A to 0 A (representative of a recycling), as hysteresis was highlighted in the measurements (values are up to 50% higher than for an increase from 0 to 6 A). As expected, the magnetic field seen by the probes varies linearly with I_{mag} for low currents ($I_{\text{mag}} \leq 0.5$ A), representing a nominal 55 mK temperature regulation (which starts at $I_{\text{mag}} \sim 0.3$ A). For higher currents ($I_{\text{mag}} \geq 2.5$ A), the slope changes but B continues to grow linearly after the transition, indicating a saturation of the *Cryoperm* and/or *Hyperco* shield(s) around the magnet. Depending on the maximal value of I_{mag}, a further hysteresis was observed. B is $\sim$ 15% higher for a descent from 20 A to 0 A than from 6 A to 0 A. An additional margin of 30% was taken on our measurements to account for a 40 A to 0 A descent during a recycling.

These curves provide the level of magnetic field outside the FPA at a given I_{mag}, and notably the magnetic field drift during a recycling. Assuming that the 55 mK cold time starts at $I_{\text{mag}} \sim 0.3$ A for a total duration of 6 hours (see above), the corresponding drifts are 5.94 nT/15 min (±4.81 pT/15 min) along x, 2.50 nT/15 min (±26.0 pT/15 min) along y, and 52.1 nT/15 min (±46.7 pT/15 min) along z. Using a conservative estimation of the Nb shield magnetic rejection ($\sim$ 5400, private discussion SRON) and the total drift in norm ($\sim$ 52.5 nT/15 min), the drift seen by the detectors should be lower than 9.72 pT/15 min. Adding the 30% margin for hysteresis, we obtain a worst-case value of 12.64 pT/15 min in all directions. This figure is retained in the energy resolution budget (Appendix I).

Nb shield attenuation factor – The final test will measure the value of the Nb shield attenuation. Due to Meissner effect, the niobium freezes the magnetic field state once it becomes superconducting (below $\leq$ 9.2 K) and rejects any further variation of the field.

[26] https://www.ngdc.noaa.gov/geomag/calculators/magcalc.shtml

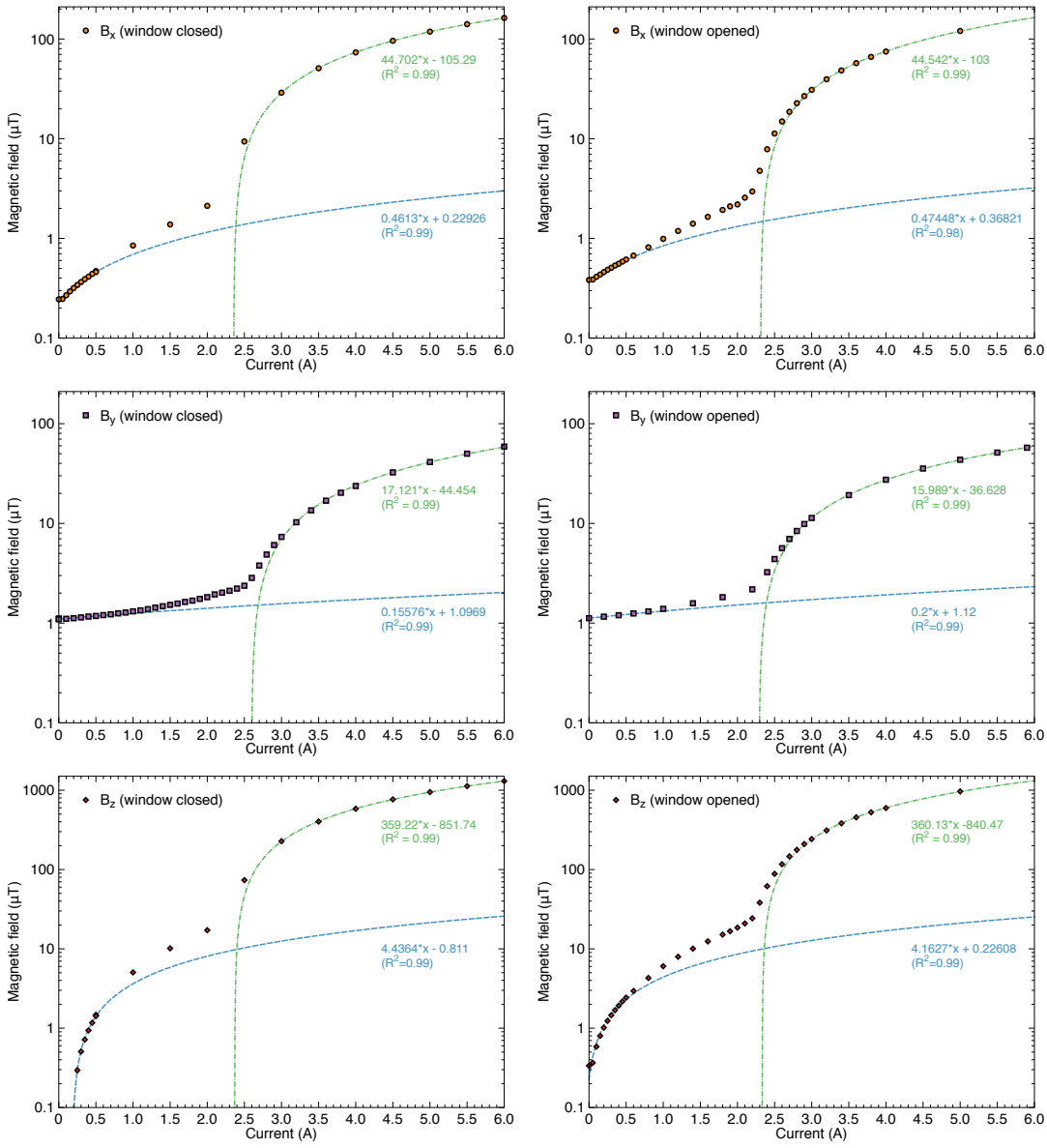

Figure 6.8: Magnetic field on the detectors in all directions (in µT) as a function of the magnet current (in A) when the µ-metal shield window is closed (*Left*) or opened (*Right*). All curves show the behaviour when the current is decreased (similarly to a recycling), as hysteresis provides a higher magnetic field otherwise. The best linear fit for $I_{\mathrm{mag}} \in [0, 0.5]\,\mathrm{A}$ and $I_{\mathrm{mag}} \in [3, 6]\,\mathrm{A}$ are given in blue dashed and green dash-dotted lines respectively. B_x is measured with the probe F in all cases, B_y and B_z are measured with the probe G.

For this test, one of the probes will be placed outside the Nb, and the other within the chimney (where the detectors will be). Simulations were performed to verify that despite the high thermal dissipation of the probe, the chimney will remain superconducting, as we find that it will reach $\sim 7.5\,\mathrm{K}$ during operations, thus guaranteeing a magnetic field

rejection (T. Delecroix, G. Roudil, private communication). To further reduce thermal dissipation in the Nb, an amagnetic sapphire rod will encapsulate the probe within the chimney. Additional copper straps will be placed between the 55 mK plate (at 4 K here) and the chimney to evacuate any excess heat. These tests shall be performed in September 2019. The result will be used to update the energy resolution budget accordingly.

6.3.3 Micro-vibrations

Future characterisation tests will measure the level of micro-vibrations in the dewar, at the detector level and in the other cold stages (notably near the PT). For this experiment, two piezoelectric uni-axial accelerometers by PCB Piezotronic$^{\text{INC}}$ will be used.[27] The first (cryogenic) sensor has a dynamic range of 100 mV/g over a frequency range of 5 kHz (±3 dB), with a resolution of 500 μg_{rms} (model 315B42), while the second (non-cryogenic) has a dynamic range of 1 V/g over a frequency range of 1.7 kHz (±3 dB), with a resolution of 30 μg_{rms} (model 393B04). These accelerometers will be placed on the 55 mK plate at the future position of the detector, in particular along the previously defined x and y axis. Measurements will be read out though a sensor signal conditioner (model 480E09), which provides a direct signal readable using the LabView software. Micro-vibration measurements are scheduled for the third trimester of 2019.

6.4 Conclusions and way forward

In this chapter, I have introduced the cryogenic test bench developed at IRAP and explained the design of its FPA which will be used in future X-ray experiments. A few results can be reminded:

- The design of the cryogenic chain will ensure a stable operation at 55 mK for a duration of 6 hours under typical power consumptions of the FPA.
- Alongside the teams at IRAP and CNES, I have contributed in the design of the overall detection chain of the experiment. Notably, I have dimensioned the activity of the ^{55}Fe radioactive source which will be used for X-ray tests. Final integration of the FPA will occur within 2019, testing is planned over the course of 2020.
- Following the procurement of the test bench, I have performed the early measurement campaigns to characterise the cryostat both in temperature stability, cold time under different power consumption configuration, and magnetic field. The dewar shows a stability below 4 μK_{rms} over the entire cold time and a magnetic shielding consistent with the current requirements.
- The clamping of the 55 mK plate is inadequate for cold operations, degrading hold time of up to 25% with respect to operations without it. An improvement in the system is under study.

The first results on the test bench are an important step forward for the X-IFU teams at IRAP and CNES. This facility provides the hardware required to perform integrated tests and to gain expertise on cryogenic X-ray detection. Beside the current measurement campaigns, *Elsa* will see its first X-ray light in 2019/2020. It will then be used to test the WFEE and the DRE, and to characterise the calibration sources planned for the X-IFU.

[27] https://www.pcb.com/

Conclusion and perspectives

During this thesis, I studied the development of the X-IFU instrument, focusing on three topics: its instrumental performances, its scientific capabilities and its calibration. These aspects are of specific importance early in the mission to optimise the design of the instrument, and prepare for its future data analysis. My results were mainly obtained numerically, exploiting the specific end-to-end simulation tools developed for the instrument: `xifupipeline` within the SIXTE framework, and `XIFUSIM`. The former is a high-level simulator to study the end-to-end performances of the instrument, from an astrophysical source to the detection of events. The latter provides instead an in-depth physical representation of the entire readout chain of TES pixels. I provide here a summary of the main results of this thesis, as well as some open points raised during my studies and perspectives of work to be tackled in future phases of the instrument.

Main results

Crosstalk studies

Starting from measurements and assumptions on the level of crosstalk between pixels in frequency domain multiplexing readout schemes, the end-to-end team implemented a fast description of crosstalk within `xifupipeline`. I participated in this work by accounting for the grading of the events in a more accurate way, and used this updated pipeline to test the count rate capability of the X-IFU in the observation of extended sources. Using two different criteria (on the total crosstalk energy deposited and on the degradation of the overall energy resolution), I have demonstrated that the X-IFU will be capable of observing bright extended sources such as the Perseus cluster and even bright supernovæ remnants (e.g. Cassiopeia A) while maintaining a high-resolution throughput above 80%.

Background studies

The knowledge of the level of the instrumental background will be an important factor in the observations of faint sources, notably in the high-energy bandpass. Using the driving science case of galaxy cluster outskirts observations, I have shown that this level should be

known to better than 2% ($\pm 1\sigma$) over 100 ks to minimise systematic effects in the observations. By using the available hardware within the instrument and on the *Athena* satellite, I have put forward multiple ways to achieve this accuracy over the course of the mission.

Feasibility of galaxy cluster observations with the X-IFU

End-to-end simulations are an excellent tool to forecast the X-IFU performances. Taking advantage of previous work, I have extended the existing simulation pipeline started by my predecessor, P. Peille, to assess the feasibility of some of the challenging science objectives of the X-IFU, in particular related to the observation of clusters of galaxies.

Starting from a sample of clusters extracted from hydrodynamical simulations, I have demonstrated that the X-IFU will be capable of observing the ICM with unprecedented accuracy, even with 100 ks exposures, and characterise the underlying chemical enrichment models by measuring for the first time rare atomic elements. Benefiting of the high collective area of *Athena*, the X-IFU will also be capable of observing clusters out to $z \sim 2$, thus providing insight on the chemical enrichment of the Universe across cosmic time.

The X-IFU will provide new results on the ICM turbulent motions as well. In this regard, I have shown that it will be capable of measuring bulk and turbulent velocities with accuracies of a few tens of km/s. Turbulence measurements rely however on predefined line diagnostics (line shift, line broadening or structure functions), which can be biased by sampling variance effects (i.e. cosmic variance) and by the statistics of the measurements. N. Clerc and I have demonstrated that errors on the diagnostics can be accurately computed using analytical formulas, without computationally cumbersome iterative approaches.

Calibration results

The calibration of the X-IFU is of utmost importance to maximise the scientific return of the mission. In particular, quantities such as the energy scale, the energy resolution or the quantum efficiency of the instrument need to be accurately known to interpret future measurements. By taking advantage of the properties of AC-biased TESs and the available hardware (in particular the onboard modulated X-ray source), I have introduced new ways to monitor and correct the energy scale of the instrument within its requirement. This study also provided interesting constraints on the design of the instrument, namely on the flux of the modulated X-ray source, or the need to pool pixel together during energy scale monitoring to reduce the overall dead time. Finally, to investigate calibration requirements, I have developed a Monte Carlo-based pipeline, which I applied here to variations in the quantum efficiency. With this approach, I showed that despite small gradients on the deposited TES absorbers (5%), no major systematic effect will be seen in the data ($\leq 1\%$).

Development of a cryogenic test bench

Simulations of the detectors can never reproduce the breadth of real physical effects. To test calibration requirements experimentally, I have participated in the development of a cryogenic facility based at IRAP and helped in the design of its detector array. Awaiting on the final integration of the hardware, I have taken the lead on various measurement campaigns to characterise the cryostat (hold time, temperature stability, magnetic field).

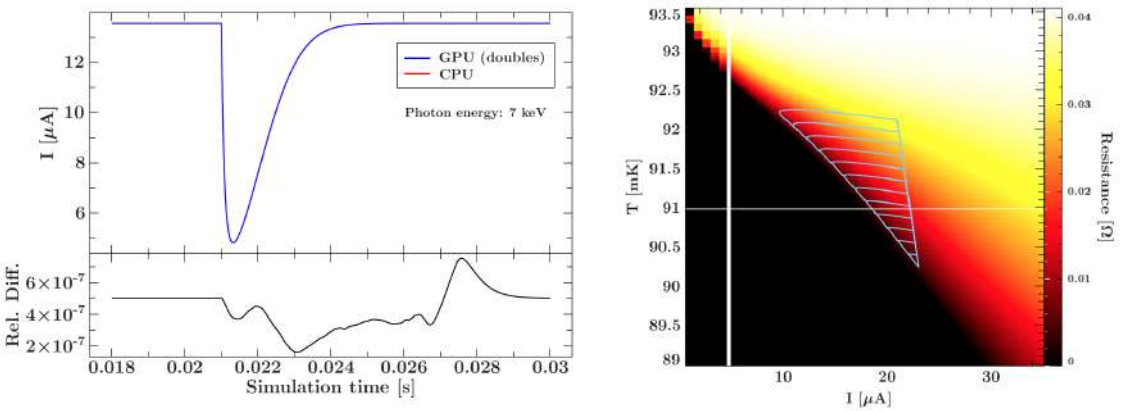

Figure I: Current developments within `XIFUSIM` (Lorenz et al., in prep.). (*Left*) Pulses simulated on one pixel with a GPU and with a CPU. For a full detector simulation (3168 pixels), the time gain is around 100. (*Right*) New transition plane (resistance, temperature, bias current – L. Gottardi, private communication) describing the AC-bias transition of the TES interpolated by `XIFUSIM`. The 'trajectory' of the pulses in time is shown in light blue for various energies (from 1 to 12 keV, with steps of 1 keV). Credits: C. Kirsch.

Perspectives and future work

End-to-end simulator developments

The current X-IFU simulation tools provide a representative, albeit simplified, view of the overall readout chain. These routines must therefore be regularly updated and improved to describe the variety of instrumental effects. As an example, `xifupipeline` is being improved with new tables and features to test the effects of cosmic rays, of thermal instabilities, and of crosstalk (spatial dependence) on the overall performances. Other limitations in the description of TESs within `XIFUSIM` were highlighted in Chapter 3. Large efforts are conducted by the end-to-end team to improve this description. More accurate TES models and a finer description of the AC-bias transition are for instance under implementation (Figure I, Lorenz et al., in prep.).

On a longer time scale, the structure of `XIFUSIM` will enable to update independently each subsystem block with new models or experimental results, creating a detailed detection chain simulator. Finally, to avoid the simplified data analysis performed in `xifupipeline` through response matrices, graphic processing unit (GPU) interfaces of `XIFUSIM` are studied to parallelise the detection on the array and apply the actual readout scheme to the data streams (filtering, triggering and energy scale function). This will enable full realistic simulations of the entire pixel array.

Constraining the IMF with the X-IFU

The initial mass function (IMF) is key to understand the production of the metallic content of the Universe. It provides the distribution in mass of stars needed to estimate the metal production of SN_{cc} explosions and AGB winds. It is also needed to determine the global

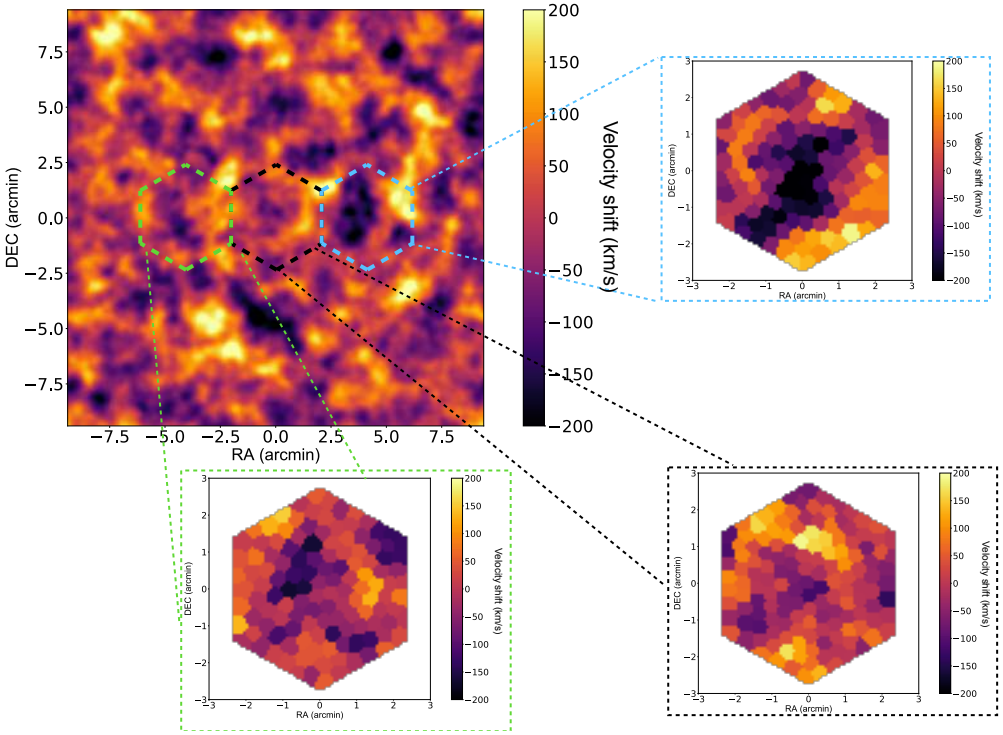

Figure II: Example of future investigations of the ICM turbulence using the error formulas derived in Chapter 4. By simulating a large grid of velocities (*Top left* – emission-measure weighted projection in km/s), we can optimise the observation strategy for a given exposure (ZuHone et al., 2016). I provide here the case of a simple radial sweep, for a total observation time of 300 ks evenly distributed between the pointings. The underlying power spectrum is simulated with $k_{\rm inj} = 150\,{\rm kpc}^{-1}$, $k_{\rm dis} = 10\,{\rm kpc}^{-1}$, and $\alpha = -11/3$.

composition of white dwarfs involved in $\rm SN_{Ia}$, although to a lesser extent, as white dwarfs undergoing $\rm SN_{Ia}$ explosions are assumed to be similar in mass prior to the event. Hence, an ill-constrained IMF can bias the enrichment models.

In the study I conducted in Chapter 4, yields were integrated assuming a Salpeter-like IMF. In the simulated sample however, the IMF is a piece-wise function derived from Chabrier (2003). To investigate the capabilities of the X-IFU in recovering the IMF, an option is, for a set of fixed models, to see the evolution of $\chi^2_{\rm red}$ on the same data set for different IMF slopes or mass cut-offs. Preliminary results are promising ($\chi^2_{\rm red}$ from 1.49 to 1.32 with the true IMF), but must be confirmed by future tests. These results would prove that X-IFU is capable of providing additional constraints on the IMF, thus validating the expected science objective.

Optimising the observation of turbulence in the intra-cluster medium

The use of analytical and semi-numerical formulas demonstrated in Chapter 4 provides a powerful and accurate tool to estimate the cosmic variance in forthcoming studies of

the ICM turbulent motions. Beside the immediate benefit in computational time of this method with respect to Monte Carlo-like approaches, the formulas derived by N. Clerc and myself have the advantage of highlighting the main contributors to the total error budget. In particular, they show the effect of the detector FoV and geometry on the cosmic variance.

The framework for new simulations of the ICM turbulence is available, and larger investigations can now be conducted. They can either focus on optimising the observational strategy of turbulence (similarly to ZuHone et al., 2016, , see Figure II), or to selectively reduce cosmic variance by using ingenious exposure strategies or innovative detector geometries. Eventually, these formulas shall be gathered in a single code repository for the community. They will allow the preparation of future observations by astronomers.

Feasibility studies of the X-IFU science cases

The end-to-end simulations I conducted are an example of what can be achieved numerically. These studies are central to improve our understanding of the X-IFU before launch, and to prepare our community for high-quality X-ray spectroscopic data (post-processing, atomic databases, hyperspectral methods). End-to-end simulations can also be perturbed in countless ways (background, calibration errors, crosstalk, geometry effects) to investigate specific features and optimise our instrumental design.

The simulator based on `xifupipeline` is now well established and can be scaled up to test the feasibility of any science objective (similarly to Cucchetti et al., 2018f; Roncarelli et al., 2018). Future investigations could include a more targeted investigation of galaxy cluster outskirts (recovery of physical parameters, observational strategies), observation of groups or studies of the dynamics of the ICM. It will be crucial to assess the feasibility of the most challenging science objectives of the X-IFU by the time of its launch. These simulations can also be used to improve our post-processing tools to face the complexity of spatially resolved high-resolution spectroscopy data. Ideas include revisiting our binning strategies (Kaastra & Bleeker, 2016), or using neural networks to improve spectral fitting (Ichinohe et al., 2018). Hyperspectral methods could also be explored.

Energy scale monitoring and calibration

Currently, no predefined analytical formula exists to describe the energy scale function of TES detectors. Although monitoring and correction techniques based on polynomial interpolations of this function should be sufficient to achieve the requirement for the X-IFU (see Chapter 5), functional forms would provide large benefits in both calibration time and accuracy. First results were obtained using the small signal solution of Equation 3.1 and a polynomial approximation of the eigenvalues τ_+ and τ_- as a function of energy (see Cucchetti et al., 2018a). Further investigations should be pursued to improve the overall knowledge of these detectors and their calibration. The various gain correction techniques presented here should also be tested in representative set-up to assess their feasibility.

Calibration pipeline

A good knowledge of the expected level of systematic errors will be needed before launch. The pipeline presented in Chapter 5 is a way to investigate how calibration uncertainties

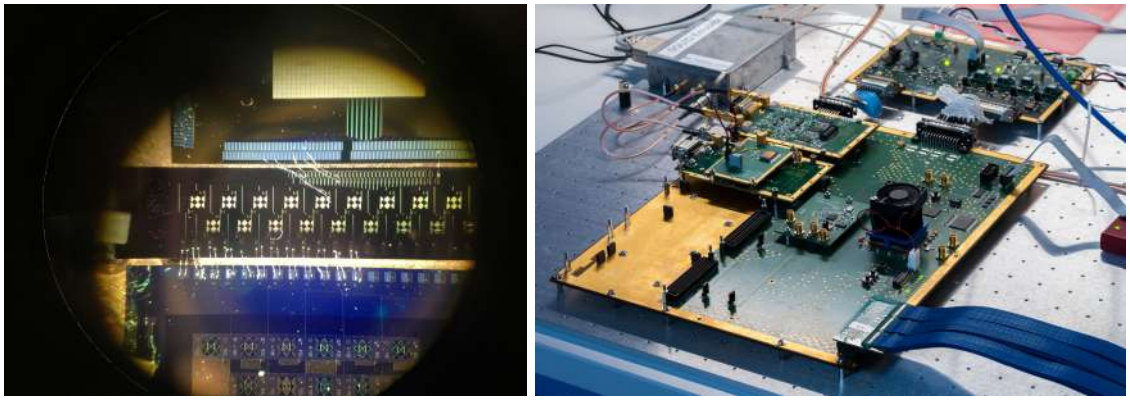

Figure III: Example of future work on the test bench. (*Left*) Development of the focal plane array. Bonding tests of the pixels on a dummy array provided by GSFC (Credits: G. Betancourt-Martinez). (*Right*) Current demonstration model of the DRE cards validated using `XIFUSIM`-simulated pulses. A copy of this set-up will be validated using the test bench (Credits: D. Murat, courtesy L. Ravera).

affect the scientific data. Unlike Drake et al. (2006), it provides an observer-oriented way to evaluate these systematic effects, bearing in mind that the end user will only have a 'calibrated' set of instrumental responses. This pipeline was already used in several studies (observations the ICM properties, Cucchetti et al. 2018c, measurement of black hole spins, Barret et al., 2019, sub.), and can be extended to any other relevant science case.

Way forward with the test bench

Since the delivery of the cryogenic test bench in 2018, experimental activities have gradually gained importance within the X-IFU team (especially at CNES and IRAP). Following the early characterisations of the test bench performed during my thesis, other measurements (e.g. micro-vibration tests) will analyse the environment of the detectors. Improvements of the 55 mK plate clamping system are also planned. In parallel, the focal plane array will be finalised (bonding, PCB, grounding, Figure III – *Left*) along with its niobium box. A first test is planned at NASA GSFC at the beginning of 2020. Once operational, the test bench will focus on a short time scale (i.e. by mission adoption in 2021) on demonstrating the proper operation of the DRE cards (see Figure III – *Right*), which are so far validated using `XIFUSIM`-simulated pulses. Later on, the test bench will characterise the calibration sources of the X-IFU. Other technologies or dedicated control programs for the flight model could also be considered for testing in the years to come.

General conclusion

The road for a complete development of the X-IFU is still long and the work started during my thesis is only a beginning. The early phases of the instrument are the most critical to ensure a design that is compliant with the scientific requirements while remaining feasible technically and financially. End-to-end simulations prove to be a powerful tool for

researchers and engineers in this phase. Even with simplified representations of complex physical phenomena, I have shown that we can provide countless information on the future operations of the instrument. In later phases, hardware and demonstration models will of course be needed to verify experimentally the most critical parts of the design. This will be an appropriate task for the cryogenic test bench at IRAP, as well as the other facilities within the consortium. Even then, numerical simulations will still be at the core of the X-IFU development to assess the feasibility of its science objectives. Finally, this effort will be vain if the calibration and the data processing are not adequate. I have underlined that the X-IFU will provide an unprecedented quantity (several Gb per observation) and complexity (3168 pixels with a 2.5 eV energy resolution) in the data. The X-ray community must be ready to handle this information. Recent missions, such as *Hitomi*, and planned missions, such as *XRISM*, will be pathfinders in this transition. The exquisite results of *Hitomi* have already proven that our knowledge of theoretical physics and our usual post-processing tools are insufficient to understand spatially resolved high-resolution X-ray spectroscopy. I am confident that the community will rise to this challenge, making the X-IFU a cornerstone in the future of soft X-ray astronomy.

Conclusion et perspectives

Au cours de cette thèse, j'ai étudié le développement de l'instrument X-IFU. J'aborde trois sujets en particulier : ses performances instrumentales, ses capacités scientifiques et sa calibration. Ces aspects sont importants dans les premières phases de la mission afin d'optimiser l'architecture de l'instrument et préparer l'analyse des données. Mes résultats ont été obtenus pour la plupart numériquement, grâce aux outils spécifiques de l'instrument : `xifupipeline` dans l'interface SIXTE et `XIFUSIM`. Le premier permet d'analyser les performances de l'instrument dans sa globalité, en partant de l'émission de photons par des sources astrophysiques jusqu'à leur détection. Le second permet d'avoir une vue représentative plus approfondie de la chaîne de lecture de l'instrument. Je présente ici une synthèse des résultats obtenus, ainsi que des points restant ouverts ou des perspectives de travail pour les futures phases de l'instrument.

Résultats principaux

Diaphonie entre les pixels

En partant des modèles actuels et des mesures des niveaux de diaphonie entre les pixels dans des chaînes de lecture de TES, l'équipe de développement des simulateurs a amélioré la prise en compte de ce phénomène au sein de `xifupipeline`. J'ai contribué à ces travaux en incluant l'effet de la classification des événements sur la diaphonie. Cela m'a ensuite permis d'évaluer les capacités en taux de comptage du X-IFU dans l'observation de sources étendues. En utilisant deux critères différents (sur le niveau total d'énergie déposée par la diaphonie et sur la dégradation de la résolution en énergie de chaque détecteur), j'ai démontré que le X-IFU sera capable d'observer des sources étendues brillantes, comme l'amas de Persée ou encore des rémanents de supernovæ (par ex. Cassiopée A), tout en gardant un débit de photons à haute résolution supérieur à 80%.

Études sur le niveau de bruit de fond instrumental

La connaissance du niveau bruit de fond instrumental sera un paramètre important dans l'observation de sources dont le flux est très faible, et plus particulièrement encore dans

la bande haute énergie de l'instrument. En utilisant le cas scientifique dimensionnant de l'observation de la périphérie des amas de galaxies, j'ai démontré que ce niveau devra être connu à mieux que 2% ($\pm 1\sigma$) sur une période de 100 ks afin d'éviter des effets systématiques dans les observations. J'ai également mis en avant diverses façons d'atteindre cette précision au cours de la mission, en tirant profit du matériel disponible au sein de l'instrument et à bord du satellite *Athena*.

Étude de faisabilité de l'observation d'amas de galaxies avec le X-IFU

Les simulations end-to-end sont des outils appropriés pour vérifier les performances instrumentales du X-IFU. En m'inspirant de travaux conduits par la communauté, j'ai étendu et amélioré les outils mis en place par mon prédécesseur, P. Peille, afin d'étudier la faisabilité des objectifs scientifiques du X-IFU, notamment ceux relatifs aux amas de galaxies.

En partant d'un échantillon représentatif d'amas tirés de simulations hydrodynamiques, j'ai montré que le X-IFU sera capable d'analyser le milieu intra-amas avec une précision inégalée, et ce même lors d'observations de 100 ks. Il pourra ainsi caractériser les modèles d'enrichissement chimique de ce gaz en mesurant, pour la première fois, les abondances de métaux rares du milieu intra-amas. Grâce à la grande surface efficace du miroir d'*Athena*, le X-IFU pourra également observer des amas jusqu'à un redshift $z \sim 2$, donnant donc des informations sur l'enrichissement chimique au cours du temps.

Le X-IFU s'intéressera aussi aux mouvements turbulents du milieu intra-amas. Il pourra notamment mesurer des vitesses turbulentes avec des précisions de quelques dizaines de km/s. Ces mesures s'appuieront toutefois sur des diagnostics spectraux bien définis (décalage des raies, élargissement spectral, fonctions de structure), qui peuvent être biaisés par des effets de variance d'échantillonnage (aussi connue sous le nom de variance cosmique) ou bien par la statistique des mesures. N. Clerc et moi-même avons montré que ces biais peuvent être déterminés de façon très précise par une méthode semi-analytique, nous permettant ainsi de nous affranchir de méthodes itératives, souvent très consommatrices en temps de calcul.

Calibration de l'instrument

La calibration du X-IFU sera très importante pour maximiser les retours scientifiques de la mission. Plus particulièrement, des quantités comme l'échelle de gain, la résolution en énergie ou l'efficacité quantique devront être connues avec grande précision pour comprendre les données de l'instrument. En utilisant les propriétés des détecteurs TES sous polarisation alternative et le matériel disponible à bord (notamment la source modulée de rayons X), j'ai introduit de nouvelles méthodes pour contrôler et corriger les dérives d'échelle de gain au niveau attendu. Cette étude a également permis de donner des contraintes sur l'architecture de l'instrument, notamment sur le flux des sources modulées de rayons X, ou le besoin de grouper les pixels lors de la correction de l'échelle de gain afin d'éviter un temps mort significatif dans les observations. Enfin, pour étudier la sensibilité aux incertitudes de calibration, j'ai développé une approche numérique Monte Carlo, que j'ai appliqué à des changements de l'efficacité quantique. Avec cet outil, j'ai par exemple démontré que malgré des petits gradients observés dans le dépôt des absorbeurs (5%), les effets systématiques sur les données restent faibles ($\leq 1\%$).

Développement d'un banc de test cryogénique

Même les simulations les plus complètes ne parviennent pas à représenter la réalité complexe des détecteurs. Des expériences sont alors nécessaires pour tester les besoins de calibration de l'instrument. Le banc de test développé à l'IRAP s'inscrit dans cette démarche. Au cours de ma thèse, j'ai aidé au développement de ce banc ainsi qu'à ses tests de tenue en froid, et sa caractérisation en température et champ magnétique.

Perspectives et travaux en cours

Améliorations des simulateurs end-to-end

Les outils de simulation développés pour le X-IFU fournissent une description représentative, bien que simplifiée, de la chaîne de détection de l'instrument. Ces programmes sont mis à jour et améliorés de façon régulière afin d'y inclure toujours plus d'effets physiques. C'est le cas de `xifupipeline`, dans lequel de nouvelles tables d'interpolation sont en cours d'implémentation pour décrire l'effet de changements de température de bain, de l'impact de rayons cosmiques sur le support des détecteurs, ou encore d'une dépendance spatiale de la diaphonie entre les pixels. J'ai pu mettre en évidence également, au Chapitre 3, des limites dans la description des détecteurs TES au sein de `XIFUSIM`. D'importants efforts sont menés par l'équipe de développement des simulateurs pour améliorer ces modèles. Cela passe notamment par une meilleure description de la transition de ces détecteurs en polarisation AC (Lorenz et al., in prep.).

À plus long terme, la structure du simulateur `XIFUSIM` mise en place au cours de ma thèse permettra de tester indépendamment chaque bloc (i.e., chaque sous-système) et de l'améliorer soit avec des modèles plus précis, soit en se basant sur des résultats expérimentaux. Enfin, pour éviter des approches simplifiées de la chaîne de lecture (comme cela est fait dans `xifupipeline`), une interface basée sur des processeurs graphiques (GPU) est en cours d'étude. L'objectif est de paralléliser la détection de photons de `XIFUSIM` à l'échelle de la matrice de plus de 3000 pixels sans perte de vitesse de calcul, et en appliquant la véritable technique de lecture prévue en vol (filtrage, déclenchement par détection du front montant de l'impulsion, application de l'échelle de gain) plutôt qu'une utilisation des matrices de réponse.

Contraindre l'IMF à l'aide du X-IFU

La fonction de masse initiale (IMF) est un paramètre clé pour comprendre l'évolution du contenu métallique de l'Univers. Elle permet de donner la distribution en masse des étoiles à l'origine de la production de métaux lors de supernovæ par effondrement du cœur ou de vents stellaires. L'IMF est aussi utile pour donner la composition des naines blanches impliquées dans des supernovæ de type Ia, bien que dans une moindre mesure, car ces événements se déroulent par définition avec des étoiles similaires en masse. Une mauvaise connaissance de l'IMF est une source de biais dans les modèles d'enrichissement chimique.

Dans l'étude menée au Chapitre 4, les rendements stellaires de métaux étaient intégrés avec une IMF de type Salpeter. Dans l'échantillon d'amas simulés, l'IMF est en réalité une fonction inspirée de Chabrier (2003). Pour étudier les capacités de X-IFU à contraindre

cette IMF, une option est de varier, pour des modèles fixés, les paramètres de l'IMF et voir l'évolution du $\chi^2_{\rm red}$. Des résultats préliminaires montrent des résultats prometteurs ($\chi^2_{\rm red}$ passe de 1.49 à 1.32 avec la nouvelle IMF), mais de nouvelles études restent nécessaires. Ces résultats permettraient de montrer que le X-IFU donnera des contraintes sur l'IMF, et ainsi valider le cas scientifique correspondant.

Optimisations des observations de la turbulence du milieu intra-amas

Les modèles analytiques et les formules démontrées au Chapitre 4 sont des outils adaptés et précis pour estimer la variance cosmique dans les mesures de turbulence du milieu intra-amas. Outre le gain immédiat en temps de calcul de cette méthode par rapport à une simulation Monte Carlo, les formules dérivées par N. Clerc et moi-même ont l'avantage de mettre en évidence les différents termes responsables de ces erreurs. En particulier, ils donnent la contribution du champ de vue et de la géométrie du détecteur sur la valeur totale de la variance cosmique.

L'outil de simulation utilisé pour tester ces formules dans le Chapitre 4 offre aussi la possibilité d'étudier des éventuelles optimisations des stratégies d'observation (comme abordé par ZuHone et al., 2016), ou de minimiser de façon sélective l'erreur totale en utilisant des stratégies d'observations spécifiques ou une géométrie innovante des détecteurs. À terme, ces formules devront être rassemblées dans un seul répertoire de codes utilisable par les astronomes pour préparer leurs futures observations.

Études de faisabilité des cas scientifiques du X-IFU

Les simulations end-to-end conduites au cours de ma thèse soulignent l'intérêt plus large de ces outils pour étudier le X-IFU. Elles sont importantes pour améliorer la compréhension d'un tel instrument avant son lancement, et pour préparer la communauté scientifique à des données spectrales rayons X à haute résolution (analyse de données, bases de données atomiques, méthodes hyperspectrales). La variété des études possibles via des simulations end-to-end (bruit de fond, incertitudes de calibration, diaphonie, effets géométriques) permet aussi de cibler certains aspects de la performance de l'instrument.

Mon simulateur end-to-end basé sur `xifupipeline` est fonctionnel. Il peut ainsi être réutilisé afin d'étudier la faisabilité d'autres cas scientifiques, de la même manière que dans Cucchetti et al. (2018f) ou encore Roncarelli et al. (2018). Il pourrait par exemple être appliqué à l'observation de la périphérie des amas de galaxies (stratégies d'observation, mesure des propriétés physiques), l'observation de groupes de galaxies ou encore à l'étude de la dynamique du milieu intra-amas. Il sera crucial de valider les objectifs scientifiques du X-IFU avant son lancement. Ces simulations sont aussi un outil pour préparer l'analyse des données du X-IFU, et plus généralement des données de spectroscopie rayons X à haute résolution spectrale résolue spatialement. De nouvelles idées incluent une optimisation du regroupement de pixels (Kaastra & Bleeker, 2016), ou l'utilisation de réseaux de neurones pour trier et ajuster les spectres à des modèles physiques (Ichinohe et al., 2018). Des méthodes hyperspectrales peuvent aussi être explorées.

L'échelle de gain et sa calibration

A l'heure actuelle, l'échelle de gain de détecteurs TES ne peut pas être décrite par une forme fonctionnelle. Elle est ainsi approchée par des polynômes d'ordre élevé. Bien que les techniques mises en avant au Chapitre 5 s'appuient sur cette réalité pour répondre aux spécifications attendues du X-IFU, des formes fonctionnelles permettraient de gagner en précision et en temps de calibration. J'ai pu donner des premiers résultats dans ce sens en partant de la solution petit signal de l'Equation 3.1, en approchant les valeurs propres τ_+ et τ_- en fonction de l'énergie par des polynômes du second ordre (Cucchetti et al., 2018a). De nouvelles études demeurent cependant nécessaires afin de converger vers une forme fonctionnelle plus précise. Enfin, les diverses techniques de correction de gain mises en avant dans ce manuscrit devront être testées dans des conditions représentatives.

Simulateur des incertitudes de calibration

Une bonne connaissance des erreurs systématiques de l'instrument sera nécessaire avant le vol. J'ai présenté au Chapitre 5 un simulateur permettant d'étudier l'effet systématique des incertitudes de calibration sur les données scientifiques. Contrairement à la méthode de Drake et al. (2006), cet outil permet aux observateurs d'évaluer ces erreurs en se plaçant dans des conditions « réelles », où l'utilisateur ne possède qu'un jeu de réponses calibrées pour effectuer ses analyses de données. Ce simulateur a déjà été utilisé dans quelques études (observation du milieu intra-amas Cucchetti et al. 2018c, mesure de spin des trous noirs, Barret et al., 2019, sub.). Il peut être étendu à tout autre cas scientifique pertinent.

Développement du banc de test

Depuis la livraison du banc cryogénique en 2018, les activités expérimentales au sein de l'IRAP et du CNES augmentent graduellement. Les premiers résultats sur la caractérisation du banc obtenus au cours ma thèse seront notamment complétés par de nouvelles mesures, afin de connaître de manière plus précise l'environnement des détecteurs (par ex., en micro-vibrations). La fixation de la platine 55 mK sur le doigt froid du cryostat sera aussi améliorée. En parallèle, le plan focal (impression du circuit, points de masse, bonding) et sa boîte en niobium seront finalisés, avant d'effectuer un test intégré à la NASA GSFC début 2020. Une fois opérationnel, le banc sera utilisé à courte échelle (i.e., pour l'adoption de la mission en 2021) pour démontrer le fonctionnement des cartes du DRE, qui ont pour l'instant été validées informatiquement à l'aide de photons simulés par `XIFUSIM`. À plus long terme, le banc servira à caractériser les sources de calibration pour le modèle de vol du X-IFU. D'autres technologies ou des programmes de pilotage spécifiques à l'instrument pourront également être testés dans les années à venir.

Conclusion générale

Le développement du X-IFU est encore long et le travail entamé au cours de ma thèse s'inscrit dans les prémices de ce projet. Les phases de conception de l'instrument sont les plus critiques, car elles permettent d'optimiser l'architecture du X-IFU afin de satisfaire ses

objectifs scientifiques, tout en garantissant un instrument réalisable techniquement et financièrement. Les simulations end-to-end sont un outil pour les ingénieurs et les chercheurs durant cette phase. Même avec des représentations simplifiées de phénomènes complexes, j'ai démontré qu'il est possible de donner de nombreuses informations sur les futures opérations de l'instrument. Lors des phases suivantes du projet, les prototypes et les modèles de démonstration seront bien sûr nécessaires pour valider les technologies critiques du X-IFU. Le banc cryogénique développé à l'IRAP s'inscrit dans cette démarche, tout comme d'autres infrastructures mises en place à travers le consortium instrument. Même à ce stade, les simulations resteront un outil indispensable pour garantir la faisabilité des objectifs scientifiques de l'instrument. Enfin, ces efforts seraient vains sans une calibration des données à la hauteur des attentes. J'ai souligné que le X-IFU produira un volume (plusieurs Gb par observation) et une complexité (3168 pixels à 2.5 eV de résolution spectrale) de données jamais rencontrés auparavant dans une mission à rayons X. La communauté rayons X se doit d'être prête d'ici le lancement en 2031. Des missions récentes, comme *Hitomi*, ou à venir, comme *XRISM*, seront des précurseurs à cette transition. Les résultats exceptionnels de *Hitomi* ont déjà démontré que notre connaissance des raies atomiques et nos outils de traitement de données ne sont pas suffisants pour de la spectroscopie haute résolution résolue spatialement. Je suis confiant que la communauté saura relever ces nouveaux défis et fera du X-IFU un instrument clé du futur de l'astronomie en rayons X.

List of Figures

List of Tables

Acronyms

AC: Alternative Current
ACIS: Advanced CCD Imaging Spectrometer
ADC: Analogue-to-Digital Converter
ADR: Adiabatic Demagnetisation Refrigerator
AGB: Asymptotic Giant Branch
AGN: Active Galactic Nucleus
APC: Astrophysique et Cosmologie
ARF: Ancillary Response File
ASIC: Application Specific Integrated Circuits
ATHENA: Advanced Telescope for High-Energy Astrophysics
BBFB: Base-Band Feedback
BCG: Brightest Cluster Galaxy
BH: Black Hole
CAD: Computer-Aided Design
CC/NCC: Cool-Core/Non-cool-core cluster
CCCM: Channel-Cut Crystal Monochromator
CCD: Charged-Coupled Device
CDM: Cold Dark Matter (also Code Domain Multiplexing)
CFEE: Cold Front-End Electronics
CFRP: Carbon-Fibre Reinforced Polymer
CMB: Cosmic Microwave Background
CNES: Centre National d'Études Spatiales
CPU: Central Processing Unit
CREME: Cosmic Ray Effect on Micro-Electronics (code)
CryoAC: Cryogenic Anti-Coincidence detector
CXB: Cosmic X-ray Background
DAC: Digital-to-Analogue Converter
DC: Direct Current

DCS: Detector Cooling System
DDS: Direct Digital Synthesiser
DEPFET: Depleted p-channel Field-Effect Transistor
DM: Dark Matter
DRE: Digital Readout Electronics
E2E: End-To-End
EBIT: Electron-Beam Ion Trap
ECAP: Erlangen Centre for Astroparticle Physics
EM: Emission-Measure
EMW: Emission-Measure-Weighted
EPIC: European Photon Imaging Camera
ERB: Energy Resolution Budget
ESA: European Space Agency
ETF: Electro-Thermal Feedback
EW: Emission-Weighted
FAA: Ferric Ammonium Alum
FB: FeedBack
FE: Front End
FoV: Field-of-View
FDM: Frequency Domain Multiplexing
FPA: Focal Plane Assembly
FPGA: Field-Programmable Gate Arrays
FW: Filter Wheel
FWHM: Full Width at Half Maximum
GCR: Galactic Cosmic Ray
GGG: Gadolinium-Gallium Garnet
GPU: Graphic Processing Unit
GRB: Gamma-Ray Burst
GSE: Ground Support Equipment
GFSC: Goddard Space Flight Center (NASA)
GW: Gravitational Wave
HETG: High-Energy Transmission Grating
HEW: Half-Energy Width
HFI: High Frequency Instrument
HWHM: Half Width at Half Maximum
ICM: Intra-Cluster Medium
ICS: Inner Cryogenic Shield
ICU: Instrument Control Unit
IPCS: Inner Passive Cryogenic Shield
IFCA: Istituto de Fisica de Cantabria
IFU: Integral Field Unit

IGM: Intergalactic Medium
IRAP: Institut de Recherche en Astrophysique et Planétologie
ISM: Interstellar Medium
ITFN: Internal Thermal Fluctuation Noise
IXO: International X-ray Observatory
JT: Joule-Thomson (cooler)
LEO: Low Earth Orbit
LNA: Low Noise Amplifier
LPA: Large Pixel Array
LSF: Line Spread Function
LUT: Look-Up Table
MAM: Mirror Assembly Module
MC: Monte Carlo
MM: Mirror Module
MOSFET: Metal-Oxyde Semiconductor Field-Effect Transistor
MW: Mass-Weighted
MXS: Modulated X-ray Source
NEP: Noise Equivalent Power
NS: Neutron Star
NXB: Non-X-ray Background
OCS: Outer Cryogenic Shield
OV: Outer Vessel
PAMELA: Payload for Antimatter/Matter Exploration and Light-nuclei Astrophysics
PCB: Printed Circuit Board
PDU: Power Distribution Unit
PHA: Pulse Height or Pulse Height Amplitude
PSF: Point Spread Function
PT: Pulse Tube (cooler)
QE: Quantum Efficiency
RGS: Reflection Grating Spectrometer
RK: Runge-Kutta
RMF: Redistribution Matrix File
RMS: Root Mean Squared
RSJ: Resistively Shunted Johnson (model)
RSS: Root Sum Squared
RTU: Remote Terminal Unit
S/N: Signal-to-Noise ratio
SIM: Science Instrument Module
SIMPUT: Simulation input (file)
SIXTE: Simulator for X-ray Telescopes
SMBH: Supermassive Black Hole

SN_e Supernovæ

SNR: Supernova Remnant (also Signal-to-Noise Ratio)

SNRD: Signal-to-Noise Ratio Density

SOHO: Solar and Heliospheric Observatory

SPH: Smoothed Particle Hydrodynamics

SPO: Silicon Pore Optics

SQUID: Superconducting Quantum Interference Device

SRG: Spectrum Roentgen-Gamma

SREM: Standard Radiation and Environment Monitor

SVOM: Space Variable Objects Monitor

SXI: Soft X-ray Imager

SXS: Soft X-ray Spectrometer

SZ: Sunayev Zel'dovich (effect)

TDM: Time Domain Multiplexing

TES: Transition Edge Sensor

TFN: Thermal Fluctuation Noise

TTR: Transformer Turns Ratio

ToO: Target of Opportunity

UFO: Ultra-Fast Outflow

UV: Ultra-Violet

WD: White Dwarf

WFEE: Warm Front-End Electronics

WHIM: Warm Hot Intergalactic Medium

WFI: Wide Field Imager

XCaT: X-IFU Calibration Team

XIS: X-ray Imaging Spectrometer

X-IFU: X-ray Integral Field Unit

XMS: X-Ray Micro-calorimeter Spectrometer

XRB: X-Ray Binary

XRISM: X-Ray Imaging Spectroscopy Mission

A The X-IFU product tree

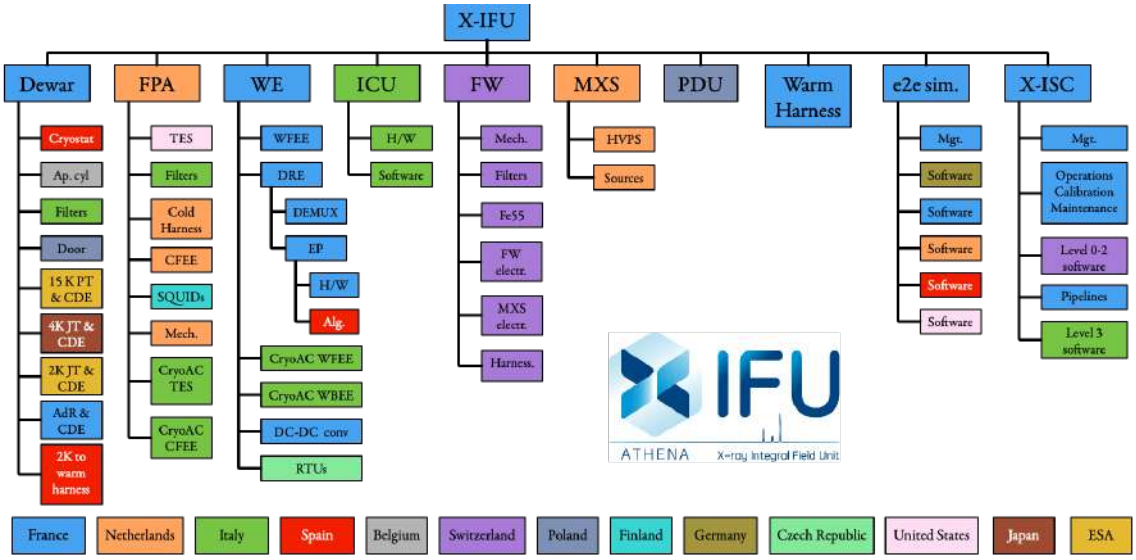

Figure i: The X-IFU product tree (courtesy D. Barret)

B The X-IFU readout chain

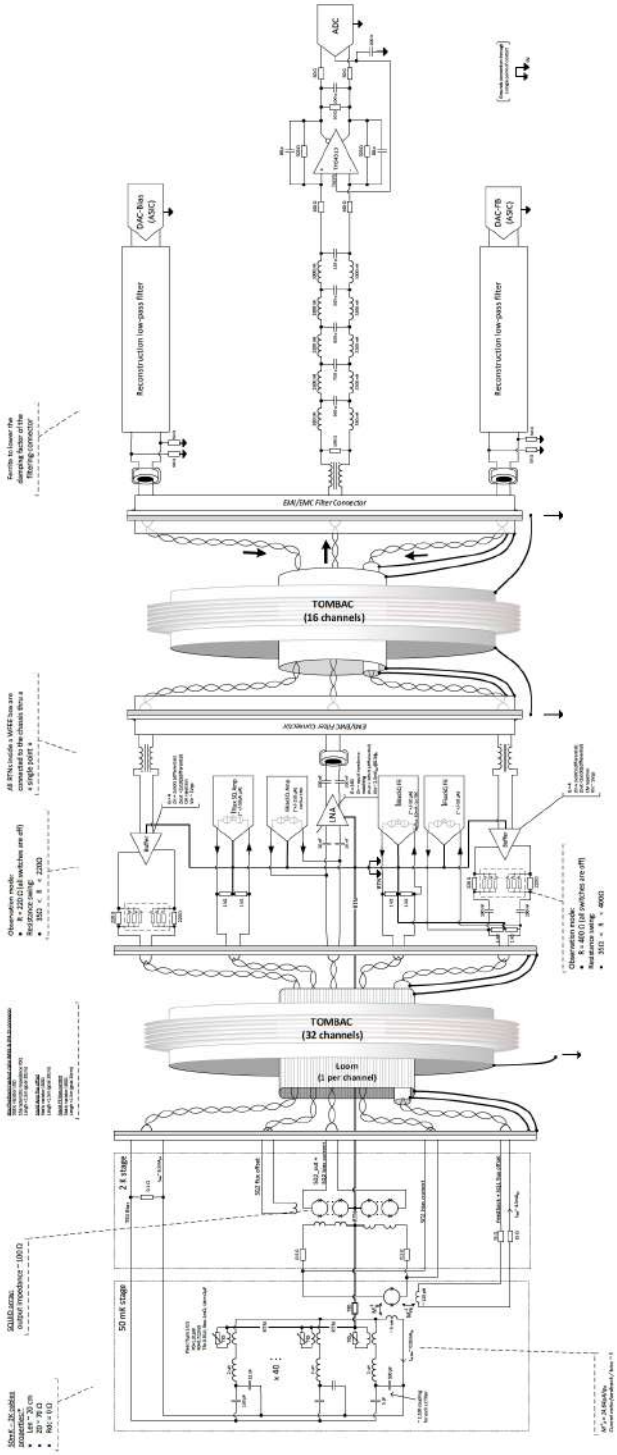

Figure ii: The X-IFU readout chain

C Examples of SIXTE .xml input files

C.1 Primary .xml file for xifupipeline

```
<instrument telescop="Athena" instrume="XIFU">
  <telescope>
    <focallength value="12.0"/>
    <fov diameter="0.5"/>
    <arf filename="sixte_xifu_cc_baselineconf_20180821.arf"/>
    <psf filename="athena_psf_onaxis_20150602.fits"/>
    <vignetting filename="athena_vig_15row_20171016.fits"/>
  </telescope>

  <detector>
    <dimensions xwidth="64" ywidth="60"/>
    <wcs xrpix="32.5" yrpix="32.5" xrval="0." yrval="0."
    xdelt="265.e-6" ydelt="265.e-6"/>
    <rmf filename="athena_xifu_sixte_v20150402.rmf"/>
    <phabackground filename="xifu_nxb_20170926.pha"/>
    <threshold_readout_lo_keV value="200.e-3"/>
    <threshold_event_lo_keV value="200.e-3"/>
    <readout mode="event"/>
  </detector>

</instrument>
```

C.2 Secondary .xml file for xifupipeline

```
<pixdetector type="x-ifu" pixeltype="LPA_75_AR0.5" npix="3832"
xoff="124.5e-6" yoff="124.5e-6">
<samplefreq value="156.25e+3"/>

    <grading num="1" name="high" pre="494" post="8192"
    rmf="athena_xifu_rmf_highres_v20150609.rmf"/>
    <grading num="2" name="mid" pre="494" post="512"
    rmf="athena_xifu_rmf_midres_v20150609.rmf"/>
    <grading num="3" name="lim" pre="494" post="256"
    rmf="athena_xifu_rmf_limres_v20170213.rmf"/>
    <grading num="4" name="low" pre="494" post="4"
    rmf="athena_xifu_rmf_lowres_v20150609.rmf"/>

    <threshold_event_lo_keV value="5.e-2"/>

    <channel_freq_list filename="lpa_freq_mux40.dat"/>

    <crosstalk>
        <thermalcrosstalk distance="249.01e-6" weight="1e-3"
        timedepfile="timedependency_LPA_75um_AR0.5.fits"/>
        <thermalcrosstalk distance="352.14e-6" weight="4e-4"
        timedepfile="timedependency_LPA_75um_AR0.5.fits"/>
        <thermalcrosstalk distance="498.01e-6" weight="8e-5"
```

```
        timedepfile="timedependency_LPA_75um_AR0.5.fits"/>
        <electricalcrosstalk filename="lut_tessim_LPA_75um.fits"
        timedepfile="timedependence_LPA_75um.fits"/>
<intermodulation filename="nlxtlk-LPA2-v4w_8192.fits"/>
    </crosstalk>


    <hexagonloop radius="0.0095961370452" pixelpitch="275e-6" cross="1">
        <pixel>
           <shape posx="$x" delx="$p" posy="$y" dely="$p"
           width="245e-6" height="245e-6"/>
        </pixel>
    </hexagonloop>

</pixdetector>
```

C.3 XIFUSIM .xml

```
<detector model="FDM" filename="pars_8.fits" hduname="Lin8_MUX8">

  <TesArray>
     <TES model="LinTES" filename="pars_8.fits" hduname="LPA75um"/>
  </TesArray>

  <SQUID model="BBFBSquid" filename="pars_8.fits" hduname="BBSquid"/>

  <DRE model="BBFB_DRE" filename="pars_8.fits"  hduname="BBDRE"/>

  <ADC model="Adc" filename="pars_8.fits" hduname="ADC_16_LPA75um"/>

  <Trigger model="TriggerDiff" filename="pars_8.fits" hduname="TrigLPA75um"/>

</detector>
```

D The X-IFU pixel properties

The X-IFU pixel baseline provided at the end of phase A in 2019 is summarised in Table i. The absorber is made of a Au/Bi bi-layer. It is a square of 271 µm, with a 4 µm spacing on each side separating the absorbers. The corresponding pixel pitch is thus 275 µm, for a filling factor of 97.11%. The TES itself is located under the absorber and is made of Mo/Au bi-layer. It has a rectangular shape of 75 µm on the longest side and an aspect ratio of 1:0.5. Table i also gathers the test bench pixel properties.

Parameter	Baseline X-IFU	Test bench
TES length / aspect ratio	75 µm / 1:0.5	120 µm / 1:1
Transition temperature T_0	87.78 mK	91.09 mK
Bath temperature T_{bath}	55 mK	55 mK
Normal resistance R_n	69.76 mΩ	30.1 mΩ
Bias point R_0/R_n	10.20%	15.0%
Heat capacity C	1.062 pJ/K	1.10 pJ/K
Thermal conductance G	59.68 pW/K	175 pW/K
Power factor n	3.0391	3.78
Transition parameter α	532.49	806
Transition parameter β	8.07	7.72
Unexplained noise term (Johnson) M	1.73	2.82
Set point current I_0	13.555 μA_{rms}	28.201 μA_{rms}
Transformer turns ratio TTR	0.9144	2.4
Critical damping inductance L_{crit}	2393.2 nH	347 nH
ETF fall time τ_{ETF}	1373.2 µs	293 µs
Damped rise/fall time τ_{crit}	316.8 µs	71 µs
Small signal ΔE_{FWHM}	1.69 eV	1.76 eV
Pixel effective bandwidth f_{eff}	423.3 Hz	1159 Hz

Table i: Baseline pixel and test bench pixel properties

E Grading scheme

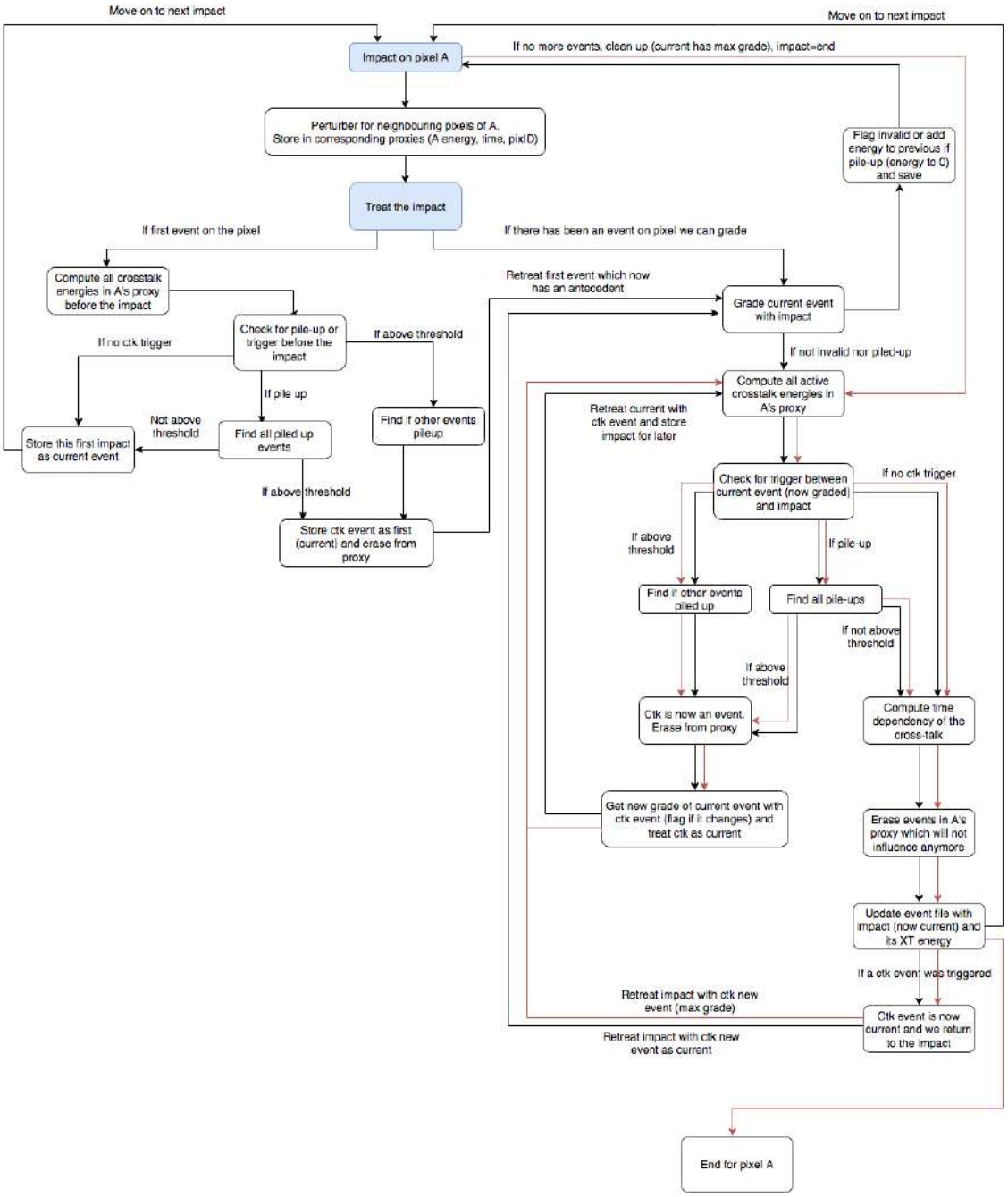

Figure iii: Grading and crosstalk algorithm flowchart for a single pixel simulated with `xifupipeline` on SIXTE

F TDM crosstalk studies

TDM is the current back-up solution of FDM for the readout of the X-IFU pixels. Within phase A, dedicated investigations on TDM were conducted to assess the main changes needed in the overall readout chain should this solution be used. I discuss here the TDM readout and present then simulation results conducted on crosstalk within this framework.

F.1 TDM readout principle

TDM was historically the first readout technique used for large arrays of micro-calorimeters (Chervenak et al., 1999; de Korte et al., 2003; Irwin & Hilton, 2005). The principle of the readout is shown in Figure iv and is based on sequential switches, which address DC-biased pixels in a "column" at different steps in time. During a certain time period δt, the first pixel in the column is read out, then the following, until all pixels in the same column are considered. To do so, the SQUIDs for each pixel are turned on and off sequentially by flux-actuated switches (Zappe, 1977; Beyer & Drung, 2008) using step functions shifted of δt, with a duty cycle of $1/N_{\rm rows}$, where $N_{\rm row}$ is the number of pixels in the column (or "rows"). This process can be parallelised to multiple columns of pixels, addressed by the same on/off signal within a row. Provided a good knowledge of the on/off cycle of each pixel, signal on the different pixels is sampled with a frequency $1/(N_{\rm row}\delta t)$.

Unlike FDM, TDM does not provide a continuous stream of signal in each pixel but in turn does not require any specific demodulation. Currently, high-frequency controllers can provide frequencies up to the MHz on the switches, allowing a sampling rate very similar to that of FDM after decimation. A major difference remains that, since pixels are read out sequentially each with their own SQUID, the total SQUID noise increases of a factor $\sqrt{N_{\rm row}}$. Although TDM SQUIDs are optimised to reduce the overall noise and need a lower bandpass than in FDM (below the MHz), the overall noise budget remains somewhat higher than that of the FDM readout.

Currently, TDM possess a solid experience and latest results on large matrices show excellent results ($\leq 2.5\,$eV on multiple columns, Doriese et al. 2016; Ullom et al. 2018). Improvements in the TDM scheme are also possible through CDM, where Walsh functions are used to simultaneously read the pixels instead of step functions (Irwin, 2009), decreasing the SQUID noise and improving performances.

F.2 Crosstalk studies

The count rate performances of the X-IFU were also tested for a TDM readout, similarly to Section 3.4.3. Though no difference is expected in the grading rejection, crosstalk mechanisms differ in the case of TDM. We distinguish four types of contributors:

- **Thermal crosstalk**: this mechanism remains one of the crosstalk contributors, with equivalent effects as for FDM.
- **Time-forward (N→N+1)**: A single feedback line service the columns related to a given SQUID. Within a row, a given electrical setting time exist between pixels. If a pulse occurs in the row N of a given column, it creates an excursion on the corresponding SQUID which remains visible even after the readout has moved towards

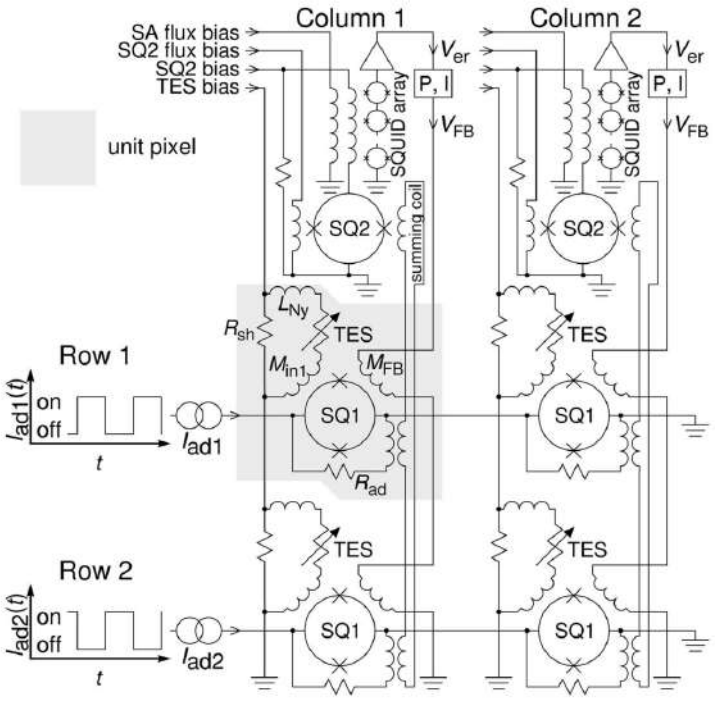

Figure iv: Reproduced from Doriese et al. (2016), Figure 1. TDM readout principle for a 2×2 pixel matrix.

the next row (N+1). Consequently, a perturbation pulse may be seen in the next pixel of the same column. This crosstalk contributor is well described by a proportional crosstalk creating a smaller version of the perpetrator pulse with a new pulse of energy $3.7 \times 10^{-3} E_p$. In the rest of the study, we denote this component as "Type 1" proportional crosstalk.

- **Distant pixel**: columns share the same feedback line. Thus, any impact in one of the rows causes small excess currents in any of the signals of the same column. This contributor is imperfectly described by a proportional crosstalk, with a new pulse in each pixel of the column of energy $3.0 \times 10^{-4} E_p$. In the rest of the study, we denote this component as "Type 2" proportional crosstalk.
- **Inductive coupling**: similarly to common impedance in the FDM case, inductive coupling between wiring neighbours or next-neighbours can induce perturbation in the signal. This contributor is described by an excess derivative pulse in the victim pixels, with a fraction $1.0 \times 10^{-3} E_p$. For simplicity, we assume that neighbours affected are the spatial neighbours and the pixels on rows N-1 and N+1 of the same column. In the rest of the study, we denote this component as derivative crosstalk.

Aside from thermal crosstalk, reused from the FDM simulations, each of the three other contributors was implemented in the SIXTE simulator using a fractional approach similar to thermal crosstalk. For proportional type crosstalk, the same time dependency as thermal crosstalk is used, while a different time dependency table is used for the derivative

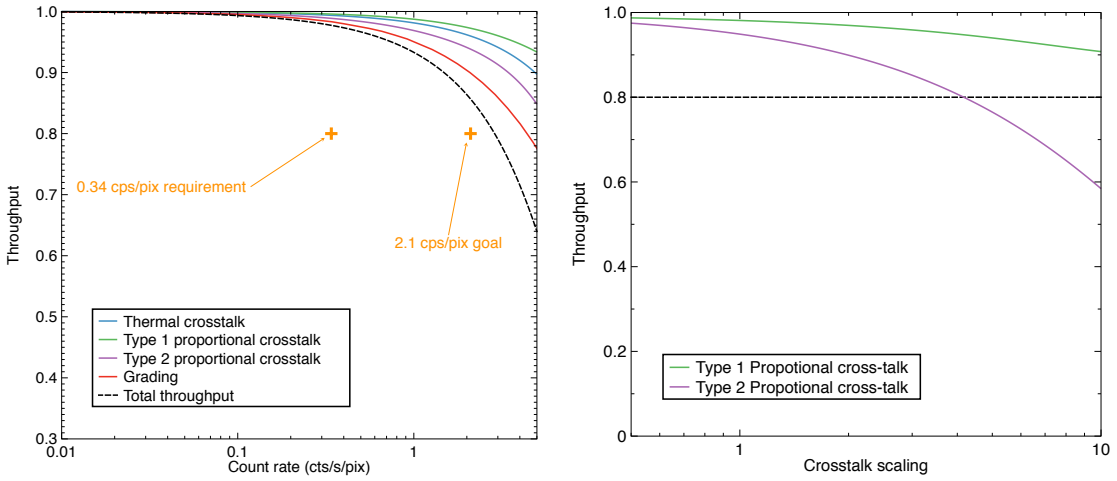

Figure v: (*Left*) Total throughput for extended sources (blacked dashed line) as a function of the count rate (cts/s/pix). In this plot, events with more than 0.2 eV of crosstalk influence are discarded. The throughput when only grading (red), thermal crosstalk (blue), type 1 proportional crosstalk (green) or type 2 proportional crosstalk (purple) are rejected are also shown. The contribution of the derivative crosstalk is neglected. (*Right*) Total throughput obtained for requirement count rate (0.34 cts/s/pix) as function of the linear scaling applied to type 1 (green) or type 2 (purple) proportional crosstalk.

crosstalk. The energy fractions were estimated through measurements performed at the National Institute for Standards (NIST, private discussion R. Doriese, J. Ullom, K. Morgan, Adams et al. 2019). The corresponding LUTs and time dependency tables were computed using `XIFUSIM` and used for crosstalk simulations in `xifupipeline`.

The count rate simulations are performed similarly to those presented in Section 3.4.3, using the same input sources and crosstalk estimation techniques. Results are shown in Figure v (*Left*). As expected the grading and thermal crosstalk contribution remain unchanged with respect to the FDM counterpart. Of the TDM crosstalk mechanisms, the proportional crosstalk dominates the others, notably type 1. This result is fairly intuitive, as for extended sources, given the similar fraction for both proportional crosstalk mechanisms, type 2 affects more pixels than type 1, thus resulting in a higher contribution. Derivative crosstalk is negligible, even at moderately high count rates and its pulse shape (different from a typical pulse) should be rejected by the optimal filtering. Similarly to FDM, both the Perseus requirement and the Cas A goal are met using a TDM readout.

To provide sizing factors for TDM readout schemes, the same study was performed by varying the contributions of the two proportional crosstalk terms by an order of magnitude, as shown in Figure v (*Right*). Derivative crosstalk was neglected, as shown to have $\leq 0.01\%$ effects on throughput even for fractions 10 times higher the estimated value. As expected, the largest constraint is set by the type 2 crosstalk, which can only accept a factor ~ 4 degradation for the requirement (and $\sim 1.5/2$ for the goal). Overall, these studies provide an interesting tool to test the count rate performances of the X-IFU for different readout schemes and provide orders of magnitude of the acceptable crosstalk for each mechanism.

G List of supernovæ models

I provide in this section the list of supernovæ models used in Chapter 4 and used in the `abunfit` Python package (courtesy F. Mernier).

Category	Name	Reference	Remarks
			SN_{Ia}
Classical	W7	1	Deflagration $\rho_9 = 2.12$
	W70	1	Deflagration $\rho_9 = 2.12$, $Z_{\rm init} = 0$
	WDD1	1	Delayed-detonation $\rho_9 = 2.12$, $\rho_{T,7} = 1.7$
	WDD2	1	Delayed-detonation $\rho_9 = 2.12$, $\rho_{T,7} = 2.2$
	WDD3	1	Delayed-detonation $\rho_9 = 2.12$, $\rho_{T,7} = 3.0$
	CDD1	1	Delayed-detonation $\rho_9 = 1.37$, $\rho_{T,7} = 1.7$
	CDD2	1	Delayed-detonation $\rho_9 = 1.37$, $\rho_{T,7} = 2.2$
	Th03	2	Mix deflagration/delayed-detonation
Bravo	DDTa	3	Delayed-detonation, fits the Tycho SNR, $\rho_{T,7} = 3.9$
	DDTb	3	(private comm., does not fit Tycho SNR, unpublished)
	DDTc	3	Delayed-detonation, fits the Tycho SNR, $\rho_{T,7} = 2.2$
	DDTd	3	(private comm., does not fit Tycho SNR, unpublished)
	DDTe	3	Delayed-detonation, fits the Tycho SNR, $\rho_{T,7} = 1.3$
	DDTf	3	(private comm., does not fit Tycho SNR, unpublished)
Ca-rich gap	CO.45HE.2	4	Ca-rich SNe, $M_{\rm CO} = 0.45$, $M_{\rm He} = 0.2$
	CO.55HE.2	4	Ca-rich SNe, $M_{\rm CO} = 0.55$, $M_{\rm He} = 0.2$
	CO.5HE.15	4	Ca-rich SNe, $M_{\rm CO} = 0.50$, $M_{\rm He} = 0.15$
	CO.5HE.2	4	Ca-rich SNe, $M_{\rm CO} = 0.50$, $M_{\rm He} = 0.2$
	CO.5HE.2C.3	4	Ca-rich SNe, $M_{\rm CO} = 0.50$, $M_{\rm He} = 0.2$, 30% mixing He-core layer
	CO.5HE.2N.02	4	Ca-rich SNe, $M_{\rm CO} = 0.50$, $M_{\rm He} = 0.2$, 2% N in He layer
	CO.5HE.3	4	Ca-rich SNe, $M_{\rm CO} = 0.50$, $M_{\rm He} = 0.3$
	CO.6HE.2	4	Ca-rich SNe, $M_{\rm CO} = 0.60$, $M_{\rm He} = 0.2$
2D	C-DEF	5	2D deflagration $\rho_9 = 2.9$
	C-DDT	5	2D delayed-detonation $\rho_9 = 2.9$, $\rho_{T,7} = 1.0$
	O-DDT	5	2D delayed-detonation $\rho_9 = 2.9$, $\rho_{T,7} = 1.0$, off-centre ignition
3D	N1def	6	3D deflagration $\rho_9 = 2.9$, 1 ignition spot
	N3def	6	3D deflagration $\rho_9 = 2.9$, 3 ignition spots
	N5def	6	3D deflagration $\rho_9 = 2.9$, 5 ignition spots
	N10def	6	3D deflagration $\rho_9 = 2.9$, 10 ignition spots
	N20def	6	3D deflagration $\rho_9 = 2.9$, 20 ignition spots
	N40def	6	3D deflagration $\rho_9 = 2.9$, 40 ignition spots
	N100Hdef	6	3D deflagration $\rho_9 = 1.0$, 100 ignition spots
	N100def	6	3D deflagration $\rho_9 = 2.9$, 100 ignition spots
	N100Ldef	6	3D deflagration $\rho_9 = 5.5$, 100 ignition spots
	N150def	6	3D deflagration $\rho_9 = 2.9$, 150 ignition spots
	N200def	6	3D deflagration $\rho_9 = 2.9$, 200 ignition spots
	N300Cdef	6	3D deflagration $\rho_9 = 2.9$, 300 centred ignition spots
	N1600def	6	3D deflagration $\rho_9 = 2.9$, 1600 ignition spots
	N1600Cdef	6	3D deflagration $\rho_9 = 2.9$, 1600 centred ignition spots

Table ii: List of enrichment models (continues on next pages, see below for references).

Category	Name	Reference	Remarks
3D	N1	7	3D delayed-detonation $\rho_9 = 2.9$, 1 ignition spot
	N3	7	3D delayed-detonation $\rho_9 = 2.9$, 3 ignition spots
	N5	7	3D delayed-detonation $\rho_9 = 2.9$, 5 ignition spots
	N10	7	3D delayed-detonation $\rho_9 = 2.9$, 10 ignition spots
	N20	7	3D delayed-detonation $\rho_9 = 2.9$, 20 ignition spots
	N40	7	3D delayed-detonation $\rho_9 = 2.9$, 40 ignition spots
	N100H	7	3D delayed-detonation $\rho_9 = 1.0$, 100 ignition spots
	N100	7	3D delayed-detonation $\rho_9 = 2.9$, 100 ignition spots
	N100L	7	3D delayed-detonation $\rho_9 = 5.5$, 100 ignition spots
	N150	7	3D delayed-detonation $\rho_9 = 2.9$, 150 ignition spots
	N200	7	3D delayed-detonation $\rho_9 = 2.9$, 200 ignition spots
	N300C	7	3D delayed-detonation $\rho_9 = 2.9$, 300 centred ignition spots
	N1600	7	3D delayed-detonation $\rho_9 = 2.9$, 1600 ignition spots
	N1600C	7	3D delayed-detonation $\rho_9 = 2.9$, 1600 centred ignition spots
	N100_Z0.5	7	3D delayed-detonation $\rho_9 = 2.9$, 100 centred ignition spots, $Z_{\rm init} = 0.5\,Z_\odot$
	N100_Z0.1	7	3D delayed-detonation $\rho_9 = 2.9$, 100 centred ignition spots, $Z_{\rm init} = 0.1\,Z_\odot$
	N100_Z0.01	7	3D delayed-detonation $\rho_9 = 2.9$, 100 centred ignition spots, $Z_{\rm init}0.01\,Z_\odot$
3D	DDT8_N100_c50	8	N100 with WD homogeneous core with 50% C (mass)
	DDT8_N100_rpc20	8	N100 with WD C-depleted core with 20% C (mass)
	DDT8_N100_rpc32	8	N100 with WD C-depleted core with 32% C (mass)
	DDT8_N100_rpc40	8	N100 with WD C-depleted core with 40% C (mass)
HWD	N5_hy	9	Hybrid WD (CO and ONe layers)
GCD	GCD200	10	Gravity-confined detonation
DbleDet	CSDD-L	11	2D converging-shock double-deton., $M_{\rm CO} = 0.45 M_\odot$
	CSDD-S	11	2D converging-shock double-deton., $M_{\rm CO} = 0.58 M_\odot$
	ELDD-L	11	2D edge-lit double-detonation, $M_{\rm CO} = 0.45 M_\odot$
	ELDD-S	11	2D edge-lit double-detonation, $M_{\rm CO} = 0.58 M_\odot$
	HeD-L	11	2D He detonation only, $M_{\rm CO} = 0.45 M_\odot$
	HeD-S	11	2D He detonation only, $M_{\rm CO} = 0.58 M_\odot$
ONe	CO15e7	12	2D detonation carbon-oxygen WD, $\rho_9 = 0.15$
	ONe10e7	12	2D detonation oxygen-neon WD, $\rho_9 = 0.10$
	ONe13e7	12	2D detonation oxygen-neon WD, $\rho_9 = 0.13$
	ONe15e7	12	2D detonation oxygen-neon WD, $\rho_9 = 0.15$
	ONe17e7	12	2D detonation oxygen-neon WD, $\rho_9 = 0.17$
	ONe20e7	12	2D detonation oxygen-neon WD, $\rho_9 = 0.20$

Category	Name	Reference	Remarks
LN18	050-1-c3-1P	13	2D deflagr., $\rho_9 = 0.5$, centred ignition, $Z_{\rm init} = 1\,Z_\odot$
	100-1-c3-1P	13	2D deflagr., $\rho_9 = 1.0$, centred ignit., $Z_{\rm init} = 1\,Z_\odot$
	100-0-c3	13	2D del.-det., $\rho_9 = 1.0$, centred ignit., $Z_{\rm init} = 0\,Z_\odot$
	100-0.1-c3	13	2D del.-det., $\rho_9 = 1.0$, centred ignit., $Z_{\rm init} = 0.1\,Z_\odot$
	100-0.5-c3	13	2D del.-det., $\rho_9 = 1.0$, centred ignit., $Z_{\rm init} = 0.5\,Z_\odot$
	100-1-c3	13	2D del.-det., $\rho_9 = 1.0$, centred ignit., $Z_{\rm init} = 1\,Z_\odot$
	100-2-c3	13	2D del.-det., $\rho_9 = 1.0$, centred ignit., $Z_{\rm init} = 2\,Z_\odot$
	100-3-c3	13	2D del.-det., $\rho_9 = 1.0$, centred ignit., $Z_{\rm init} = 3\,Z_\odot$
	100-5-c3	13	2D del.-det., $\rho_9 = 1.0$, centred ignit., $Z_{\rm init} = 5\,Z_\odot$
	300-1-c3-1P	13	2D deflagr., $\rho_9 = 3.0$, centred ignit., $Z_{\rm init} = 1\,Z_\odot$
	300-0-c3	13	2D del.-det., $\rho_9 = 3.0$, centred ignit., $Z_{\rm init} = 0\,Z_\odot$
	300-0.1-c3	13	2D del.-det., $\rho_9 = 3.0$, centred ignit., $Z_{\rm init} = 0.1\,Z_\odot$
	300-0.5-c3	13	2D del.-det., $\rho_9 = 3.0$, centred ignit., $Z_{\rm init} = 0.5\,Z_\odot$
	300-1-c3	13	2D del.-det., $\rho_9 = 3.0$, centred ignit., $Z_{\rm init} = 1\,Z_\odot$
	300-2-c3	13	2D del.-det., $\rho_9 = 3.0$, centred ignit., $Z_{\rm init} = 2\,Z_\odot$
	300-3-c3	13	2D del.-det., $\rho_9 = 3.0$, centred ignit., $Z_{\rm init} = 3\,Z_\odot$
	300-5-c3	13	2D del.-det., $\rho_9 = 3.0$, centred ignit., $Z_{\rm init} = 5\,Z_\odot$
	500-1-c3-1P	13	2D deflagr., $\rho_9 = 5.0$, centred ignit., $Z_{\rm init} = 1\,Z_\odot$
	500-0-c3	13	2D del.-det., $\rho_9 = 5.0$, centred ignit., $Z_{\rm init} = 0\,Z_\odot$
	500-0.1-c3	13	2D del.-det., $\rho_9 = 5.0$, centred ignit., $Z_{\rm init} = 0.1\,Z_\odot$
	500-0.5-c3	13	2D del.-det., $\rho_9 = 5.0$, centred ignit., $Z_{\rm init} = 0.5\,Z_\odot$
	500-1-c3	13	2D del.-det., $\rho_9 = 5.0$, centred ignit., $Z_{\rm init} = 1\,Z_\odot$
	500-2-c3	13	2D del.-det., $\rho_9 = 5.0$, centred ignit., $Z_{\rm init} = 2\,Z_\odot$
	500-3-c3	13	2D del.-det., $\rho_9 = 5.0$, centred ignit., $Z_{\rm init} = 3\,Z_\odot$
	500-5-c3	13	2D del.-det., $\rho_9 = 5.0$, centred ignit., $Z_{\rm init} = 5\,Z_\odot$
Det	det_0.81	14	1D pure detonation, $M_{\rm CO} = 0.81 M_\odot$, $\rho_7 = 1.0$
	det_0.88	14	1D pure detonation, $M_{\rm CO} = 0.88 M_\odot$, $\rho_7 = 1.45$
	det_0.97	14	1D pure detonation, $M_{\rm CO} = 0.97 M_\odot$, $\rho_7 = 2.4$
	det_1.06	14	1D pure detonation, $M_{\rm CO} = 1.06 M_\odot$, $\rho_7 = 4.15$
	det_1.06_0.075Ne	14	1D pure detonation, $M_{\rm CO} = 1.06 M_\odot$, $\rho_7 = 4.15$, C/O/Ne mass fraction = 0.425/0.5/0.075
	det_1.15	14	1D pure detonation, $M_{\rm CO} = 1.15 M_\odot$, $\rho_7 = 7.9$
Merger	09_09	15	3D violent WD merger (double-degen.), 0.9+0.9 $M_\odot$
	11_09	16	3D violent WD merger (double-degen.), 1.1+0.9 $M_\odot$
Merger2	09_076	17	3D violent WD merger (double-degen.), 0.9+0.76 $M_\odot$, $Z_{\rm init} = 1\,Z_\odot$
	09_076_Z0.01	17	3D violent WD merger (double-degen.), 0.9+0.76 $M_\odot$, $Z_{\rm init} = 0.01\,Z_\odot$
6D	Sh18_Ma_b_Zc_d	18	3D dynamically-driven double-degenerate double detonation, 159 models in total for different WD masses (Ma $\in \{0.8, 0.85, 0.9, 1.0, 1.1\}\,M_\odot$), C/O compositions (b $\in \{30/70, 50/50\}$), metallicity $Z_{\rm init}$ (Zc $\in \{0, 0.005, 0.01, 0.02\}\,Z_\odot$), and normalizations of the ^{12}C+^{16}O reaction rate (d $\in \{0.1, 1.0\}$)

Category	Name	Reference	Remarks
			SN_{cc}
Classical	Ch04_0	a	$Z_{\rm init} = 0\,Z_\odot$
	Ch04_1E-6	a	$Z_{\rm init} = 1\times10^{-6}\,Z_\odot$
	Ch04_1E-4	a	$Z_{\rm init} = 1\times10^{-4}\,Z_\odot$
	Ch04_1E-3	a	$Z_{\rm init} = 1\times10^{-3}\,Z_\odot$
	Ch04_6E-3	a	$Z_{\rm init} = 6\times10^{-3}\,Z_\odot$
	Ch04_2E-2	a	$Z_{\rm init} = 2\times10^{-2}\,Z_\odot$
Classical	No06_0	b	$Z_{\rm init} = 0\,Z_\odot$
	No06_0.001	b	$Z_{\rm init} = 1\times10^{-3}\,Z_\odot$
	No06_0.004	b	$Z_{\rm init} = 4\times10^{-3}\,Z_\odot$
	No06_0.02	b	$Z_{\rm init} = 2\times10^{-2}\,Z_\odot$
Classical	Ro10_0	c	$Z_{\rm init} = 0\,Z_\odot$, $M \in [8, 40]\,M_\odot$
	Ro10_2E-6	c	$Z_{\rm init} = 2\times10^{-6}\,Z_\odot$, $M \in [8, 40]\,M_\odot$
	Ro10_2E-4	c	$Z_{\rm init} = 2\times10^{-4}\,Z_\odot$, $M \in [8, 40]\,M_\odot$
	Ro10_2E-3	c	$Z_{\rm init} = 2\times10^{-3}\,Z_\odot$, $M \in [8, 40]\,M_\odot$
	Ro10_2E-2	c	$Z_{\rm init} = 2\times10^{-2}\,Z_\odot$, $M \in [8, 40]\,M_\odot$
Updated	No13_SNcc_0	d	Core-collapse $Z_{\rm init} = 0\,Z_\odot$
	No13_SNcc_0.001	d	Core-collapse $Z_{\rm init} = 1\times10^{-3}\,Z_\odot$, $M \in [11, 140]\,M_\odot$
	No13_SNcc_0.004	d	Core-collapse $Z_{\rm init} = 4\times10^{-3}\,Z_\odot$, $M \in [11, 140]\,M_\odot$
	No13_SNcc_0.008	d	Core-collapse $Z_{\rm init} = 8\times10^{-3}\,Z_\odot$, $M \in [11, 140]\,M_\odot$
	No13_SNcc_0.02	d	Core-collapse $Z_{\rm init} = 2\times10^{-2}\,Z_\odot$, $M \in [11, 140]\,M_\odot$
	No13_SNcc_0.05	d	Core-collapse $Z_{\rm init} = 5\times10^{-2}\,Z_\odot$, $M \in [11, 140]\,M_\odot$
	No13_PISNe_0	d	Pair-instability SN_e $Z_{\rm init} = 0\,Z_\odot$, $M \in [140, 300]\,M_\odot$
	No13_SNe_0	d	Core-collapse $M \in [11, 140]\,M_\odot$ and pair-instability $M \in [140, 300]\,M_\odot$, $Z_{\rm init} = 0\,Z_\odot$
	No13_HNe_0	d	Hyper-novæ $Z_{\rm init} = 0\,Z_\odot$
	No13_HNe_0.001	d	Hyper-novæ $Z_{\rm init} = 1\times10^{-3}\,Z_\odot$, $M \in [20, 140]\,M_\odot$
	No13_HNe_0.004	d	Hyper-novæ $Z_{\rm init} = 4\times10^{-3}\,Z_\odot$, $M \in [20, 140]\,M_\odot$
	No13_HNe_0.008	d	Hyper-novæ $Z_{\rm init} = 8\times10^{-3}\,Z_\odot$, $M \in [20, 140]\,M_\odot$
	No13_HNe_0.02	d	Hyper-novæ $Z_{\rm init} = 2\times10^{-2}\,Z_\odot$, $M \in [20, 140]\,M_\odot$
	No13_HNe_0.05	d	Hyper-novæ $Z_{\rm init} = 5\times10^{-2}\,Z_\odot$, $M \in [20, 140]\,M_\odot$
Simulated	He0210_SNcc_0	e,f	Core-collapse $Z_{\rm init} = 0\,Z_\odot$, $M \in [10, 100]\,M_\odot$
	He0210_PISNe_0	e,f	Pair-instability SN_e $Z_{\rm init} = 0\,Z_\odot$, $M \in [140, 260]\,M_\odot$
	He0210_SNe_0	e,f	Core-collapse $M \in [10, 100]\,M_\odot$ and pair-instability $M \in [140, 260]\,M_\odot$, $Z_{\rm init} = 0\,Z_\odot$
New	Su16_N20	g	Incl. neutrino transport, calibrated for a Nomoto & Hashimoto (1988) progenitor to explode as SN1987A
	Su16_W18	g	Incl. neutrino transport, calibrated for a Utrobin et al. (2015) progenitor to explode as SN1987A
			AGB
Classical	K10_1E-4	α	$Z_{\rm init} = 1\times10^{-4}\,Z_\odot$, $M \in [1, 6]\,M_\odot$
	K10_4E-3	α	$Z_{\rm init} = 4\times10^{-3}\,Z_\odot$, $M \in [1, 6]\,M_\odot$
	K10_8E-3	α	$Z_{\rm init} = 8\times10^{-3}\,Z_\odot$, $M \in [1, 6]\,M_\odot$
	K10_2E-2	α	$Z_{\rm init} = 2\times10^{-2}\,Z_\odot$, $M \in [1, 6]\,M_\odot$
Updated	No13_AGB_0.001	β	$Z_{\rm init} = 1\times10^{-3}\,Z_\odot$, $M \in [0.9, 6.5]\,M_\odot$
	No13_AGB_0.004	β	$Z_{\rm init} = 4\times10^{-3}\,Z_\odot$, $M \in [0.9, 6.5]\,M_\odot$
	No13_AGB_0.008	β	$Z_{\rm init} = 8\times10^{-3}\,Z_\odot$, $M \in [0.9, 6.5]\,M_\odot$
	No13_AGB_0.002	β	$Z_{\rm init} = 2\times10^{-2}\,Z_\odot$, $M \in [0.9, 6.5]\,M_\odot$

References:

SN_{Ia}: (1) Iwamoto et al. (1999) (2) Thielemann et al. (2003) (3) Badenes et al. (2006) (4) Waldman et al. (2011) (5) Maeda et al. (2010) (6) Fink et al. (2014) (7) Seitenzahl et al. (2013) (8) Ohlmann et al. (2014) (9) Kromer et al. (2015) (10) Seitenzahl et al. (2016) (11) Sim et al. (2012) (12) Marquardt et al. (2015) (13) Leung & Nomoto (2018) (14) Sim et al. (2010) (15) Pakmor et al. (2010) (16) Pakmor et al. (2012) (17) Kromer et al. (2013) (18) Shen et al. (2018)

SN_{cc}: (a) Chieffi & Limongi (2004) (b) Nomoto et al. (2006) (c) Romano et al. (2010) (d) Nomoto et al. (2013) (e) Heger & Woosley (2002) (f) Heger & Woosley (2010) (g) Sukhbold et al. (2016)

AGB: (α) Karakas (2010) (β) Nomoto et al. (2013)

H List of calibration lines and MXS configurations

H.1 List of lines

I provide here the full list of lines used for all atomic studies, derived from the NIST database (https://physics.nist.gov/PhysRefData/XrayTrans/Html/search.html) or taken from Nordfors (1955); Fischer & Baun (1965); Bearden (1967); Krause & Oliver (1979); Schweppe et al. (1994); Hölzer et al. (1997). The width of the line is given in terms of FWHM (2γ) and the amplitude is normalised to the strongest of the two lines.

Element	Line	Energy (eV)	FWHM (eV)	Amplitude
Ne	$K_{\alpha 1}$	849.09	0.24	0.5
	$K_{\alpha 2}$	848.61	0.24	1
Mg	$K_{\alpha 1}$	1253.4	0.36	0.5
	$K_{\alpha 2}$	1353.6	0.36	1
Al	$K_{\alpha 1}$	1486.5	0.43	0.5
	$K_{\alpha 2}$	1486.9	0.43	1
	$K_{\alpha 3}$	1492.3	1.34	0.03851
	$K_{\alpha 4}$	1496.4	0.96	0.05375
	$K_{\alpha 5}$	1498.4	1.252	0.04121
Si	$K_{\alpha 1}$	1739.67	0.58	0.5
	$K_{\alpha 2}$	1741.16	0.60	1
Ca	$K_{\alpha 1}$	3687.56	0.98	0.5
	$K_{\alpha 2}$	3690.98	0.98	1
Ti	$K_{\alpha 1}$	4504.9201	1.16	0.5
	$K_{\alpha 2}$	4510.8991	1.18	1
	$K_{\beta,a}$	4931.81	1.24	0.5
	$K_{\beta,b}$	4932.51	1.24	1
Cr	$K_{\alpha 1,1}$	5403.986	4.740	0.036
	$K_{\alpha 1,2}$	5405.551	2.224	0.386
	$K_{\alpha 2,1}$	5410.583	5.149	0.045
	$K_{\alpha 2,2}$	5412.745	3.138	0.085
	$K_{\alpha 2,3}$	5414.099	1.760	0.237
	$K_{\alpha 2,4}$	5414.874	1.457	0.822
	$K_{\alpha 2,5}$	5418.304	1.988	0.015
	$K_{\beta a}$	5935.31	15.98	0.055
	$K_{\beta,b}$	5942.04	6.69	0.082
	$K_{\beta,c}$	5944.93	3.37	0.151
	$K_{\beta,d}$	5946.24	1.9	0.337
	$K_{\beta,e}$	5947	1.7	0.67

Table iii: List of lines used for atomic studies. Equivalent amplitudes are relative to the highest amplitude of the specific line (continues on next page).

Element	Line	Energy (eV)	FWHM (eV)	Amplitude
Mn	$K_{\alpha 1,1}$	5886.495	4.216	0.1
	$K_{\alpha 1,2}$	5887.743	2.361	0.372
	$K_{\alpha 2,1}$	5894.829	4.499	0.068
	$K_{\alpha 2,2}$	5896.532	2.663	0.096
	$K_{\alpha 2,3}$	5897.867	2.043	0.264
	$K_{\alpha 2,4}$	5898.853	1.715	0.79
	$K_{\alpha 2,5}$	5899.417	0.969	0.0714
	$K_{\alpha 2,6}$	5902.712	1.5528	0.0106
Fe	$K_{\alpha 1,1}$	6389.106	2.339	0.060
	$K_{\alpha 1,2}$	6390.275	4.433	0.102
	$K_{\alpha 1,3}$	6391.190	2.487	0.339
	$K_{\alpha 2,1}$	6400.653	4.833	0.088
	$K_{\alpha 2,2}$	6402.077	2.803	0.136
	$K_{\alpha 2,3}$	6403.295	1.965	0.376
	$K_{\alpha 2,4}$	6404.148	1.613	0.697
Co	$K_{\alpha 1,1}$	6913.078	4.463	0.043
	$K_{\alpha 1,2}$	6914.659	2.773	0.131
	$K_{\alpha 1,3}$	6915.713	2.406	0.314
	$K_{\alpha 2,1}$	6927.676	4.555	0.107
	$K_{\alpha 2,2}$	6929.388	2.695	0.205
	$K_{\alpha 2,3}$	6930.425	1.795	0.809
	$K_{\alpha 2,4}$	6930.941	0.808	0.041
Cu	$K_{\alpha 1,1}$	8026.504	3.571	0.111
	$K_{\alpha 1,2}$	8027.993	2.666	0.334
	$K_{\alpha 2,1}$	8045.367	3.358	0.090
	$K_{\alpha 2,2}$	8047.837	2.285	0.957
	$K_{\beta,a}$	8897.387,	8.08	0.068
	$K_{\beta,b}$	8903.109	3.52	0.388
	$K_{\beta,c}$	8905.532	3.52	0.757
	$K_{\beta,d}$	8908.462	3.55	0.171
	$K_{\beta,e}$	8911.393	5.31	0.055
Ga	$K_{\alpha 1}$	9224.835	2.59	0.51
	$K_{\alpha 2}$	9251.674	2.66	1
As	$K_{\alpha 1}$	10507.50	3.08	0.514
	$K_{\alpha 2}$	10543.2674	3.17	1
Br	$K_{\alpha 1}$	11877.75	3.6	0.514
	$K_{\alpha 2}$	11924.36	3.76	1

H.2 MXS configurations and line centroid uncertainties

After discussion with SRON, and following the results presented in de Vries et al. (2018), we considered the following MXS configurations:

I. Single line configuration obtained with 400 nm of Cu. The fluorescence yields per line are: 90% Cu K_α / 10% Cu K_β
II. Two-line configuration (so-called "*Hitomi*-like") obtained with a layer of 250 nm of Cu on top of 150 nm of Cr. The fluorescence yields per line are: 45% Cr K_α / 5% Cr K_β / 45% Cu K_α / 5% for Cu K_β
III. Three-line configuration obtained with a 250 nm of Cu, above a 150 nm of Cr, on top of 150 nm of Ti. The fluorescence yields per line are: 20% Ti K_α / 2% Ti K_β / 34% Cr K_α / 4% Cr K_β / 36% Cu K_α / 4% Cu K_β
IV. Four-line configuration obtained with 250 nm of Cu, above 150 nm of Cr, above 150 nm of Ti, on top of 700 nm of Si. The yields per line are: 10% Si K_α / 1% Si K_β / 20% Ti K_α / 2% Ti K_β / 30% Cr K_α/ 3% Cr K_β / 31% Cu K_α / 3% Cu K_β

An additional ^{55}Fe source was also considered for line studies (which creates a Mn K_α doublet through Auger electron loss). Using the previous lines, we can compute the uncertainty on the line centroid as a function of the number of counts in the line (Figure vi). For each of the lines considered (Si, Ti, Mn, Cr, Cu), we summarise in Table iv the number of counts required to get a 0.2 eV (FWHM) uncertainty on the line centroid, as per the current X-IFU requirements on the energy scale. Table v provides the required number of counts to verify such requirement in each MXS configuration.

Line	Counts
Si K_α	326
Ti K_α	460
Cr K_α	735
Mn K_α	875
Cu K_α	945

Table iv: Counts needed to achieve 0.2 eV (FWHM) statistical accuracy of the centroid.

Lines	I	II	III	IV
Si K_α	/	/	/	326
Ti K_α	/	/	551	652
Cr K_α	/	945	932	978
Cu K_α	945	945	945	1 010
Total counts in lines (with K_β)	1 050	2 100	2 625	3 220
Total counts in lines (all included)	3 150	6 300	7 875	9 660

Table v: Counts in each line needed to achieve the 0.2 eV accuracy on the line centroid in each line, assuming the MXS configurations. In the case of a correction made on a pool of N_{pixels} pixels, these numbers can be divided by N_{pixels}.

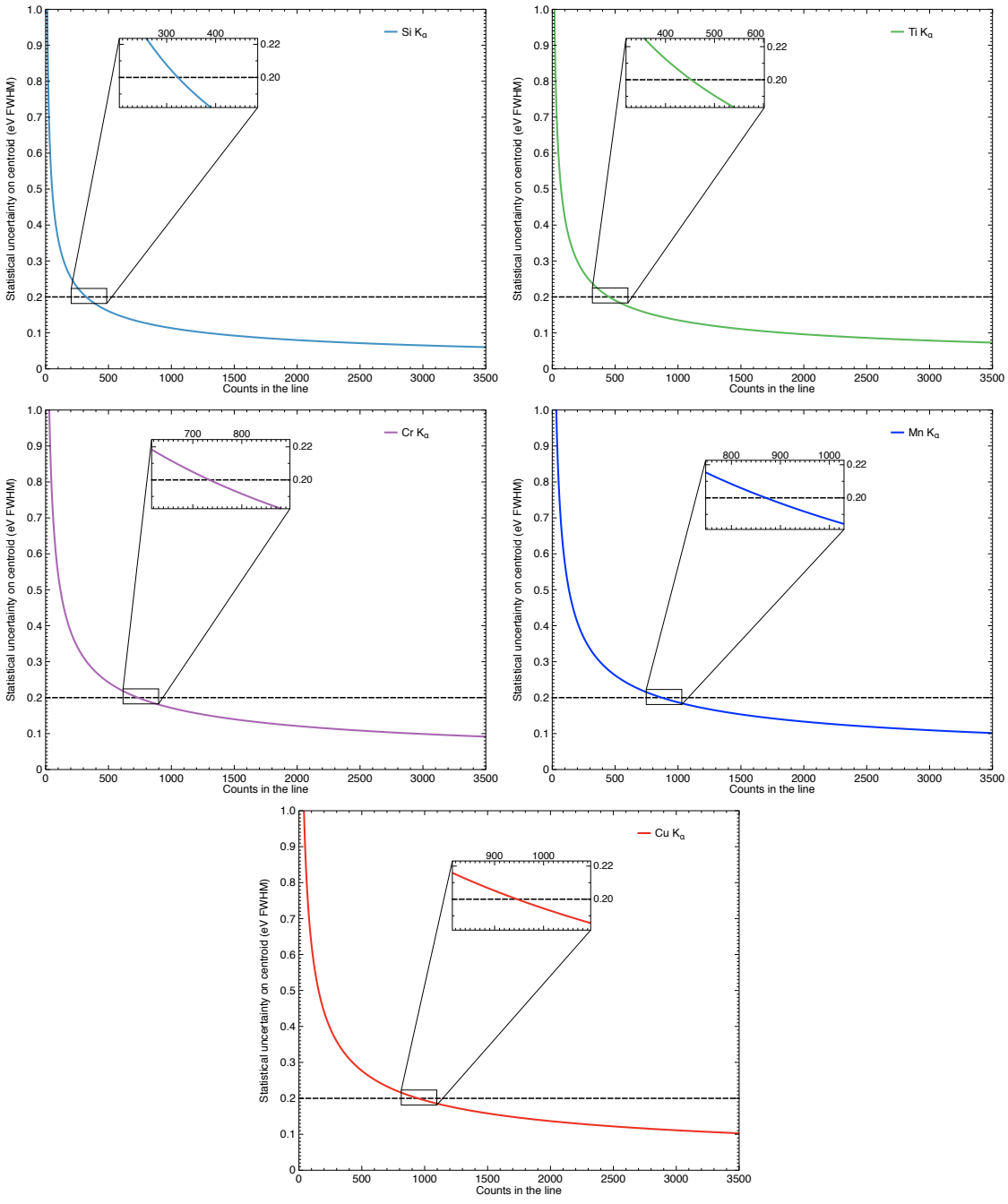

Figure vi: Best fit in $1/N_{\text{counts}}$ of the average uncertainty on the centroid position (in eV FWHM) for Si K_α, Ti K_α, Cr K_α Mn K_α, and Cu K_α. The horizontal blacked dashed line shows the 0.2 eV requirement. The sub-panels magnify the curve around its intersection with the requirement.

I Test bench additional material

I.1 Harness design

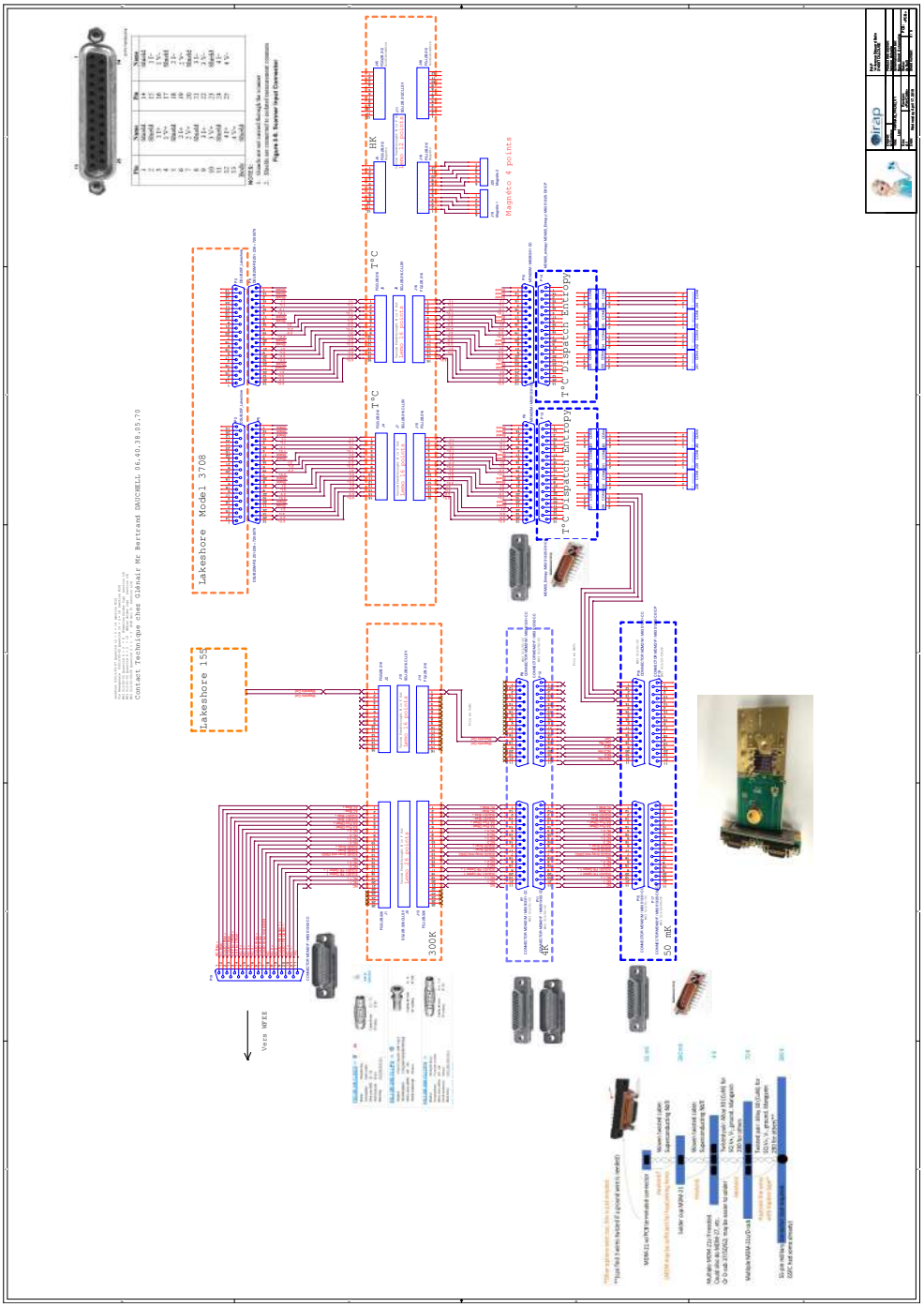

Figure vii: Test bench harness and wiring

I.2 Energy resolution budget

The energy resolution budget of the test bench uses the following assumptions:

- Record length degradation: 1%
- Nb shielding: 5400 (worst-case, to be measured in 2019)
- SQUID mutual inductance: $36\,\mu A/\phi_0$
- Temperature sensitivity: $45.8\,meV/\mu K_{rms}$ (obtained through simulation)
- Magnetic sensitivity: $8\,eV/nT$ (measured by GSFC, worst-case)
- ADR drift: $68.25\,nT/15\,min$ in normalisation (measured + 30% hysteresis margin)
- Temperature stability: $4\,\mu K_{rms}$ (measured)

Table vi: Test bench provisional energy resolution budget (continues on next page)

Contributor	eV (FWHM)	Noise	Drift	Other	Comments
Total energy resolution	**3.50**	**3.01**	**1.45**	**1.02**	
FPA + detector	3.06				
DRE + WFEE	0.97				
All except array	2.34				
Finite record length degradation	0.42				1%
RSS of contributions		**2.98**	**1.45**	**1.02**	
Instantaneous gain accuracy			**0.20**		Requirement
Sensor array	**2.57**	**2.50**	**0.00**	**0.57**	
Detector Intrinsic		2.50			NEP measurement (S. Smith)
AC losses				0.20	X-IFU ERB
Non-optimal set point				0.50	X-IFU ERB
Thermal crosstalk				0.20	X-IFU ERB
Focal Plane Assembly	**1.63**	**1.11**	**1.15**	**0.30**	
SQUIDs		1.11			SRON measurement ($5\,pA/\sqrt{Hz}$)
Shunt resistor		0.00			$R_{shunt} = 0.1\Omega$ ($0.07\,pA/\sqrt{Hz}$)
Gain drifts			0.10		As per X-IFU ERB
Electrical crosstalk					
Active				0.20	FPA DM ERB
Passive				0.20	FPA DM ERB
Spurious signals				0.10	DRE simulations (L. Ravera)
Radiated susceptibility					
0.1 − 20 GHz			0.50		Worst-case allocation
DC-kHz fields			0.24		$12.64\,pT/15$ min equivalent drift
EMC margin			1.00		Engineering margin
WFEE	**0.60**	**0.60**	**0.01**	**0.10**	
LNA noise		0.60			$2.67pA/\sqrt{Hz}$ (X-IFU ERB)
Electrical gain drits					
LNA drifts			0.01		$0.13pA/\sqrt{Hz}$ (X-IFU ERB)
FE SQUID input bias		0.01	0.01		$0.13pA/\sqrt{Hz}$ (X-IFU ERB)
FE SQUID output bias		0.01	0.01		$0.13pA/\sqrt{Hz}$ (X-IFU ERB)
Amp SQUID output bias		0.01	0.01		$0.13pA/\sqrt{Hz}$ (X-IFU ERB)
Amp SQUID output bias		0.01	0.01		$0.13pA/\sqrt{Hz}$ (X-IFU ERB)
Crosstalk				0.10	X-IFU ERB

Contributor	eV (FWHM)	Noise	Drift	Other	Comments
DRE	**0.75**	**0.67**	**0.14**	**0.30**	
DAC Noise					
AC bias line		0.20	0.10		2.54pA/$\sqrt{\text{Hz}}$
BBFB line		0.57	0.10		2.54pA/$\sqrt{\text{Hz}}$
ADC		0.30	0.01		1.33pA/$\sqrt{\text{Hz}}$ (X-IFU ERB)
Spurious signals				0.20	X-IFU ERB
Decimation filter				0.10	X-IFU ERB
Decimation filter				0.20	X-IFU ERB
Dewar	**1.07**	**0.61**	**0.72**	**0.52**	
Cryostat					
Themal stability			0.43		$4\,\mu\text{K}_{\text{rms}}$ (measured)
Other thermal stability					
Cable resistance			0.20		X-IFU ERB
Cable capacitance			0.20		X-IFU ERB
Mechanical stability					
Vibration			0.50		Estimated, to be measured
Micro-phonics				0.50	Estimated worst-case
Aperture Window					
Themal shot noise				0.00	Included in pixel NEP
Optical stray-light				0.02	Flight worst-case
Harness					
Cable noise					
AC bias		0.09			1.33pA/$\sqrt{\text{Hz}}$ (X-IFU ERB)
Signal bias		0.30			1.33pA/$\sqrt{\text{Hz}}$ (X-IFU ERB)
BBFB/FE SQUID input bias		0.09			1.33pA/$\sqrt{\text{Hz}}$ (X-IFU ERB)
Crosstalk					
Intra-channel				0.10	FPA DM ERB
Inter-channel				0.10	FPA DM ERB
Conducted susceptibility		0.50			Worst-case allocation
Magnetic coil		0.07	0.01		$3.65\,\text{pT}_{\text{rms}}$ equivalent
Thermistor		0.10	0.01		For $4\,\mu\text{K}_{\text{rms}}$ measurements
Margin	**0.87**	**0.50**	**0.50**	**0.50**	**25 x 0.1 eV allocations**

Bibliography

Abbott, B. P., Abbott, R., Abbott, T. D., et al. 2016a, ApJ Letters, 818, L22

Abbott, B. P., Abbott, R., Abbott, T. D., et al. 2016b, Physical Review Letters, 116, 061102

Abbott, B. P., Abbott, R., Abbott, T. D., et al. 2017, ApJ Letters, 851, L35

Abbott, B. P., Abbott, R., Abbott, T. D., et al. 2018, Physical Review Letters, 121, 161101

Abramowicz, M. A. & Fragile, P. C. 2013, Living Reviews in Relativity, 16, 1

Adams, J., Bandler, S., Chervenak, J., et al. 2019, XIFU-DD-10000-00422-CNES X-IFU TDM detection chain definition document v1.0, Tech. rep., Athena X-IFU Consortium

Agostinelli, S., Allison, J., Amako, K., et al. 2003, Nuclear Instruments and Methods in Physics Research Section A: Accelerators, Spectrometers, Detectors and Associated Equipment, 506, 250

Aird, J., Comastri, A., Brusa, M., et al. 2013, ArXiv e-prints 1306.2325

Akamatsu, H., Gottardi, L., de Vries, C. P., et al. 2016, Journal of Low Temperature Physics, 184, 436

Akamatsu, H., Gottardi, L., van der Kurr, J., et al. 2018, Journal Of Low Temperature Physics

Allen, S. W., Evrard, A. E., & Mantz, A. B. 2011, Annual Review of Astron. and Astrophys, 49, 409

Alpher, R. A., Bethe, H., & Gamow, G. 1948, Phys. Rev., 73, 803

Anders, E. & Grevesse, N. 1989, Geochimica Cosmochimica Acta, 53, 197

Arnaud, K. A. 1996, in Astronomical Society of the Pacific Conference Series, Vol. 101, Astronomical Data Analysis Software and Systems V, ed. G. H. Jacoby & J. Barnes, 17

Arnaud, M., Pointecouteau, E., & Pratt, G. W. 2005, Astronomy and Astrophysics, 441, 893

Asplund, M., Grevesse, N., Sauval, A. J., & Scott, P. 2009, Annual Review of Astron. and Astrophys., 47, 481

Bacon, R., Accardo, M., Adjali, L., et al. 2010, in Proc. SPIE, Vol. 7735, Ground-based and Airborne Instrumentation for Astronomy III, 773508

Badenes, C., Borkowski, K. J., Hughes, J. P., Hwang, U., & Bravo, E. 2006, ApJ, 645, 1373

Bandler, S. R., Figueroa-Feliciano, E., Iyomoto, N., et al. 2006, Nuclear Instruments and Methods in Physics Research A, 559, 817
Barbera, M., Lo Cicero, U., Sciortino, L., et al. 2018a, in Society of Photo-Optical Instrumentation Engineers (SPIE) Conference Series, Vol. 10699, Space Telescopes and Instrumentation 2018: Ultraviolet to Gamma Ray, 106991R
Barbera, M., Lo Cicero, U., Sciortino, L., et al. 2018b, Journal of Low Temperature Physics, 193, 793
Barcons, X., Barret, D., Decourchelles, A., et al. 2011, ESA reports
Barret, D., Cucchetti, E., Lefkir, M., et al. 2018a, ASST-TN-0001 X-IFU sensitivity analysis v2, Tech. rep., Athena X-IFU Consortium
Barret, D., Lam Trong, T., den Herder, J.-W., et al. 2016, in Proc. SPIE, Vol. 9905, Space Telescopes and Instrumentation 2016: Ultraviolet to Gamma Ray, 99052F
Barret, D., Lam Trong, T., den Herder, J.-W., et al. 2018b, in Society of Photo-Optical Instrumentation Engineers (SPIE) Conference Series, Vol. 10699, Space Telescopes and Instrumentation 2018: Ultraviolet to Gamma Ray, 106991G
Barthelmy, S. D., Barbier, L. M., Cummings, J. R., et al. 2005, Space Science Reviews, 120, 143
Bavdaz, M., Wille, E., Ayre, M., et al. 2018, in Society of Photo-Optical Instrumentation Engineers (SPIE) Conference Series, Vol. 10699, Space Telescopes and Instrumentation 2018: Ultraviolet to Gamma Ray, 106990X
Bavdaz, M., Wille, E., Wallace, K., et al. 2013, in Proc. SPIE, Vol. 8861, Optics for EUV, X-Ray, and Gamma-Ray Astronomy VI, 88610L
Bearden, J. A. 1967, Reviews of Modern Physics, 39, 78
Beck, A. M., Murante, G., Arth, A., et al. 2016, MNRAS, 455, 2110
Behrens, A., Andritschke, R., Bonholzer, M., et al. 2018, in Society of Photo-Optical Instrumentation Engineers (SPIE) Conference Series, Vol. 10699, Space Telescopes and Instrumentation 2018: Ultraviolet to Gamma Ray, 106994I
Bernardeau, F. 2013, ArXiv e-prints 1311.2724
Berti, E. & Volonteri, M. 2008, ApJ, 684, 822
Bertone, G. & Hooper, D. 2018, Rev. Mod. Phys., 90, 045002
Beyer, J. & Drung, D. 2008, Superconductor Science Technology, 21, 105022
Bhardwaj, A., Elsner, R. F., Randall Gladstone, G., et al. 2007, Planetary Space Science, 55, 1135
Biffi, V., Dolag, K., & Böhringer, H. 2013, MNRAS, 428, 1395
Biffi, V., Mernier, F., & Medvedev, P. 2018a, ArXiv e-prints 1811.01955
Biffi, V., Planelles, S., Borgani, S., et al. 2017, MNRAS, 468, 531
Biffi, V., Planelles, S., Borgani, S., et al. 2018b, MNRAS, 476, 2689
Biviano, A., Murante, G., Borgani, S., et al. 2006, Astronomy and Astrophysics, 456, 23
Blanton, E. L., Randall, S. W., Clarke, T. E., et al. 2011, ApJ, 737, 99
Blumenthal, G. R., Faber, S. M., Primack, J. R., & Rees, M. J. 1984, Nature, 311, 517
Böhringer, H., Matsushita, K., Churazov, E., Ikebe, Y., & Chen, Y. 2002, Astronomy and Astrophysics, 382, 804
Bonafede, A., Dolag, K., Stasyszyn, F., Murante, G., & Borgani, S. 2011, MNRAS, 418, 2234

Boyle, W. S. & Rodgers, Jr., K. F. 1959, Journal of the Optical Society of America (1917-1983), 49, 66
Bozzo, E., Barbera, M., Genolet, L., et al. 2016, in Proc. SPIE, Vol. 9905, Space Telescopes and Instrumentation 2016: Ultraviolet to Gamma Ray, 990561
Branduardi-Raymont, G., Sciortino, S., Dennerl, K., et al. 2013, ArXiv e-prints 1306.2332
Bromm, V. & Yoshida, N. 2011, Annual Review of Astron and Astrophys, 49, 373
Bruijn, M. P., van der Linden, A. J., Ferrari, L., et al. 2018, Journal of Low Temperature Physics, 193, 661
Bryan, G. L. & Norman, M. L. 1998, ApJ, 495, 80
Burbidge, E. M., Burbidge, G. R., Fowler, W. A., & Hoyle, F. 1957, Reviews of Modern Physics, 29, 547
Bykov, A. M., Churazov, E. M., Ferrari, C., et al. 2015, Space Science Reviews, 188, 141
Cameron, A. G. W. 1957, ApJ, 62, 9
Canizares, C. R., Davis, J. E., Dewey, D., et al. 2005, Publications of the ASP, 117, 1144
Cappellari, M. & Copin, Y. 2003, MNRAS, 342, 345
Cappi, M., Done, C., Behar, E., et al. 2013, ArXiv e-prints 1306.233
Cash, W. 1979, ApJ, 228, 939
Cavaliere, A. & Fusco-Femiano, R. 1976, Astronomy and Astrophysics, 49, 137
Cavaliere, A. & Fusco-Femiano, R. 1978, Astronomy and Astrophysics, 70, 677
Cavaliere, A. G., Gursky, H., & Tucker, W. H. 1971, Nature, 231, 437
Chabrier, G. 2003, Publications of the ASP, 115, 763
Chandrasekhar, S. 1931, ApJ, 74, 81
Charles, I., Daniel, C., André, J., et al. 2016, in Proc. SPIE, Vol. 9905, Space Telescopes and Instrumentation 2016: Ultraviolet to Gamma Ray, 99052J
Chen, S., Prêle, D., Beillimaz, C., et al. 2018, in Space Telescopes and Instrumentation 2018: Ultraviolet to Gamma Ray, Vol. 10699, 10699 – 10699 – 15
Chervenak, J. A., Irwin, K. D., Grossman, E. N., et al. 1999, Applied Physics Letters, 74, 4043
Chieffi, A. & Limongi, M. 2004, ApJ, 608, 405
Churazov, E., Forman, W., Jones, C., & Böhringer, H. 2003, ApJ, 590, 225
Churazov, E., Sunyaev, R., Forman, W., & Böhringer, H. 2002, MNRAS, 332, 729
Churazov, E., Vikhlinin, A., Zhuravleva, I., et al. 2012, MNRAS, 421, 1123
Clarke, J. 1994, Scientific American, 271, 46
Clerc, N., Cucchetti, E., Pointecouteau, E., & Peille, P. 2019, arXiv e-prints
Clerc, N., Ramos-Ceja, M. E., Ridl, J., et al. 2018, Astronomy and Astrophysics, 617, A92
Clowe, D., Bradač, M., Gonzalez, A. H., et al. 2006, ApJ Letters, 648, L109
Cobo, B., Ceballos, M. T., Peille, P., et al. 2018, in Society of Photo-Optical Instrumentation Engineers (SPIE) Conference Series, Vol. 10699, Space Telescopes and Instrumentation 2018: Ultraviolet to Gamma Ray, 106994S
Collon, M. J., Vacanti, G., Barriere, N., et al. 2018, in Society of Photo-Optical Instrumentation Engineers (SPIE) Conference Series, Vol. 10699, Space Telescopes and Instrumentation 2018: Ultraviolet to Gamma Ray, 106990Y
Croston, J. H., Sanders, J. S., Heinz, S., et al. 2013, ArXiv e-prints 1306.2323
Cucchetti, E., Clerc, N., Pointecouteau, E., Peille, P., & Pajot, F. 2019, arXiv e-prints

Cucchetti, E., Eckart, M. E., Peille, P., et al. 2018a, in Society of Photo-Optical Instrumentation Engineers (SPIE) Conference Series, Vol. 10699, Space Telescopes and Instrumentation 2018: Ultraviolet to Gamma Ray, 106994M
Cucchetti, E., Eckart, M. E., Peille, P., et al. 2018b, Journal of Low Temperature Physics, 193, 931
Cucchetti, E., Pajot, F., Pointecouteau, E., et al. 2018c, in Society of Photo-Optical Instrumentation Engineers (SPIE) Conference Series, Vol. 10699, Space Telescopes and Instrumentation 2018: Ultraviolet to Gamma Ray, 106994O
Cucchetti, E., Pointecouteau, E., Barret, D., et al. 2018d, in Proc. SPIE, Vol. 10699, Space Telescopes and Instrumentation 2018: Ultraviolet to Gamma Ray
Cucchetti, E., Pointecouteau, E., Peille, P., et al. 2018e, in Society of Photo-Optical Instrumentation Engineers (SPIE) Conference Series, Vol. 10699, Space Telescopes and Instrumentation 2018: Ultraviolet to Gamma Ray, 106994L
Cucchetti, E., Pointecouteau, E., Peille, P., et al. 2018f, Astronomy and Astrophysics, 620, A173
Cyburt, R. H., Fields, B. D., Olive, K. A., & Yeh, T.-H. 2016, Rev. Mod. Phys., 88, 015004
D'Andrea, M., Lotti, S., Macculi, C., et al. 2017, Experimental Astronomy, 44, 359
D'Andrea, M., Macculi, C., Argan, A., et al. 2018, Journal of Low Temperature Physics, 193, 958
De Grandi, S., Ettori, S., Longhetti, M., & Molendi, S. 2004, Astronomy and Astrophysics, 419, 7
De Grandi, S. & Molendi, S. 2001, ApJ, 551, 153
de Grandi, S. & Molendi, S. 2009, Astronomy and Astrophysics, 508, 565
de Korte, P. A. J., Beyer, J., Deiker, S., et al. 2003, Review of Scientific Instruments, 74, 3807
De Luca, A. & Molendi, S. 2004, Astronomy and Astrophysics, 419, 837
de Plaa, J. 2013, Astronomische Nachrichten, 334, 416
de Plaa, J., Kaastra, J. S., Werner, N., et al. 2017, Astronomy and Astrophysics, 607, A98
de Plaa, J., Werner, N., Bleeker, J. A. M., et al. 2007, Astronomy and Astrophysics, 465, 345
de Plaa, J., Werner, N., Bykov, A. M., et al. 2006, Astronomy and Astrophysics, 452, 397
de Vries, C. P., den Herder, J. W., Costantini, E., et al. 2010, in Proc. SPIE, Vol. 7732, Space Telescopes and Instrumentation 2010: Ultraviolet to Gamma Ray, 773213
de Vries, C. P., Fioretti, V., den Herder, J.-W., Schyns, E., & Pinto, S. D. 2018, in Society of Photo-Optical Instrumentation Engineers (SPIE) Conference Series, Vol. 10699, Space Telescopes and Instrumentation 2018: Ultraviolet to Gamma Ray, 1069965
de Vries, C. P., Schouten, R. M., van der Kuur, J., Gottardi, L., & Akamatsu, H. 2016, in Proc. SPIE, Vol. 9905, Space Telescopes and Instrumentation 2016: Ultraviolet to Gamma Ray, 99055V
De Young, D. S. 1978, ApJ, 223, 47
Deaver, B. S. & Fairbank, W. M. 1961, Physical Review Letters, 7, 43
Decourchelle, A., Costantini, E., Badenes, C., et al. 2013, ArXiv e-prints 1306.2335
Demianski, M., Piedipalumbo, E., Sawant, D., & Amati, L. 2017a, Astronomy and Astrophysics, 598, A112

Demianski, M., Piedipalumbo, E., Sawant, D., & Amati, L. 2017b, Astronomy and Astrophysics, 598, A113
Demtröder, W. 2003, Widths and Profiles of Spectral Lines (Berlin, Heidelberg: Springer Berlin Heidelberg), 59–95
den Hartog, R., Audley, M. D., Beyer, J., et al. 2012, Journal of Low Temperature Physics, 167, 652
den Hartog, R., Barret, D., Gottardi, L., et al. 2014, in Proc. SPIE, Vol. 9144, Space Telescopes and Instrumentation 2014: Ultraviolet to Gamma Ray, 91445Q
den Hartog, R., Boersma, D., Bruijn, M., et al. 2009, in American Institute of Physics Conference Series, Vol. 1185, American Institute of Physics Conference Series, ed. B. Young, B. Cabrera, & A. Miller, 261–264
den Hartog, R., Kirsch, C., de Vries, C., et al. 2018, Journal Of Low Temperature Physics
den Hartog, R., Peille, P., Kilbourne, C., & Geoffray. 2019, XIFU-TN-SYS-00319-CNES X-IFU energy resolution budget v1.3, Tech. rep., Athena X-IFU Consortium
den Herder, J. W., Brinkman, A. C., Kahn, S. M., et al. 2001, Astronomy and Astrophysics, 365, L7
Doriese, W. B., Adams, J. S., Hilton, G. C., et al. 2009, AIP Conference Proceedings, 1185, 450
Doriese, W. B., Morgan, K. M., Bennett, D. A., et al. 2016, Journal of Low Temperature Physics, 184, 389
Dovciak, M., Matt, G., Bianchi, S., et al. 2013, ArXiv e-prints 1306.2331
Drake, J. J., Ratzlaff, P., Kashyap, V., et al. 2006, in Proc. SPIE, Vol. 6270, Society of Photo-Optical Instrumentation Engineers (SPIE) Conference Series, 62701I
Duldig, M. L. 1994, Proceedings of the Astronomical Society of Australia, 11, 110
Eckart, M. E., Adams, J. S., Bailey, C. N., et al. 2012, Journal of Low Temperature Physics, 167, 732
Eckart, M. E., Adams, J. S., Boyce, K. R., et al. 2018, Journal of Astronomical Telescopes, Instruments, and Systems, 4, 021406
Eckert, D., Molendi, S., Vazza, F., Ettori, S., & Paltani, S. 2013, Astronomy and Astrophysics, 551, A22
Eckert, D., Vazza, F., Ettori, S., et al. 2012, Astronomy and Astrophysics, 541, A57
Enpuku, K., Shimomura, Y., & Kisu, T. 1993, Journal of Applied Physics, 73, 7929
Ettori, S., Baldi, A., Balestra, I., et al. 2015, Astronomy and Astrophysics, 578, A46
Ettori, S., Donnarumma, A., Pointecouteau, E., et al. 2013a, Space Science Reviews, 177, 119
Ettori, S., Pratt, G. W., de Plaa, J., et al. 2013b, ArXiv e-prints 1306.2322
Ezer, C., Bulbul, E., Nihal Ercan, E., et al. 2017, ApJ, 836, 110
Fabian, A. C. 1994, Annual Review of Astron. and Astrophys., 32, 277
Fabian, A. C. 2012, Annual Review of Astron. and Astrophys., 50, 455
Fabian, A. C., Reynolds, C. S., Taylor, G. B., & Dunn, R. J. H. 2005, MNRAS, 363, 891
Fabian, A. C., Sanders, J. S., Taylor, G. B., et al. 2006, MNRAS, 366, 417
Fink, M., Kromer, M., Seitenzahl, I. R., et al. 2014, MNRAS, 438, 1762
Fioretti, V., Bulgarelli, A., Molendi, S., et al. 2018, ApJ, 867, 9
Fischer, D. W. & Baun, W. L. 1965, Journal of Applied Physics, 36, 534

Fritz, G., Henry, R. C., Meekins, J. F., Chubb, T. A., & Friedman, H. 1969, Science, 164, 709
Fürmetz, M., Pietschner, D., & Meidinger, N. 2016, in Proc. SPIE, Vol. 9905, Space Telescopes and Instrumentation 2016: Ultraviolet to Gamma Ray, 99052E
Galloway, D. K., Muno, M. P., Hartman, J. M., Psaltis, D., & Chakrabarty, D. 2008, ApJ Supplements, 179, 360
Gamow, G. 1946, Phys. Rev., 70, 572
Gamow, G. 1953, Astronomical Journal, 58, 39
Gardini, A., Rasia, E., Mazzotta, P., et al. 2004, MNRAS, 351, 505
Garmire, G. P., Bautz, M. W., Ford, P. G., Nousek, J. A., & Ricker, Jr., G. R. 2003, in Proc. SPIE, Vol. 4851, X-Ray and Gamma-Ray Telescopes and Instruments for Astronomy., ed. J. E. Truemper & H. D. Tananbaum, 28–44
Gaskin, J., Elsner, R., Ramsey, B., et al. 2015, in 2015 IEEE Aerospace Conference, 1–15
Gaskin, J. A., Dominguez, A., Gelmis, K., et al. 2018, in Society of Photo-Optical Instrumentation Engineers (SPIE) Conference Series, Vol. 10699, Space Telescopes and Instrumentation 2018: Ultraviolet to Gamma Ray, 106990N
Gaspari, M., Brighenti, F., D'Ercole, A., & Melioli, C. 2011, MNRAS, 415, 1549
Gaspari, M. & Churazov, E. 2013, Astronomy and Astrophysics, 559, A78
Gaspari, M., Churazov, E., Nagai, D., Lau, E. T., & Zhuravleva, I. 2014, Astronomy and Astrophysics, 569, A67
Gaspari, M., McDonald, M., Hamer, S. L., et al. 2018, ApJ, 854, 167
Gaspari, M., Ruszkowski, M., & Sharma, P. 2012, ApJ, 746, 94
Gaspari, M. & Sądowski, A. 2017, ApJ, 837, 149
Gastaldello, F. & Molendi, S. 2002, ApJ, 572, 160
Genel, S., Vogelsberger, M., Springel, V., et al. 2014, MNRAS, 445, 175
Georgakakis, A., Carrera, F., Lanzuisi, G., et al. 2013, ArXiv e-prints 1306.2328
George, I. M. & Fabian, A. C. 1991, MNRAS, 249, 352
Giacconi, R., Gursky, H., Paolini, F. R., & Rossi, B. B. 1962, Physical Review Letters, 9, 439
Gilli, R., Comastri, A., Brunetti, G., & Setti, G. 1999, Nature, 4, 45
Gilli, R., Comastri, A., & Hasinger, G. 2007, Astronomy and Astrophysics, 463, 79
Gottardi, L., Smith, S. J., Kozorezov, A., et al. 2018, Journal of Low Temperature Physics, 193, 209
Gültekin, K., Richstone, D. O., Gebhardt, K., et al. 2009, ApJ, 698, 198
Gunn, J. E. & Gott, III, J. R. 1972, ApJ, 176, 1
Hagen, N., Kupinski, M., & Dereniak, E. L. 2007, Applied Optics, 46, 5374
Hasinger, G., Miyaji, T., & Schmidt, M. 2005, Astronomy and Astrophysics, 441, 417
Heger, A. & Woosley, S. E. 2002, ApJ, 567, 532
Heger, A. & Woosley, S. E. 2010, ApJ, 724, 341
Henke, B. L., Gullikson, E. M., & Davis, J. C. 1993, Atomic Data and Nuclear Data Tables, 54, 181
Herrmann, S., Koch, A., Obergassel, S., et al. 2018, in Society of Photo-Optical Instrumentation Engineers (SPIE) Conference Series, Vol. 10709, High Energy, Optical, and Infrared Detectors for Astronomy VIII, 1070935

Hillebrandt, W., Kromer, M., Röpke, F. K., & Ruiter, A. J. 2013, Frontiers of Physics, 8, 116
Hitomi Collaboration. 2016, Nature, 535, 117 EP
Hitomi Collaboration. 2017, Nature, 551, 478 EP
Hitomi Collaboration. 2018a, Publications of the Astronomical Society of Japan, 70, 9
Hitomi Collaboration. 2018b, Publications of the Astronomical Society of Japan, 70, 12
Hitomi Collaboration. 2018c, Publications of the Astronomical Society of Japan, 70, 13
Hitomi Collaboration. 2018d, Publications of the Astronomical Society of Japan, 70, 10
Hoekstra, H., Bartelmann, M., Dahle, H., et al. 2013, Space Science Reviews, 177, 75
Hoevers, H. F. C., Ridder, M. L., Germeau, A., et al. 2005, Applied Physics Letters, 86, 251903
Hölzer, G., Fritsch, M., Deutsch, M., Härtwig, J., & Förster, E. 1997, Physical Review A: General Physics, 56, 4554
Hoshino, A., Henry, J. P., Sato, K., et al. 2010, Publications of the Astronomical Society of Japan, 62, 371
Houck, J. C. & Denicola, L. A. 2000, in Astronomical Society of the Pacific Conference Series, Vol. 216, Astronomical Data Analysis Software and Systems IX, ed. N. Manset, C. Veillet, & D. Crabtree, 591
Hubble, E. 1925, The Observatory, 48, 139
Hubble, E. 1929, Proceedings of the National Academy of Science, 15, 168
Humphrey, P. J. & Buote, D. A. 2006, ApJ, 639, 136
Iben, Jr., I. & Renzini, A. 1983, Annual Review of Astron. and Astrophys., 21, 271
Ichinohe, Y., Yamada, S., Miyazaki, N., & Saito, S. 2018, MNRAS, 475, 4739
Inogamov, N. A. & Sunyaev, R. A. 2003, Astronomy Letters, 29, 791
Irwin, K. D. 2009, in American Institute of Physics Conference Series, Vol. 1185, American Institute of Physics Conference Series, ed. B. Young, B. Cabrera, & A. Miller, 229–236
Irwin, K. D. & Hilton, G. C. 2005, Transition-Edge Sensors, ed. C. Enss, 63
Irwin, K. D., Hilton, G. C., Wollman, D. A., & Martinis, J. M. 1996, Applied Physics Letters, 69, 1945
Iwamoto, K., Brachwitz, F., Nomoto, K., et al. 1999, ApJ Supplement, 125, 439
Iyomoto, N., Bandler, S. R., Brekosky, R. P., et al. 2008, Journal of Low Temperature Physics, 151, 506
Jackson, B. D., den Hartog, R., van der Kuur, J., et al. 2018, in Space Telescopes and Instrumentation 2018: Ultraviolet to Gamma Ray, Vol. 10699
Jahoda, K., Swank, J. H., Giles, A. B., et al. 1996, in Proc. SPIE, Vol. 2808, EUV, X-Ray, and Gamma-Ray Instrumentation for Astronomy VII, ed. O. H. Siegmund & M. A. Gummin, 59–70
Jaklevic, R. C., Lambe, J., Silver, A. H., & Mercereau, J. E. 1964, Physical Review Letters, 12, 159
Jansen, F., Lumb, D., Altieri, B., et al. 2001, Astronomy and Astrophysics, 365, L1
Jeans, J. H. 1902, Philosophical Transactions of the Royal Society of London Series A, 199, 1
Jonker, P., O'Brien, P., Amati, L., et al. 2013, ArXiv e-prints 1306.2336
Kaastra, J. 2008, Spectral diagnostics for IXO, Tech. rep., IXO Consortium
Kaastra, J., Finoguenov, A., Nicastro, F., et al. 2013, ArXiv e-prints 1306.2324

Kaastra, J. S. & Bleeker, J. A. M. 2016, Astronomy and Astrophysics, 587, A151
Kaastra, J. S., Mewe, R., & Nieuwenhuijzen, H. 1996, in UV and X-ray Spectroscopy of Astrophysical and Laboratory Plasmas, ed. K. Yamashita & T. Watanabe, 411–414
Kalberla, P. M. W., Burton, W. B., Hartmann, D., et al. 2005, Astronomy and Astrophysics, 440, 775
Karakas, A. I. 2010, MNRAS, 403, 1413
Khatri, R. & Gaspari, M. 2016, MNRAS, 463, 655
Kilbourne, C. A., Doriese, W. B., Bandler, S. R., et al. 2008, in Proc. SPIE, Vol. 7011, Space Telescopes and Instrumentation 2008: Ultraviolet to Gamma Ray, 701104
King, A. & Pounds, K. 2015, Annual Review of Astron. and Astrophys., 53, 115
King, I. R. 1966, Astronomical Journal, 71, 64
Kirkpatrick, C. C., McNamara, B. R., & Cavagnolo, K. W. 2011, Astrophysical Journal, Letters, 731, L23
Kirsch, C. 2016, Master's thesis, Erlangen center for astroparticle physics
Kirsch, M. G., Briel, U. G., Burrows, D., et al. 2005, in Proc. SPIE, Vol. 5898, UV, X-Ray, and Gamma-Ray Space Instrumentation for Astronomy XIV, ed. O. H. W. Siegmund, 22–33
Klebesadel, R. W., Strong, I. B., & Olson, R. A. 1973, ApJ Letters, 182, L85
Knoedler, C. M. 1983, Journal of Applied Physics, 54, 2773
Kolmogorov, A. N. 1941, Akademiia Nauk SSSR Doklady, 30, 301
Komatsu, E., Smith, K. M., Dunkley, J., et al. 2011, ApJ, Supplement, 192, 18
Koyama, K., Tsunemi, H., Dotani, T., et al. 2007, Publications of the ASJ, 59, 23
Krause, M. O. & Oliver, J. H. 1979, Journal of Physical and Chemical Reference Data, 8, 329
Krause, O., Tanaka, M., Usuda, T., et al. 2008, Nature, 456, 617
Kravtsov, A. V. & Borgani, S. 2012, Annual Review of Astron. and Astrophys, 50, 353
Kromer, M., Fink, M., Stanishev, V., et al. 2013, MNRAS, 429, 2287
Kromer, M., Ohlmann, S. T., Pakmor, R., et al. 2015, MNRAS, 450, 3045
Kühl, P., Gómez-Herrero, R., & Heber, B. 2016, Solar Physics, 291, 965
Lattimer, J. M. 2012, Annual Review of Nuclear and Particle Science, 62, 485
Lau, E. T., Kravtsov, A. V., & Nagai, D. 2009, ApJ, 705, 1129
Lea, S. M., Silk, J., Kellogg, E., & Murray, S. 1973, ApJ Letters, 184, L105
Leccardi, A. & Molendi, S. 2008a, Astronomy and Astrophysics, 487, 461
Leccardi, A. & Molendi, S. 2008b, Astronomy and Astrophysics, 486, 359
Leccardi, A., Rossetti, M., & Molendi, S. 2010, Astronomy and Astrophysics, 510, A82
Lehmer, B. D., Xue, Y. Q., Brandt, W. N., et al. 2012, ApJ, 752, 46
Lenz, D. D. & Ayres, T. R. 1992, Publications of the ASP, 104, 1104
Leung, S.-C. & Nomoto, K. 2018, ApJ, 861, 143
Li, N. & Laizet, S. 2010, Cray User Group 2010 conference, Edinburgh
Lindeman, M. A., Bandler, S., Brekosky, R. P., et al. 2004, Nuclear Instruments and Methods in Physics Research A, 520, 348
Lodders, K., Palme, H., & Gail, H.-P. 2009, Landolt Börnstein, 712
Loewenstein, M. 2013, ApJ, 773, 52
Lorenz, M. 2017, Master's thesis, Erlangen center for astroparticle physics
Lotti, S., Cea, D., Macculi, C., et al. 2014, Astronomy and Astrophysics, 569, A54

Lotti, S., Macculi, C., D'Andrea, M., et al. 2018a, in Society of Photo-Optical Instrumentation Engineers (SPIE) Conference Series, Vol. 10699, Space Telescopes and Instrumentation 2018: Ultraviolet to Gamma Ray, 106991Q
Lotti, S., Mineo, T., Jacquey, C., et al. 2018b, Experimental Astronomy, 45, 411
Lotti, S., Mineo, T., Jacquey, C., et al. 2017, Experimental Astronomy, 44, 371
Luukanen, A., Kinnunen, K. M., Nuottajärvi, A. K., et al. 2003, Physical Review Letters, 90, 238306
Macculi, C., Argan, A., D'Andrea, M., et al. 2016, in Proc. SPIE, Vol. 9905, Space Telescopes and Instrumentation 2016: Ultraviolet to Gamma Ray, 99052K
MacFadyen, A. I. & Woosley, S. E. 1999, Astrophysical Journal, 524, 262
Maeda, K., Röpke, F. K., Fink, M., et al. 2010, ApJ, 712, 624
Mantz, A. B., Allen, S. W., Morris, R. G., et al. 2017, MNRAS, 472, 2877
Maoz, D., Mannucci, F., & Nelemans, G. 2014, Annual Review of Astron. and Astrophys, 52, 107
Markevitch, M. & Vikhlinin, A. 2007, Physics Reports, 443, 1
Marquardt, K. S., Sim, S. A., Ruiter, A. J., et al. 2015, Astronomy and Astrophysics, 580, A118
Martínez, V. J., Arnalte-Mur, P., & Stoyan, D. 2010, Astronomy and Astrophysics, 513, A22
Martucci, M., Munini, R., Boezio, M., et al. 2018, ApJ Letters, 854, L2
Mather, J. C. 1982, Applied Optics, 21, 1125
Mather, J. C., Cheng, E. S., Eplee, Jr., R. E., et al. 1990, ApJ Letters, 354, L37
Matteucci, F. & Chiappini, C. 2005, Publications of the Astron. Soc. of Australia, 22, 49
Maul, M. K., Strandberg, M. W., & Kyhl, R. L. 1969, Physical Review, 182, 522
Mazzotta, P., Mazzitelli, G., Colafrancesco, S., & Vittorio, N. 1998, Astrophysics and Space Science, 133, 403
Mazzotta, P., Rasia, E., Moscardini, L., & Tormen, G. 2004, MNRAS, 354, 10
McCammon, D. 2005, Thermal Equilibrium Calorimeters - An Introduction, ed. C. Enss, 1
McCammon, D., Almy, R., Apodaca, E., et al. 2002, ApJ, 576, 188
McCammon, D., Moseley, S. H., Mather, J. C., & Mushotzky, R. F. 1984, Journal of Applied Physics, 56, 1263
McDonald, M., Bayliss, M., Benson, B. A., et al. 2012, Nature, 488, 349
McNamara, B. R. & Nulsen, P. E. J. 2007, Annual Review of Astron. and Astrophys., 45, 117
McNamara, B. R. & Nulsen, P. E. J. 2012, New Journal of Physics, 14, 055023
McQuinn, M. 2016, Annual Review of Astron. and Astrophys., 54, 313
Meidinger, N., Barbera, M., Emberger, V., et al. 2017, in Society of Photo-Optical Instrumentation Engineers (SPIE) Conference Series, Vol. 10397, Society of Photo-Optical Instrumentation Engineers (SPIE) Conference Series, 103970V
Meidinger, N., Eder, J., Fürmetz, M., et al. 2015a, in Proc. SPIE, Vol. 9601, UV, X-Ray, and Gamma-Ray Space Instrumentation for Astronomy XIX, 96010H
Meidinger, N., Nandra, K., Plattner, M., et al. 2015b, Journal of Astronomical Telescopes, Instruments, and Systems, 1, 014006
Merloni, A., Predehl, P., Becker, W., et al. 2012, ArXiv e-prints 1209.3114

Mernier, F., Biffi, V., Yamaguchi, H., et al. 2018, ArXiv e-prints 1811.01967
Mernier, F., de Plaa, J., Kaastra, J. S., et al. 2017, Astronomy and Astrophysics, 603, A80
Mernier, F., de Plaa, J., Lovisari, L., et al. 2015, Astronomy and Astrophysics, 575, A37
Mernier, F., de Plaa, J., Pinto, C., et al. 2016a, Astronomy and Astrophysics, 592, A157
Mernier, F., de Plaa, J., Pinto, C., et al. 2016b, Astronomy and Astrophysics, 595, A126
Merrill, P. W. 1956, Publications of the Astron. Soc. of Australia, 68, 70
Miller, J. M. 2007, Annual Review of Astron. and Astrophys., 45, 441
Miller, J. M., Parker, M. L., Fuerst, F., et al. 2013, ApJ Letters, 775, L45
Miller, M. C. & Miller, J. M. 2015, Physics Reports, 548, 1
Miniati, F. 2015, ApJ, 800, 60
Minin, S. & Kamalabadi, F. 2009, Applied Optics, 48, 6913
Mitchell, R. J., Culhane, J. L., Davison, P. J. N., & Ives, J. C. 1976, MNRAS, 175, 29P
Mitsuda, K., Bautz, M., Inoue, H., et al. 2007, Publications of the ASJ, 59, S1
Miville-Deschenes, M.-A., Joncas, G., & Durand, D. 1995, ApJ, 454, 316
Mohammadzadeh, A., Evans, H., Nieminen, P., et al. 2003, IEEE Transactions on Nuclear Science, 50, 2272
Molendi, S., Eckert, D., De Grandi, S., et al. 2016, Astronomy and Astrophysics, 586, A32
Molendi, S. & Pizzolato, F. 2001, ApJ, 560, 194
Moretti, A., Campana, S., Lazzati, D., & Tagliaferri, G. 2003, ApJ, 588, 696
Morganti, R. 2017, Frontiers in Astronomy and Space Sciences, 4, 42
Morrison, R. & McCammon, D. 1983, ApJ, 270, 119
Moseley, S. H., Kelley, R. L., Schoelkopf, R. J., Szymkowiak, A. E., & McCammon, D. 1988, IEEE Transactions on Nuclear Science, 35, 59
Moseley, S. H., Mather, J. C., & McCammon, D. 1984, Journal of Applied Physics, 56, 1257
Motch, C., Wilms, J., Barret, D., et al. 2013, ArXiv e-prints 1306.2334
Mushotzky, R. F. & Loewenstein, M. 1997, ApJ Letters, 481, L63
Nagai, D., Vikhlinin, A., & Kravtsov, A. V. 2007, ApJ, 655, 98
Nakar, E., Gottlieb, O., Piran, T., Kasliwal, M. M., & Hallinan, G. 2018, ApJ, 867, 18
Nandra, K., Barret, D., Barcons, X., et al. 2013, ArXiv e-prints 1306.2307
Nandra, K., Barret, D., Barcons, X., et al. 2014, ESA White paper
Nandra, K., George, I. M., Mushotzky, R. F., Turner, T. J., & Yaqoob, T. 1997, ApJ, 476, 70
Navarro, J. F., Frenk, C. S., & White, S. D. M. 1997, ApJ, 490, 493
Nicastro, F., Elvis, M., Krongold, Y., et al. 2013, ApJ, 769, 90
Nicastro, F., Kaastra, J., Krongold, Y., et al. 2018, Nature, 558, 406
Nomoto, K. & Hashimoto, M. 1988, Physics Reports, 163, 13
Nomoto, K., Kobayashi, C., & Tominaga, N. 2013, Annual Review of Astron. and Astrophys, 51, 457
Nomoto, K., Tominaga, N., Umeda, H., Kobayashi, C., & Maeda, K. 2006, Nuclear Physics A, 777, 424
Nordfors, B. 1955, Proceedings of the Physical Society A, 68, 654
O'Dea, C. P., Baum, S. A., Privon, G., et al. 2008, ApJ, 681, 1035
Ohlmann, S. T., Kromer, M., Fink, M., et al. 2014, Astronomy and Astrophysics, 572, A57
Olivero, J. 1977, Journal of Quantitiative Spectroscopy and Radiative Transfer, 17, 233

Oosterbroeck, T. 2018, ATHENA - Telescope Reference Design and Effective Area Estimates (v2.5), Tech. report, ESA
Özel, F. & Freire, P. 2016, Annual Review of Astron. and Astrophys., 54, 401
Padovani, P. & Matteucci, F. 1993, ApJ, 416, 26
Pajot, F., Lam Trong, T., den Herder, J.-W., Piro, L., & Cappi, M. 2018, Journal Of Low Temperature Physics
Pakmor, R., Kromer, M., Röpke, F. K., et al. 2010, Nature, 463, 61
Pakmor, R., Kromer, M., Taubenberger, S., et al. 2012, ApJ Letters, 747, L10
Peille, P., Ceballos, M. T., Cobo, B., et al. 2016, in Proc. SPIE, Vol. 9905, Space Telescopes and Instrumentation 2016: Ultraviolet to Gamma Ray, 99055W
Peille, P., Dauser, T., den Hartog, R., et al. 2019, XIFU-TN-SYS-00175-CNES X-IFU throughput budget v2.1, Tech. rep., Athena X-IFU Consortium
Peille, P., Dauser, T., Kirsch, C., et al. 2018a, Journal Of Low Temperature Physics
Peille, P., den Hartog, R., Macculi, C., et al. 2018b, in Society of Photo-Optical Instrumentation Engineers (SPIE) Conference Series, Vol. 10699, Space Telescopes and Instrumentation 2018: Ultraviolet to Gamma Ray, 106994K
Penzias, A. A. & Wilson, R. W. 1965, ApJ, 142, 419
Peterson, J. R., Kahn, S. M., Paerels, F. B. S., et al. 2003, ApJ, 590, 207
Pfeffermann, E., Briel, U. G., Hippmann, H., et al. 1987, in Proc. SPIE, Vol. 733, Soft X-ray optics and technology, ed. E.-E. Koch & G. Schmahl, 519
Planck Collaboration, Ade, P. A. R., Aghanim, N., et al. 2016, Astronomy and Astrophysics, 594, A13
Planck Collaboration, Aghanim, N., Akrami, Y., et al. 2018, arXiv e-prints 1807.06209
Planelles, S., Schleicher, D. R. G., & Bykov, A. M. 2015, Space Science Reviews, 188, 93
Plucinsky, P. P., Haberl, F., Dewey, D., et al. 2008, in Proc. SPIE, Vol. 7011, Space Telescopes and Instrumentation 2008: Ultraviolet to Gamma Ray, 70112E
Pointecouteau, E., Reiprich, T. H., Adami, C., et al. 2013, ArXiv e-prints 1306.2319
Porter, F. S., Chiao, M. P., Eckart, M. E., et al. 2016, Journal of Low Temperature Physics, 184, 498
Pounds, K. A., Reeves, J. N., King, A. R., et al. 2003, MNRAS, 345, 705
Pratt, G. W., Arnaud, M., Biviano, A., et al. 2019, Space Science Reviews, 215, 25
Pratt, G. W., Arnaud, M., Piffaretti, R., et al. 2010, Astronomy and Astrophysics, 511, A85
Pratt, G. W., Croston, J. H., Arnaud, M., & Böhringer, H. 2009, A&A, 498, 361
Prêle, D., Voisin, F., Beillimaz, C., Chen, S., & Goldwurm, A. 2016, Journal of Astronomical Telescopes, Instruments, and Systems, 2, 046002
Press, W. H. & Schechter, P. 1974, ApJ, 187, 425
Psaltis, D. 2008, Living Reviews in Relativity, 11, 9
Rasia, E., Borgani, S., Ettori, S., Mazzotta, P., & Meneghetti, M. 2013, ApJ, 776, 39
Rasia, E., Borgani, S., Murante, G., et al. 2015, ApJ, Letters, 813, L17
Rasia, E., Ettori, S., Moscardini, L., et al. 2006, MNRAS, 369, 2013
Rasia, E., Mazzotta, P., Bourdin, H., et al. 2008, ApJ, 674, 728
Rau, A., Nandra, K., Aird, J., et al. 2016, in Proc. SPIE, Vol. 9905, Space Telescopes and Instrumentation 2016: Ultraviolet to Gamma Ray, 99052B

Ravera, L., Barret, D., den Herder, J. W., et al. 2014a, in Proc. SPIE, Vol. 9144, Space Telescopes and Instrumentation 2014: Ultraviolet to Gamma Ray, 91442L
Ravera, L., Cara, C., Ceballos, M. T., et al. 2014b, in Proc. SPIE, Vol. 9144, Space Telescopes and Instrumentation 2014: Ultraviolet to Gamma Ray, 91445T
Ravera, L., Gumuchian, P., Clénet, A., et al. 2018, in Society of Photo-Optical Instrumentation Engineers (SPIE) Conference Series, Vol. 10699, Space Telescopes and Instrumentation 2018: Ultraviolet to Gamma Ray, 106994V
Reeves, J. N., O'Brien, P. T., & Ward, M. J. 2003, ApJ Letters, 593, L65
Reiprich, T. H., Basu, K., Ettori, S., et al. 2013, Space Science Reviews, 177, 195
Renzini, A. & Andreon, S. 2014, MNRAS, 444, 3581
Revnivtsev, M., Sazonov, S., Jahoda, K., & Gilfanov, M. 2004, Astronomy and Astrophysics, 418, 927
Riess, A. G., Strolger, L.-G., Tonry, J., et al. 2004, ApJ, 607, 665
Roelens, M., Eyer, L., Mowlavi, N., et al. 2017, MNRAS, 472, 3230
Romano, D., Karakas, A. I., Tosi, M., & Matteucci, F. 2010, Astronomy and Astrophysics, 522, A32
Roncarelli, M., Cappelluti, N., Borgani, S., Branchini, E., & Moscardini, L. 2012, MNRAS, 424, 1012
Roncarelli, M., Gaspari, M., Ettori, S., et al. 2018, Astronomy and Astrophysics, 618, A39
Rosati, P., Borgani, S., & Norman, C. 2002, Annual Review of Astron. and Astrophys, 40, 539
Rossetti, M. & Molendi, S. 2010, Astronomy and Astrophysics, 510, A83
Rubin, V. C. & Ford, Jr., W. K. 1970, ApJ, 159, 379
Rybicki, G. B. & Lightman, A. P. 1979, Radiative processes in astrophysics
Sakai, K., Adams, J. S., Bandler, S. R., et al. 2018, Journal of Low Temperature Physics, 193, 356
Salpeter, E. E. 1955, ApJ, 121, 161
Salpeter, E. E. 1964, ApJ, 140, 796
Sanders, J. S. 2006, MNRAS, 371, 829
Sarazin, C. L. 1988, Sky, 76, 639
Sazonov, S. Y. & Revnivtsev, M. G. 2004, Astronomy and Astrophysics, 423, 469
Schaye, J., Crain, R. A., Bower, R. G., et al. 2015, MNRAS, 446, 521
Schindler, S. & Diaferio, A. 2008, Space Science Reviews, 134, 363
Schmid, C. 2012, Master's thesis, Erlangen Center for Astroparticle Physics
Schmid, C., Smith, R., & Wilms, J. 2013, SIMPUT - A File Format for Simulation Input, Tech. report, HEASARC, Cambridge (MA)
Schweppe, J., Deslattes, R. D., Mooney, T., & Powerll, C. J. 1994, Journal of Electron Spectroscopy and Related Phenomena, 67, 463
Sciortino, S., Rauw, G., Audard, M., et al. 2013, ArXiv e-prints 1306.2333
Seidel, G. M. & Beloborodov, I. S. 2004, Nuclear Instruments and Methods in Physics Research A, 520, 325
Seitenzahl, I. R., Ciaraldi-Schoolmann, F., Röpke, F. K., et al. 2013, MNRAS, 429, 1156
Seitenzahl, I. R., Kromer, M., Ohlmann, S. T., et al. 2016, Astronomy and Astrophysics, 592, A57

Seta, H., Tashiro, M. S., Ishisaki, Y., et al. 2012, IEEE Transactions on Nuclear Science, 59, 366
Shen, K. J., Boubert, D., Gänsicke, B. T., et al. 2018, ApJ, 865, 15
Silk, J. & Mamon, G. A. 2012, Research in Astronomy and Astrophysics, 12, 917
Silk, J. & Rees, M. J. 1998, Astronomy and Astrophysics, 331, L1
Sim, S. A., Fink, M., Kromer, M., et al. 2012, MNRAS, 420, 3003
Sim, S. A., Röpke, F. K., Hillebrandt, W., et al. 2010, ApJ Letters, 714, L52
Simionescu, A., Allen, S. W., Mantz, A., et al. 2011, Science, 331, 1576
Simionescu, A., Nakashima, S., Yamaguchi, H., et al. 2019a, MNRAS, 483, 1701
Simionescu, A., Werner, N., Mantz, A., Allen, S. W., & Urban, O. 2017, MNRAS, 469, 1476
Simionescu, A., ZuHone, J., Zhuravleva, I., et al. 2019b, Space Science Reviews, 215, 24
Smith, R. 2013, SIMX: Event simulator, Astrophysics Source Code Library
Smith, R. K., Brickhouse, N. S., Liedahl, D. A., & Raymond, J. C. 2001, ApJ, Letters, 556, L91
Smith, S. 1936, ApJ, 83, 23
Smith, S. J., Adams, J. S., Bailey, C. N., et al. 2013, Journal of Applied Physics, 114, 074513
Smith, S. J., Adams, J. S., Bandler, S. R., et al. 2016, in Proc. SPIE, Vol. 9905, Space Telescopes and Instrumentation 2016: Ultraviolet to Gamma Ray, 99052H
Smoot, G. F., Bennett, C. L., Kogut, A., et al. 1992, ApJ Letters, 396, L1
Snowden, S. L., Freyberg, M. J., Plucinsky, P. P., et al. 1995, ApJ, 454, 643
Springel, V. 2005, MNRAS, 364, 1105
Springel, V. & Hernquist, L. 2003, MNRAS, 339, 289
Stark, J. P., Davison, P. J. N., & Culhane, J. L. 1976, MNRAS, 174, 35P
Stefanescu, A., Bautz, M. W., Burrows, D. N., et al. 2010, Nuclear Instruments and Methods in Physics Research A, 624, 533
Steinborn, L. K., Dolag, K., Hirschmann, M., Prieto, M. A., & Remus, R.-S. 2015, MNRAS, 448, 1504
Stever, S. L., Couchot, F., Coron, N., Janssen, R. M. J., & Maffei, B. 2018, in Society of Photo-Optical Instrumentation Engineers (SPIE) Conference Series, Vol. 10698, Space Telescopes and Instrumentation 2018: Optical, Infrared, and Millimeter Wave, 1069863
Strüder, L., Briel, U., Dennerl, K., et al. 2001, Astronomy and Astrophysics, 365, L18
Sturm, E., González-Alfonso, E., Veilleux, S., et al. 2011, ApJ Letters, 733, L16
Sukhbold, T., Ertl, T., Woosley, S. E., Brown, J. M., & Janka, H.-T. 2016, ApJ, 821, 38
Sunyaev, R. A. & Zeldovich, Y. B. 1972, Comments on Astrophysics and Space Physics, 4, 173
Szymkowiak, A. E., Kelley, R. L., Moseley, S. H., & Stahle, C. K. 1993, Journal of Low Temperature Physics, 93, 281
Takahashi, T., Kokubun, M., Mitsuda, K., et al. 2018, Journal of Astronomical Telescopes, Instruments, and Systems, 4, 021402
Tanaka, T., Uchida, H., Nakajima, H., et al. 2018, Journal of Astronomical Telescopes, Instruments, and Systems, 4, 011211

Tashiro, M., Maejima, H., Toda, K., et al. 2018, in Society of Photo-Optical Instrumentation Engineers (SPIE) Conference Series, Vol. 10699, Space Telescopes and Instrumentation 2018: Ultraviolet to Gamma Ray, 1069922
Thielemann, F.-K., Argast, D., Brachwitz, F., et al. 2003, in From Twilight to Highlight: The Physics of Supernovae, ed. W. Hillebrandt & B. Leibundgut, 331
Thielemann, F.-K., Eichler, M., Panov, I. V., & Wehmeyer, B. 2017, Annual Review of Nuclear and Particle Science, 67, 253
Tombesi, F., Cappi, M., Reeves, J. N., et al. 2010, Astronomy and Astrophysics, 521, A57
Tornatore, L., Borgani, S., Dolag, K., & Matteucci, F. 2007, MNRAS, 382, 1050
Tornatore, L., Borgani, S., Matteucci, F., Recchi, S., & Tozzi, P. 2004, MNRAS, 349, L19
Treberspurg, W., Andritschke, R., Hauser, G., et al. 2018a, Journal of Instrumentation, 13, P09014
Treberspurg, W., Müller-Seidlitz, J., Meidinger, N., et al. 2018b, in Society of Photo-Optical Instrumentation Engineers (SPIE) Conference Series, Vol. 10699, Space Telescopes and Instrumentation 2018: Ultraviolet to Gamma Ray, 106994F
Truong, N., Rasia, E., Mazzotta, P., et al. 2018, MNRAS, 474, 4089
Tsujimoto, M., Mitsuda, K., Kelley, R. L., et al. 2018, Journal of Astronomical Telescopes, Instruments, and Systems, 4, 011205
Turner, M. J. L., Abbey, A., Arnaud, M., et al. 2001, Astronomy and Astrophysics, 365, L27
Tylka, A. J., Adams, J. H., Boberg, P. R., et al. 1997, IEEE Transactions on Nuclear Science, 44, 2150
Ueda, Y., Akiyama, M., Ohta, K., & Miyaji, T. 2003, ApJ, 598, 886
Ullom, J. N., Adams, J. S., Alpert, B. K., et al. 2018, in Space Telescopes and Instrumentation 2018: Ultraviolet to Gamma Ray, Vol. 10699
Ullom, J. N., Doriese, W. B., Hilton, G. C., et al. 2004, Applied Physics Letters, 84, 4206
Urban, O., Werner, N., Allen, S. W., Simionescu, A., & Mantz, A. 2017, MNRAS, 470, 4583
Usoskin, I. G., Alanko-Huotari, K., Kovaltsov, G. A., & Mursula, K. 2005, Journal of Geophysical Research (Space Physics), 110, A12108
Utrobin, V. P., Wongwathanarat, A., Janka, H.-T., & Müller, E. 2015, A&A, 581, A40
van der Kuur, J., Gottardi, L., Akamatsu, H., et al. 2018, Journal of Low Temperature Physics, 193, 626
van der Kuur, J., Gottardi, L. G., Akamatsu, H., et al. 2016, in Proc. SPIE, Vol. 9905, Space Telescopes and Instrumentation 2016: Ultraviolet to Gamma Ray, 99055R
Vazza, F., Brunetti, G., Kritsuk, A., et al. 2009, Astronomy and Astrophysics, 504, 33
Verbunt, F. 1993, Annual Review of Astron. and Astrophys., 31, 93
Verner, D. A., Ferland, G. J., Korista, K. T., & Yakovlev, D. G. 1996, ApJ, 465, 487
Vikhlinin, A., Kravtsov, A., Forman, W., et al. 2006, ApJ, 640, 691
Vogelsberger, M., Genel, S., Springel, V., et al. 2014, MNRAS, 444, 1518
Vogelsberger, M., Marinacci, F., Torrey, P., et al. 2018, MNRAS, 474, 2073
Voit, G. M. 2018, ApJ, 868, 102
Voit, G. M., Kay, S. T., & Bryan, G. L. 2005, MNRAS, 364, 909
Volonteri, M. 2012, Science, 337, 544

von Kienlin, A., Eraerds, T., Bulbul, E., et al. 2018, in Society of Photo-Optical Instrumentation Engineers (SPIE) Conference Series, Vol. 10699, Space Telescopes and Instrumentation 2018: Ultraviolet to Gamma Ray, 106991I
Waldman, R., Sauer, D., Livne, E., et al. 2011, ApJ, 738, 21
Walker, S., Simionescu, A., Nagai, D., et al. 2019, Space Science Reviews, 215, 7
Warren, J. S., Hughes, J. P., Badenes, C., et al. 2005, ApJ, 634, 376
Webbink, R. F. 1984, ApJ, 277, 355
Wei, J., Cordier, B., Antier, S., et al. 2016, ArXiv e-prints 1610.06892
Weinberg, D. H., Mortonson, M. J., Eisenstein, D. J., et al. 2013, Physics Reports, 530, 87
Weisskopf, M. C., Brinkman, B., Canizares, C., et al. 2002, Publications of the ASP, 114, 1
Weisskopf, M. C., Tananbaum, H. D., Van Speybroeck, L. P., & O'Dell, S. L. 2000, in Proc. SPIE, Vol. 4012, X-Ray Optics, Instruments, and Missions III, ed. J. E. Truemper & B. Aschenbach, 2–16
Wells, D. C., Greisen, E. W., & Harten, R. H. 1981, Astronomy and Astrophysics, Supplement, 44, 363
Werner, N., Böhringer, H., Kaastra, J. S., et al. 2007, in Heating versus Cooling in Galaxies and Clusters of Galaxies, ed. H. Böhringer, G. W. Pratt, A. Finoguenov, & P. Schuecker, 309
Werner, N., de Plaa, J., Kaastra, J. S., et al. 2006, Astronomy and Astrophysics, 449, 475
Werner, N., Durret, F., Ohashi, T., Schindler, S., & Wiersma, R. P. C. 2008, Space Science Reviews, 134, 337
Werner, N., Urban, O., Simionescu, A., & W., A. S. 2013, Nature, 502, 656 EP
Whelan, J. & Iben, Jr., I. 1973, ApJ, 186, 1007
White, S. D. M., Navarro, J. F., Evrard, A. E., & Frenk, C. S. 1993, Nature, 366, 429
Wiersma, R. P. C., Schaye, J., & Smith, B. D. 2009, MNRAS, 393, 99
Willingale, R., Pareschi, G., Christensen, F., & den Herder, J.-W. 2013, ArXiv e-prints 1307.1709
Wilms, J., Allen, A., & McCray, R. 2000, ApJ, 542, 914
Wilms, J., Brand, T., Barret, D., et al. 2014, in Proc. SPIE, Vol. 9144, Space Telescopes and Instrumentation 2014: Ultraviolet to Gamma Ray, 91445X
Wilms, J., Smith, S. J., Peille, P., et al. 2016, in Proc. SPIE, Vol. 9905, Space Telescopes and Instrumentation 2016: Ultraviolet to Gamma Ray, 990564
Wise, J. H. 2012, ArXiv e-prints 1201.482
Wollman, D. A., Irwin, K. D., Hilton, G. C., & Martinis, J. M. 1997, in APS March Meeting Abstracts, C20.05
Wong, K.-W., Sarazin, C. L., & Ji, L. 2011, ApJ, 727, 126
Woosley, S. E. & Weaver, T. A. 1995, ApJ, Supplement, 101, 181
Wright, B. S. & Li, B. 2018, Physical Review D, 97, 083505
Zappe, H. 1977, IEEE Transactions on Magnetics, 13, 41
Zhang, W. W., Allgood, K. D., Biskach, M. P., et al. 2018, in Society of Photo-Optical Instrumentation Engineers (SPIE) Conference Series, Vol. 10699, 106990O
Zhuravleva, I., Churazov, E., Arévalo, P., et al. 2015, MNRAS, 450, 4184
Zhuravleva, I., Churazov, E., Sunyaev, R., et al. 2013, MNRAS, 435, 3111
Zhuravleva, I., Churazov, E. M., Schekochihin, A. A., et al. 2014, ApJ Letters, 788, L13

ZuHone, J. A., Markevitch, M., Brunetti, G., & Giacintucci, S. 2013, ApJ, 762, 78
ZuHone, J. A., Markevitch, M., & Zhuravleva, I. 2016, ApJ, 817, 110
Zwicky, F. 1937, ApJ, 86, 217